School of Civil and Mechanical Engineering

Dynamic Analysis and Design of Monolithic and Segmental Concrete Bridge Columns against Impact Loads

Van Tin Do

This thesis is presented to the Degree of

Doctor of Philosophy

of

Curtin University

July 2019

Declaration

To the best of my knowledge and belief this thesis contains no material previously published by any other person except where due acknowledgment has been made.

This thesis contains no material which has been accepted for the award of any other degree or diploma in any university.

Signature: … ████████████████████ (VAN TIN DO)

Date: ……12/07/2019…..

DEDICATION

To my beloved family: my father, my (late) mother, my sisters, and my brother!

To my thesis advisors (Professor Hong Hao and Dr. Thong Pham)!

ABSTRACT

In the recent decades, vehicle collisions with columns or bridge piers occur more frequently due to the urbanization with more vehicles on the more congested road leading to an increased number of accidents, as well as the increase of terrorist attacks targeting on the transportation infrastructure. These accidental and deliberated events raise concerns on protecting structures against vehicle collisions since a huge impact force from a collision event not only causes severe damage to columns, which might lead to collapse of entire bridge structure and paralysis of the transport systems, but also costs human lives. Despite the occurrence of such extreme events and their highly destructive consequences, the dynamic performances and impact-resistant capacities of reinforced concrete (RC) columns under vehicle collisions are not well understood, hence bridge piers are not necessarily effectively designed to resist such impact loads. Currently, to estimate the impact force and design column structures against a collision event, an equivalent static force (ESF) is commonly adopted in design codes and provisions. Although this method is straightforward, it ignores the dynamic effects on structures under impact loads, i.e. inertia resistance, strength enhancement of materials, and structural vibrations. Thus, the ESF-based analysis may produce an un-conservative design of columns under vehicle collisions and does not have an ability to predict real behaviours of structures under impact loading conditions. Therefore, a comprehensive investigation on the dynamic behaviours of RC columns against impact loads is required while a simplified design procedure which reliably predicts the impact responses of the columns is also needed for effective design of bridge piers.

Extensive research efforts have been conducted on the dynamic performances of precast concrete segmental columns (PCSCs) since this type of columns has been increasingly adopted in the construction industry in recent years owing to their many advantages as compared to the monolithic ones. These include significantly improving the construction quality, improving work-zone safety, decreasing on-site construction time and site interruption, and diminishing environmental impacts. However, most of the previous studies focused on the seismic performance and seismic-resistant capacity of PCSCs while understanding of the impact behaviours of the PCSCs, i.e. number of joint openings, relative shear slippage between segments, and column failure modes, is very limited. The dynamic analysis of PCSCs against impact loads is, therefore, crucial when designing new PCSCs. In the meantime, an effective strengthening method is also required to improve the performance of existing PCSCs.

The primary objectives of this dissertation are to analyse the dynamic performances of monolithic and segmental bridge columns subjected to impact loads and to propose a practical design procedure for the columns against vehicle collisions. Pros and cons of these two types

I

of the columns in resisting the impact force from vehicle collisions are then investigated and discussed. Moreover, an effective strengthening method is suggested to enhance the impact-resistant capacity of PCSCs. This dissertation, therefore, can be reasonably divided into two parts, with the first part focusing on the dynamic analysis and design of monolithic RC columns under vehicle collisions and the second part centring on the impact responses and analysis of PCSCs. Particularly, in Chapter 2, a numerical model of a monolithic bridge column subjected to truck impacts, which is simulated in the commercial software LS-DYNA and carefully validated by experimental results, is developed and presented. The variation of the column inertia resistance, bending moment, and shear force during the impact force phase is examined. Furthermore, the numerical results are utilised to explain different column failure modes observed in real collision events. The numerical model is also employed to develop the impact force profiles of a RC column induced by vehicle impacts and determine the dynamic shear model of the column under impact loads (Chapter 3). A comprehensive design procedure of a RC column against vehicle impacts with consideration of the dynamic effects of structures is proposed in Chapter 4.

In the second part, a detailed simulation methodology of a PCSC subjected to impact loads, including modelling the prestressing, strain rate effects, and contact between segments is introduced in Chapter 5. The accuracy of the numerical model is carefully verified against experimental impact testing results. The effect of initial impact conditions and column properties, i.e. impact velocity, concrete strength, number of segments, and initial prestress load, on the column responses are also examined in this chapter. The advantages of the PCSC in absorbing the impact energy and mitigating the column damage from vehicle collisions as compared to the monolithic column are discussed in Chapter 6. Practical equations to determine the bending moment required to open the segment joint and estimate the maximum bending capacity of the PCSC at the joint are also proposed. Furthermore, steel tubes are utilised to cover concrete segments to protect the PCSC against impact loads (Chapter 7). The numerical results demonstrate that the proposed strengthening method with all concrete segments covered by steel tubes can effectively mitigate the damage of PCSCs under impact loads and thus significantly increase the impact resistance capacity of the column.

ACKNOWLEDGMENT

LIST OF PUBLISHED WORK

This thesis contains **a series of published work** which have been co-authored. The bibliographical details of the work and where it appears in the thesis are outlined below.

Chapter 2

Do, T. V., Pham, T. M., & Hao, H. (2018). Dynamic responses and failure modes of bridge columns under vehicle collision. *Engineering Structures, 156*, 243-259. https://doi.org/10.1016/j.engstruct.2017.11.053

Chapter 3

Do, T. V., Pham, T. M., & Hao, H. (2019). Impact force profile and failure classification of reinforced concrete bridge columns against vehicle impact. *Engineering Structures, 183*, 443-458. https://doi.org/10.1016/j.engstruct.2019.01.040

Chapter 4

Do, T. V., Pham, T. M., & Hao, H. (2019). Proposed Design Procedure for Reinforced Concrete Bridge Columns against Vehicle Collisions. Structures, 22(2019), 213-229. https://doi.org/10.1016/j.istruc.2019.08.011

Chapter 5

Do, T. V., Pham, T. M., & Hao, H. (2018). Numerical investigation of the behavior of precast concrete segmental columns subjected to vehicle collision. *Engineering Structures, 156*, 375-393. https://doi.org/10.1016/j.engstruct.2017.11.033

Chapter 6

Do, T. V., Pham, T. M., & Hao, H. (2019). Impact response and capacity of precast concrete segmental versus monolithic bridge columns. *Journal of Bridge Engineering, 24*(6), 04019050. https://doi.org/10.1061/(ASCE)BE.1943-5592.0001415

Chapter 7

Do, T. V., Pham, T. M., & Hao, H. (2019). Effects of steel confinement and shear keys on the impact responses of precast concrete segmental columns. *Journal of Constructional Steel Research, 158*, 331-349. https://doi.org/10.1016/j.jcsr.2019.04.008

STATEMENT OF CONTRIBUTION OF OTHERS

This research project was initiated by Prof. Hong Hao, who defined the overall objectives of the entire project, guided the research approach and possible research methodologies, and secured the financial support. In each publication, Dr. Thong Pham advised aims and objectives of the work while the candidate (Van Tin Do) who is also the first author of the publications was responsible for conducting the literature review, developing the numerical models, conducting numerical simulations, analysing and interpreting the simulation results, and writing the manuscript drafts. Dr. Thong Pham and Prof. Hong Hao then provided additional intellectual input in the discussions of the results and revised the manuscript before and during submission. The attribution of the authorship is signed by co-authors and attached in the appendix.

LIST OF RELEVANT ADDITIONAL PUBLICATIONS

The additional publications relevant to the thesis but not forming part of it with the bibliographical details are listed below.

Keynote presentations

1. Hao, H., Zhang, X., Li, C., & **Do, T. V.** (2017). Impact response and mitigation of precast concrete segmental columns. *12th International Conference on Shock and Impact Loads on Structures.*, Singapore.

2. Hao, H., **Do, T. V.,** & Pham, T. M (2018). Response of Precast Concrete Segmental Columns versus Conventional Monolithic Columns under Vehicle Impact. *3rd International Conference on Transportation Infrastructure and Materials: Smart and Sustainable Transportation Infrastructure (ICTIM)*, Tianjin, China.

3. Hao, H., **Do, T. V.**, & Pham, T. M. (2018). Structural Performance Evaluation of Prefabricated Concrete Segmental Columns and Conventional Monolithic Columns against Vehicle Impact. *7th International Conference on the Protection of Structures against Hazards*, Hanoi, Vietnam.

Journal papers

1. Zhang, X., Hao, H., Li, C., & **Do, T. V.** (2018). Experimental study on the behavior of precast segmental column with domed shear key and unbonded Post-Tensioning tendon under impact loading. Engineering Structures, 173, 589-605.

2. Li, C., Bi, K., Hao, H., Zhang, X., & **Do, T. V.** (2019). Cyclic test and numerical study of precast segmental concrete columns with BFRP and TEED. *Bulletin of Earthquake Engineering*, 1-20.

3. **Do, T. V.**, Pham, T. M., & Hao, H. (2019). Stress wave propagation and response of precast concrete segmental columns under blast loads. (Under review).

Conference proceeding papers

1. **Do, T. V.**, Pham, T. M., & Hao, H. (2018). Performances of Reinforced Concrete Bridge Columns under Vehicle Impact. *5th International Conference on Protective Structures*, Poznan, Poland.

TABLE OF CONTENTS

LIST OF FIGURES

XIV

XV

LIST OF TABLES

CHAPTER 1
INTRODUCTION

1.1. Preamble

Recent development of transportation systems and increase in traffic volume in urban areas together with the increase of terrorism activities targeting on the transportation infrastructure raises concerns on protecting structures against vehicle collisions and impact loads since the number of accidental and deliberated impact events has been significantly increased in the past few decades. A collision from a medium truck or heavy truck associated with high impact velocity might cause severe damage and failure of an impacted structural component which could result in collapse of entire structure system, paralyse of transport network, and cost human lives. It was reported that collisions from vehicles and vessels are the third reason causing collapse of bridge structures in the United States in recent decades (Agrawal et al., 2011). Several extreme collision events occurred in the US from 1965 to 2008 were documented by Buth et al. (2010) in which the failure of impacted bridge piers and the collapse of superstructures were observed, e.g. the accident in Corsicana, Texas in 2002 and in Canton, Texas in 2008. Moreover, truck collisions to column structures and their devastating consequences were also observed in developed and developing countries all around the world, e.g. in China, due to the significant increase of the transportation sector and the development of complex traffic systems. For example, death of two people and shutdown of the affected transport system for two months were reported in Hunan, China in 2009 when the heavy truck collided to a bridge pier (Chen & Xiao, 2012). In June 2018, another truck collision to a bridge pier also happened in Harbin-Dalian Expressway in China with the collapse of the impacted pier and the death of the driver (Chen, 2018). These serious repercussions not only show the vulnerability of bridge piers and columns under impact loads but also indicate the inadequacy of the current design codes and provisions in predicting the responses of structures under vehicle collisions. Apart from colliding by vehicles, during the service life, columns and bridge piers might experience impacts loads from various sources, e.g. falling rocks, ship and barge impacts, and flying debris impacts when the columns are constructed in mountain areas, rivers, or in disaster areas with the frequent occurrence of storms or tornados (Larsen, 1993; Volkwein et al., 2011). Therefore, it is crucial to understand and accurately predict the dynamic responses of column structures and bridge piers under vehicle collisions and impact loads.

Currently, to design column structures against a collision event, the impact force is usually simplified as an equivalent static force (ESF) in design guides and provisions (AASHTO, 2012; CEN, 2002, 2006; SA/SNZ, 2002). For instance, based on the collision tests on the rigid steel column from a heavy truck trailer (Buth et al., 2011; Buth et al., 2010) and the open

literature, AASHTO (2012) suggested to use the horizontal static force of 2,668 kN to apply on a column or a bridge pier at 1.5 m above the ground level when designing these structures against vehicle collisions. It is noted that this magnitude of the static force is constant irrespective of column properties and initial impact conditions. SA/SNZ (2002) and CEN (2002) provided a simplified equation to estimate the maximum equivalent static force from a vehicle collision on a structure by considering the initial kinetic energy of the vehicle and deformation of both the vehicle and the impacted structure. CEN (2006) classified collision events in two groups, i.e. soft impact and hard impact, depending on the relative stiffness between a vehicle and an impacted column. The maximum equivalent static force from a vehicle impact is then determined based on the total mass of the vehicle, impact velocity, and the equivalent elastic stiffness of the softer part of the vehicle and the impacted column in the impact event. Although this ESF method is straightforward to define the impact force and design structures against vehicle collisions, the effects of high loading rate of impact loads, i.e. inertia resistance, stress wave propagation, structure vibrations, and strain rate effects, on the structural responses have been ignored. This simplification thus may produce un-conservative designs of structures subjected to vehicle impacts, as reported in previous studies (Do et al., 2018, 2019; El-Tawil et al., 2005; Sharma et al., 2012). Moreover, the variation of column failures, e.g. global flexural response, shear crack at column top, and diagonal and punching shear failures at the impacted area, observed in real collision events (Buth et al., 2011; Chen & Xiao, 2012; Chen, 2018), cannot be predicted and explained by using the provided ESF in the design guides. Owing to the limitations of the ESF method, experimental works and numerical simulations have been conducted in previous studies to investigate the dynamic responses of column structures under vehicle collisions (Abdelkarim & ElGawady, 2017; Chen et al., 2016; Chen et al., 2015; El-Tawil et al., 2005; Sharma et al., 2012). However, in general, these studies either focused on estimating only the peak impact force (PIF) on structures or defining the column failures under vehicle collisions while the structural response characteristics, i.e. axial force, bending moment, and shear force, were not well examined. The influences of inertia resistance and strain rate effects in resisting the impact force were not explicitly investigated either. In addition, previous numerical studies usually ignored damage of concrete at the impact point when predicting the impact force. These numerical simulations assumed concrete as either an elastic or a rigid structure. Since the local contact stiffness and the interaction of the impacted concrete and a car play an essential role in the impact force, these simplifications may lead to unreliable predictions. Therefore, a comprehensive numerical model which accurately predicts the dynamic responses of column structures under vehicle collisions is required. A design procedure which considers the dynamic effects of high loading rates of impact loads is also sought.

2

Furthermore, together with conventional monolithic reinforced concrete (RC) columns, precast concrete segmental columns (PCSCs) are also one of the most popular structures in the construction industry where a number of bridge structures or buildings using this type of column have been considerably increased in the recent years (Culmo, 2011; Ou, 2007). As compared to cast-in-place monolithic RC columns, PCSCs offer more advantages in both economic and structural aspects. The use of PCPCs which are commonly prepared off-site significantly reduces construction periods, improves constructability, diminishes environmental influences, and decreases on-site interruption (Dawood, 2010; Ou, 2007). Also, the casting and curing of column segments in a workshop provide a possible solution to introduce a new construction technique, i.e. strengthening methods, or apply advanced materials, i.e. geo-polymer concrete, and ultra-high performance concrete, which usually requires heat curing and/or careful mixing. Together with the economic benefits, the advantages of PCSCs in resisting the cyclic loads and seismic loads as compared to the monolithic columns have also been confirmed in previous studies (Bu et al., 2015; Marriott et al., 2009; Wang et al., 2014). However, the responses of PCSCs under impact loads have received insufficient attention with only a few studies on the impact performances of the PCSC (Chung et al., 2014; Zhang et al., 2016). Therefore, more studies on the impact responses of the PCSC are also required to boost the application of this accelerated column in the construction industry.

1.2. Research objectives

From the above review, the primary goal of this research is to investigate the dynamic responses of both monolithic reinforced concrete (RC) columns and precast concrete segmental columns (PCSCs) under impact loads or vehicle collisions. The specific objectives of this dissertation are:

1. To develop comprehensive numerical models to accurately predict the dynamic responses of both monolithic RC columns and PCSCs under impact loads or vehicle collisions. The variation of bending moment, shear force, axial force, and inertial force in the columns during the impact events will be investigated.

2. To propose a vehicle impact force profile model for design purposes in which the effects of column parameters, impact conditions, and column failure are taken into consideration.

3. To determine the dynamic capacity of a monolithic RC column under impact loads or vehicle collisions.

4. To propose a comprehensive procedure to design a RC column under different impact conditions of vehicles.

5. To investigate the dynamic responses of precast concrete segmental columns under vehicle collisions.

6. To study the advantages of PCSCs in resisting the impact loads as compared to the monolithic RC column.

7. To propose an effective strengthening method and shear key design to enhance the impact resistance capacity of PCSCs.

1.3. Research outlines

This dissertation consists of eight chapters and classified into two parts, where part 1 is for monolithic RC columns and part 2 focuses on PCSCs. The contents of the 7 chapters are summarised as follows:

Part 1: Monolithic RC columns

A detailed 3-dimensional (3D) finite element (FE) model of a monolithic reinforced concrete (RC) column subjected to impact loads is firstly developed by using the FE code LS-DYNA in Chapter 2. The accuracy of the numerical model is validated against experimental results. The validated numerical model is then used to develop a full-scale bridge specimen under collisions by a truck model. Variation of the induced bending moment, shear force, axial force, and acceleration along the column height, as well as the column failure under various initial conditions of the vehicle model, is investigated. The numerical simulations are also used to reproduce and explain all failure modes of RC columns under vehicle collision as observed in real events.

Following Chapter 2, the influences of parameters of monolithic columns, i.e. cross-section dimension, reinforcement ratios, slenderness, initial axial force, and initial conditions of a vehicle, i.e. vehicle mass, engine mass, and vehicle velocity, on the impact force time history and column responses are systematically investigated in Chapter 3. Based on the simulation results, the impact force profile model representing collisions from the heavy truck and medium truck on RC columns is then proposed. Moreover, from the shear mechanism of RC columns under impact loads, the maximum dynamic shear capacity of the column is also determined. A classification of column responses and failures under impact loads or vehicle collisions is also proposed.

In Chapter 4, the maximum induced bending moment and shear force at critical sections in the monolithic columns, i.e. impact location, column base, column top, and an intermediate section, caused by vehicle impacts are determined. A complete procedure to design a RC column under vehicle collisions is then proposed in this chapter. Two design examples, which represent two different failure modes of RC columns under vehicle collisions, are presented.

Part 2: Precast concrete segmental columns

To study the dynamic performances of precast concrete segmental columns (PCSCs) under impact loads, a detailed 3D FE model of a PCSC with an unbonded posttensioned tendon is developed in Chapter 5. The contact between column segments and prestress force in the unbonded tendon and concrete are carefully considered in the simulation. The numerical results are fully validated by experimental results. The effect of number of segments, concrete strength, initial prestress load, and impact velocity on the dynamic responses of the PCSC is studied.

In Chapter 6, two full-scale bridge specimens using two types of columns, i.e. a monolithic RC column and a PCSC are developed. The advantages of the PCSC in resisting impact loads as compared to the monolithic RC column are investigated. Empirical equations to estimate the bending moment at the opening stage of segment joints and the ultimate bending moment of the PCSC are then proposed.

From the failure mode of PCSCs under impact loads and vehicle collisions as reported in Chapters 5 and 6, steel tubes are then used to improve the performance of the PCSC. Two different confinement schemes, i.e. partial strengthening at two local impacted segments and fully strengthening at all concrete segments, are investigated in Chapter 7. The response of the two strengthened columns under different impact conditions is then compared. The effects of using steel shear keys at segment joints on reducing the lateral shear slippage between column segments and preventing the shear failure of posttensioned tendons are also examined.

Chapter 8 summaries the findings, conclusions, and recommendations for future works.

It is worth mentioning that this thesis is compiled by combining the technical papers prepared by the candidate during his PhD study. Each technical paper forms a chapter from Chapter 2 to Chapter 7. The published technical papers in the chapters are formatted by the candidate according to the requirements from Curtin University. References cited by each technical paper are included at the end of each chapter.

1.4. References

AASHTO. (2012). *AASHTO LRFD bridge design specifications (customary U.S. units)*. 6th Ed., Washington, DC.

Abdelkarim, O. I., & ElGawady, M. A. (2017). Performance of bridge piers under vehicle collision. *Engineering Structures, 140*, 337-352.

Agrawal, A. K., Xu, X., & Chen, Z. (2011). *Bridge vehicle impact assessment* (C-07-10). University Transportation Research Center.

Bu, Z.-Y., Ou, Y.-C., Song, J.-W., Zhang, N.-S., & Lee, G. C. (2015). Cyclic loading test of unbonded and bonded posttensioned precast segmental bridge columns with circular section. *Journal of Bridge Engineering, 21*(2), 04015043.

Buth, C. E., Brackin, M. S., Williams, W. F., & Fry, G. T. (2011). *Collision loads on bridge piers: phase 2. Report of guidelines for designing bridge piers and abutments for vehicle collisions* (FHWA/TX-11/9-4973-2). College Station, TX.

Buth, C. E., Williams, W. F., Brackin, M. S., Lord, D., Geedipally, S. R., & Abu-Odeh, A. Y. (2010). *Analysis of large truck collisions with bridge piers: phase 1. Report of guidelines for designing bridge piers and abutments for vehicle collisions* (FHWA/TX-10/9-4973-1). College Station, TX.

CEN. (2002). *Actions on structures. Part 1-1: General actions-densities, self-weight, imposed loads for building*. Brussels, Belgium: BS EN 1991-1-1:2002.

CEN. (2006). *Actions on structures. Part 1-7: General actions-accidental actions*. Brussels, Belgium: BS EN 1991-1-1:2002.

Chen, L., El-Tawil, S., & Xiao, Y. (2016). Reduced models for simulating collisions between trucks and bridge piers. *Journal of Bridge Engineering, 21*(6), 04016020.

Chen, L., & Xiao, Y. (2012). Review of studies on vehicle anti-collision on bridge piers. *Journal of Highway and Transportation Research and Development, 29*(8), 78-86.

Chen, L., Xiao, Y., Xiao, G., Liu, C., & Agrawal, A. K. (2015). Test and numerical simulation of truck collision with anti-ram bollards. *International Journal of Impact Engineering, 75*, 30-39.

Chen, Y. (2018). Sudden! A large truck of Hadda Express broke the pier and one driver was killed! The two cars collided in the Hulan section of the waterfront, 5 dead and 7 injured. (In Chinese). Retrieved from http://www.sohu.com/a/235733631_349365

Chung, C. H., Lee, J., & Gil, J. H. (2014). Structural performance evaluation of a precast prefabricated bridge column under vehicle impact loading. *Structure and Infrastructure Engineering, 10*(6), 777-791.

Culmo, M. P. (2011). *Accelerated bridge construction-experience in design, fabrication and erection of prefabricated bridge elements and systems*. Washington, DC.

Dawood, H. M. M. M. (2010). *Seismic behavior and design of segmental precast post-tensioned* (Master's Thesis). Washington State University Retrieved from http://www.dissertations.wsu.edu/Thesis/Summer2010/H_Dawood_062510.pdf

Do, T. V., Pham, T. M., & Hao, H. (2018). Dynamic responses and failure modes of bridge columns under vehicle collision. *Engineering Structures, 156*, 243-259.

Do, T. V., Pham, T. M., & Hao, H. (2019). Impact force profile and failure classification of reinforced concrete bridge columns against vehicle impact. *Engineering Structures, 183*, 443-458.

El-Tawil, S., Severino, E., & Fonseca, P. (2005). Vehicle collision with bridge piers. *Journal of Bridge Engineering, 10*(3), 345-353.

Larsen, O. D. (1993). *Ship collision with bridges: The interaction between vessel traffic and bridge structures* (Vol. 4): IABSE.

Marriott, D., Pampanin, S., & Palermo, A. (2009). Quasi-static and pseudo-dynamic testing of unbonded post-tensioned rocking bridge piers with external replaceable dissipaters. *Earthquake Engineering & Structural Dynamics, 38*(3), 331-354.

Ou, Y.-C. (2007). *Precast segmental post-tensioned concrete bridge columns for seismic regions* (Doctoral dessertation). State University of New York at Buffalo Retrieved from https://ubir.buffalo.edu/xmlui/handle/10477/42969

SA/SNZ. (2002). *Structural design actions Part 1: Permanent, imposed and other actions* Sydney, NSW 2001; Wellington 6020: AS/NZS 1170.1:2002.

Sharma, H., Hurlebaus, S., & Gardoni, P. (2012). Performance-based response evaluation of reinforced concrete columns subject to vehicle impact. *International Journal of Impact Engineering, 43*, 52-62.

Volkwein, A., Schellenberg, K., Labiouse, V., Agliardi, F., Berger, F., Bourrier, F., . . . Jaboyedoff, M. (2011). Rockfall characterisation and structural protection-a review. *Natural Hazards and Earth System Sciences, 11*, 2617-2651.

Wang, Z., Ge, J., & Wei, H. (2014). Seismic performance of precast hollow bridge piers with different construction details. *Frontiers of Structural and Civil Engineering, 8*(4), 399-413.

Zhang, X., Hao, H., & Li, C. (2016). Experimental investigation of the response of precast segmental columns subjected to impact loading. *International Journal of Impact Engineering, 95*, 105-124.

PART 1
DYNAMIC ANALYSIS AND DESIGN OF MONOLITHIC REINFORCED CONCRETE COLUMNS

CHAPTER 2

DYNAMIC RESPONSES AND FAILURE MODES OF BRIDGE COLUMNS UNDER VEHICLE COLLISION

ABSTRACT[1]

The dynamic responses and failure modes of reinforced concrete bridge columns under vehicle collision have been numerically investigated in this study by using a numerical model verified against some experimental testing data. The numerical results show that the peak impact force (PIF) from the collision is governed by the vehicle engine and the vehicle velocity while the impulse of the impact force is influenced by the initial momentum of the total mass. It is, therefore, suggested that not only the total vehicle mass and the vehicle velocity but also the engine's mass need to be considered to determine the impact force on structures under vehicle collision. The engine's mass significantly affects the peak impact force, the moment, the shear force and thus the damage of the column. The lateral impact force considerably affects the column axial force and a relation between the PIF and the increase of the axial force is proposed for the design purpose. The numerical model is able to reproduce and provide an explanation of most of the common failure modes observed in real impact events including flexural failure, shear failure, and punching shear damage. In addition, the influences of four different methods of the superstructure modelling, i.e. uniformly distributed load, lumped mass, simplified beam model, and 3D detailed model on the behaviour of the bridge column under vehicle impact are also investigated.

2.1. Introduction

Due to the significant development of cities and transportation infrastructure as well as the increase of traffic in urban areas, vehicle collision with bridge structures or buildings occurs more often around the world (Agrawal et al., 2011; Buth et al., 2010). Heavy trucks collide to bridge structures may cause catastrophic consequences on human life and infrastructure systems. According to Federal Highway Administration, a vehicle or a vessel collision is the third leading reasons which cause a bridge collapse in the United States (US) (Agrawal et al., 2011). Buth et al. (2010) reported 19 extreme cases of vehicle collision with bridge columns in the US. Among these accidents, some collisions led to the collapse of the superstructures,

---

such as the truck accident in Texarkana, 1984 or in Corsicana, 2002 as shown in Figure 2-1a. In the world, in April 2009, a heavy tank truck hit a bridge column in Beijing – Zhuhai Expressway in Hunan, which caused a severe damage to the column (see Figure 2-1b), the deaths of two passengers, and resulted in the closing down of the traffic systems for over two months (Chen & Xiao, 2012). Despite the occurrence of such accidents and their devastating consequences, the impact-resistant capacity of concrete columns under vehicle collision is still not well predicted and designed. The behaviours of the column during an impact event, i.e. the axial force, bending moment, shear force, and failure modes need to be investigated.

(a) Texas in 2003 (Buth et al., 2010)   (b) China in 2009 (Chen & Xiao, 2012)

Figure 2-1 Truck collision with bridge columns.

To design structures against vehicle impact, an equivalent static force (ESF) approach is provided in several design codes and reports (AASHTO, 2012; Abdelkarim & ElGawady, 2016; Abdelkarim & ElGawady, 2017; CEN, 2002). Buth et al. (2011) used a tractor trailer to conduct a large-scale collision test on a steel column. A series of finite element models were also built based on the experimental results. Based on these results and the open literature, AASHTO (2012) recommended that an ESF of 2,668 kN acting on bridge columns or piers at a distance of 1.5 m above the ground level is used for the design purpose. BSI (CEN, 2002) recommended a simplified equation to determine the impact force on structures based on the energy conservation between the kinetic energy and the deformation of structures. From the vehicle's kinetic energy, the vehicle's deformation, and the column deformation, the ESF can be defined as follows:

$$ESF = \frac{0.5mv^2}{\delta_c + \delta_d} \tag{2-1}$$

in which *ESF* is the impact force on structures (kN), *m* is the gross mass of the vehicle (kg), *v* is the vehicle's velocity (m/s), δ_c is the deformation of the vehicle model, which is defined as the change in length between the centre of mass and vehicle nose (mm), and δ_d is the deformation of the barrier at the impact point (mm).

El-Tawil et al. (2005) conducted numerical simulations of two detailed bridge structures and vehicle models to study truck collisions on bridge columns. The peak impact force (PIF) and the ESF from the simulations were also reported. The ESF was defined as the static force required to generate the similar lateral displacement which is equal to that of displacement under dynamic load at the impact point. The results indicated that the current AASHTO-LRFD design provision could be un-conservative in some circumstances. Calibrated with El-Tawil et al. (2005) simulation results, Abdelkarim and ElGawady (2017) conducted a series of numerical simulations of reinforced concrete bridge columns under different vehicle impact conditions to evaluate the AASHTO-LRFD vehicle collision force provisions. The effects of 13 column parameters on the impact force were also studied. The equation for estimating kinetic-energy based equivalent static force which is a function of the vehicle mass and the vehicle velocity was proposed without finite element analysis requirements as follows:

$$ESF = 33\sqrt{mv^2} \tag{2-2}$$

where *ESF* is the equivalent static load (kN), *m* is the mass of the vehicle (ton) and *v* is the vehicle velocity (m/s).

It is worth mentioning that the dynamic behaviours of bridge columns such as vibration and dynamic capacity were not considered in these provisions and the proposed methods. Previous studies (Pham & Hao, 2016, 2017a) showed that the dynamic bending moment and shear force of a reinforced concrete (RC) beam against impact loading are significantly different from those under static loading. Because of the effects of the inertia force varied along the beams, both positive and negative bending moments were observed in the simply supported beam with the positive bending moment at the mid-span and the negative bending moment at the two ends. Besides, the maximum shear force was recorded at the mid-span of the beam (Pham & Hao, 2017a). These phenomena are unique for beams against impact force and it is difficult for the static equivalent method to capture these behaviours. Sharma et al. (2012) modelled the collision with some vehicle models with different velocities to examine the shear force of concrete columns. The numerical results indicated that the dynamic shear force of the reinforced concrete column under vehicle impact is not only greater than the static counterpart but also varying with different collision conditions. A proposed procedure to estimate the dynamic shear force demand based on the performance level of the column was also developed. These previous studies indicated that the impact response of a bridge column including bending moment, shear force, and axial force need to be taken into consideration, whereas the ESF method does not necessarily lead to accurate estimations.

In terms of the failure modes of bridge columns subjected to a collision, several types of failure modes, i.e. flexural cracks, shear failure, punching shear failure, and brutal damage were observed in real impact events and documented (Buth et al., 2010) as shown in Figure 2-2. It is very clear from the figure that the failure modes of the bridge columns are significantly different under various loading conditions. These failure modes could not be predicted by using the ESF method but can only be observed in real dynamic analyses. An experimental test of a scaled column under pendulum impact force by Zhang et al. (2016) showed severe flexural cracks occurred at the column mid-height while a diagonal shear failure was observed at the column base. Besides, the experimental tests by Demartino et al. (2017) showed that a brittle shear failure starting from the column base to the impact point and some flexural cracks at the column mid-height were observed on RC columns subjected to lateral impact. Moreover, bending moment variation along a column under impact loading was presented by Thilakarathna et al. (2010). The results showed that the impacted column generated the third order vibration mode under impact load resulting in high bending moment and shear force at the column top, which may lead to an excessive shear failure. These variations of the failure modes have not been thoroughly explained in the literature and require more studies to understand the mechanism behind.

(a) Flexural cracks   (b) Shear failure at the column top (c) Shear failure at the impact point

(d) Punching shear failure   (e) Shear failure   (f) Brutal damage

Figure 2-2 Failure modes of bridge columns under vehicle collision (Buth et al., 2010).

Furthermore, to study bridge or building columns under dynamic loads, superstructures previously were simulated by a constant uniformly distributed load (Li et al., 2017), a lumped mass (Sha & Hao, 2013), or a simplified beam model (El-Tawil et al., 2005). It is well-known that the inertia force and the damping produced from the structural mass and stiffness, i.e. superstructure components are crucial to resist the dynamic loading. Different types of superstructure modelling may lead to different failures of the column due to its inertia force distribution. Therefore, the detailed 3D model should be developed and the effects of the superstructure modelling simplifications on the performance of the bridge column need be examined.

In this paper, the impact responses and performances of bridge columns under vehicle collision are investigated with a detailed 3D model which is built with the commercial software LS-DYNA (Hallquist, 2007). The accuracy of the numerical model is verified against the testing results of the pendulum impact tests on a conventional column by Zhang et al. (2016). The impact force, vibration, axial force, bending moment, shear force, and the failure modes of columns under different loading conditions, i.e. different vehicle mass and vehicle velocities are examined. The influences of the superstructure model on the performances of bridge column are also investigated.

2.2. Numerical model calibration

2.2.1. Experimental pendulum impact tests

The experimental test of a scaled column under pendulum impact reported by Zhang et al. (2016) is simulated in this study to verify the numerical model. The testing data including the detailed design of the column, material properties, and the pendulum impact system is briefly described in this section.

The overall dimension of the rectangular testing column was 800 mm in height, 100 mm in depth, and 100 mm in width, which was a quarter-scale column model, as shown in Figure 2-3. A footing of 400 mm x 400 mm x 140 mm (L x W x H) was built to bolt the column onto the strong laboratory floor. The added mass (288 kg), which represents superstructure in reality, consisting of a single concrete block and 5 steel plates, was placed on top of the column. The single concrete block had the dimension of 400 mm x 400 mm x 450 mm (L x W x H, 173 kg) and the total weight of the 5 pieces of steel plates was 115 kg. The flexural tensile strength and compressive strength at 28 days of concrete were 5 MPa and 34 MPa, respectively. The column consisted of four 6 mm-diameter longitudinal bars (f_y = 500 MPa) extended from the bottom footing to the top of the column and 4 mm-diameter stirrups (f_y = 300 MPa) at a spacing of 40 mm. The pendulum impact testing system consisting of a steel frame, 2.8 m long pendulum arm, an inclinometer, and a 300 kg steel impactor is shown in

Figure 2-3. The steel impactor could be lifted to a different angle in order to generate different initial impact energy.
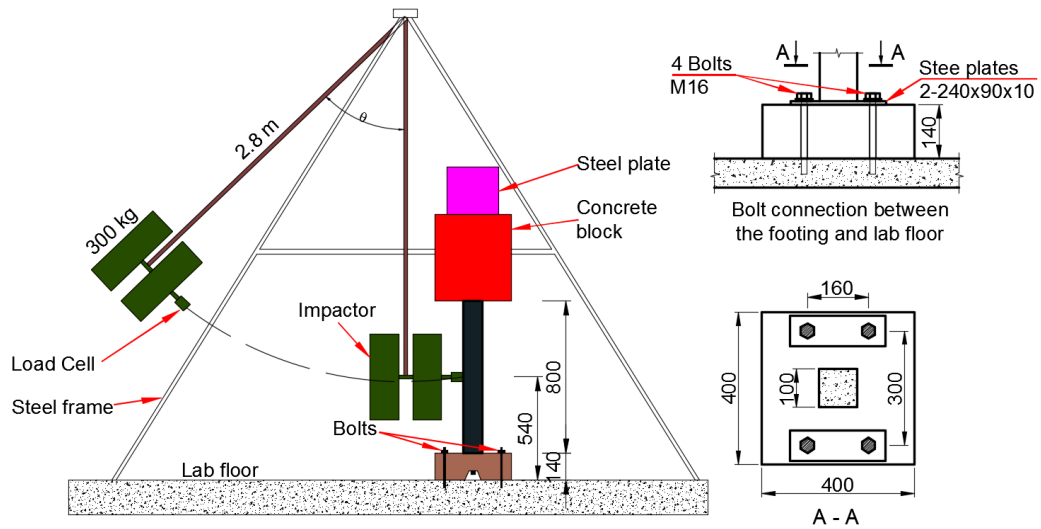
Figure 2-3 The schematic view and the bolt connection of the pendulum impact test [Data from (Zhang et al., 2016)].

2.2.2. Numerical model

2.2.2.1 Finite element model
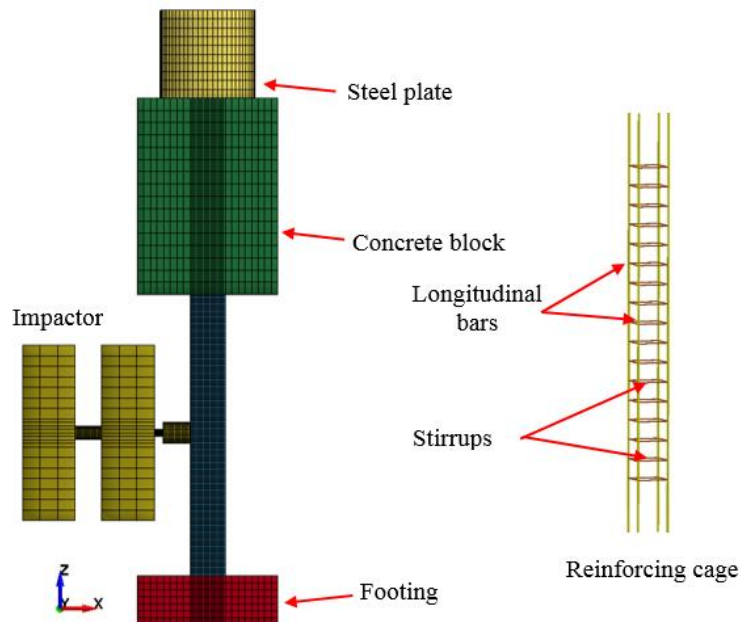
Figure 2-4 Numerical model of the scaled column under pendulum impact test.

A three dimensional (3D) nonlinear numerical model is built to simulate the experimental pendulum impact test reported by Zhang et al. (2016), as shown in Figure 2-4. A hexahedral element with 1 integration point (SOLID_64) is employed to represent the concrete elements, steel impactor, and steel plates while 3-nodes beam elements with 2x2 Gauss quadrature

integration (BEAM_161) are used for steel reinforcements. The results from the convergence test show that the simulation results converge when the mesh size of concrete elements is 5 mm. Further decrease in the concrete element size shows a slight difference of the results but cost more computational time and may lead to computer memory overflow. To reduce the simulation cost, the maximum mesh size of the steel impactor and the added mass are 50 mm. The LS-DYNA contact algorithm named *Contact_Automatic_Surface_to_Surface is employed to simulate the contact between the steel impactor and the RC column. Besides, perfect bond between reinforcing steel reinforcement, stirrups, and surrounding concrete is assumed in this study.

In the experimental tests, the footing was anchored to laboratory floor through four bolts (see Figure 2-3). No horizontal/vertical displacement or rotation at the joint connection between the footing and the floor were recorded during the experimental test (Zhang et al., 2016). Hence, all of the nodes on the bottom face of the footing are constrained at all degrees of freedom in the numerical model.

2.2.2.2 Material model

In the present study, the *Mat_Concrete_Damage_Rel3 (MAT_072R3) material model is selected for modelling the concrete where the plasticity, shear failure damage, and strain-rate effect are taken into account. The reliability of this material model in simulating and predicting the behaviour of concrete structures under extreme dynamic loads has been confirmed by previous studies (Chen et al., 2015; Hao et al., 2013; Li et al., 2017). In this study, the unconfined compressive strength of the concrete material is 34 MPa. An elastic-plastic material model named *Mat_Piecewise_Linear_Plasticity (MAT_24) is employed to model the steel reinforcements. The mass density and Young's modulus are 7,800 kg/m^3, and 200 GPa, respectively. The yield strength of the longitudinal steel is 500 MPa while the corresponding value of the transverse reinforcement is 300 MPa. The strain rate curves of these steel materials are defined and given below. For the steel pendulum impactor and anchor plate, the LS-DYNA material model named *MAT_ELASTIC (MAT_001) is selected, in which the steel yield strength, mass density, and Young's modulus are 300 MPa, 7,800 kg/m3, and 200 GPa, respectively.

In addition, *MAT_ADD_EROSION function in LS-DYNA is employed to automatically remove concrete elements which no longer contribute to resisting the impact force. The erosion is a numerical tool to avoid great mesh distortions. This erosion feature has been commonly adopted in studying the impact and blast response (Li et al., 2017; Pham & Hao, 2017a, 2017b). In the present study, the value of 0.7 is used for the erosion criterion of concrete material after trials, which yields good agreement with the experimental results.

2.2.2.3 Strain rate effects

Under high impact and blast loads, the mechanical properties of concrete and steel are recognised to be different from those under quasi-static condition where both the compressive and tensile strengths increase (Chen et al., 2015; Hao et al., 2013). The effect of strain rate on the behaviour of the material and hence on the numerical simulation has been reported by the previous study (Hao et al., 2013; Malvar & Crawford, 1998; Ngo, 2005; Pham & Hao, 2017a). To quantify the strength increment of the materials, the ratio of dynamic-to-static strength, i.e., dynamic increase factor (DIF) versus strain rate has been introduced. In this study, the DIF curves of concrete compressive and tensile strength given by Hao and Hao (2014) are adopted. It should be noted that the contribution to strength increment of the end friction confinement and lateral inertia confinement from the dynamic tests has been eliminated in the proposed equations. These DIF curves have also been experimentally verified by the split Hopkinson pressure bar tests (Hao & Hao, 2014; Hao et al., 2013). In addition, the DIF for steel reinforcements defined by Malvar and Crawford (1998) is used in this simulation.

The compressive DIF of concrete at the strain rate $\dot{\varepsilon}_d$ is given by the following equation:

$$CDIF = \frac{f_{cd}}{f_{cs}} = \begin{cases} 0.0419(\log \dot{\varepsilon}_d) + 1.2165 & for\,(\dot{\varepsilon}_d \le 30s^{-1}) \\ 0.8988(\log \dot{\varepsilon}_d)^2 - 2.8255(\log \dot{\varepsilon}_d) + 3.4907 & for\,(\dot{\varepsilon}_d > 30s^{-1}) \end{cases} \quad (2\text{-}3)$$

where *CDIF* is the DIF for the concrete in compression, f_{cd} is the dynamic compressive strength at the strain rate $\dot{\varepsilon}_d$, and f_{cs} is the static compressive strength.

The DIF of the tensile strength is

$$TDIF = \frac{f_{td}}{f_{ts}} = \begin{cases} 0.26(\log \dot{\varepsilon}_d) + 2.06 & for\,(\dot{\varepsilon}_d \le 1s^{-1}) \\ 2(\log \dot{\varepsilon}_d) + 2.06 & for\,(1s^{-1} < \dot{\varepsilon}_d \le 2s^{-1}) \\ 1.44331(\log \dot{\varepsilon}_d) + 2.2276 & for\,(2s^{-1} < \dot{\varepsilon}_d \le 150s^{-1}) \end{cases} \quad (2\text{-}4)$$

where *TDIF* is the DIF for the concrete in tension, f_{td} is the dynamic tensile strength at the strain rate $\dot{\varepsilon}_d$, and f_{ts} is the static tensile strength.

The relationship between both the tensile and compressive strength DIF of steel and strain rate is defined by the following equations:

$$DIF = \left(\frac{\dot{\varepsilon}}{10^{-4}}\right)^{\alpha} \quad (2\text{-}5a)$$

$$\alpha = 0.074 - \frac{0.04f_y}{414} \quad (2\text{-}5b)$$

16

where f_y is the yield strength of steel in MPa. It should be noted that in this study DIF is held as constant when the strain rate is higher than 160 s^{-1} to prevent an overestimation of the DIF of the steel material at very high strain rates.

2.2.2.4 Results and validation

Figure 2-5 and Figure 2-6 show the comparisons of the response of the RC column under impact loading between the experimental test and the numerical simulation. The impact force time histories are presented in Figure 2-5a. The peak impact force and the impact duration in the test were about 22 kN and 30 ms, respectively, while the corresponding results in the simulation are 23.7 kN and 35 ms. The minor difference can be found in the PIF and the duration because the surface of the concrete column which affected the contact interaction between the impactor and the column was not perfectly flat and smooth in the test as compared to that of the numerical model. The local stiffness of the tested column was thus slightly smaller than the simulated column. As a result, the impact force in the test has a smaller PIF but longer duration compared to the simulation. In addition, the displacement time history at mid-height of the column from FE model also agrees well with the experimental test (see Figure 2-5b). The maximum and the residual lateral displacements of the column measured in the test were 7.5 mm and 1.5 mm, respectively. The corresponding values from the simulation are 7.6 mm and 1.8 mm, respectively.

| (a) Impact force time history | (b) Displacement at the centre of column |
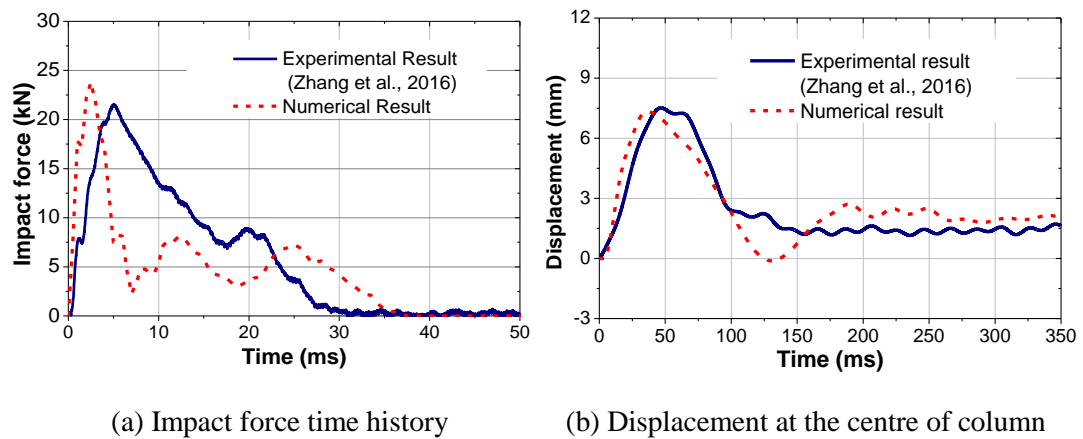
Figure 2-5 Model verification – RC column under the impact with velocity 0.64 m/s.

The plastic strain along the RC column is shown in Figure 2-6 to compare with the damage in the experimental test. Both flexural and shear cracks are observed in the numerical model and in the experimental test in which the flexural cracks happened at the impacted area while the shear cracks were at the column base. Concrete damage is also observed in the simulation at the column top as compared to the experimental result. In general, the dynamic behaviours of the column in the experimental test are well simulated in the numerical model. The verification

has shown that the FE model yields reliable predictions of the column responses to impact loading and it is able to capture the impact force, lateral displacement, plastic deformation and the failure modes of the RC column.

Experimental test   Numerical simulation
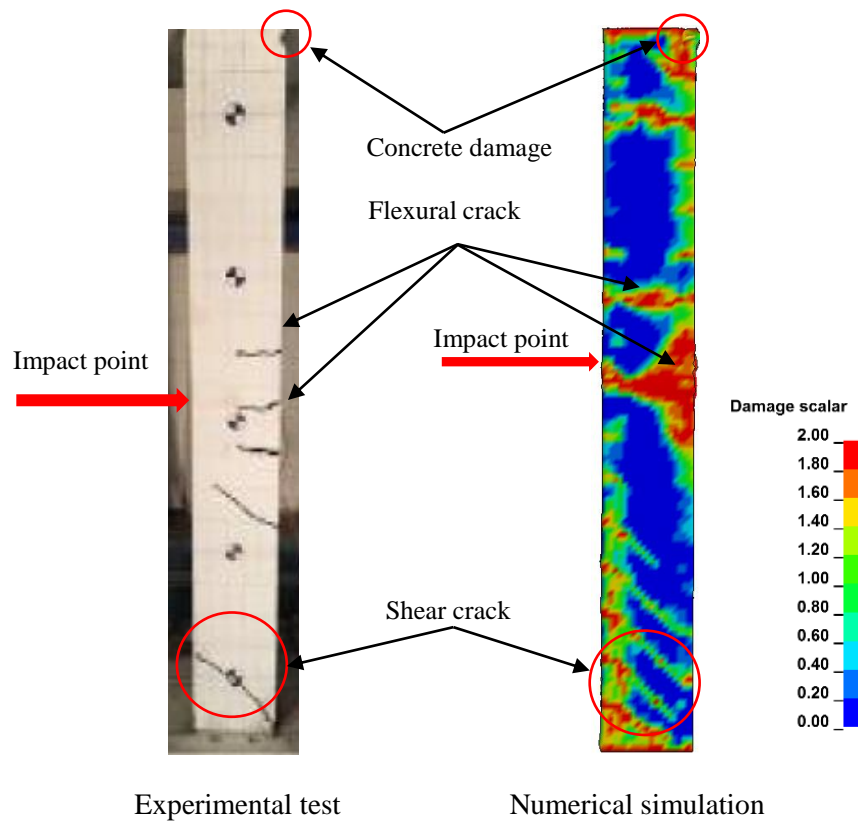
Figure 2-6 Concrete damage versus plastic strain of the column.

2.3. Numerical simulations of bridge column under vehicle collisions

2.3.1. Bridge specimens

The detailed 3-D finite element model of a typical bridge specimen is developed in this section with the same material models, modelling method and strain rate effect. It is previously indicated by Consolazio and Davidson (2008) that a bridge model consisting of one bridge column and two spans provides an accurate prediction of the dynamic responses of multi-span bridges. As such, in this study, the considered bridge model consists of one single column, footing, superstructures, and two abutment supporters as shown in Figure 2-7a and Table 2-1. The bridge column has a rectangular section which is 1,200 mm x 1,200 mm in cross-section and 9,600 mm in height. The concrete footing has dimensions of 5,200 mm x 5,200 mm x 1,500 mm. A solid cap beam of trapezoidal shape is placed on top of the column to transmit the superstructure's weight to the substructure. In this study, the section properties and dimensions of the superstructure which is the prototype single-cell box girder with 40 m length are obtained from the previous study by Megally et al. (2001), as shown in Figure 2-7b. The total gravity load consisting of the superstructure (about 4,000 kN), cap beam (267 kN) and

the column itself (331 kN) is about 4,600 (kN). The column, cap beam, superstructures and footing of these models are modelled by using hexahedral elements with 1 integration point (SOLID_64).
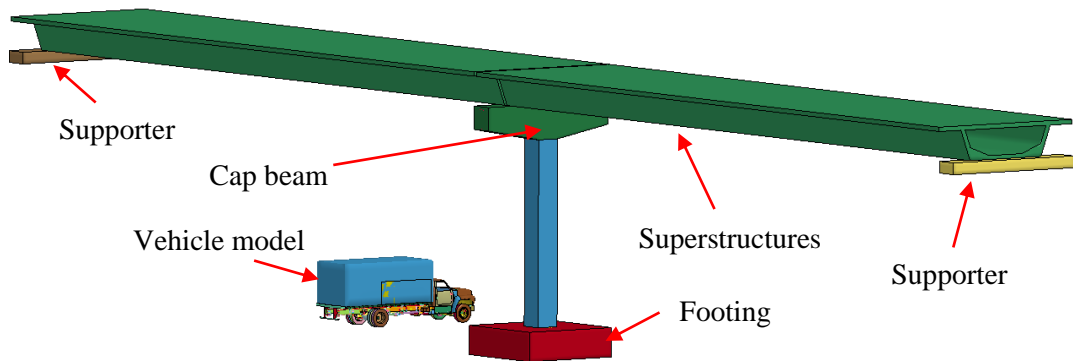
(a) 3D –view of the bridge column with superstructures
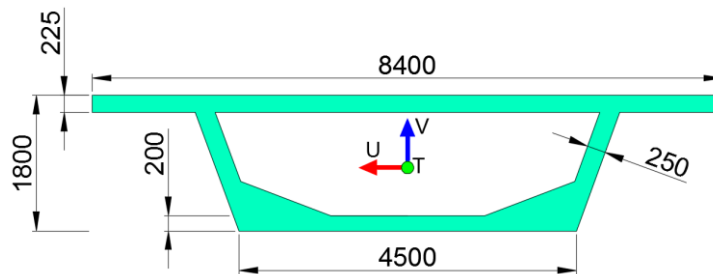
(b) Detailed section view of the superstructure

Figure 2-7 FE model of the bridge specimen (all dimensions in mm).

Typically, the bridge superstructures are connected to the column through rubber or bearing pads. However, the previous study by El-Tawil et al. (2005) showed that the influences of bearing pad stiffness are marginal to the impact behaviour of a bridge column. A normal concrete surface to surface contact between a superstructure and a bridge column was used in the experimental test by Sideris et al. (2014). Therefore, in the present simulation, the girder is assumed to rest on top of the cap beam without bearing pads to reduce the computational costs. The surface to surface contact between the superstructure and the cap beam is thus adopted in this study. The other end of the girder is designed to sit on a simplified solid block representing concrete abutment. The friction interface between girder and pier, and between girder and abutments are assumed in the model (see Figure 2-7a) with the coefficient of friction of 0.6 (ACI, 2008).

2.3.2. Vehicle model

The Ford reduced model (35,400 elements) single unit truck (SUT) is employed in this study to represent the vehicle collision on the bridge column (see Figure 2-8). The total mass of the

Ford truck model is 8 ton with the engine's weight of 0.64 ton and the added mass of 2.8 ton. In this model, both the engine and the cargo are simulated by an elastic material with the modulus 110 GPa and 2 GPa, respectively. It is highly appreciated to note that this vehicle model was shared by Abdelkarim and ElGawady (2016) and Sharma et al. (2012). An experimental test on this model was conducted to verify the accuracy of the numerical model by FHWA/NHTSA National Crash Analysis Centre at the George Washington University with a high correlation between numerical and experimental results. The mass of the vehicle model can be adjusted by changing the weight of the vehicle engine and the added cargo. In this study, the vehicle's mass is in the range of 8 ton to 16 ton while the vehicle velocity varies from 40 km/h to 140 km/h.

Table 2-1 Detailed dimensions of the bridge specimens.

Parameters	Bridge specimen	
Column height	9,600	mm
Section width	1,200	mm
Section depth	1,200	mm
Superstructure span length	40,000	mm
Longitudinal steel	24D30	
Lateral steel	D16a200	
Cap beam		
Width	7,600	mm
Height	1,500	mm
Depth	1,200	mm
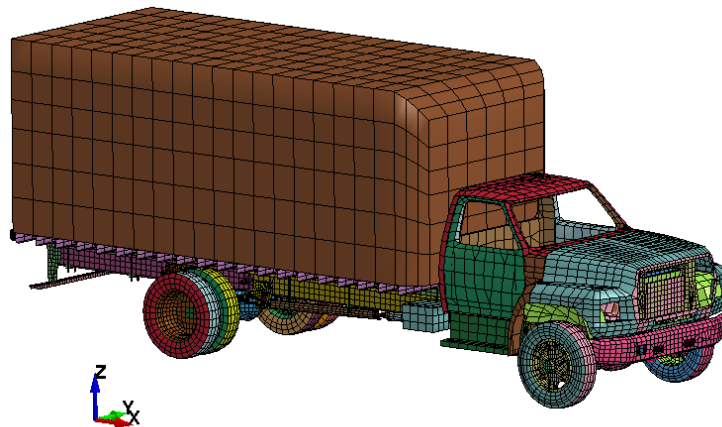
Figure 2-8 3D view of the vehicle model.

2.4. Numerical simulation results and effects of the peak impact force

Intensive numerical simulations are conducted in this study to investigate the behaviours of the bridge columns subjected to vehicle collisions. Different initial loading conditions including vehicle's engine mass, total vehicle mass, and velocity together with different superstructure modelling techniques are employed as presented in Table 2-2.

20

Table 2-2 Parametric study.

Case	Superstructures	Engine mass	Vehicle mass	Velocity	Momentum	Impulse	PIF	Peak axial force
		kg	kg	km/h	kN.s	kN.s	kN	kN
C1	3D Model	640	8,000	40	88.9	86.9	930	4,700
C2	3D Model	640	8,000	60	133.3	130.2	1,870	5,000
C3	3D Model	640	8,000	80	177.8	176.4	3,460	5,230
C4	3D Model	640	8,000	90	200.0	199.8	4,596	6,070
C5	3D Model	640	8,000	100	222.2	220.5	8,260	7,223
C6	3D Model	640	8,000	120	266.7	266.1	12,000	9,800
C7	3D Model	640	8,000	140	311.1	--	16,400	12,400
C8	3D Model	1,000	8,000	100	222.2	--	11,400	8,970
C9	3D Model	2,000	8,000	100	222.2	--	18,500	13,500
C10	3D Model	640	16,000	100	444.4	--	9,010	7,660
C11	3D Model	1,000	16,000	100	444.4	--	11,900	9,310
C12	3D Model	2,000	16,000	100	444.4	--	18,400	13,700
C13	3D Model	1,000	8,000	140	311.1	--	20,150	14,610
C14	3D Model	2,000	8,000	140	311.1	--	30,000	21,000
C15	UDL	640	8,000	90	200.0	195.5	4,250	**
C16	LMM	640	8,000	90	200.0	200.5	4,284	**
C17	Beam model	640	8,000	90	200.0	198.4	4,360	**
C18	UDL	640	8,000	120	266.7	--	11,998	**
C19	LMM	640	8,000	120	266.7	--	12,000	**
C20	Beam model	640	8,000	120	266.7	267.6	12,075	**

-- Simulation was terminated due to severe damage of the column and/or the vehicle model

UDL: Uniformly distributed load; LMM: Lumped mass model; ** The value is not under consideration

2.4.1. Impact force time histories

The typical impact force time history of the bridge column subjected to the truck collision is presented in Figure 2-9a. It is noted that the time step is used at 0.5 ms in the simulation. Under the velocity of 100 km/h, the first peak force (about 2,950 kN) occurs when the vehicle's bumper collides with the column while the second peak (about 8,260 kN) is produced by the vehicle's engine impact. After dropping to about 1,000 kN, the impact force then slightly increases to about 2,000 kN due to the impacting of the vehicle's cargo. The collision ends at about 180 ms when the vehicle finally separates from the column. It is noted that the bumper impact represents for the impact of all vehicle parts in front of the engine box. Figure 2-9b shows the impact force time histories with different impact velocities ranging from 60 km/h

to 140 km/h. It is very clear that the maximum peak impact force is generated when the vehicle's engine collides with the column with very short duration from 5 ms to 10 ms while the added cargo mass yields smaller impact force with longer duration (about 120 ms). Moreover, increasing the vehicle velocity results in a significant increase of the peak impact force as shown in Figure 2-9. The maximum impact force due to the collision is about 1,870 kN when the vehicle's velocity is 60 km/h. The corresponding values increase to 3,460 kN, 4,596 kN, 8,260 kN, 12,000 kN, and 16,400 kN with the vehicle velocity of 80 km/h, 90 km/h, 100 km/h, 120 km/h, and 140 km/h, respectively. The impulse of these collisions is equal to the initial momentum (see Figure 2-10), which confirms the applicability of the momentum-impulse theorem in this problem and the reliability of the numerical results.

(a) Vehicle velocity of 100 km/h   (b) Different vehicle velocities
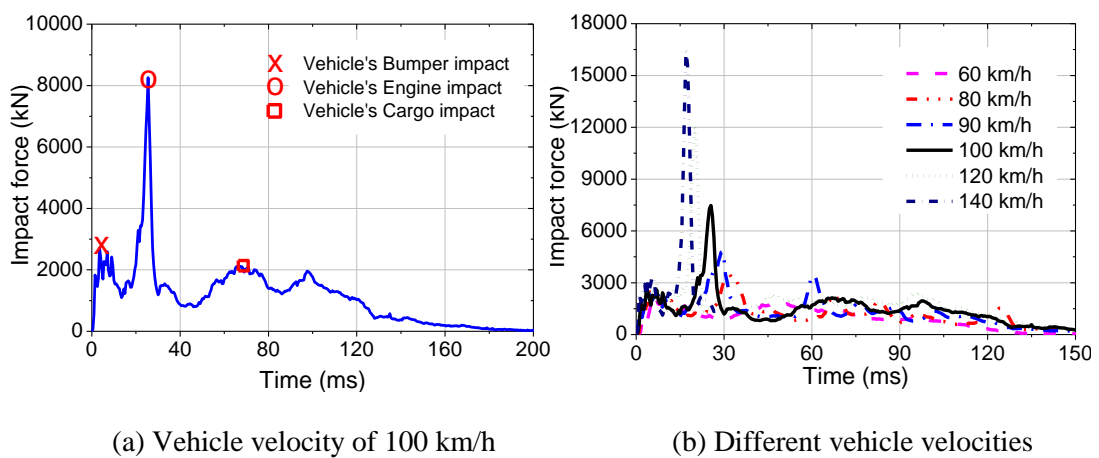
Figure 2-9 Impact force time history under Ford truck model (8 ton) collision.
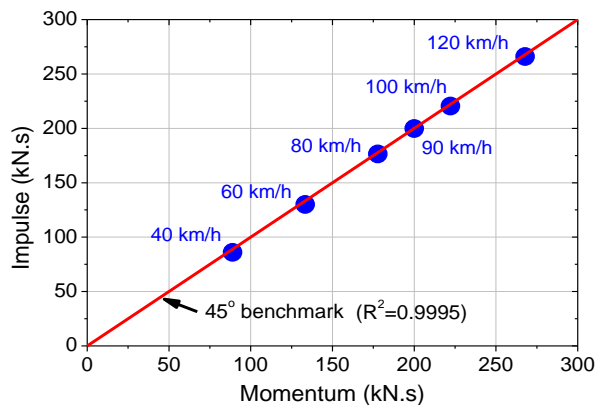
Figure 2-10 The impulse - initial momentum conservation.

On the other hand, to examine the effect of the different vehicle parts on the impact force, the weight of the vehicle's engine is varied between 0.64 ton and 2 ton while the cargo ranges from 2.8 ton to 10.8 ton. As shown in Figure 2-11, the engine's weight has significant influences on the impact force when the column is subjected to the same vehicle velocity. By increasing the engine's weight from 0.64 ton to 2 ton with the constant total mass, the PIF substantially increases from 8,260 kN to 18,500 kN. Under a certain vehicle velocity, similar

22

PIFs are observed when these columns are collided with the same vehicle engine's mass even though different trucks with significantly different masses (8 ton and 16 ton) are used in the simulation. These results indicate the maximum impact force is governed by the vehicle's engine instead of the total mass of the vehicle.

(a) Vehicle's mass of 8 ton (100 km/h)   (b) Vehicle's mass of 16 ton (100 km/h)
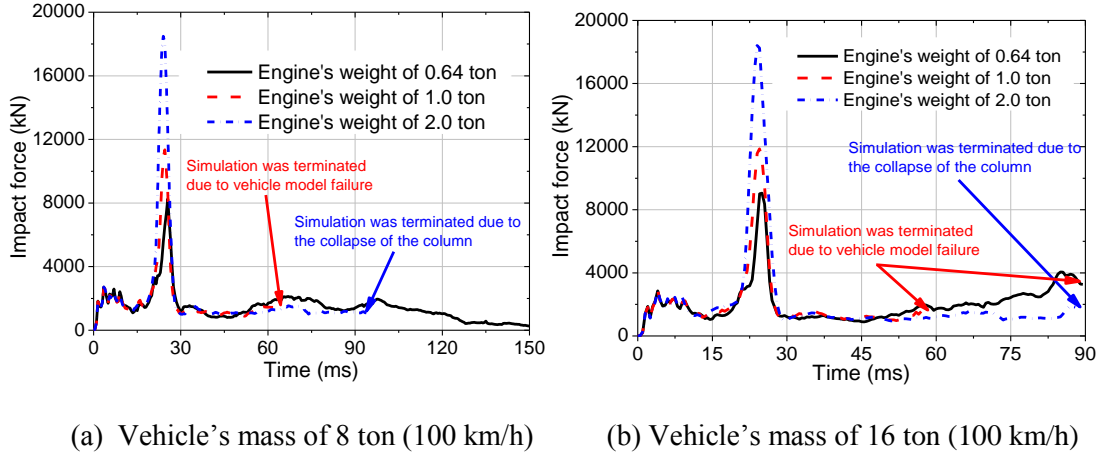
Figure 2-11 Comparisons of the impact force time histories with different vehicle mass.
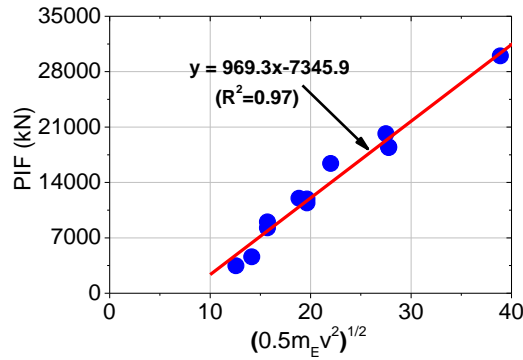
Figure 2-12 The PIF – initial kinetic energy relation.

From the above observations, the PIF of the vehicle collision is significantly affected by the vehicle engine's mass and the vehicle velocity while the impulse of the impact event depends on the initial momentum of the vehicle. Therefore, to determine the impact force of the column under vehicle collision, not only the total vehicle mass and the vehicle velocity but also the vehicle engine's mass should be taken into consideration. The relation between PIF and initial kinetic energy of the vehicle engine is also shown in Figure 2-12. Based on the numerical results, the PIF of the vehicle collision can be determined by the following expression:

$$PIF(kN) = 969.3\sqrt{0.5m_E v^2} - 7345.9 \qquad (2\text{-}6)$$

where m_E is the engine's mass (ton) ($0.64 <= m_E <= 2$ ton); v is the vehicle velocity (m/s) ($22 < v < 40$) ($10 < \sqrt{0.5m_E v^2} < 40$).

2.4.2. Axial force

In the static analysis, the lateral equivalent static force yields a bending moment and a shear force in the column but not the axial force. The influence of lateral impact force on the axial force of the column has not been reported yet in the literature. It is well-known that under high loading rate, the compression stress from an impact event propagates from the impact area to the two ends of structures (Fujikake et al., 2009). The resultant stress wave in the column forms a dynamic axial force in the column. However, the relation between the lateral impact force and axial force in the concrete column is still unknown. In this study, the LS_DYNA keyword named Database_Cross_Section_Set is used to evaluate the axial force, bending moment, and shear force at various sections in the concrete column (see Figure 2-13a). The cross section force is calculated by summing up element forces in a group set (Hallquist, 2007).
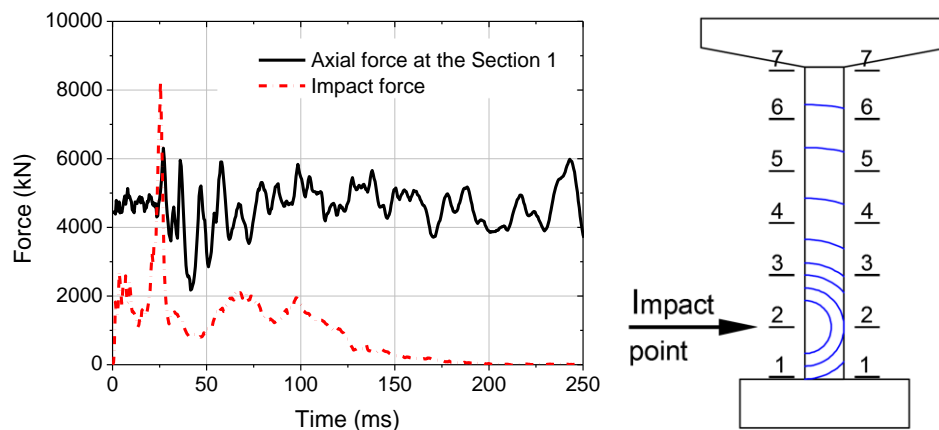
(a) Axial compression force during the impact force phase
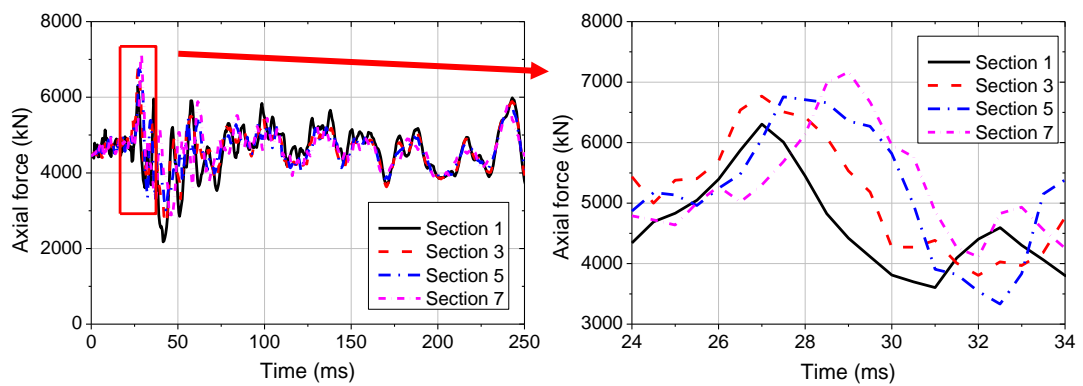
(b) Axial compression force along the column

Figure 2-13 Axial compression force under vehicle impact with velocity 100 km/h.

Figure 2-13 shows the axial compression force under the Ford truck impact with the velocity of 100 km/h. It should be noted that the positive value in the figure stands for the compression force in the cross section. When the impact force reaches the peak owing to the engine's impact, the axial compression force also increases from about 4,600 kN (dead load) to nearly

24

6,400 kN (about 1.4 times) (see Figure 2-13a). As shown in the figure, the axial force fluctuates significantly within the impact duration associated with the impact force because of the stress wave propagation and reflection. After the force phase, the axial force returns back and vibrates around its initial level. The lowest level of the compression force is about 2,200 kN (about 50% of the dead load). The axial force along the column at the different locations are also compared in Figure 2-13b. Because of the similar distance from the impact point, the axial forces in Section 1 and Section 3 show a similar trend and they reach the maximum axial force at the same time while the axial force at Section 5 and Section 7 increases to its peak slower because of its longer distance to the impact point. These results indicate that the increase of the axial force in the column is caused by the stress wave propagation from the impact point to the column ends. After about 100 ms, the axial force at those sections then vibrates around the dead load level with a similar frequency. This vibration results from the vertical stress wave propagation in the column and the vertical vibration of the superstructure produced by the impact event.
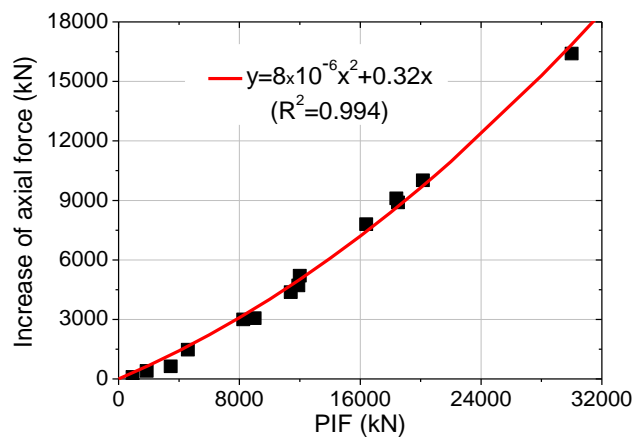
Figure 2-14 Increase of the axial force versus peak impact force.

To quantify the effect of the peak impact force on the axial compression force, the peak impact force versus the increase of the axial force is plotted in Figure 2-14. It should be mentioned that the increase of the axial force in Figure 2-14 is defined by subtracting the peak axial force (Table 2-2) to the constant dead load (4,600 kN). As can be seen from the figure, the increase of the axial force in the column is about 3.5 times of the total dead load when the PIF is 30,000 kN. Therefore, it is crucial to consider the variation of the axial force in the column during the impact loading. Based on the simulation results, the increase in the axial compression force can be defined by the following equation:

$$A_I = 8\left(\frac{PIF}{1000}\right)^2 + 0.32PIF \tag{2-7}$$

in which A_I is the increase in the axial force (kN), *PIF* is the peak impact force (kN).

25

2.4.3. Bending moment

The time histories of the column bending moment resulted from the Ford truck collision at 100 km/h are presented in Figure 2-15. Different from the static case, under the vehicle collision both positive and negative bending moment are observed in the column. The maximum positive bending moment occurs at the impact point (about 3,163 kNm) while the maximum negative bending moment at the column top and the column base are 3,251 kNm and 3,539 kNm, respectively. It should be noted that bending moment is not zero at the column top because the friction between the pier top and the girder and the large inertia resistance owing to the bridge superstructure mass resist the free movement of the bridge column.

0 – 11.5 ms   11.5 – 22.5 ms   22.5 – 30 ms   30 – 36 ms   40 – 150 ms
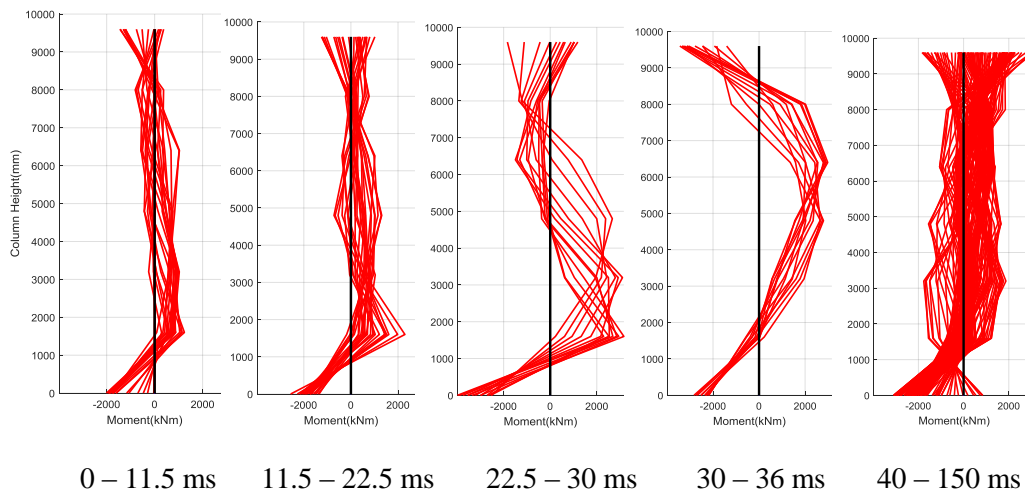
Figure 2-15 Bending moment diagrams of the bridge column during the force phase.

To examine the bending moment during the peak impact force in detail, the inertia distribution and the bending moment diagram (from 25 ms to 34 ms) are plotted in Figure 2-16. As can be seen from Figure 2-16a that only a part of the column reacts to the impact at the peak impact force (25.5 ms). The acceleration at the impact point is about 564 m/s^2 while the length of the active part is almost a half of the column. The compressive stress then propagates from the impact point to the column ends causing the vibration of the whole column. When the column top starts vibrating (around $t = 29$ ms), the distribution of the inertia force along the column significantly changes to a high order vibration mode. That variation of the inertia force together with the effect of the superstructure results in the change of the bending moment shape, as shown in Figure 2-16b. The results show that the assumption of the linear distribution of the inertia force under impact load is unreasonable after the stress from the impact point reaches the column top. With the effect of the superstructures, the bending moment at the top of the column reaches the maximum value of 3,251 kNm at $t = 34$ ms while the corresponding value at mid-height of the column is 2,858 kNm. These results also prove that the bending moment diagram of the column under impact loading cannot be accurately predicted by using the ESF

method. Moreover, the use of the single degree of freedom method (SDOF) in predicting the behaviour of the structures under impact loads might not yield reliable predictions because of the involvement of stress wave propagation and the column vibration at higher modes during the impact loading phase.
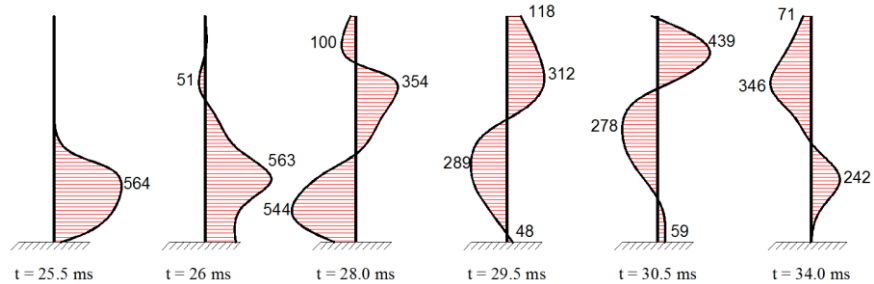
(a) Acceleration along the column (m/s^2)
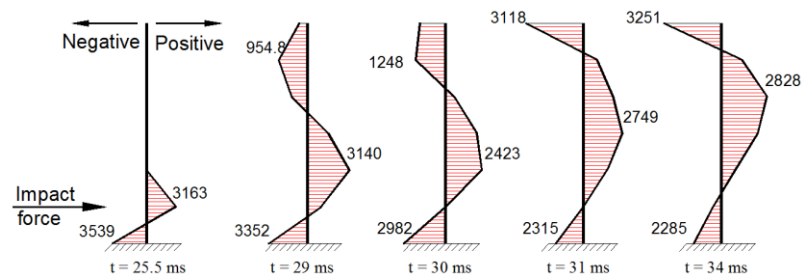
(b) Bending moment (kNm)

Figure 2-16. Acceleration and bending moment variation along the column (25.5 ms-34 ms).

Figure 2-17 describes the bending moment along the column resulted from different impact scenarios at a critical instant. The bending moments are examined at critical sections including at the impact point, the column base, the intermediate section, and the column top. It is noted that the intermediate section, which locates between the impact point and the column top, varies under different impact scenarios. The critical bending moments at the impact point and the column base occur at the instant of the maximum impact force while the critical bending moment at the intermediate section happens when the column top starts vibrating. As shown in Figure 2-17a, the maximum bending moment at the impact point and the column base shows an unique shape for different impact scenarios and its magnitude increases with the PIF. When the PIF increases from 3,460 kN (C3) to 30,000 kN (C14), the maximum positive bending moment at the impact area noticeably increases from 1,208 kNm to 6,629 kNm while the maximum negative bending moment at the column base rises from 2,227 kNm to 8,039 kNm.

In addition, the shape of the bending moment diagram is changed due to the different distributions of the inertia force. At the instant when the column top starts vibrating, the maximum negative bending moment also occurs at the intermediate section. The column with

a larger PIF shows a higher negative bending moment at the intermediate section while the location of that section is closer to the impact point than the counterparts, as illustrated in Figure 2-17b. Moreover, when the PIF increases, the maximum negative bending moment at the column top and the positive bending moment at the two third of column show a major development (see Figure 2-17c). Except for the case of Column C14, a significant relative slippage between the superstructure and the column occurs due to the huge shear force at the column top, which dissipates a large amount of energy and reduces the connection constraints. As a result, the maximum bending moment at top of the Column C14 is smaller than those of the other columns (see Figure 2-17c). These changes of the bending moment at the different time and location under different impact loading conditions cause different column failure modes which will be clearly discussed in the later section.
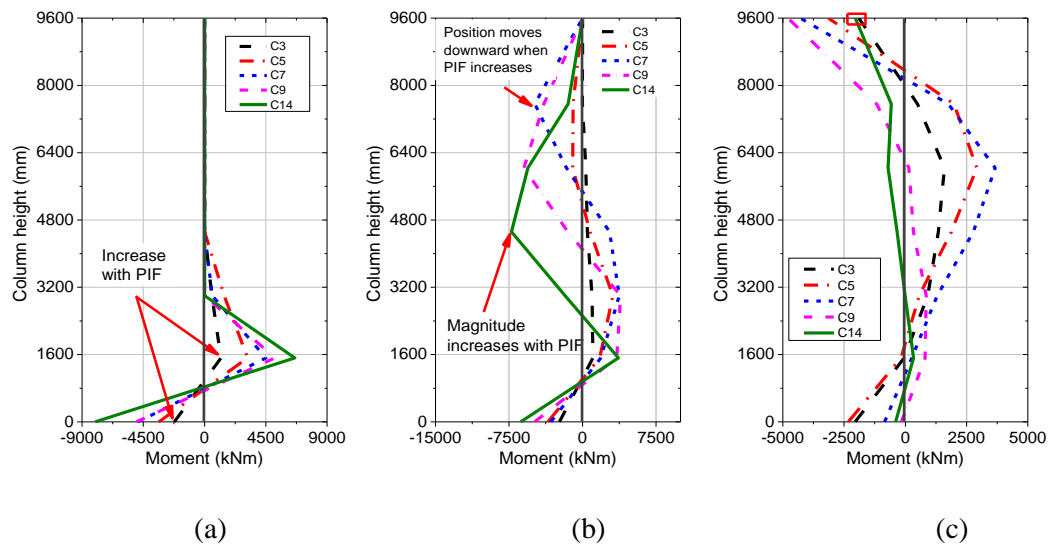
Figure 2-17 Bending moment diagrams under different loading conditions (kNm): (a) At the peak impact force; (b) When the column top starts vibrating; (c) When the bending moment at the top reaches the maximum value.

In general, there are four critical sections that need to be considered under impact events. The position of the positive moment at the impact point and the negative moment at the column base is stable and their magnitudes are proportional to the PIF. Because of the restraint of superstructures, the negative bending moment at the column top may also cause failure. More interestingly, the bending moments at the intermediate sections which always happen at both sides of the column. The positive moment and negative moment may cause damage to the two different sides of the column. Quantitative analyses are crucial to identify whether damage would occur at one side or both sides of the column.

2.4.4. Shear force
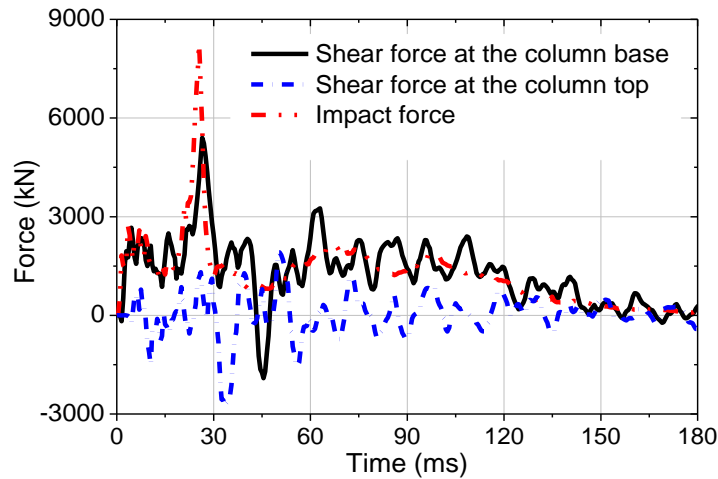
(a) Shear force time histories at the column base and column top
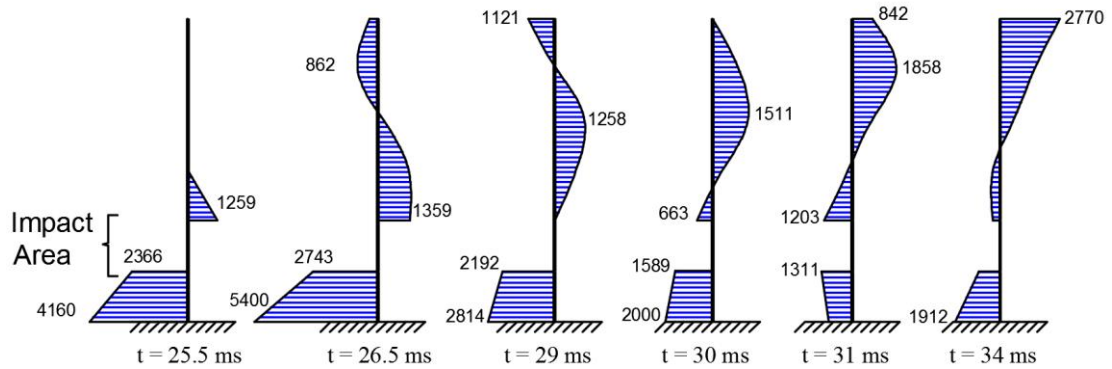
(b) Shear force variation along the column from 25.5 ms to 34 ms

Figure 2-18 Shear force diagram under the Ford truck collision at velocity 100 km/h.

The shear force time histories at the base and at the top of column compared to the impact force are shown in Figure 2-18a (C5). In the initial period of the impact force (before 20 ms) the shear force at the column base is approximately equal to the impact force while the shear force at the column top is very trivial. That is because of the insignificant contribution of the inertia force during that period. Thus, the impact force is primarily transferred to the column base. When the impact force suddenly increases to the peak value of 8,260 kN at 25.5 ms, the peak shear force at the column base increases to about 5,400 kN. It is worth mentioning that the shear force at the base of the column is smaller than the peak impact force because of the resistance of the inertia force which distributes along the part of the column as shown in Figure 2-16a. Furthermore, the shear force at the column top reaches the maximum value of about 2,770 kN at $t = 34$ ms, when the maximum bending moment at the column top is also observed. Similar to the variation of the bending moment, the dynamic shear force diagram varies considerably during the force phase, as presented in Figure 2-18b. The impact force together

29

with the inertia force distribution causes a significant variation of the peak dynamic shear force in terms of locations and time, which results in the dissimilar failure modes of the bridge column under impact loading. These results illustrate that the inertia force plays a crucial role in the shear force distribution of the bridge column under the vehicle collision and the shear force at the two ends of the column needs to be carefully considered.

A significant variation of the shear force in the bridge column under different impact loading conditions is observed as shown in Figure 2-19. Doubling the PIF from 8,260 kN (C5) to 16,400 kN (C7) increases the shear force twice, such as the maximum shear force at the base significantly increases from 5,400 kN to 10,300 kN while that the corresponding value at the column top rises from 2,770 kN (positive side) to 5,750 kN (negative side). However, the shear force at the column base of the Column C9 and C14 is almost similar to Column C7 while they have a huge difference in the PIF (18,500 kN versus 30,000 kN). That is because the shear forces in these cases exceed the shear capacity and cause an excessive local failure, i.e. diagonal shear failure (C9) and punching shear failure (C14).

(a) C5   (b) C7   (c) C9   (d) C14
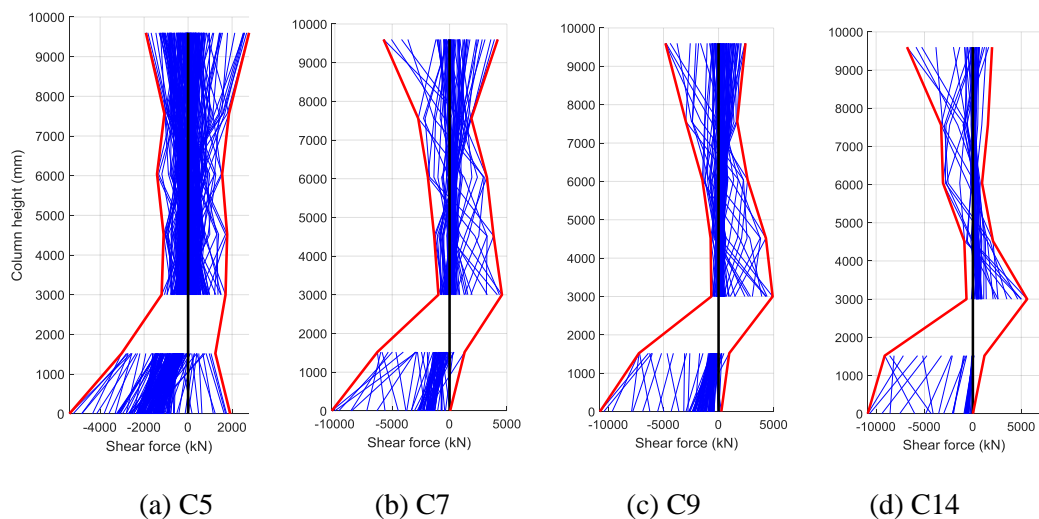
Figure 2-19. Comparison of the shear force diagrams under different impact loading conditions.

2.5. Column failure modes

Based on the bending moment and shear force from the above section, several failure modes of the bridge column under vehicle collision are shown in Figure 2-20. The numerical simulation in this study is able to reproduce the common failure modes observed in vehicle collision accidents shown in Figure 2-2. In the first case, the bridge column shows a minor concrete damage at the impact area when it is impacted by the Ford truck of velocity 80 km/h (Column C3) with the PIF of about 3,461 kN. When the impact velocity increases to 120 km/h (Column C6) producing a PIF of 12,000kN, flexural cracks are observed at the impact point and column mid–height by a positive bending moment and at the two ends by a negative

bending moment (Figure 2-20b). These flexural cracks are similar with the cracks observed in the real vehicle collision as presented in Figure 2-2a. Additionally, when the vehicle velocity increases to 140 km/h (Column C7) with the PIF of about 16,400 (kN), a large diagonal shear crack at the column top is observed on the negative side (see Figure 2-20c), which is caused by a combination of the huge flexural bending moment (see Figure 2-17b) and shear force (see Figure 2-19b) at the column top. That observation explains the crack at the column top under vehicle impact illustrated in Figure 2-2b. From these three columns, it is clear that the increase of the vehicle velocity from 80 km/h to 140 km/h with the engine's mass 0.64 ton, the damage of the bridge column considerably varies from the minor local concrete damage at the impact area to the global responses of the column. On the other hand, the diagonal shear failure at the column base which was experienced under the vehicle collision in Texas in 2007 (see Figure 2-2c) has been numerically obtained when the column is collided by the truck model with velocity100 km/h and the engine's mass 2 ton (C9). In addition, the large peak impact force yields a huge negative bending moment near the impact area. That bending moment together with the large shear force results in another huge diagonal shear crack at the two third of the column (see Figure 2-20d). Furthermore, when the velocity increases to 140 km/h with 2-ton engine that generates the PIF of 30,000 kN (C14), a severe local punching failure is observed in the column at the impact area as shown in Figure 2-20e. The bridge column collapses as a result of that impact event. That failure mode of the bridge column was previously experienced in the vehicle collision in Texas in 2002, as shown in Figure 2-2d.

From the above observations, the failure mode of the column significantly changes from the flexural cracks to punching shear failure with the increase of the vehicle velocity and the engine mass. It is important to note that these failure modes of the bridge column cannot be predicted by using a simplified ESF method. Therefore, dynamic analyses of the bridge column under vehicle collision are necessary in order to capture the true responses and failures.

Moreover, as mentioned previously in Section 2.4.1, the engine's mass governs the PIF and thus affects the column response and failure even though the total vehicle mass remains unchanged. With the same total vehicle mass and vehicle velocity, the PIF increases with the engine's mass as shown in Figure 2-11 and this increase leads to higher moment and shear force in the column. As a result, the damage mode and level of the column change with the engine's mass when the total mass of the vehicle is 8 ton and the vehicle speed is 100 km/h as shown in Figure 2-21. Therefore, this observation again confirms that the engine's mass needs be taken into consideration when designing the RC bridge columns to resist vehicle impact.
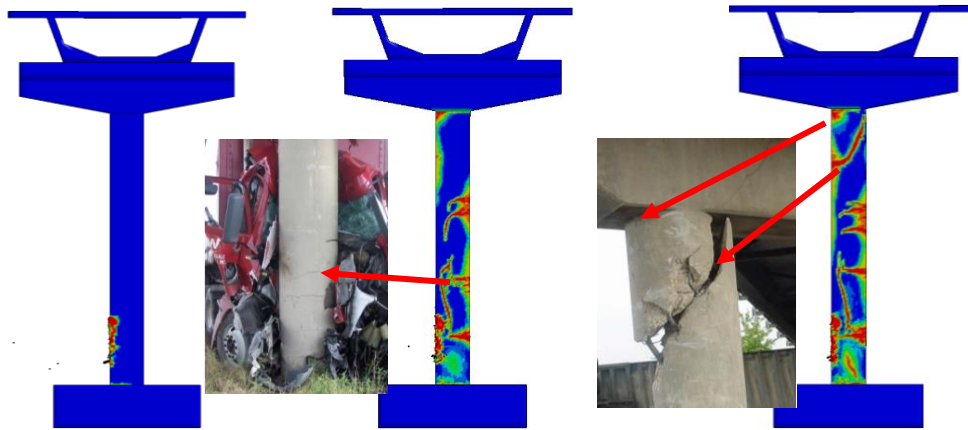
(a) Minor local damage (C3) (b) Flexural cracks (C6) (c) Shear cracks at the column top (C7)

Ground level
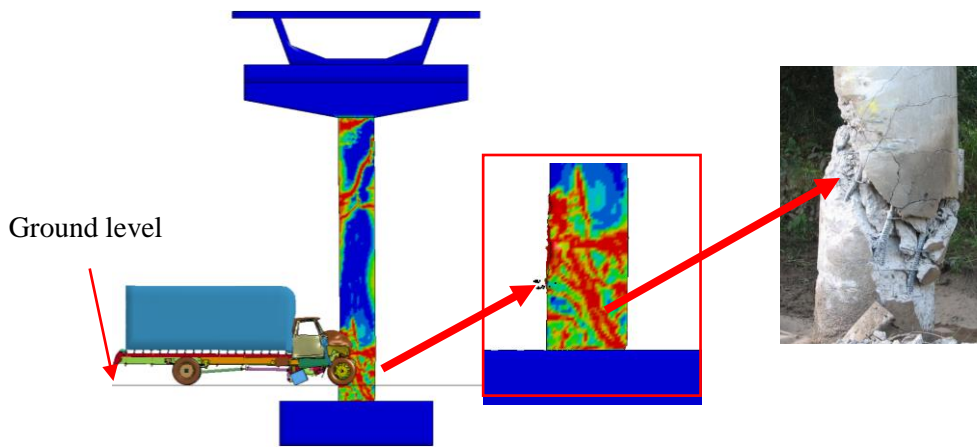
(d) Shear cracks at the two ends (C9)

Ground level
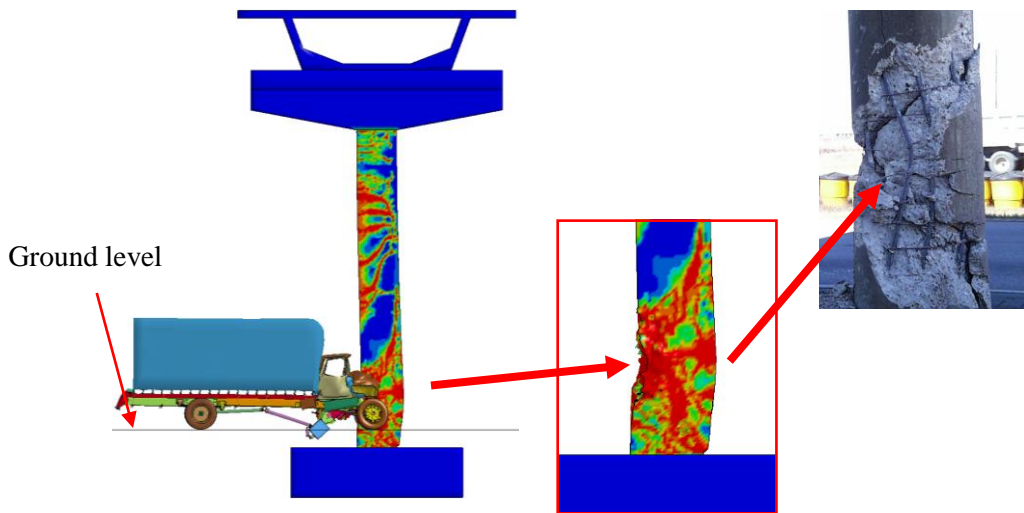
(e) Punching shear (C14)

Figure 2-20 Different failure modes of the bridge column under vehicle collision.

| | | |
| 0.64-ton engine | 1.0-ton engine | 2.0-ton engine |
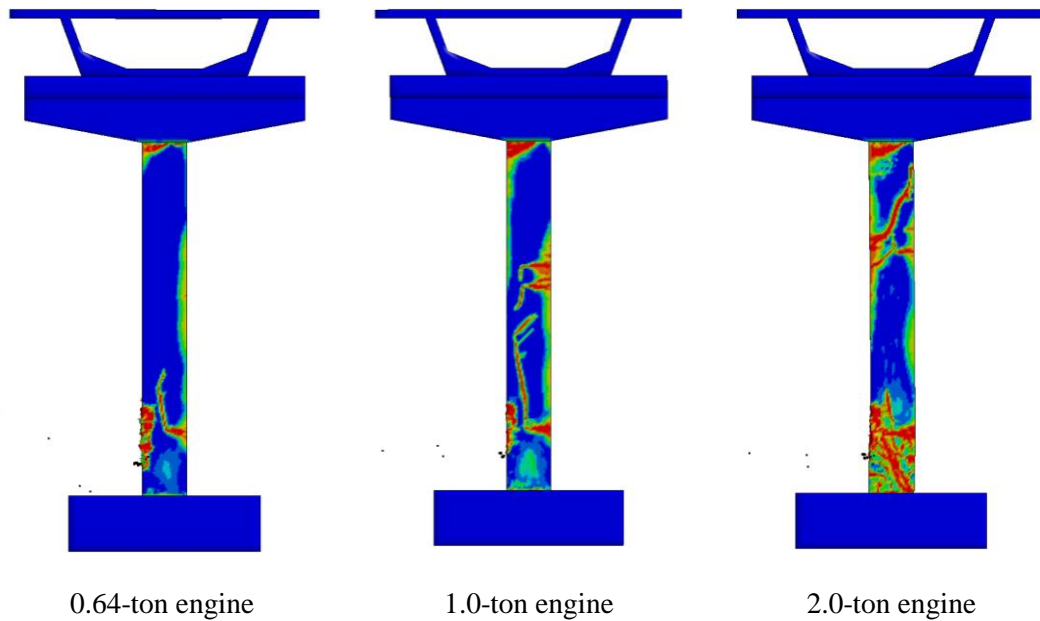
Figure 2-21 Different failure modes under varied engine's mass (vehicle mass = 8 ton and *v* = 100 km/h).

2.6. Effects of superstructure modelling techniques

In literature different researchers have used different simplification approaches to model the bridge superstructure when studying the bridge column subjected to impact loads (El-Tawil et al., 2005; Li et al., 2017; Sha & Hao, 2013). In this study, three different types of simplified modelling of superstructure including the uniformly distributed load, the lumped mass model, and the simplified beam model are considered and the results are compared with those from the detailed 3D model to examine the influences of simplified modelling of superstructure on column responses (see Figure 2-22). The simulation results of the four methods including the impact force time histories, lateral displacement, and failure modes are presented in this section. Under the Ford SUT 8 ton collision, the impact force time histories of the four models are shown in Figure 2-23. It is very clear from the figure that the impact force time histories of the four models show only a slight difference. When the impact velocity is 90 km/h, the PIFs of the four model show a very small variation of 8%. The impact impulses of the four model are almost similar (about 200 kN.s) as shown in Table 2-2. Under the vehicle velocity of 120 km/h, the PIFs of the four models are approximately 12,000 kN and the corresponding impulses are 267.7 kN.s. A similar observation was reported in the study of bridge pier subjected to barge impact by Sha and Hao (2013). These results indicate that different modelling of the superstructure has an insignificant influences on the predicted impact force. This is because the impact force during the force phase is resulted from the similar impactor–structure interaction and the initial momentum (Pham & Hao, 2016, 2017a) while the superstructure mass provides inertial resistance to the column top, but has little influence on the local vehicle-structure interaction although it affects the global response of the column. As

33

a result, the superstructure modelled by the four different techniques yields similar impact force time histories.

Although the similar impact force time histories are recorded, the lateral displacement of the column in the four models is significantly different in terms of the maximum lateral displacement and the vibration duration, as illustrated in Figure 2-24. The maximum positive and negative lateral displacements of the bridge column with 3D superstructure modelling are about 4.26 mm and 0.82 mm, respectively. This unsymmetrical displacement is due to the slippage between the superstructure and the column and the viscous damping of the column. From Figure 2-24, the vibration period is estimated about 594 ms. It is important to note that the lateral displacement of the column under dynamic impact loading has two different phases, i.e. the force phase and the free vibration phase.

| 3D detailed model | Uniformly distributed load | Lumped mass model | Simplified beam model |

(a)   (b)   (c)   (d)
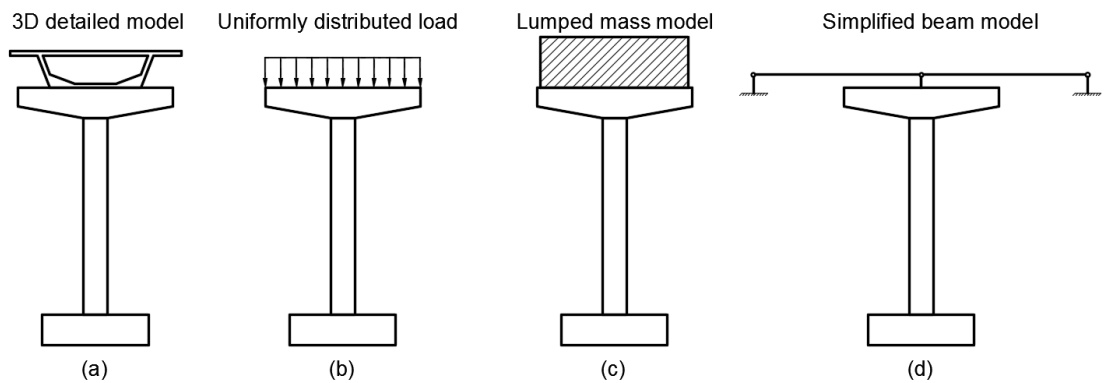
Figure 2-22 Different superstructure modelling.

(a) 90 km/h   (b) 120 km/h
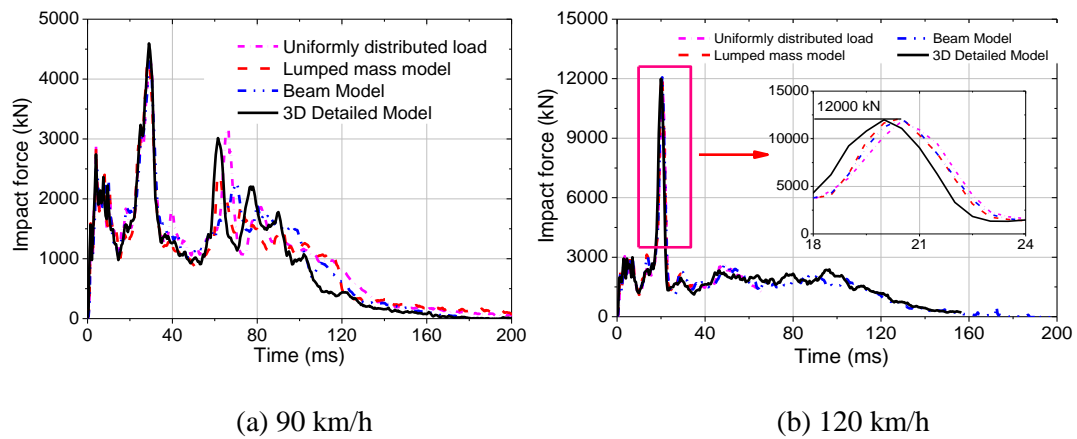
Figure 2-23 Impact force time histories of the four models under the Ford truck collision.

When the superstructure is simplified by the uniformly distributed load on the column top, the maximum displacement is 17 mm. The vibration period of the column estimated from the simulation is about 400 ms. The natural vibration period of this model is shorter than the 3D model because it neglects the mass of the superstructures which results in a longer natural

vibration period. The natural vibration period of the column in the case of the uniformly distributed load can also be theoretically verified by the following equation:

$$T_1 = 2\pi\sqrt{\frac{m}{k}} = 2\pi\sqrt{\frac{m}{\dfrac{3EI}{L^3}}} = 405(ms) \tag{2-8}$$

where m is the total mass of the column, 67,046 kg, k is the global stiffness of column under lateral static load, E is the Young's modulus of concrete material, $4700\sqrt{f_c}$, f_c is the compressive strength of concrete, i.e. 34 MPa in the present study; I is the moment of inertia, L is the length of the column.

(a) 3D Model　　　　　　　　　(b) Uniformly distributed load

(c) Lumped mass model　　　　　　(d) Simplified beam model
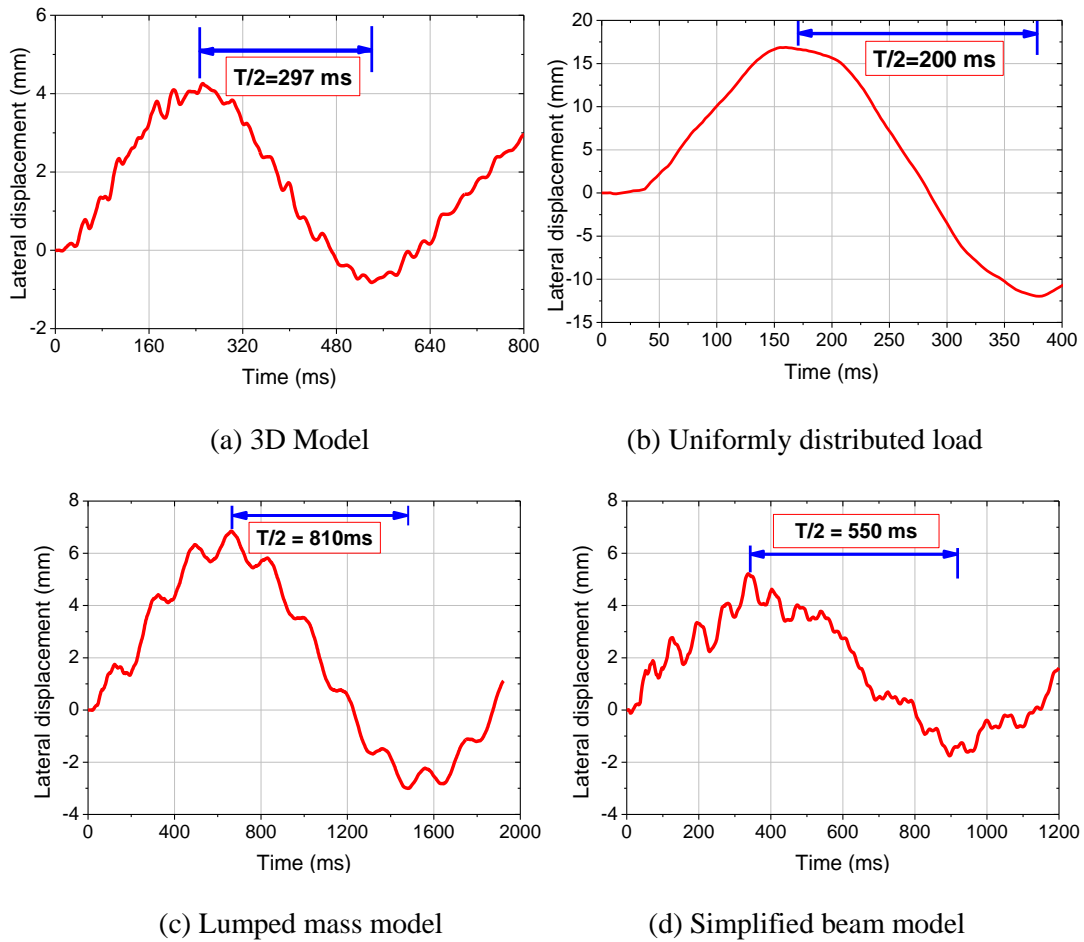
Figure 2-24 Lateral displacement of the bridge column under the collision of 90 km/h

On the other hand, in the lumped mass model, a smaller maximum lateral displacement (7 mm) but higher vibration period (1,620 ms) are observed as compared to those of the 3D model (see Figure 2-24b). Based on the weight of the lumped mass, the natural period of the column can also be theoretically verified:

$$T_1 = 2\pi \sqrt{\dfrac{m + m_{add}}{\dfrac{3EI}{(L + H_T)^3}}} = 1,680(ms) \tag{2-9}$$

where m_{add} is the mass of the superstructures, 400,000 kg; H_T is the height of the cap beam and the lumped block (3.4 m).

The lumped mass model over predicts the actual vibration period of the column because it ignores the effect of the superstructure stiffness on the lateral stiffness of the column. Moreover, the mass of the superstructure, which distributes along the 40-m beam and results in the resistance of the superstructure, does not concentrate on top of the column. As a result, the contribution of the superstructure on the column vibration is different from the lumped mass model. The lateral displacement of the bridge column with the simplified beam model is presented in Figure 2-24c. The maximum lateral displacement is 5 mm and the column vibration duration is about 1,100 ms. The column, in this case, has more restraint than that of the 3D model since there is no slippage between superstructure and the column. Hence, the stiffness of the column in the simplified beam model is higher than that of the 3D model.

Cracks of the four bridge columns under the vehicle impact with velocity 120 km/h are shown in Figure 2-25. Although the impact force time histories are similar, modelling the superstructure by different techniques shows different crack patterns. As illustrated in Figure 2-25, modelling the superstructure by simplified beam model can yield similar cracks on the bridge column to those of the 3D model. The crack pattern in the uniformly distributed load model is more severe than that of the 3D model while the lumped mass model shows less column damages.

(a) 3D detail   (b) Uniformly distributed load   (c) Lumped mass   (d) Beam model
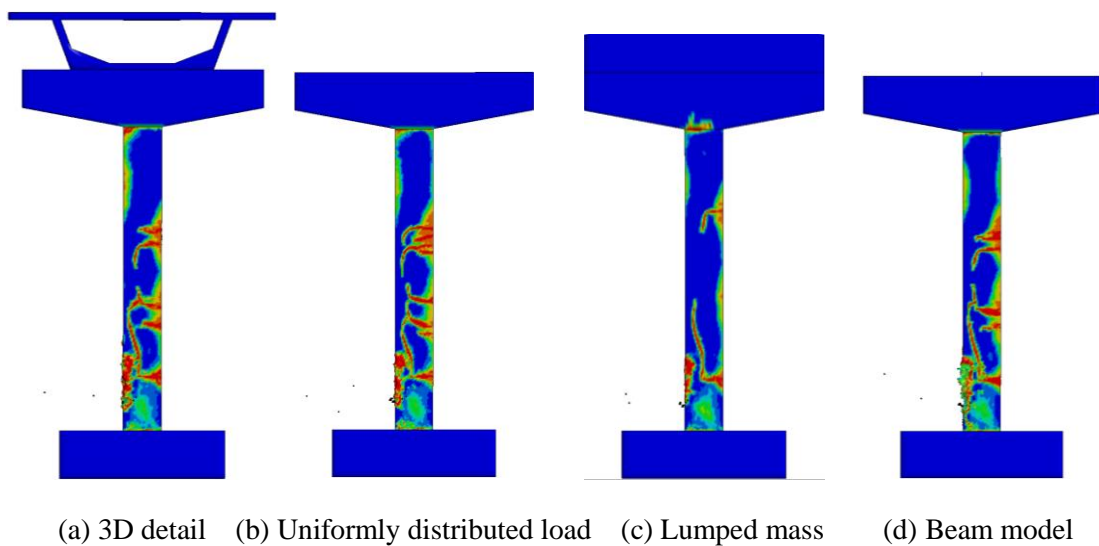
Figure 2-25 Cracks of the bridge column under the velocity of 120 km/h.

From the above comparisons, it can be concluded that simplifying the superstructure by a simple model such as uniformly distributed load, lumped mass or beam model can well predict the impact force but not the lateral displacement and the failure modes. The uniformly distributed load model ignores the contribution of the superstructure mass and stiffness on the behaviour of the column while the lumped mass model neglects the lateral stiffness of the superstructure and overestimates the superstructure mass acting on the column top. The simplified beam model could not simulate the relative displacement between the column and the superstructure. These results indicate that a simplified model can be used to predict the impact force but not the lateral displacement and damage of the column.

2.7. Conclusions

This study numerically investigates the response and failure of bridge columns under vehicle collision. The numerical results are carefully calibrated against the pendulum impact testing results with very good match. The full bridge model is then built based on the validated model. Responses of the bridge column subjected to different vehicle impact conditions are simulated. The effects of the dynamic impact loading on the axial force, the bending moment, the shear force, and the failure modes of the bridge column have been examined. The findings in this study can be summarised as follows:

1. The engine's mass significantly affects the PIF, the moment, the shear force and thus the damage of the column but it has not been considered in the literature.

2. The peak impact force on a bridge column can be predicted from vehicle engine's mass and the vehicle impact velocity while the impulse from the collision can be estimated from the momentum-impulse conservation.

3. The impact force causes a considerable increase of the axial force thus it should be considered in the design. This influence has not been reported in the literature yet.

4. The acceleration along the column fluctuates significantly with different modes during the impact loading. Because of the stress wave propagation and column responding at high modes to vehicle impact, the assumption of the linear distribution of the inertia force along the column is un-conservative in some scenarios. The use of the SDOF in predicting the behaviour of the structures under impact loads might not yield reliable predictions either.

5. The bending moments and shear forces vary significantly during an impact event and they highly relate to the inertial force distribution. The bending moment at the critical sections, i.e. the column base, the impact point, the intermediate section, and the column top needs careful dynamic analyses in the design stage for reliable predictions.

6. The numerical simulation is able to simulate the failure modes observed in vehicle collision accidents.

7. Simplified modelling of the bridge superstructure in predicting the column responses to vehicle impact can yield good predictions of impact force, but not the overall column responses.

2.8. References

AASHTO. (2012). *AASHTO LRFD bridge design specifications (customary U.S. units)*. 6th Ed., Washington, DC.

Abdelkarim, O. I., & ElGawady, M. A. (2016). Performance of hollow-core FRP–concrete–steel bridge columns subjected to vehicle collision. *Engineering Structures, 123*, 517-531.

Abdelkarim, O. I., & ElGawady, M. A. (2017). Performance of bridge piers under vehicle collision. *Engineering Structures, 140*, 337-352.

ACI. (2008). *Building code requirements for structural concrete (ACI 318-08) and commentary (ACI318R-08)*. Farmington Hills, MI: ACI 318.

Agrawal, A. K., Xu, X., & Chen, Z. (2011). *Bridge vehicle impact assessment* (C-07-10). University Transportation Research Center.

Buth, C. E., Brackin, M. S., Williams, W. F., & Fry, G. T. (2011). *Collision loads on bridge piers: phase 2. Report of guidelines for designing bridge piers and abutments for vehicle collisions* (FHWA/TX-11/9-4973-2). College Station, TX.

Buth, C. E., Williams, W. F., Brackin, M. S., Lord, D., Geedipally, S. R., & Abu-Odeh, A. Y. (2010). *Analysis of large truck collisions with bridge piers: phase 1. Report of guidelines for designing bridge piers and abutments for vehicle collisions* (FHWA/TX-10/9-4973-1). College Station, TX.

CEN. (2002). *Actions on structures. Part 1-1: General actions-densities, self-weight, imposed loads for building*. Brussels, Belgium: BS EN 1991-1-1:2002.

Chen, L., & Xiao, Y. (2012). Review of studies on vehicle anti-collision on bridge piers. *Journal of Highway and Transportation Research and Development, 29*(8), 78-86.

Chen, W., Hao, H., & Chen, S. (2015). Numerical analysis of prestressed reinforced concrete beam subjected to blast loading. *Materials & Design, 65*, 662-674.

Consolazio, G., & Davidson, M. (2008). Simplified dynamic analysis of barge collision for bridge design. *Transportation Research Record: Journal of the Transportation Research Board,*(2050), 13-25.

Demartino, C., Wu, J. G., & Xiao, Y. (2017). Response of shear-deficient reinforced circular RC columns under lateral impact loading. *International Journal of Impact Engineering, 109*, 196-213.

El-Tawil, S., Severino, E., & Fonseca, P. (2005). Vehicle collision with bridge piers. *Journal of Bridge Engineering, 10*(3), 345-353.

Fujikake, K., Li, B., & Soeun, S. (2009). Impact response of reinforced concrete beam and its analytical evaluation. *Journal of Structural Engineering, 135*(8), 938-950.

Hallquist, J. O. (2007). *LS-DYNA keyword user's manual.* Livermore Software Technology Corporation. Vol. 970. (pp. 299-800).

Hao, Y., & Hao, H. (2014). Influence of the concrete DIF model on the numerical predictions of RC wall responses to blast loadings. *Engineering Structures, 73*, 24-38.

Hao, Y., Hao, H., Jiang, G. P., & Zhou, Y. (2013). Experimental confirmation of some factors influencing dynamic concrete compressive strengths in high-speed impact tests. *Cement and Concrete Research, 52*, 63-70.

Li, J., Hao, H., & Wu, C. (2017). Numerical study of precast segmental column under blast loads. *Engineering Structures, 134*, 125-137.

Malvar, L. J., & Crawford, J. E. (1998). *Dynamic increase factors for steel reinforcing bars [C]*. Paper presented at the The Twenty-Eighth DoD Explosives Safety Seminar Held, Orlando, USA

Megally, S. H., Garg, M., Seible, F., & Dowell, R. K. (2001). *Seismic performance of precast segmental bridge superstructures* (SSRP-2001/24). University of California, San Diego.

Ngo, T. D. (2005). *Behaviour of high strength concrete subject to impulsive loading* (Doctoral dessertation). The University of Melbourne

Pham, T. M., & Hao, H. (2016). Impact behavior of FRP-strengthened RC beams without stirrups. *Journal of Composites for Construction, 20*(4), 04016011.

Pham, T. M., & Hao, H. (2017a). Effect of the plastic hinge and boundary conditions on the impact behavior of reinforced concrete beams. *International Journal of Impact Engineering, 102*, 74-85.

Pham, T. M., & Hao, H. (2017b). Plastic hinges and inertia forces in RC beams under impact loads. *International Journal of Impact Engineering, 103*, 1-11.

Sha, Y., & Hao, H. (2013). Laboratory tests and numerical simulations of barge impact on circular reinforced concrete piers. *Engineering structures, 46*, 593-605.

Sharma, H., Hurlebaus, S., & Gardoni, P. (2012). Performance-based response evaluation of reinforced concrete columns subject to vehicle impact. *International Journal of Impact Engineering, 43*, 52-62.

Sideris, P., Aref, A. J., & Filiatrault, A. (2014). Large-scale seismic testing of a hybrid sliding-rocking posttensioned segmental bridge system. *Journal of Structural Engineering, 140*(6), 04014025.

Thilakarathna, H. M. I., Thambiratnam, D., Dhanasekar, M., & Perera, N. (2010). Numerical simulation of axially loaded concrete columns under transverse impact and vulnerability assessment. *International Journal of Impact Engineering, 37*(11), 1100-1112.

Zhang, X., Hao, H., & Li, C. (2016). Experimental investigation of the response of precast segmental columns subjected to impact loading. *International Journal of Impact Engineering, 95*, 105-124.

CHAPTER 3

IMPACT FORCE PROFILE AND FAILURE CLASSIFICATION OF REINFORCED CONCRETE BRIDGE COLUMNS AGAINST VEHICLE IMPACT

ABSTRACT[2]

Numerical simulations are utilised in this study to define the impact force profile generated by vehicle collisions on reinforced concrete bridge columns (RCBCs) and classify the dynamic responses and failure of the columns under collision events. The results indicate that both the column properties (i.e. dimension of the cross-section and concrete strength) and initial conditions of vehicles (i.e. vehicle velocity, engine mass, and vehicle mass) play a crucial role in determining the impact force profile from the vehicle collision. A new vehicle impact force model is proposed for engineers to use in design of RCBCs under vehicle collisions in which the influence of shear failure of the column on impact force is considered. Based on the shear mechanism of RCBCs under impact events, the maximum dynamic shear capacity of a column is defined. Furthermore, the bending moment and shear force distributions, as well as the failure mode of RCBCs have been classified into two categories, i.e. flexural response and shear response governed failure with respect to the peak impact force (PIF) on the column. For the flexural response governed failure mode, flexural cracks at the intermediate sections are formed in the positive side of the column, while the diagonal shear or punching shear failure at the impact area together with negative flexural-shear cracks occur in the column if the shear failure mode dominant the column responses.

3.1. Introduction

Vehicle collisions on reinforced concrete bridge columns (RCBCs) from accidents or terrorist attacks occasionally occur. For better protection of bridge structures against vehicle impact a higher demand for the load-carrying capacity of the bridge columns is required. A collision from a heavy-duty vehicle may cause collapse of the whole bridge structure and cost human lives, such as in Texas, 2002 (Buth et al., 2010) or in Hunan, 2009 (Chen & Xiao, 2012). Moreover, a terrorist attack on a bridge column could paralyse the whole traffic system in urban vicinity areas. These accidents and attacks require more attention and understanding for

---

better designs of RCBCs to resist vehicle impacts. Researchers previously tackled this problem through either experimental tests (Buth et al., 2011), numerical simulations (Abdelkarim & ElGawady, 2017; Agrawal et al., 2013; Agrawal et al., 2011; Do et al., 2018a; Sharma et al., 2012), or reduced modelling and analyses (Al-Thairy & Wang, 2013; Chen et al., 2016) to study the structural behaviours under impact loads. Among these approaches, the last two methods are more and more widely utilised as compared to the former because of not only high cost and safety concerns associated with the experimental tests but also the ability of achieving high accuracy in predicting the dynamic responses of structures with advanced numerical and analytical models.

Previous researches gave suggestions and recommendations for design of structures to resist vehicle collisions (AASHTO, 2012; Abdelkarim & ElGawady, 2017; CEN, 2002, 2006; Chen et al., 2016; Do et al., 2018a; Do et al., 2018c; El-Tawil et al., 2005; SA/SNZ, 2002). Current design codes and standards commonly adopt a simplified equivalent static force (ESF) to define the impact force from vehicle collision on structures. This approach is straightforward for engineers to estimate the collision force for design analysis of structures. For example, based on the experimental tests on the rigid steel column (Buth et al., 2011) and the open literature, AASHTO (2012) recommended a constant value of about 2,668 kN irrespective of the vehicle loading conditions for design of RCBC to resist vehicle impact. SA/SNZ (2002) and CEN (2002) suggested a simple equation to calculate the horizontal impact force in which the initial kinetic energy of the vehicle, vehicle deformation, and column displacement are taken into account. CEN (2006) distinguished between soft impact, in which the impacted structure absorbs a large amount of energy, and hard impact where the impact energy mostly dissipated by the vehicle, in estimating the equivalent impact force. The maximum impact force on structures is determined based on the elastic behavior of both the vehicle model and structures. However, the deficiencies of the current design guides in predicting the impact force and structural responses are recognised by previous studies (Abdelkarim & ElGawady, 2017; Do et al., 2018a; El-Tawil et al., 2005). A series of numerical simulations of RCBC subjected to vehicle impacts have been conducted by Abdelkarim and ElGawady (2017) to estimate the impact force on structures from collision events. Based on numerical simulation results, an equation to estimate the impact force from vehicle impact on RCBCs based on the kinetic energy of the vehicle model has been proposed. Full-scale models of medium and light truck models have also been used to investigate the impact force and response of steel bollards (Al-Thairy & Wang, 2013) and concrete-filled steel tubular bollards (Hu & Li, 2016) under vehicle collisions. From these studies, some simplified models to estimate the maximum vehicle impact force on steel structures and barriers have been proposed (Al-Thairy & Wang, 2013; Hu & Li, 2016). However, those studies mainly concentrated on predicting the peak

impact force (PIF) on the structure while the impact force profile and duration, as well as the dynamic response of the structures and the parameters affecting the dynamic structural responses, i.e. strain rate effect, vibration characteristics, and inertia force effect are not considered. It is worth mentioning, as will also be demonstrated in this paper, that the peak impact force causes local damage including punching shear or diagonal shear while the global response of the column which may induce different failure modes at other critical sections, such as column top and intermediate sections as systematically presented in the previous study by Do et al. (2018a), is more correlated to the impact force impulse. Because the current design practice depends mainly on the equivalent static analysis, the reliability and applicability of those proposed models and recommendations based on PIF only are questionable. By presenting the dynamic bending moment, shear force, and acceleration of a RCBC during collision events, Do et al. (2018a) indicated that the use of the ESF is un-conservative in estimating the impact behaviour of the RCBC since the dynamic bending moment and shear force of the column might cause damage which could not be predicted by an equivalent static analysis. An equation to predict the PIF was then proposed in which the mass of the truck's engine is used instead of the total mass of the truck model. The study also provided clear explanations of various observed failure modes of RCBCs in real vehicle accidents. Nevertheless, the latter study was based on a particular column, the influences of the column parameters, such as column height, cross-section dimension, axial force ratio, and steel reinforcements on the impact force profile and the dynamic capacity of the column were not considered in the study. Chen et al. (2016) conducted extensive parametric studies on the medium truck collisions on circular and rectangular bridge piers. By separating the impact of the vehicle engine and cargo, the vehicle model was simplified to an equivalent two-degree of freedom model. A coupled mass-spring-damper (CMSD) was developed and validated against numerical results. This study also considered the effects of pier parameters on the time histories of the impact force. However, the elastic material model was used for concrete in the study and the design of the column was almost rigid. Thus, the column could not yield large deformation and displacement by the first peak force caused by engine impact. Importantly, no concrete damage and column failure were considered in the study. Therefore, the numerical results do not necessarily reflect the actual impact behaviour of bridge piers.

The present study aims to propose an impact force profile that would be induced by a vehicle impacting on RCBCs. The effects of column properties e.g. column height, cross-section dimension, axial force ratio, and steel reinforcements under different loading conditions are also considered. Furthermore, based on the shear mechanism of the RCBC under impact load, the maximum achievable impact force from the vehicle collision acting on the column is determined. The responses and failures of the RCBCs are then classified into two categories,

i.e. flexural response and shear response, which provide a valuable guidance for engineers in predicting the impact behaviours of the RCBCs.

3.2. Numerical model development and its verification

3.2.1. Experimental test and model description
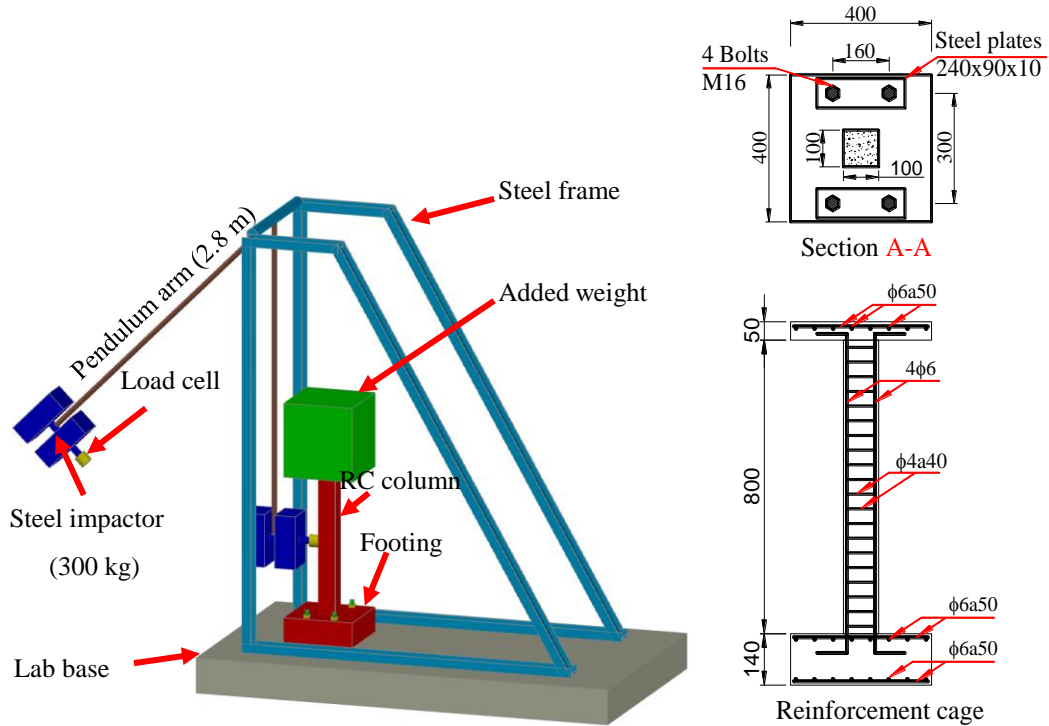
(a) Experimental test 3D view and the column design of the experimental test
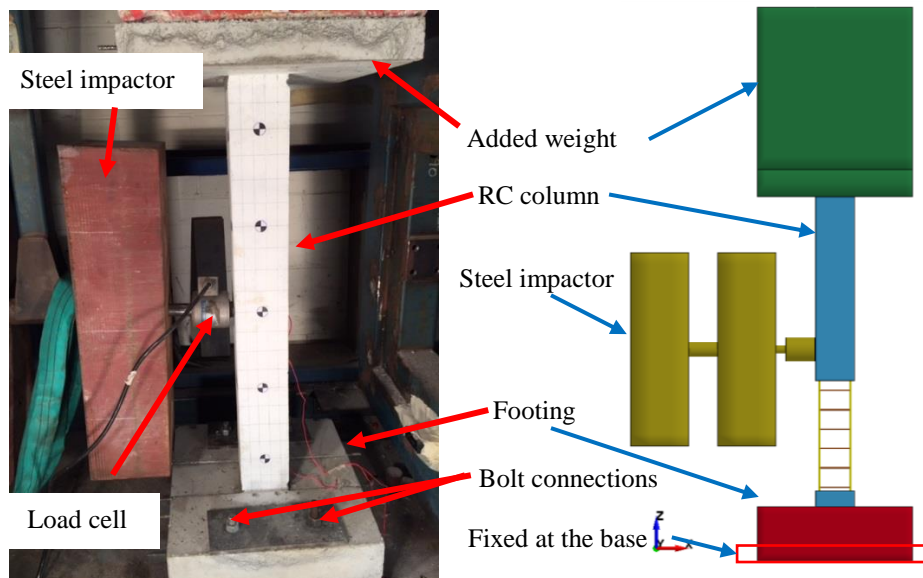
(b) Test set up (Zhang et al., 2016) and FE model of the RC column with the steel impactor

Figure 3-1 Experimental test and FE model of the RC column under pendulum impact load.

In this study, a three dimensional (3D) finite element (FE) model of a bridge column is developed and verified based on the experimental impact test on a quarter scaled reinforced concrete (RC) column by Zhang et al. (2016). The schematic view, column design, and the pendulum impact test setup are shown in Figure 3-1a. To simulate the impact response of the tested column in the numerical model, the concrete column, steel impactor, footing and the added weight are modelled by hexahedral elements with 1 integration point while the longitudinal and transverse reinforcements are modelled by 3-nodes beam elements with 2 x 2 Gauss quadrature integration. In the simulation, the contact between the reinforcement bars and the surrounding concrete is assumed as a perfectly bonded since no slippage between the reinforcements and concrete was observed in the experiments. In addition, the LS-DYNA contact algorithm named *Contact_Automatic_Surface_to_Surface is utilised to model the impacting contact between the steel impactor and the RC column. Since no displacements or rotation at the connection between the footing and the floor was observed during the test (Zhang et al., 2016), the column is fixed at the bottom face of the footing in the FE model. The numerical model of the pendulum impact test on the RC column is shown in Figure 3-1b.

3.2.2. Material models and strain rate effects

The material models of the simulation and their strain rate effects were presented in Sections 2.2.2.2 and 2.2.2.3 so they are not presented in this section.

3.2.3. Model verification and comparisons

The comparison between the numerical results and experimental tests of the small-scaled monolithic RC column has been presented in Section 2.2.2.4.

3.2.4. Verification of full-scale bridge column under vehicle collisions

From the above comparisons, the numerical simulation has ability to simulate the impact force, lateral displacement, and failure modes of the scaled RC column under low impact velocity of the lab test. However, concerns about the responses of a large-scaled RC column under high impact velocity of collision accidents still remain. Thus, in this section, a full-scale bridge column under real vehicle accident on IH-30 near Mount Pleasant, Texas (Buth et al., 2010) is employed and simulated to verify the accuracy of the current simulation. In this accidental collision, the bridge column which had a circular cross-section of 762 mm was impacted by a heavy-truck-trailer with the total mass of 30 ton. The column was designed with eight-30-mm-diameter longitudinal bars and 10-mm-diameter transverse bars at 150 mm spacing (Buth et al., 2010). By using the above material model, strain rate effects, and modelling techniques, a 3D FE model of the mentioned column is built and impacted by the heavy-truck-trailer model as presented in Figure 3-2a. The properties of the reinforcements and concrete used in the numerical simulation are obtained from the design of the actual bridge material (Buth et al.,

2010). It should be mentioned that the vehicle model was adopted in the previous study and shared by Sharma et al. (2012). The truck information will be presented in Section 3.3. Because no impact force and displacement of the column were reported from the collision, the failure mode of the column in the simulation is used to compare with the real accident as presented in Figure 3-2b.
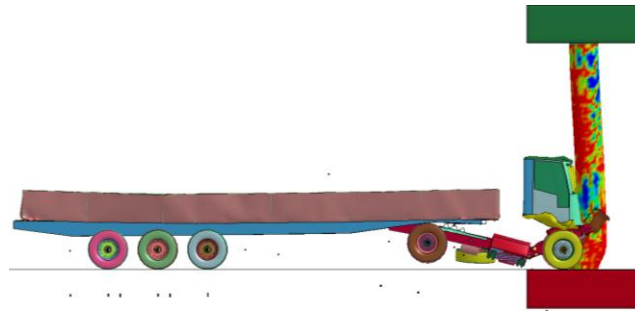
(a) Numerical model of the full-scale bridge column and heavy truck-trailer collision
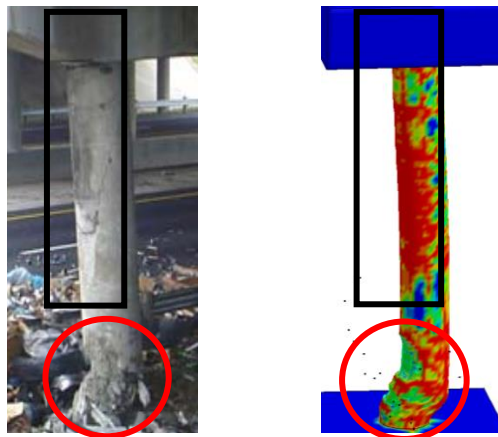
Real accidient (Buth et al., 2010)   Simulation

(b) Comparison of the column failure modes

Figure 3-2 Numerical verification of the full-scale bridge model under heavy truck-trailer collision.

The figure shows that the failure of the column i.e. diagonal shear at the base, flexural – shear failure at the column mid-height, and flexural crack at the column top from the real vehicle collision are well simulated in the numerical model. These verifications show the reliability and accuracy of the current simulation techniques in predicting the impact responses of the RC structures with different sizes under wide ranges of velocities.

3.3. Simulation of bridge specimens and vehicle models

The numerical model of a full-scale RC bridge is developed in this section based on the previously validated material models, strain rate effects, contact definitions, and modelling techniques. The RC bridge consists of one single RCBC, two hollow-section girders as

superstructures and two concrete abutments, as shown in Figure 3-3. Similar bridge model was also employed in previous studies to investigate the pier responses (Abdelkarim & ElGawady, 2016; El-Tawil et al., 2005) and the accuracy of this modelling approach in simulating and predicting the dynamic response of RC columns under impact loading has been confirmed (Consolazio & Davidson, 2008). The reference RCBC (C0) used in this study is 1,200 mm x 1,200 mm (*D* x *W*) in cross-section and 9,600 mm in height (*H*) while the overall dimensions of the hollow beam are obtained from Megally et al. (2001) with the span length of 40 m. The weight of the superstructure which equals 10% of the vertical compressive capacity of the column is transmitted to the RC column through a cap beam placed on the column top (see Figure 3-3). The coefficient of friction between the superstructure and the cap beam or the concrete abutment is assumed to be 0.6 (Bakis et al., 2002; Do et al., 2018a). No bearing pad or rubber is included in the model due to its insignificant effect on the behaviours of the column under vehicle impact (El-Tawil et al., 2005). The column is reinforced with twenty-four 30-mm-diameter longitudinal rebars extending from the footing to the cap beam and 14-mm-diameter transverse bars at 200 mm spacing. In the numerical simulation, the footing, RCBC, cap beam, superstructure, and abutments are simulated by hexahedral elements with one integration point (constant stress solid elements) while the steel reinforcements were modelled by 3 nodes-beam elements. The convergence test is conducted to determine the optimal mesh size of the concrete and steel element based on a balance between simulation accuracy and computational efficiency. The numerical results converge when the mesh size of concrete is 20 mm. Since the response of the column during the impact force phase is the primary concern in this study, the implicit simulation is terminated at about 300 - 500 ms (a half of natural period of the column). Therefore, the system damping is ignored in the present study.
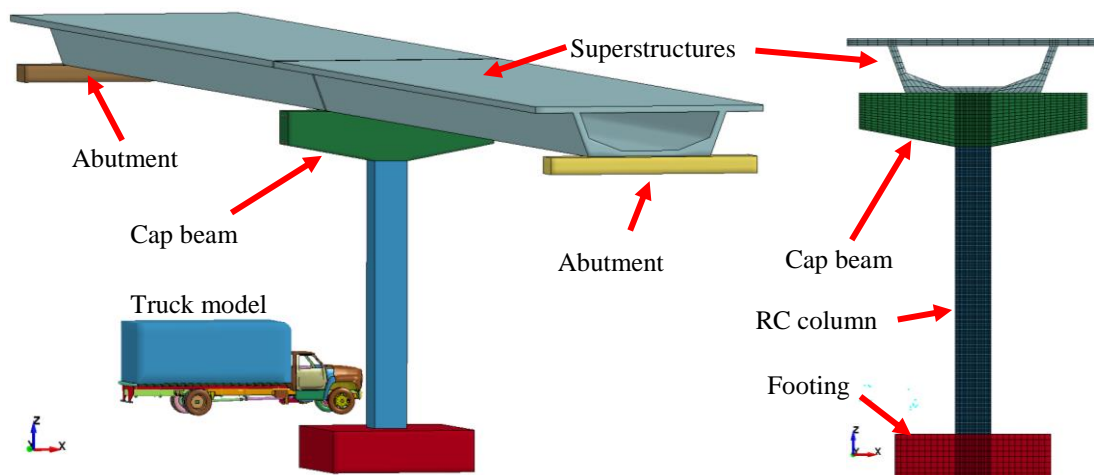
Figure 3-3 FE model of the RC bridge specimen.

The heavy truck trailer as mentioned previously (see Figure 3-2) and a medium Ford truck model (see Figure 3-3) are used to represent the truck impact on the RCBC in this study. The

medium truck model has been commonly used to analyse the impact behaviours of structures under vehicle collision (Abdelkarim & ElGawady, 2016; Abdelkarim & ElGawady, 2017; Chen et al., 2016; Chen et al., 2015; Do et al., 2018a, 2019; El-Tawil et al., 2005; Sharma et al., 2012). The Ford truck model was modelled and validated by FHWA/NHTSA National Crash Analysis Centre at the George Washington University. The total mass and engine mass of the Ford truck model are 8 ton and 0.64 ton, respectively. In this study, the vehicle model is assumed to impact at 1.5 m above the top face of the footing as shown in Figure 3-3a. Without loss of generality, three loading cases of the medium truck are firstly considered in this study including (1) Load 1: the vehicle velocity of 100 km/h with the engine mass of 0.64 ton, (2) Load 2: the vehicle velocity of 100 km/h with the engine mass of 2.0 ton, and (3) Load 3: the vehicle velocity of 120 km/h with the engine mass of 2.0 ton. These loading conditions are chosen since they cause three different failure modes of the columns consisting of flexural cracks, local diagonal shear failure, and punching shear failure at the impact area (Do et al., 2018a). It should be noted that the numerical results from different vehicle velocities from 60 km/h to 140 km/h in the previous study (Do et al., 2018a) are utilised in this study to propose the impact force profile. The total mass of the medium truck ranging from 2.7 ton to 11.8 ton is used in these simulations as suggested by Sharma et al. (2012). The proposed impact force profile is applicable for both the medium truck and the heavy truck. The total mass and the engine mass of the heavy truck trailer are 12 ton and 1.5 ton, respectively. To investigate the impact force profile of the heavy truck collision under wide ranges of vehicle mass and velocity, the total mass of the heavy truck trailer varies from 17 ton to 37 ton while the vehicle velocity increases from 80 km/h to 110 km/h. It is worth mentioning that the light truck with the total mass smaller than 2.7 ton (Sharma et al., 2012) is not considered in this study because of its less significance on the column response (Abdelkarim & ElGawady, 2017; El-Tawil et al., 2005). In this study, the contact algorithm named the penalty method via the ASTS contact keywords is used to define the contact between the vehicle model and the RCBC. Four main parameters need to be defined in this contact algorithm including the penalty formulation (*SOFT*), the penalty scale factor (*SLSFAC*), and the scale factor for slave stiffness (*SFS*) and master stiffness (*SFM*). In the simulations, the standard penalty formulation (*SOFT* = 0) is employed while the default value of penalty scale factor (*SLSFAC*) at 0.1 is adopted. Moreover, the default value of *SFS/SFM* at 1.0/1.0 is used. The corresponding parameters in this study are adopted from the previous study (Pham et al., 2018).

In the following sections, the RCBCs with different column heights, cross-section dimension, transverse reinforcements, axial load ratio, and longitudinal reinforcements under three different loading conditions are examined. These column parameters are chosen because of their significant contribution to the column global stiffness, shear capacity, and flexural

capacity of the column which govern the impact performances, crack patterns, and damage of the RCBC. Firstly, the column cross-section is kept constant at 1,200 mm x 1,200 mm while five different column heights, i.e. 4,800 mm, 6,000 mm, 7,200 mm, 9,600 mm, and 12,000 mm are considered to investigate the influences of the slenderness ratio (H/D = 4, 5, 6, 8, and 10) of the column on the impact force and failure modes of the column. Moreover, five cross-section dimensions with D x W (depth x width) = 600 mm x 600 mm, 800 mm x 800 mm, 1,200 mm x 1,200 mm, 1,500 mm x 1,500 mm, and 2,000 mm x 2,000 mm are considered while the slenderness ratio of these columns is kept at 8. Furthermore, three different transverse reinforcement ratios, i.e. 0.09% (d8s200), 0.26% (d14s200), and 0.53% (d14s100) are used to examine the effects of the transverse reinforcements in controlling the response of the column. The bending moment capacity of the column influenced by the initial axial load and the longitudinal reinforcement ratios is also taken into consideration. The initial axial force applied on the column is increased from 10% to 20%, 40%, and 60% of the column axial compressive capacity while the longitudinal reinforcements vary from 0.63% (24d22) to 1.16% (24d30) and 1.70% (24d36), respectively. Table 3-1 summarises the considered column configurations and the corresponding numerical results.

3.4. Vehicle impact force profile model

3.4.1. Medium truck model (mass < 12 ton)

The impact force time histories on the RCBC C0 from the first loading condition (Load 1) is presented in Figure 3-4. Based on the understanding from the previous studies (Chen et al., 2016; Do et al., 2018b, 2019) and the numerical results in this study, the impact force time histories from a truck impact on the RCBC can be idealised in four stages as shown in Figure 3-4. Firstly, the truck bumper collides on the RCBC generating the first impact force plateau P_1 with duration t_{P1}. The impact force then increases to the F_1 due to the collision of the vehicle engine with duration t_{F1}. After that, the impact force drops to P_2 and keeps constant due to the impact of the truck rails and vehicle parts placed between the engine and the cargo with duration t_{P2}. Finally, the impact of vehicle cargo causes the second peak, F_2, on the column. The impact of the cargo increases the force from P_2 to F_2 in the period of t_{F2}, and the impact force then decreases to zero at 165 ms. The above impact force and duration corresponding to various vehicle impact scenarios and bridge configurations are determined based on the numerical simulations in this study. It should be noted that the total impact force duration is taken as 165 ms in this study. The value is approximated based on many simulation cases carried out in the study. It is noted, however, the value is valid only for the medium truck model considered in the study. For other vehicle models and other impact scenarios, the total impact duration might be different.
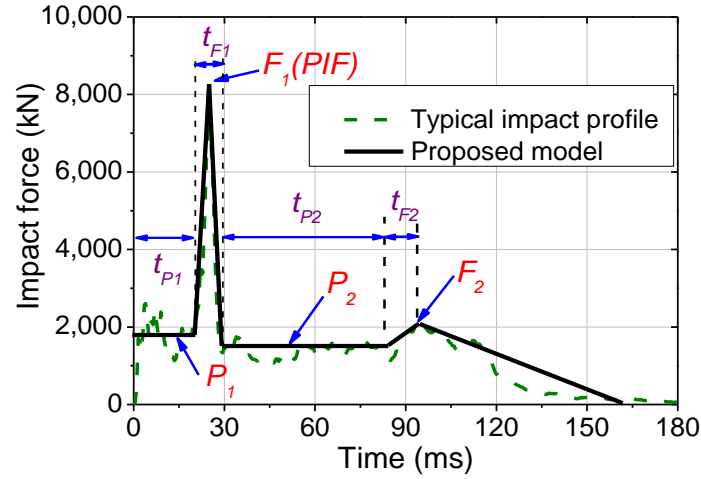
Figure 3-4 A simplified model of the vehicle impact force time histories from the medium truck.

It is well-known that the truck engine colliding on the column occurs only after the bumper totally deformed due to the collision. Thus, the duration of the first stage primarily depends on the gap between the bumper and the vehicle engine. Besides, the impact duration definitely relates to the impact interaction, impact velocity, and the relative stiffness between impactors and structures. By presenting the force-deformation curves of the bumper during the impact event, the previous studies (Chen et al., 2016; Hu & Li, 2016) indicated that stiffness of the bumper is marginal compared to that of a bridge pier. Therefore the duration of this phase is normally short compared to the total duration of a collision event (see Figure 3-4). From the numerical results, it is found that the velocity of the vehicle slightly reduces from V when impact starts to about $0.9V$ when the engine impacts on the column in which V is the initial vehicle velocity (m/s) upon collision. To represent the velocity during this period, the average velocity of $0.95V$ is assumed. The duration of the bumper impact phase can then be obtained from the gap between the bumper and the engine box, L_{1M} *(mm)*, and the velocity of the truck, V *(m/s)*, expressed as follows:

$$t_{P1} = \frac{L_{1M}}{0.95V} \, (ms) \tag{3-1}$$

Generally, L_{1M} is 660 mm (Hu & Li, 2016), 550 mm (Chen et al., 2016), and 500 mm (Chen et al., 2015), depending on the vehicle model. In this study, L_{1M} is taken as 550 mm for the medium-duty truck model collided on the RC column. This number can be easily changed to fit a particular truck in real design.

In each simulation, P_1 can be determined by dividing the total impulse of the bumper's impact to the impact duration t_{P1}, (see Figure 3-5a) which is given in Table 3-1. As can be seen that P_1 significantly depends on the column width and impact velocity of the truck while the

influence of the slenderness, initial axial force ratio, and steel reinforcements is marginal and can be negligible. P_1 shows a proportional increase trend with the increase of the column width, as shown in Figure 3-5b. This is because the increase in the column width increases the contact area between the bumper and the column, resulting in a higher impact force. Besides, the relationship between the force P_1 and the impact velocity which obtained from (Do et al., 2018a) is also plotted in Figure 3-5c.

(a)   (b)   (c)
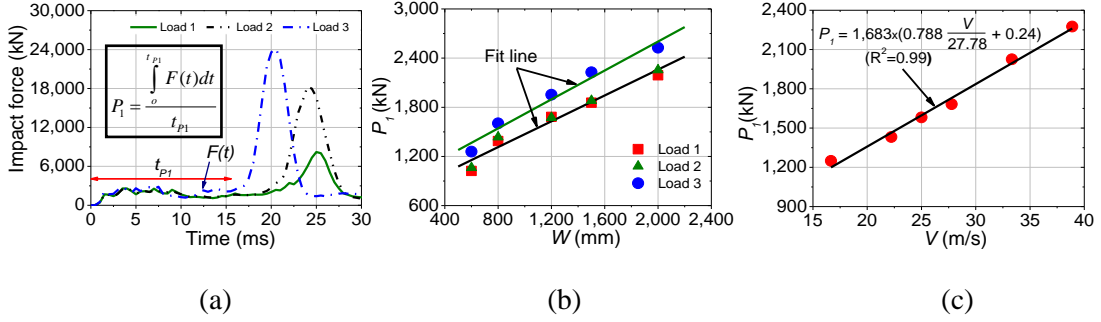
Figure 3-5 The first phase of the impact force time histories: (a) Model of P1 and t_{P1}; (b) Column dimension versus P1 relationships; (c) Vehicle velocity versus P1 relationships.

(a)   (b)   (c)
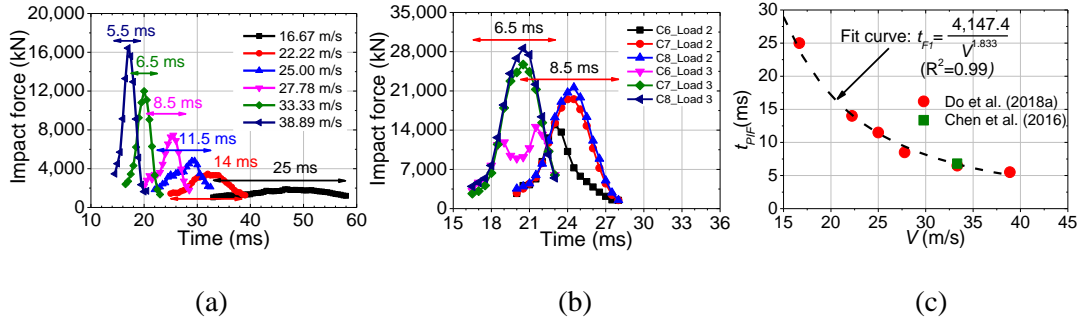
Figure 3-6 The second phase of the impact force time histories: (a) The impact force corresponding to different vehicle velocities; (b) The impact force of different columns; (c) Vehicle velocity versus t_{F1} relationships.

Based on these numerical results, the force P_1 can be generalised as follows:

$$P_1 = P_0 \times k_1 \times k_2 \,(kN) \tag{3-2}$$

$$k_1 = 0.788 \frac{V}{27.78} + 0.240 \tag{3-3}$$

$$k_2 = 0.559 \frac{W}{1200} + 0.441 \tag{3-4}$$

where k_1 and k_2 are the dimensionless coefficients describing the effects of the dimension and impact velocity on P_1, respectively (see Figure 3-5b and c); W is the column width (mm); $P_0 = 1,683 (kN)$ is the average value obtained from the simulations corresponding to a column

width of 1,200 mm and the impact velocity of 100 km/h. The column section of 1,200 mm x 1,200 mm and velocity of 100 km/h are selected since these values are commonly used in the real application.

The truck's engine then impacts on the column through the vehicle bumper which has been deformed due to the truck's frontal impact and currently placed between the engine box and the column. The impact force from the engine causes the deformation of the vehicle bumper which not only dissipates an amount of the impact energy but also affects the contact stiffness between the column and the engine box. The previous study by Pham et al. (2018) has indicated that a minor change of the contact stiffness between a structure and an impactor may cause a significant difference in the impact force. Thus, the impulse from the engine impact is complicated and might not be easily predicted from the theory of momentum – impulse conversion. Hence, the F_1 and the impact duration of the engine impact in this study is estimated through the numerical results. The variation of the t_{F1} under different loading conditions are presented in Figure 3-6. According to the previous results from Chen et al. (2016) and Do et al. (2018a), the influences of the vehicle speed on the impact duration of the engine impact is also presented in Figure 3-6. It is clear that the increase in the impact velocity (from 16.67 m/s to 38.89 m/s) shows a substantial decrease in the impact duration (from 25 ms to 5.5 ms). Figure 3-6b shows that t_{F1} is almost unchanged even though the column width increases from 800 mm to 2,000 mm when these columns are under the same loading conditions. Moreover, by comparing Figure 3-6a and Figure 3-6b, with the same impact speed (27.78 m/s – Load 2) but different engine's mass (0.64 ton compared to 2.0 ton), the duration of the engine impact is also similar (8.5 ms). These results demonstrate the relative independence of the duration t_{F1} on the engine's mass and the column's width but this duration is affected by the impact velocity. From the above observations, t_{F1} can be estimated from the truck velocity by the following equation (see Figure 3-6c):

$$t_{F1} = \frac{4,147.4}{V^{1.833}} (ms) \tag{3-5}$$

F_1 highly depends on the cross-section dimension, impact velocity, and the engine mass while the influence of the other parameters is insignificant, as given in Table 3-1. Furthermore, the insignificant effect of structure span and concrete strength on the PIF, which is the same as F_1 defined in this study, have been previously reported (Do et al., 2018b; Pham & Hao, 2017; Zhao et al., 2017). F_1 on the RCBC with different column cross-sections under three conditions is also plotted in Figure 3-7. It can be seen that F_1 from the engine impact increases with the engine mass and vehicle velocity, but cannot be higher than the maximum dynamic shear capacity of the column, P_{dyn}^{max} (Columns C5 and C6) which will be determined and discussed in the subsequent section. This is because when the impact force from the engine impact

reaches the P_{dyn}^{max}, it induces the punching shear cracks on the column, resulting in a slight movement of the shear plug. This relative displacement of the impacted area of the column affects the vehicle - column interaction and reduces the impact force on the column. Moreover, considering the equilibrium condition of vehicle impact, F_1 cannot be larger than the total column resistance because the column would fail if it reaches the column resistance. Based on the above observations, F_1 on the RCBC can be updated from the previous studies (Do et al., 2018a) by considering the failure of the concrete column as:

$$F_1(kN) = 969.3\sqrt{0.5m_e V^2} - 7,345.9 \le P_{dyn}^{max} \qquad (16.7 \text{ m/s} < V < 40 \text{ m/s}) \qquad (3\text{-}6)$$

where m_e is the mass of the engine (ton); P_{dyn}^{max} is the maximum dynamic shear capacity of the column.
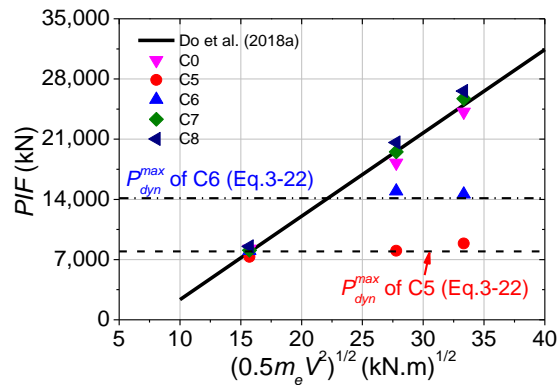
Figure 3-7 The PIF of the RCBCs with different section dimensions under different loading conditions.

In the third stage, the impact force drops to P_2 and lasts until the vehicle cargo collides on the column. As presented in Figure 3-8a, the cargo gradually moves 1,600 mm before colliding on the frontal parts, e.g. the vehicle cabin and the bumper, and resulting in the second peak on the column (see Figure 3-8b). It should be noted that although the distance between the cargo and the cabin is about 480 mm, the cargo collides on the cabin after moving about 1,600 mm because of the densification of the frontal parts of the vehicle. The cargo stops impacting on the column at about 165 ms after shifting about 2,400 mm. As shown in Figure 3-8a, those values are independent of the vehicle velocity. A similar observation is also reported in the previous study by Chen et al. (2016) when the cargo stops colliding on the structure after moving about 2,500 mm. The displacement time history of the cargo is thus simplified as a bi-linear curve as illustrated in Figure 3-8c. In the first part, the cargo displacement increases linearly with time, having a slope coefficient of *0.85V*. The coefficient is 0.85 owing to the reduction of the vehicle velocity due to the collision and the effect of the frame stiffness. It is assumed that when the cargo moves about 2,400 mm, it will cause the second peak, F_2 on the

column and the impact force time histories then decreases linearly to zero at 165 ms. Thus, the impact duration t_{P2} and t_{F2} can be determined as follows:

$$t_{P2} = \frac{1,600}{0.85V} - t_{P1} - t_{PIF} = \frac{1,303}{V} - \frac{4,147.4}{V^{1.833}} \, (ms) \qquad (3\text{-}7)$$

$$t_{F2} = \frac{2,400}{0.85V} - \frac{1,600}{0.85V} = \frac{940}{V} \, (ms) \qquad (3\text{-}8)$$

(a)   (b)

(c)
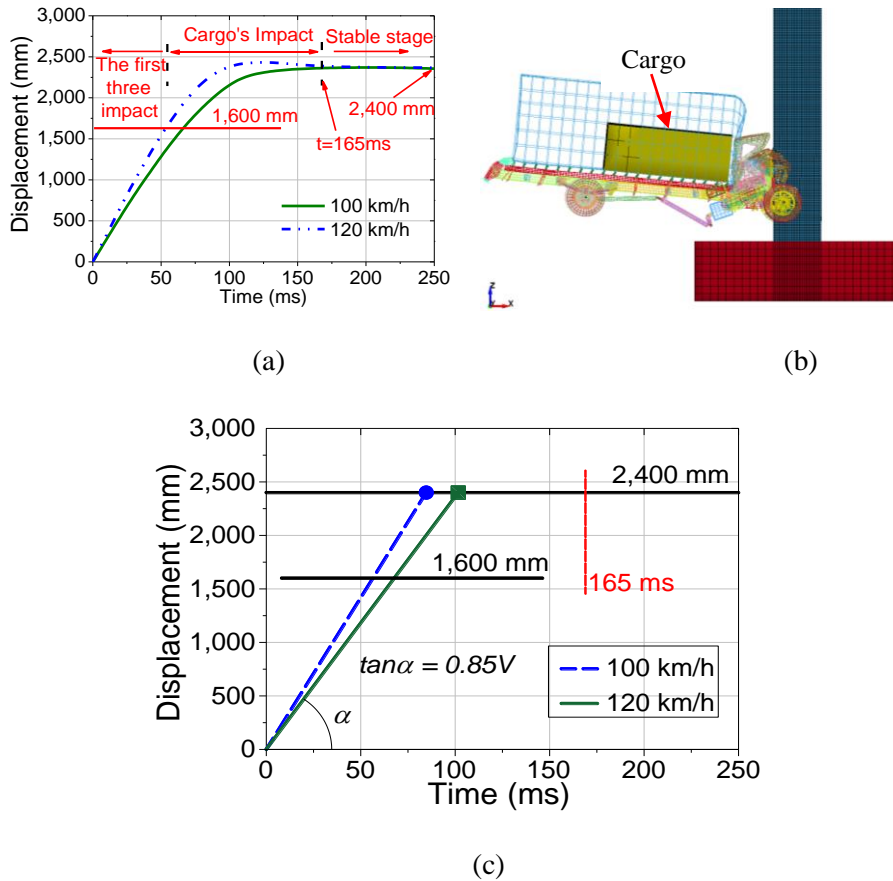
Figure 3-8 The cargo's impact on the RCBC: (a) The cargo displacement time histories; (b) Vehicle deformation when the cargo collides on the column; (c) Simplified model of the cargo displacement.

Additionally, P_2 is determined by dividing the total impulse of the third stage to the impact duration t_{P2}. In each simulation, the impulse of the third impact is defined by integrating the impact force time histories from the numerical simulation. As given in Table 3-1, The P_2 is almost identical in all the simulations. Thus, the influences of the column parameters and the initial conditions of the vehicle model on P_2 is neglected. In this study, the P_2 is taken as 1,290 kN after averaging from all the numerical results. Eventually, the second peak, F_2, from the cargo impact can be defined based on the initial momentum – impulse conversion as adopted in the previous studies (Do et al., 2018a, 2019), as given below:

$$F_2 = \frac{1000mV - \left[P_1\left(t_{P1} + \frac{t_{PIF}}{4}\right) + PIF\frac{t_{PIF}}{2} + P_2\left(\frac{t_{PIF}}{4} + t_{P2} + \frac{t_{F2}}{2}\right) \right]}{\frac{1}{2}\left[165 - (t_{P1} + t_{PIF} + t_{P2})\right]} \; (kN) \geq 0 \qquad (3\text{-}9)$$

where m is the total mass of the vehicle model (ton).

In case the diagonal shear failure or punching shear failure occurs on the RCBC resulting from the F_1, the impact force time histories will last until the impact energy fully transfers to the column without the second peak from the cargo's impact, as presented in Figures 3-9b, c, and e. This is because the failure of the column leads to the movement of the column together with the vehicle model in the impacted area resulting in the considerable reduction of the column resistance. It is worth mentioning that previous studies usually neglect vehicle-column interaction and local damage of column in predicting the impact force of the RCBC, which might not lead to accurate predictions as demonstrated above, but overpredict the impact force from cargo. The impact duration of P_2 can be calculated as follows:

$$t_{P2b} = \frac{1000mV - \left[P_1\left(t_{P1} + \frac{t_{PIF}}{4}\right) + PIF\frac{t_{PIF}}{2} + P_2\frac{t_{PIF}}{4} \right]}{P_2} \; (ms) \qquad (3\text{-}10)$$

where t_{P2b} (ms) is the duration of the third stage when the column exhibits a shear failure due to F_1.

The comparisons of the proposed impact force profile and the numerical simulation for various loading conditions are presented in Figure 3-9. Moreover, to verify the reliability of the proposed model on predicting the impact force time histories of collision events with different vehicle mass, the total mass of the vehicle is increased from 8 ton to 11 ton by increasing the cargo mass from 3 ton to 6 ton while the mass of the engine is 0.64 ton. As presented in Figure 3-10, the proposed model also provides a good estimation of the impact force time histories including the impact force peaks, duration, and impulse in the wide range of the vehicle mass. These comparisons and verification indicate that the proposed vehicle impact force profile model for medium truck reliably predicts the impact force of vehicle collisions on bridge piers with various vehicle's mass, engine mass, vehicle velocity, and structural properties. It should be noted that the cargo, which has a higher mass than vehicle engine, impacts on the columns in these examples do not induce a large peak force F_2 because the column has suffered substantial damage due to the engine impact. If the column is very stiff and does not suffer prominent damage due to engine impact, cargo impact would generate a large impact force F_2, as observed in some previous studies that either assumed the column is rigid or linear elastic (Chen et al., 2016, 2017).

(a) Case C0 – Load 1

(b) Case C0 – Load 2

(c) Case C0 – Load 3

(d) Case C6 – Load 1

(e) Case C6 – Load 2

(f) Case C7 – Load 2
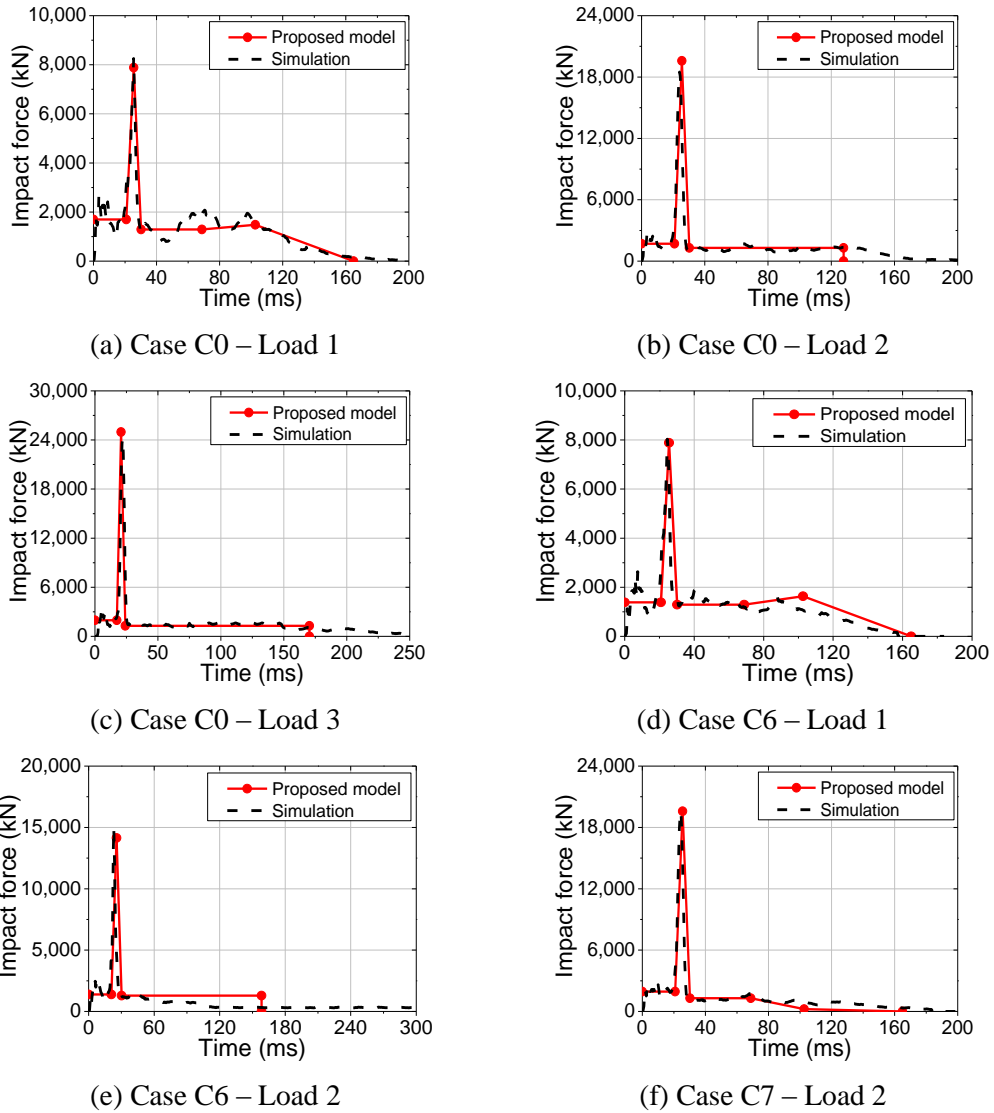
Figure 3-9 The comparison between the proposed model and the numerical simulation
(medium truck).
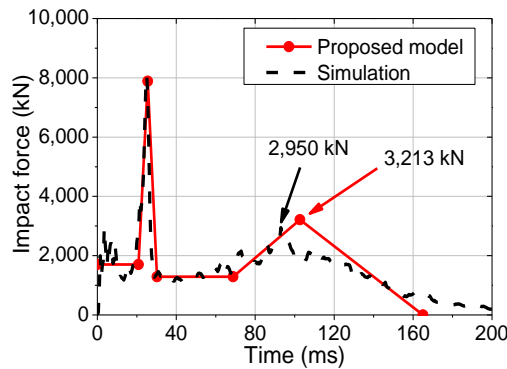
Figure 3-10 Comparisons between the proposed model and numerical simulation with the
vehicle mass of 11 ton ($V = 100$ km/h; $m_e = 0.64$ Ton, $m = 11$ ton).

Table 3-1 Numerical results of vehicle impacts on the RCBC (Medium truck).

No	Parameter		Dimensions (mm)			Load 1			Load 2			Load 3		
			W (mm)	D (mm)	H (mm)	P_1 (kN)	F_1 (kN)	P_2 (kN)	P_1 (kN)	F_1 (kN)	P_2 (kN)	P_1 (kN)	F_1 (kN)	P_2 (kN)
C0	Reference		1,200	1,200	9,600	1,636	8,261	1,408	1,673	18,247	1,129	1,952	24,174	1,356
C1	Slenderness	4	1,200	1,200	4,800	1,637	8,214	1,505	1,694	17,706	1,119	1,976	24,182	1,433
C2		5	1,200	1,200	6,000	1,668	7,504	1,355	1,736	18,520	1,041	1,933	23,549	1,300
C3		6	1,200	1,200	7,500	1,632	7,852	1,365	1,691	18,222	1,202	1,899	23,515	1,426
C4		10	1,200	1,200	12,000	1,642	7,591	1,389	1,701	18,130	1,155	1,962	24,425	1,354
C5	Cross section dimensions		600	600	6,000	1,023	7,321	1,064	1,062	8,036	1,233	1,259	8,876	1,108
C6			800	800	6,400	1,387	8,037	1,342	1,436	14,956	1,043	1,603	14,593	1,086
C7			1,500	1,500	12,000	1,855	8,079	1,347	1,882	19,522	1,254	2,228	25,708	1,586
C8			2,000	2,000	16,000	2,191	8,544	1,360	2,256	20,611	1,181	2,527	26,589	1,241
C9	Transverse reinforcements	d8a200	1,200	1,200	9,600	1,603	7,839	1,174	1,746	18,766	1,133	1,961	23,491	1,601
C10		d14a100	1,200	1,200	9,600	1,645	8,310	1,214	1,697	18,645	1,200	1,972	23,795	1,647
C11	Longitudinal reinforcements	24d22	1,200	1,200	9,600	1,647	8,008	1,382	1,730	18,777	1,255	1,937	22,050	1,366
C12		24d36	1,200	1,200	9,600	1,649	8,290	1,343	1,795	17,966	1,121	1,919	21,830	1,469
C14	Initial axial load	20%	1,200	1,200	9,600	1,645	8,725	1,334	1,762	18,240	1,117	1,959	23,478	1,474
C15		40%	1,200	1,200	9,600	1,636	8,502	1,297	1,682	18,866	1,109	1,960	22,766	1,490
C16		60%	1,200	1,200	9,600	1,638	8,385	1,289	1,795	18,075	1,028	1,954	23,415	1,517

3.4.2. Heavy truck trailer

To verify the accuracy of the proposed impact force profile on different vehicle models and velocities, the heavy trailer model is considered in this section. The vehicle velocity of the heavy trailer considered in the analysis increases from 80 km/h to 110 km/h (H1 – H3) and the total mass ranges from 17 ton to 37 ton (H4 – H5), as given in Table 3-2. The impact force time histories on the RCBC from the heavy trailer is shown in Figure 3-11. Similar to the medium truck model, the impact force time histories of the heavy truck also includes four stages in which the impact of bumper and truck rails create two plateau stages (P1 and P2) while the engine and cargo impact cause two peak impact forces (F1 and F2) during the whole impact process. As mentioned previously, each vehicle model has different length and characteristics leading to a different impact duration and its amplitude. The numerical results of the heavy truck impacted on the RCBC are given in Table 3-2. From the numerical simulation results and using the same analysis methods as in the previous section, the impact duration of each impact stage from the heavy truck can be summarised as follows:

$$t_{P1} = \frac{L_{1H}}{0.95V}(ms) \tag{3-11}$$

$$t_{P2} = \frac{800}{0.85V}(ms) \tag{3-12}$$

$$t_{F2} = 2.1(m-12)+5.6(ms) \tag{3-13}$$

where L_{1H} (ms) is taken as 940 mm for the heavy truck model collided on the RC column.

(a) Different vehicle velocities   (b) Different vehicle mass
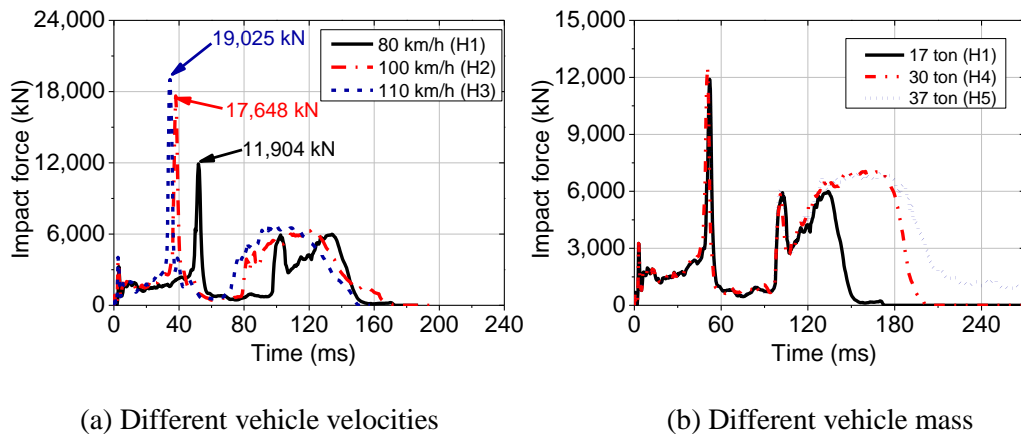
Figure 3-11 Impact force time histories of the heavy truck model collided to the RCBC.

It should be noted that as observed from the numerical simulations, the Eqs. (3-2), (3-5), and (3-6) to define P_1, t_{F1}, and F_1, respectively, of the heavy truck are similar to these for the medium truck. Moreover, the second plateau P_2 is suggested as 850 kN for the heavy truck trailer. As previously discussed, if a column survives from the engine impact, it then suffers

the impact from the cargo. In this study, the cargo mass of the heavy truck is increased from 5 ton to 25 ton in the analyses, the peak impact force from the cargo impact, F_2, is almost similar in these simulations as expected (see Figure 3-11b). Even though the columns in these simulations do not fail by the impact of the engine, it causes local damage to concrete at the impact area. As a result, the contact stiffness between the column and the truck model is significantly reduced when the cargo impacts the column. The reduction of the contact stiffness thus reduces the peak value of the cargo impact (Pham et al., 2018) as compared to the engine impact although the mass of the cargo is considerably larger than that of the engine. However, the impulse of the second peak impact force is greater than the first one, which reflects the huge kinetic energy carried by the cargo. It is worth mentioning that although the peak impact force of the cargo impact is approximately unchanged, the impulse from the cargo impact significantly increases when the mass and the velocity of the cargo increases, as shown in Figure 3-11. From the numerical results, the second peak impact force F_2 is taken as 7,000 kN in this study (see Table 3-2). The total impact duration, t_{total}, from the heavy truck collision to the RCBC thus can be obtained in the following equation:

$$t_{total} = t_{P1} + t_{PIF} + t_{P2} + t_{F2} + t_{F2-R} (ms)$$ (3-14a)

$$t_{F2-R} = \frac{1000mV - \left[P_1 \left(t_{P1} + \frac{t_{PIF}}{4} \right) + PIF \frac{t_{PIF}}{2} + P_2 \left(\frac{t_{PIF}}{4} + t_{P2} \right) + (P_2 + F_2) \frac{t_{F2}}{2} \right]}{\frac{1}{2} F_2} (ms)$$ (3-14b)

where t_{F2-R} (ms) is the duration from the peak impact force, F_2, to zero point.

Table 3-2 Numerical results of vehicle impacts on the RCBC (Heavy truck trailer).

No	Vehicle model			First phase		Second phase		Third phase		Fourth phase	
	m	m_e	V	t_{P1}	P_1	T_{F1}	$F1$	t_{P2}	P_2	t_{F2}	F_2
	(ton)	(ton)	(km/h)	(ms)	(kN)	(ms)	(kN)	(ms)	(kN)	(ms)	(kN)
H1	17	1.5	80	46.5	1,623	11.5	11,904	40.0	750	38.0	6,000
H2	17	1.5	100	35.0	1,834	9.5	17,648	34.0	985	39.5	6,250
H3	17	1.5	110	31.0	1,848	8.0	19,025	30.5	960	34.0	6,610
H4	30	1.5	80	46.5	1,682	11.5	12,252	39.5	808	50.0	7,071
H5	37	1.5	80	46.5	1,651	11.5	11,867	39.5	768	60.0	6,926

It is noted that the impact duration, t_{P2}, is estimated by using Eq. (3-10) in both scenarios: (1) diagonal shear or punching shear failure occurred at the vicinity of the impacted area due to the first peak impact force F_1 and (2) no added mass applied to the heavy truck model. The comparisons between the proposed impact force profile model for the heavy truck and the numerical simulation results are presented in Figure 3-12. The comparison shows that the

proposed impact force profile, the peak impact forces from the engine and the cargo impact, impact duration of each single impact phase, and the total impact duration can be well predicted.

(a) H1   (b) H3   (c) H5
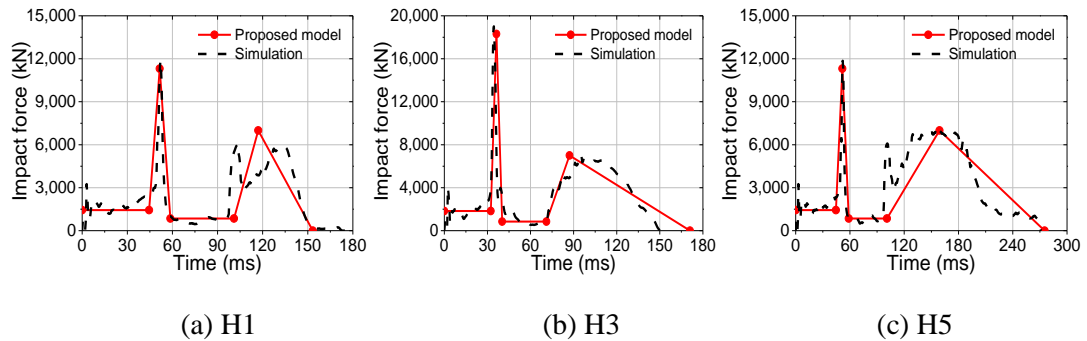
Figure 3-12 The comparison between the proposed model and the numerical simulation (heavy truck trailer).

There is a consensus that the change of vehicle model may slightly change the duration and the magnitude of impact force in each impact stage. Therefore, the use of two vehicle models in the simulation does not imply that these results are applicable for only these two particular vehicle models. The numerical results in this study demonstrate that even the vehicle models are different, the PIF caused by the vehicle engine and the impulse of the collision show a consistent trend. The variations of the column properties do not have a significant influence on the PIF either. It should be highlighted that the PIF and the impulse of the impact are the crucial parameters determining the response of RCBC under vehicle collision (Do et al., 2018a, 2019). To design bridge columns against vehicle collisions, the input information for estimating impact loads includes vehicle speed, engine mass, total mass of the vehicle, the frontal design of the vehicle, and the gap between the engine mass and cargo mass. With these parameters, the proposed equations can be used to estimate the impact force time histories. The proposed impact force models also fit well with RC columns of rectangular or square sections with different sizes. However, the use of other column cross-section types, e.g. circular section and concrete-filled steel tube, may have a slight influence on the magnitude of the impact force since the contact stiffness between the vehicle model and column is changed. Therefore, studies on the effects of cross-section types on the impact force are required. The accuracy of the proposed method also needs to be carefully validated in future works.

3.5. Shear mechanism of RC structures

The shear mechanism of the concrete structures under impact loads has been experimentally and numerically investigated in previous studies (Pham & Hao, 2016; Saatci, 2007; Yi et al., 2016; Zhao et al., 2017). In these studies, the punching shear failure is the most common failure scenario of the concrete beams under severe impact loading conditions. Likewise, the

example rectangular RC columns impacted by a vehicle model showed punching shear failure at the impact area when the PIF reaches 30,000kN, which is larger than the shear capacity of the column section, caused by the engine impact (Do et al., 2018a) (see Figure 3-13a). Based on the shear failure mode of the concrete structures under impact loads, with the crack patterns related to punching shear failure as shown in Figure 3-13b, the dynamic shear capacity of the column, P_{dyn}^{max}, can be written as

$$P_{dyn}^{max} = 2 \times (DIF_c \times V_c + DIF_s \times V_s) + \sum ma \tag{3-15}$$

$$V_c = f_t \times \cos\alpha \times \frac{W \times D}{\sin\alpha} = f_t \times W \times D \tag{3-16}$$

where DIF_c and DIF_s are the dynamic increase factors of the concrete and steel material strength in the diagonal section, respectively; V_c and V_s are the contribution of the concrete and the steel reinforcement to resist the shear force, respectively; m and a are the mass and acceleration of the shear plug, respectively; f_t is the tensile strength of the concrete; α is the inclined angle of the diagonal crack ($\alpha = 45^\circ$).

At PIF   +2.0 ms post PIF   Punching shear

(a) Column punching shear failure   (b) Simplified punching shear model
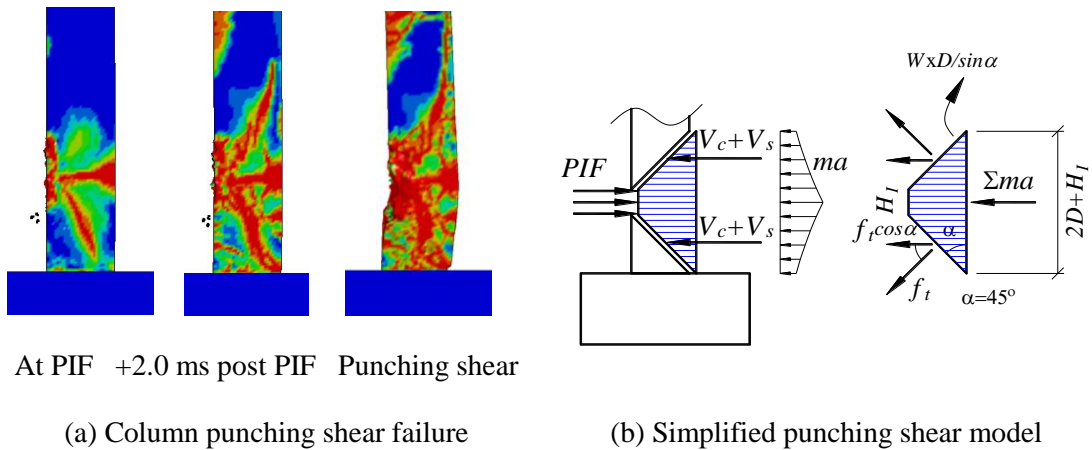
Figure 3-13 Shear mechanism of the RCBC under vehicle impact.

In the previous studies, the contribution of transverse reinforcements and FRP wraps to the shear capacity of the concrete beams have been examined. Four different transverse reinforcement ratios, e.g. 0.0%, 0.1%, 0.2 %, and 0.4% were examined under drop-weight tests by Saatci (2007). The experimental tests showed that the increase of the shear reinforcement reduced the crack width of the concrete beams but all the tested beams experienced shear-plug cracks under the impact load. It is worth mentioning that although the shear strength of the concrete and transverse reinforcements of the tested beam exceeded the impact force, the diagonal shear cracks at two sides of the impact point, forming punching shear was observed for the beam even with the highest transverse reinforcement ratio of 0.4%. A similar observation was also obtained in the previous studies based on numerical simulations (Pham

et al., 2018; Yi et al., 2016) where the punching shear failure was formed in the concrete beams under impact loads even though the shear reinforcements were significantly increased. The use of FRP U- wraps improved the shear resistance of concrete beams under impact load by reducing the shear crack width and increasing the stability of the concrete beams as reported by Pham and Hao (2016). However, the punching shear cracks still occurred at the impact point when the impact force reaches its peak. These studies demonstrated that the use of the shear reinforcement or FRP wraps might reduce the crack width and increase the post-impact behaviour of the concrete structures but showed a minor contribution to resisting the punching shear failure of the reinforced concrete beams. To examine the performance of reinforced concrete columns under vehicle impact, the strain time histories of concrete and steel are plotted in Figure 3-14 (C0-Load 2). It is clear that when damage to concrete occurs due to the tensile failure at strain of $1.75e^{-4}$ at about 25.5 ms, the strain of transverse reinforcement ($1.75e^{-4}$) is about 7% of its yield strain ($2.5e^{-3}$). It is assumed that the concrete and the steel reinforcement are perfectly bonded. Thus, when the column exhibits the punching shear cracks, the strain of the shear reinforcement equals the failure strain of the concrete, ε_c^t. Hence, the total tensile force, V_s, in the shear reinforcements can be estimated as follows:

$$V_s = E_s \varepsilon_c^t \times 2A_s \times n \tag{3-17}$$

$$A_s \approx \frac{W \times D \times \delta}{4n} \tag{3-18}$$

where E_s is the Young's modulus of the steel reinforcements; A_s is the cross-section area of a single shear rebar; n is the number of steel legs in one side of the shear-plug; δ is the shear reinforcement ratio. From Eq. (3-16) and Eq. (3-17), the V_s can be determined by the following equation:

$$V_s = \frac{E_s \varepsilon_c^t}{2 f_t} \times \delta \times W \times D \times f_t = \frac{E_s}{E_c^t} \times \frac{\delta}{2} \times V_c \tag{3-19}$$

Normally, the shear reinforcement ratio, δ, in the previous studies ranged from 0.5% to 1%. Therefore, from Eq. (3-19) at the peak impact force, the contribution of the shear reinforcement to the total shear capacity of the column is minor compared to the concrete (2.5-5%). This is why the increase of the shear reinforcement from the previous studies showed a minor effect on the shear capacity in preventing the occurrence of the punching shear cracks in concrete structures. It should be highlighted that after the occurrence of punching shear cracks in concrete structures, the contribution of the shear reinforcement is then crucial in controlling the stability of the structures (see Figure 3-14b). In brief, the shear reinforcements significantly improve the shear resistance of RC structures but do not help to prevent cracks in concrete

from occurring. In dynamic response, once cracks occur, they allow relative movement between the shear plug and the vicinity parts. This slight relative movement has little effect on the shear resistance of the structures under static loads, however, it significantly reduces the inertia resistance since the vehicle and the shear plug can move together. This is the reason why once shear cracks happen in the columns under impact, the peak impact force cannot increase further. The dynamic shear capacity of the RCBC, neglecting the contribution of the shear reinforcements, can be estimated by the following equation:

$$P_{dyn}^{\max} = 2 \times DIF_c \times f_t \times D \times W + a \times \rho_c \times \left(D + H_I\right) \times D \times W \tag{3-20}$$

where H_I is the height of the impact area caused by the engine box, as given in Figure 3-13b.

(a)

(b)
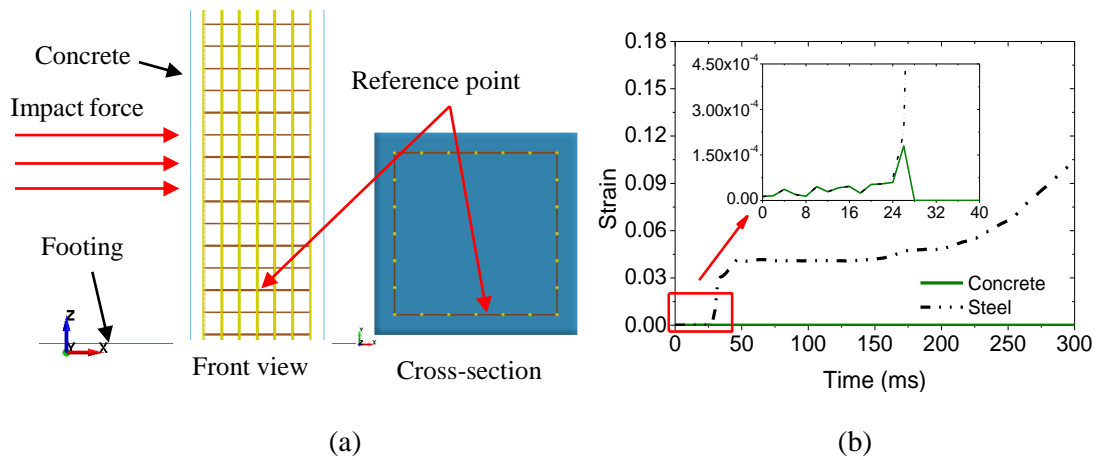
Figure 3-14 Strain of concrete and transverse steel under impact load.

It should be mentioned that each concrete and steel element in the shear-plug area has a different DIF and different acceleration. It is very complicated and difficult to determine these values by solving the dynamic equilibrium equation. Adhikary et al. (2013) proposed an empirical equation to predict DIF of the maximum capacity of a RC deep beam under impact load based on the shear span ratio, loading rate, longitudinal and shear reinforcement ratio. However, the contribution of the inertia force was neglected in that study due to the loading rate was under 2 (m/s). In this study, the effect of the DIF and inertia force in the shear plug area is simplified by using a dimensionless coefficient, k_T, as follows:

$$P_{dyn}^{\max} = 2 \times \left(DIF_c + \frac{a \times \rho_c \times \left(D + H_I\right)}{f_t} \right) \times f_t \times D \times W = k_T \times f_t \times D \times W \tag{3-21}$$

From the numerical results, the punching shear failure occurs on the column C5 and C6 when the PIFs reach 8,036 kN and 14,593 kN, respectively. Moreover, when the PIF is 30,000 kN, the punching shear failure also happen at the impact area on the reference column (C0) (Do et al., 2018a). From Eq. (3-21), the value of k_T in these three cases are 6.56, 6.7, and 6.12, respectively. Based on these results, in this study, k_T is suggested as 6.5. Hence, the dynamic

shear capacity of the RCBC, which is also the largest peak impact force that could be generated from a vehicle impact, is:

$$P_{dyn}^{max} = 6.5 \times \frac{f_c}{10} \times D \times W \qquad (3\text{-}22)$$

where f_c is the compressive strength of concrete.

The maximum dynamic shear capacity of the column is defined based on the contribution of concrete, reinforcements, and inertia in two sides of the shear plug, as shown in Figure 3-13b. However, the diagonal shear crack on the two sides will not happen at the same time because of the boundary condition effects. The lower side of the shear plug is close to the footing and it is affected by the boundary condition while the top side of the shear plug does not connect to the boundary. For a RC column under vehicle collision, to form a punching shear failure on the column, a diagonal shear crack firstly occurs at the column base due to the influence of the boundary condition and then another diagonal shear crack occurs on the other side of the impact point on the column, as illustrated in Figure 3-13a. This phenomenon is observed consistently in the numerical simulations and can be physically explained based on the effect of the inertial resistance and the boundary effect. Therefore, when the PIF from collision events is larger than the dynamic shear capacity of the column, it will cause a diagonal shear failure. Because the shear resistance along the column is identical, the dynamic shear capacity of one side of the shear plug is $0.5P_{dyn}^{max}$. Based on the proposed equation, it can be concluded that when the PIF from a collision event is higher than $0.5P_{dyn}^{max}$, the diagonal shear failure at the impact area will occur in the RC column at the column base. If the PIF is equal to P_{dyn}^{max}, punching shear failure occurs. The comparison of the proposed equation with the numerical and experimental results are given in Table 3-3. Moreover, the numerical results also illustrate the significant contribution of the column properties, i.e. column dimension and concrete strength in determining the impact force profile from vehicle collisions. When the PIF on the column is larger than a half of the maximum dynamic shear capacity of the column, which depends on the column cross-section dimension and the tensile strength of concrete, either diagonal shear or punching shear failure occurs in the column, the second PIF from the cargo impact will not happen, leading to the change of the impact force profile.

3.6. Column responses and failure classification

Figure 3-15 shows the maximum bending moment and shear force in the RCBCs with different cross-section dimensions and column heights generated by vehicle impact. It should be noted that those curves are plotted by connecting the maximum value of the bending moment and shear force at multiple sections along the column. Those values at different sections occur at

a different time instant, but all occur during the impact of the vehicle engine. The variation of the bending moment and shear force was presented and explained in the previous study (Do et al., 2018a). The envelop curves are considered in this study while the time difference between the occurrence of these maximum values is not considered because the maximum values are the primary concerns in column design rather than the time instant when they occur.
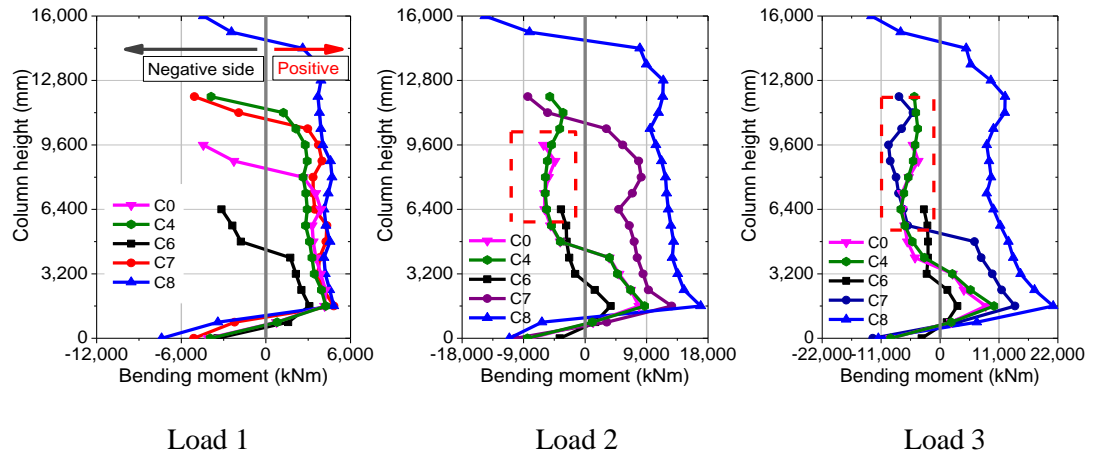
(a) Maximum bending moment along the RCBC
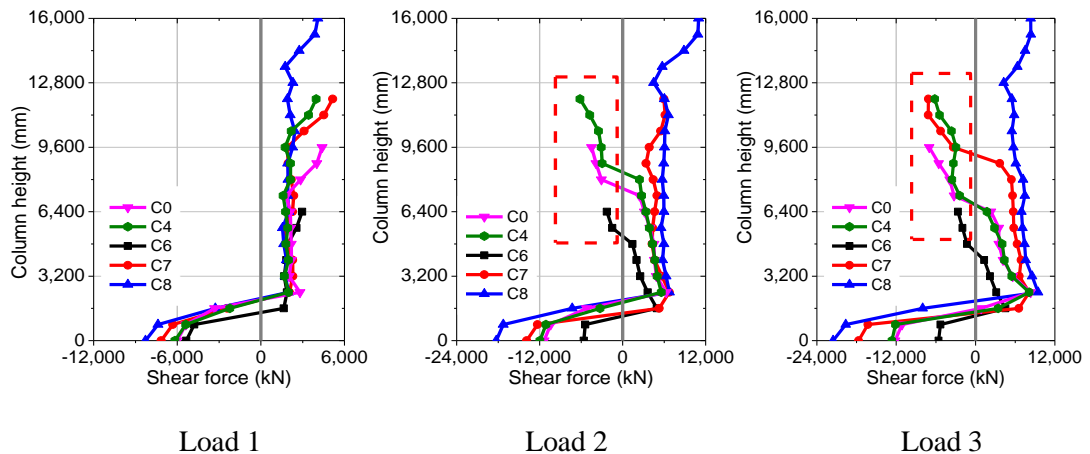
(b) Maximum shear force along the RCBC

Figure 3-15 Maximum bending moment and shear force of the RCBC under vehicle impact.

As can be seen from the figure, the bending moment and shear force diagram of the column can be divided into two separate groups, i.e. flexural response in which the negative bending moment occurs at the base and the column top while the positive bending moment happens at the impact point and the intermediate section, e.g. Figure 3-15a - Load 1 ($V = 100$ km/h, $m_e = 0.64$ ton) and shear response where the bending moment at the intermediate section occurs in the negative side of the column, e.g. Figure 3-15a - Load 2 ($V = 100$ km/h, $m_e = 2.0$ ton) and Load 3 ($V = 120$ km/h, $m_e = 2.0$ ton). As shown in Figure 3-15a, under Load 1, similar maximum bending moment curves are achieved in the Columns C0, C4, and C6-8 where the

flexural response is observed in these columns with no diagonal shear or punching shear failure. When the RCBCs are impacted by Load 2, the diagonal shear crack forms in the Columns C0 and C4 while the punching shear occurs in the column C6 (see Table 3-3) resulting in a significant change in the maximum bending moment curve. These three columns thus suffer shear failure with the maximum bending moment at the intermediate section shifting from the positive side to the negative side of the column. The bending moment shape of the columns C7 and C8 in Load 2 is almost unchanged compared to that under the first loading condition and no shear crack occurs at the column base after the PIF. The PIF increases to about 26,000 kN under Load 3, the Column C7 suffers a diagonal shear crack at the base which leads to the change of the bending moment curve from the flexural response to shear response (see Figure 3-15a – Load 3). Besides, the bending moment shape of the Columns C0, C4, and C6 is similar to that under the previous loading condition but the intermediate section suffering flexural damage moves downward towards the impact point while the bending moment shape of the Column C8 is similar to that under the first two loading conditions. The maximum shear force of those columns under the three loading conditions are also plotted in Figure 3-15b. It is very clear from the figure that when the column is under flexural response, the shear force at the base reaches the maximum value on the negative side while the shear force at the top occurs on the positive side (see Figure 3-15b - Load 1). However, when the shear cracks occur at the column base, the maximum shear force at the column top moves to the negative side (Column C0, C4, and C6 in Load 2-3; C7 in Load 3).

The change of the bending moment and shear force when a shear crack occurs in the column at the base can be explained by the formation of a shear plastic hinge at the impact area, as shown in Figure 3-16. When impact does not induce shear failure in the vicinity of the collision point, with the large inertia resistance from superstructures and the short duration of the engine impact, the column responses to the impact force follow a column with fixed boundary conditions at the two ends (see Figure 3-16a) even though the rigidity of the two ends is different, implying the large mass on top of the column provides a large inertial resistance, making the top of the column similar to having a fixed boundary condition during the impact of the engine. However, when impact induces shear cracks in the column, i.e. diagonal shear and punching shear which form a shear plastic hinge at the impact point, the column reacts to the impact force as a fixed-fixed column with the hinge at the impact point, the bending moment and shear force distribution of the column change (see Figure 3-16b). Moreover, it is worth mentioning that although the PIF applied on the above columns is similar when these columns are under the same loading condition, the column with larger cross-section shows a larger maximum bending moment and shear force at critical sections (see Figure 3-15 – Load 2-3). This is because according to the dynamic equilibrium equation when two columns with

different cross-sections are impacted with a similar impact force, the column with larger cross-section will provide a higher elastic resistance because of the larger column stiffness, which leads to larger bending moment and shear force in the column.

(a) No shear crack occurs   (b) When diagonal shear or punching shear occurs
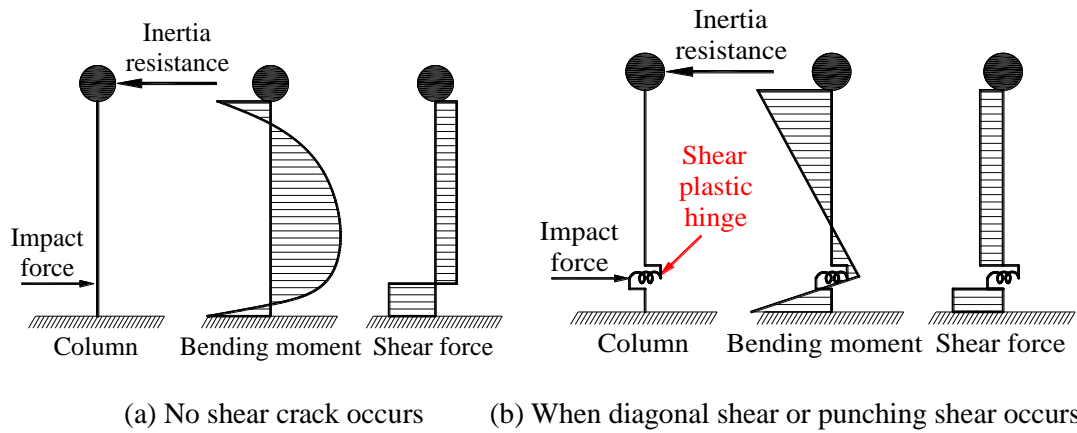
Figure 3-16 Simple response of the column under impact force.

C6   C0   C4   C7   C8   C6   C0   C4   C7   C8   C6   C0   C4   C7   C8

(a) Load 1   (b) Load 2   (c) Load 3
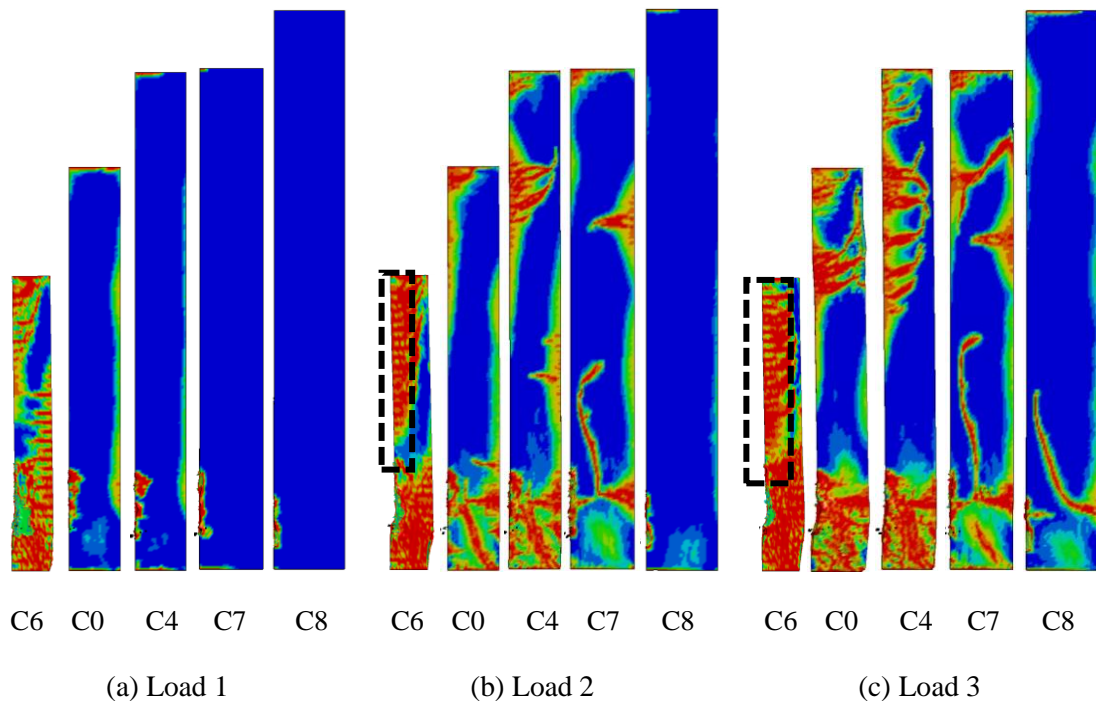
Figure 3-17 Crack patterns and failure modes of the RCBC under vehicle impacts.

The crack patterns and failure of those columns impacted by the three impact loading conditions are also presented in Figure 3-17. As can be seen that when punching shear failure (C6) happens in the RCBC, negative flexural cracks occur in the vicinity of the impact point (1 – 2 m) in both Load 2 and Load 3. A similar observation was reported in the previous study by Zhao et al. (2017) in which the maximum bending in the negative side was formed at 1.5 m away from the impact point when the beam experienced the punching shear failure. For the Columns C0 and C4, the flexural response is observed when these columns are under the

66

impact of Load 1. When a diagonal shear failure forms at the impact area, a flexural – shear crack happens in the negative side of the column in both Load 2 and Load 3 (see Figures 3-17b and 3-17c). Furthermore, after yielding the diagonal shear crack at the base (see Figure 3-17c), Column C7 exhibits another flexural – shear crack near the column top. No shear failure and flexural – shear crack in the negative side of the column is observed in the Column C8 in all of the loading conditions.

Increase of the PIF $\left[PIF = 969.3 \sqrt{\dfrac{m_e V^2}{2}} - 7,345.9\right]$

Flexural response	Shear response	
$PIF < \dfrac{P_{dyn}^{max}}{2}$	$\dfrac{P_{dyn}^{max}}{2} \leq PIF \leq P_{dyn}^{max} = 6.5 \times D \times W \times \dfrac{f_c{'}}{10}$	
Flexural cracks	Diagonal shear failure	Punching shear failure
Moment Shear force	Moment Shear force	Moment Shear force
Flexural cracks occur in the positive side of the column. The intermediate section also forms in the positive side	Diagonal shear failure at the column base. The intermediate section forms in the negative side at close to the top.	Punching shear failure at the column base. The intermediate section moves downward and forms close to the impact area.

Figure 3-18 Column response and failure classification under different PIF.

From the above observations and discussions, the column responses and failures are classified into two categories: flexural response and shear response as summarised in Figure 3-18. The column shows a flexural response when the PIF from the vehicle impact is smaller than $0.5P_{dyn}^{max}$ and no diagonal shear crack forms in the column. Under this condition, the intermediate section and flexural cracks occur on the positive side of the column. When the PIF is higher than $0.5P_{dyn}^{max}$, a diagonal shear crack appears at the column base leading to the formation of flexural cracks on the negative side of the column. The increase of PIF in this range will lead to the downward trend of the intermediate section with flexural cracks. When the PIF reaches the maximum dynamic shear capacity of the column, P_{dyn}^{max}, the punching shear failure occurs in the column with the intermediate section of flexural cracks being formed closer to the impact point and at $1.5 - 2$ m above the impact point.

Table 3-3 Comparison between the proposed equation and available results.

| Reference | No | ID | Structural properties | | | Numerical result (kN) | Experimental result (kN) | Failure | Proposed equation (kN) | Error (%) |
			W (mm)	D (mm)	f_c (Mpa)					
This study	1	C5	600	600	34.0	8,036	--	Punching shear	7,956	10.4
	2	C6	800	800	34.0	14,593	--	Punching shear	14,144	3.1
Do et al. (2018a)	4	C14	1,200	1200	34.0	30,000	--	Punching shear	31,824	6.1
Pham et al. (2018)	5	Beam 1	150	250	46.0	1,000	--	Punching shear cracks	1,121	12.0
	6	Beam 2	150	250	52.0	1,420	1,390	Punching shear cracks	1,268	8.7
Yi et al. (2016)	7	BD4	150	310	41.4	1,470	1,465	Punching shear	1,242	15.2
Zhao et al. (2017)	8	B-868-7.14	200	500	24.8	--	1,480	Punching shear	1,612	8.9
	9	C-868-7.14	200	500	26.3	--	1,735	Punching shear	1,709	1.5
	10	D-868-7.14	200	500	25.0	--	1,679	Punching shear	1,625	3.2
This study	11	C0	1,200	1,200	34.0	18,247	--	Diagonal shear failure	31,824	--
	12	C1	1,200	1,200	34.0	17,706	--	Diagonal shear failure	31,824	--
	13	C2	1,200	1,200	34.0	18,520	--	Diagonal shear failure	31,824	--
	14	C3	1,200	1,200	34.0	18,222	--	Diagonal shear failure	31,824	--
	15	C4	1,200	1,200	34.0	18,130	--	Diagonal shear failure	31,824	--
	16	C7	1,500	1,500	34.0	25,708	--	Diagonal shear failure	49,725	--

Note:--The value is not available or is not considered in this study

3.7. Conclusions

This study numerically investigates the impact behaviour of RCBCs under vehicle collision. A series of FE models of full-scale bridge columns under collision of a medium truck and a large trailer are built and simulated. The effects of column parameters on the impact force time histories and the column response under three different conditions have been examined. The findings of this study can be summarised as follows:

1. An analytical model is proposed to predict the vehicle impact loading profile on rectangular RC columns corresponding to four continuous stages, i.e. bumper impact, engine impact, truck rail impact, and cargo impact. The results indicate that the vehicle impact force time histories depend on both the column parameters and initial conditions of the vehicle model. A good agreement between the proposed model and numerical simulations has been achieved.

2. Owing to the damage of the column to vehicle engine impact, the cargo impacts of all the considered numerical cases do not generate a peak impact force larger than that from engine impact, but could generate a larger impulse depending on the impact conditions and cargo mass. The results imply that in most common cases of bridge columns, the peak impact force is associated with the vehicle engine impact while the maximum impulse could be associated with either engine impact or cargo impact. Assuming a rigid column or neglecting column damage in numerical simulations likely overestimate the impact force, especially the cargo impact force.

3. The maximum dynamic shear capacity of the column has been defined in which the column cross-section dimension and concrete strength provide the most contribution to the shear capacity before cracking while the contribution of the steel reinforcement is significant only after concrete cracking.

4. Based on the maximum dynamic shear capacity of the column and the PIF from the collision, the column failure mode can be classified into two separate groups, i.e. flexural failure $\left(PIF < 0.5 P_{dyn}^{\max} \right)$ and shear failure $\left(PIF \geq 0.5 P_{dyn}^{\max} \right)$. In the design, the dynamic resistant capacity of column needs to be provided to resist the column global damage, i.e. flexural cracks at the base, impact area, intermediate section, and column top, as well as the local failures, i.e. diagonal shear failure and punching shear failure.

3.8. References

AASHTO. (2012). *AASHTO LRFD bridge design specifications (customary U.S. units)*. 6th Ed., Washington, DC.

Abdelkarim, O. I., & ElGawady, M. A. (2016). Performance of hollow-core FRP–concrete–steel bridge columns subjected to vehicle collision. *Engineering Structures, 123*, 517-531.

Abdelkarim, O. I., & ElGawady, M. A. (2017). Performance of bridge piers under vehicle collision. *Engineering Structures, 140*, 337-352.

Adhikary, S. D., Li, B., & Fujikake, K. (2013). Strength and behavior in shear of reinforced concrete deep beams under dynamic loading conditions. *Nuclear Engineering and Design, 259*, 14-28.

Agrawal, A. K., Liu, G. Y., & Alampalli, S. (2013). Effects of truck impacts on bridge piers. *Advanced Materials Research, 639*, 13-25.

Agrawal, A. K., Xu, X., & Chen, Z. (2011). *Bridge vehicle impact assessment* (C-07-10). University Transportation Research Center.

Al-Thairy, H., & Wang, Y. (2013). An assessment of the current Eurocode 1 design methods for building structure steel columns under vehicle impact. *Journal of Constructional Steel Research, 88*, 164-171.

Bakis, C. E., Ganjehlou, A., Kachlakev, D. I., Schupack, M., Balaguru, P., Gee, D. J., . . . Gentry, T. R. (2002). Guide for the design and construction of externally bonded FRP systems for strengthening concrete structures. *Reported by ACI Committee, 440*(2002)

Buth, C. E., Brackin, M. S., Williams, W. F., & Fry, G. T. (2011). *Collision loads on bridge piers: phase 2. Report of guidelines for designing bridge piers and abutments for vehicle collisions* (FHWA/TX-11/9-4973-2). College Station, TX.

Buth, C. E., Williams, W. F., Brackin, M. S., Lord, D., Geedipally, S. R., & Abu-Odeh, A. Y. (2010). *Analysis of large truck collisions with bridge piers: phase 1. Report of guidelines for designing bridge piers and abutments for vehicle collisions* (FHWA/TX-10/9-4973-1). College Station, TX.

CEN. (2002). *Actions on structures. Part 1-1: General actions-densities, self-weight, imposed loads for building*. Brussels, Belgium: BS EN 1991-1-1:2002.

CEN. (2006). *Actions on structures. Part 1-7: General actions-accidental actions*. Brussels, Belgium: BS EN 1991-1-1:2002.

Chen, L., El-Tawil, S., & Xiao, Y. (2016). Reduced models for simulating collisions between trucks and bridge piers. *Journal of Bridge Engineering, 21*(6), 04016020.

Chen, L., El-Tawil, S., & Xiao, Y. (2017). Response spectrum-based method for calculating the reaction force of piers subjected to truck collisions. *Engineering Structures, 150*, 852-863.

Chen, L., & Xiao, Y. (2012). Review of studies on vehicle anti-collision on bridge piers. *Journal of Highway and Transportation Research and Development, 29*(8), 78-86.

Chen, L., Xiao, Y., Xiao, G., Liu, C., & Agrawal, A. K. (2015). Test and numerical simulation of truck collision with anti-ram bollards. *International Journal of Impact Engineering, 75*, 30-39.

Consolazio, G., & Davidson, M. (2008). Simplified dynamic analysis of barge collision for bridge design. *Transportation Research Record: Journal of the Transportation Research Board,*(2050), 13-25.

Do, T. V., Pham, T. M., & Hao, H. (2018a). Dynamic responses and failure modes of bridge columns under vehicle collision. *Engineering Structures, 156*, 243-259.

Do, T. V., Pham, T. M., & Hao, H. (2018b). Numerical investigation of the behavior of precast concrete segmental columns subjected to vehicle collision. *Engineering Structures, 156*, 375-393.

Do, T. V., Pham, T. M., & Hao, H. (2018c, 19-23/08). *Performances of Reinforced Concrete Bridge Columns under Vehicle Impact*. Paper presented at the 5th International Conference on Protective Structures, Poznan, Poland

Do, T. V., Pham, T. M., & Hao, H. (2019). Impact Response and Capacity of Precast Concrete Segmental versus Monolithic Bridge Columns. *Journal of Bridge Engineering, 24*(6), 04019050.

El-Tawil, S., Severino, E., & Fonseca, P. (2005). Vehicle collision with bridge piers. *Journal of Bridge Engineering, 10*(3), 345-353.

Hu, B., & Li, G.-Q. (2016). Maximum Impact Force of Truck Frontal Crashing into Antiram Bollard Systems. *Journal of Structural Engineering, 142*(12), 04016125.

Megally, S. H., Garg, M., Seible, F., & Dowell, R. K. (2001). *Seismic performance of precast segmental bridge superstructures* (SSRP-2001/24). University of California, San Diego.

Pham, T. M., & Hao, H. (2016). Impact behavior of FRP-strengthened RC beams without stirrups. *Journal of Composites for Construction, 20*(4), 04016011.

Pham, T. M., & Hao, H. (2017). Effect of the plastic hinge and boundary conditions on the impact behavior of reinforced concrete beams. *International Journal of Impact Engineering, 102*, 74-85.

Pham, T. M., Hao, Y., & Hao, H. (2018). Sensitivity of impact behaviour of RC beams to contact stiffness. *International Journal of Impact Engineering, 112*, 155-164.

SA/SNZ. (2002). *Structural design actions Part 1: Permanent, imposed and other actions* Sydney, NSW 2001; Wellington 6020: AS/NZS 1170.1:2002.

Saatci, S. (2007). *Behaviour and modelling of reinforced concrete structures subjected to impact loads* (Doctoral dessertation). University of Toronto Retrieved from http://www.vectoranalysisgroup.com/theses/thesis_saatci.pdf

Sharma, H., Hurlebaus, S., & Gardoni, P. (2012). Performance-based response evaluation of reinforced concrete columns subject to vehicle impact. *International Journal of Impact Engineering, 43*, 52-62.

Yi, W.-J., Zhao, D.-B., & Kunnath, S. K. (2016). Simplified approach for assessing shear resistance of reinforced concrete beams under impact loads. *ACI Structural Journal, 113*(4), 747-756.

Zhang, X., Hao, H., & Li, C. (2016). Experimental investigation of the response of precast segmental columns subjected to impact loading. *International Journal of Impact Engineering, 95*, 105-124.

Zhao, D.-B., Yi, W.-J., & Kunnath, S. K. (2017). Shear Mechanisms in Reinforced Concrete Beams under Impact Loading. *Journal of Structural Engineering, 143*(9), 04017089.

CHAPTER 4

PROPOSED DESIGN PROCEDURE FOR REINFORCED CONCRETE BRIDGE COLUMNS AGAINST VEHICLE COLLISIONS

ABTRACT[3]

In this study, analytical investigation and numerical simulations are utilised to examine the responses of reinforced concrete bridge columns (RCBC) against vehicle collisions. Based on the numerical results, a simplified approach is developed for analysis and design of RCBCs to resist vehicle collisions. RCBCs impacted by a medium truck and a heavy truck trailer at different velocities are considered. Based on the numerical results, empirical equations to determine the maximum shear force and bending moment at column critical sections are proposed. A single-degree-of-freedom (SDOF) system is employed to predict the dynamic response of the column. A procedure to design RCBCs under vehicle collision with either flexural bending or brittle shear failure governed response of the column is proposed. Two design examples of RCBC under medium truck impact and heavy truck impact are given in this study to demonstrate the proposed procedure.

4.1. Introduction

In recent decades, a number of vehicle collision accidents with bridge structures have been documented in the open literature and media (Agrawal et al., 2011; Buth et al., 2010). Collisions from heavy-duty trucks or high-velocity vehicles may cause failures of substructures, cost human life, and paralyse transportation systems in urban areas. Therefore, it is crucial to understand and consider the responses of reinforced concrete (RC) columns/bridge piers under vehicle collisions in the design stage. Studies on the performance and response of structures under impact loads and vehicle collisions have attracted a number of research interests and efforts. Currently, three methods including an equivalent static force (ESF) (AASHTO, 2012; Abdelkarim & ElGawady, 2016; Abdelkarim & ElGawady, 2017; CEN, 2002; El-Tawil et al., 2005; SA/SNZ, 2002), damage assessment of column structures (Sharma et al., 2012; Zhou & Li, 2018), and dynamic analysis (Chen et al., 2017; Chung et al.,

2014; Do et al., 2018, 2019a; Fan et al., 2019; Fan et al., 2018; Jiříček & Foglar, 2016) have been utilised to examine the response of column structures under vehicle collisions.

Among these three methods, the ESF is commonly used in design specifications and guides since it is straightforward for engineers to use in design analysis. For instance, AASHTO (2012) suggests the ESF of 2,668 kN applied to the column at 1.5 m above the ground level to design bridge columns under vehicle impacts. CEN (2006) recommends an equation to predict the maximum contact force from the vehicle collision based on the initial kinetic energy of the truck model and the stiffness of the softer one of the column structure and the vehicle model in a contact event. CEN (2002) and SA/SNZ (2002) estimate the maximum static force from collision events by considering the vehicle velocity, vehicle mass, and deformation of both column and vehicle model. However, many studies have indicated that these design approach based on ESF analysis could result in un-conservative designs since the influences of the dynamic responses of structures and high loading rate of the impact force have been completely neglected (Do et al., 2018; Sharma et al., 2012). Moreover, the ESF method could not predict some of the failure modes of RCBCs as observed in real vehicle collisions and mentioned in the previous reports (Buth et al., 2010; Do et al., 2018), e.g. diagonal shear closes to the column top and combined flexural-shear damage at the column mid-height. In addition, the actual dynamic response of RCBCs is also completely different from a prediction by using the ESF method, especially during the impact force phase. Therefore, concerns are still persisted about the applicability of those design methods and recommendations.

To overcome the limitations of the ESF, the damage assessment method has been proposed based on failures of reinforced concrete columns under various loading conditions (Sharma et al., 2012; Zhou & Li, 2018). Sharma et al. (2012) used four different vehicle models ranging from 8 ton to 50 ton together with various impact velocities between 65 km/h and 161 km/h to impact on the RCBCs. Based on the dynamic shear force from the collisions and the dynamic shear capacity of the column, the impact performance of the RCBC has been categorised in three groups, i.e. fully operational with no concrete damage, an operational structure with concrete damage, and total collapse of structures. However, the mentioned study mainly considered the failure at the column base whereas the flexural failure or shear failure at the top or the mid-height of the column as observed in some real accidents was not considered. Zhou and Li (2018) used the damage index, λ, which was defined by dividing the local ESF to static shear capacity of the column, to categorise the damage of the column in four groups, i.e. slight damage ($0 \leq \lambda \leq 0.2$), moderate damage ($0.2 \leq \lambda \leq 0.6$), severe damage ($0.6 \leq \lambda \leq 1$) and collapse ($\lambda \geq 1$). It should be noted that the local ESF in the latter study is the averaged integration of the impact force time histories in 50 ms during the impact duration.

However, in that study, neither the behaviours of the RCBC under high impact velocity (higher than 80 km/h) nor the dynamic effects associated with the high-speed and high peak impact force (PIF) were considered.

In the third approach, detailed finite element (FE) models were used and the time histories of the impact force and the dynamic response of the column such as shear force, bending moment, and inertia force have been predicted (Chen et al., 2017; Do et al., 2018, 2019b). Based on simulations of vehicle model impacted on a rigid column, response spectra for the PIFs from the engine and cargo were proposed by Chen et al. (2017). The time histories of the reaction force at the column base was then estimated. Since the column was assumed rigid in the simulation, the contribution of the vehicle-column interaction and inertia resistance which significantly affect the shear force and bending moment of the column were not considered in the study. The dynamic response of the column such as shear failure, shear cracks or flexural response was, therefore, not mentioned and discussed. Do et al. (2018) developed detailed FE models and carried out numerical simulations to investigate the dynamic behaviours and responses of the RCBC under vehicle collision. The study indicated that with different initial conditions, which causes a different PIF, the column could exhibit different failure modes from minor damage due to flexural response to diagonal shear failure or punching shear failure. Empirical relations of the PIF and the total impact impulse as a function of the initial velocity of the vehicle model, engine mass, and total vehicle mass were proposed based on intensive numerical simulation results. In a subsequent study, the equations to estimate the entire impact force profile including vehicle bumper's impact, engine impact, vehicle trail's impact, and cargo impact together with the column dynamic shear capacity have been proposed by Do et al. (2019a). Based on the PIF from a collision event and the dynamic shear capacity of RCBCs, the shape of the shear force and bending moment distributions along the column and the column failure mode have been divided into two separated groups, i.e. flexural responses and shear responses (Do et al., 2019a). Although the detailed FE model simulations were proven yielding accurate predictions of column responses (Do et al., 2018, 2019a), they are not straightforward to use in design analysis. Therefore, a straightforward procedure to reliably predict dynamic responses of RCBC under vehicle impact is still required for design analysis.

This study aims to propose a design procedure of RCBC to resist vehicle collisions by taking into consideration the vehicle impact condition, vehicle-column interaction, and dynamic effects on column responses. By adopting the impact force time histories models from the truck impact and classifications of the column failure proposed by Do et al. (2019a), a procedure to estimate the column internal forces and predict the column failure mode is proposed in this study. The proposed procedure avoids detailed FE model simulations but

yields accurate estimations of the maximum shear force and bending moment at column critical sections and lateral displacement of the RCBC under vehicle impacts. Two design examples of RCBCs under vehicle collisions are presented in this study to demonstrate the proposed procedure for its use in design analysis.

4.2. Simulation of vehicle collision of RCBC and its verification

4.2.1. Numerical model of RCBC and vehicle model

In this study, to develop the procedure for estimating the column responses and verifying its accuracy, a numerical simulation of a full-scale bridge structure is built in LS-DYNA (Hallquist, 2007). The bridge structure consists of a single RC column, two spans of superstructures, and concrete abutments (see Figure 4-1a). In numerical analyses, responses of five square columns with the size of 800 mm, 1,000 mm, 1,200 mm, 1,500 mm, and 2,000 mm are considered under multiple impact conditions of two vehicle models as shown in Figure 4-1b and Table 4-1. The cross-section dimensions of the superstructures are adopted from Megally et al. (2001) but its span length, L_{span}, is varied with column cross-section dimensions to keep the total dead load from the superstructures to be 10% of the column compression capacity of each column model in the analysis. The slenderness of these columns keeps at 8, similar to that considered in the experimental studies by Zhang et al. (2016) and Pham et al. (2018). The column is buried under the ground level with a depth of 0.5 m (see Figure 4-1a). The superstructures are designed to sit on the top of the cap beam and concrete abutments, modelled with a surface to surface contact with a friction coefficient of 0.6 (ACI, 2008). In this study, the concrete is simulated by hexahedral elements with one integration point while the material named *Mat_072RL3 is employed to model the dynamic behaviours of the concrete with uniaxial compressive strength of 34 MPa. In addition, the dynamic increment factor (DIF) for concrete strength which was suggested by Hao and Hao (2014) is selected in the simulation to quantify the strength increment of the concrete under dynamic loads. Longitudinal and transverse reinforcements which have a nominal yield strength of 500 MPa, are modelled by 3-node beam-elements (Hughes-Liu with cross section integration). An elastic-plastic material model (Mat_024) is adopted to model the behaviour of these reinforcements while the DIF for steel reinforcements proposed by Malvar and Crawford (1998) is chosen. The superstructures, concrete abutments, and column footing are simulated by hexahedral elements with the elastic material model (Mat_001) being used. From Chapter 3, based on the concrete strength and the cross-section dimension of the column, the column dynamic shear capacity can be estimated as

$$P_{dyn}^{\max} = \frac{6.5 W D f_t}{1,000} \ (kN) \tag{4-1}$$

where *W* and *D* are the column width and depth, respectively (mm), and f_t is the concrete tensile strength (MPa). The dynamic shear capacity of the five columns is given in Table 4-1.

Two different vehicle models, i.e. a medium truck model named Ford truck single unit (8 ton) and a heavy truck model (30 ton), as presented in Figure 4-2, are employed in this study to collide on the RCBCs. These vehicle models have been widely used in the open literature (Abdelkarim & ElGawady, 2016; Chen et al., 2016; El-Tawil et al., 2005; Sharma et al., 2012) to examine the dynamic responses and failures of structures under vehicle collisions. The initial conditions of these vehicle models considered in this study are presented in Table 4-2. The contact keyword namely Automatic_Surface_to_Surface is used to simulate the vehicle – column interaction. It should be noted that this contact algorithm allows simulating the impact force time histories between two impacting parts in collision events (Hallquist, 2007).
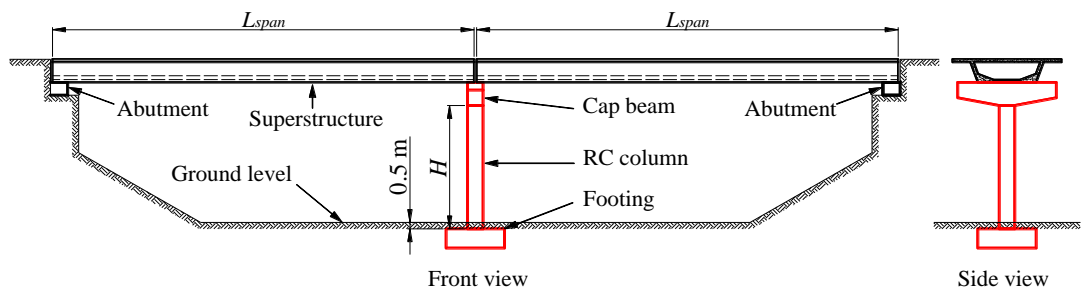
(a) The schematic view of the prototype bridge specimen
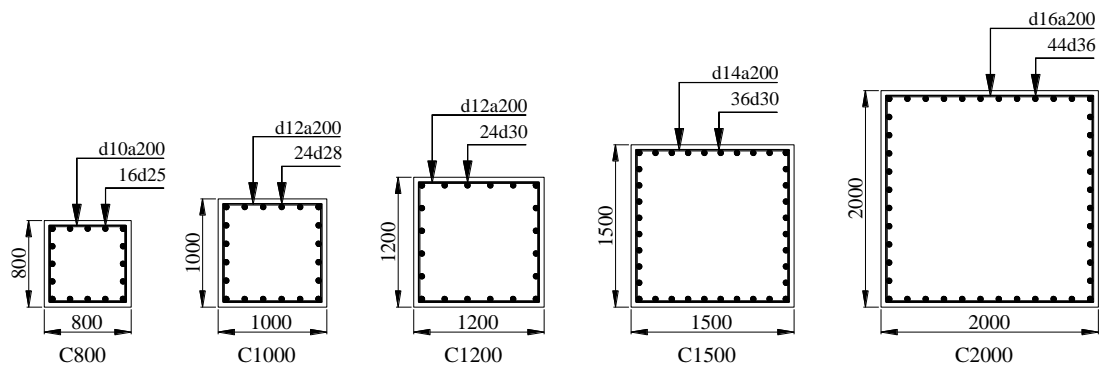
(b) Column cross-section

Figure 4-1 The RCBC specimen and column properties.
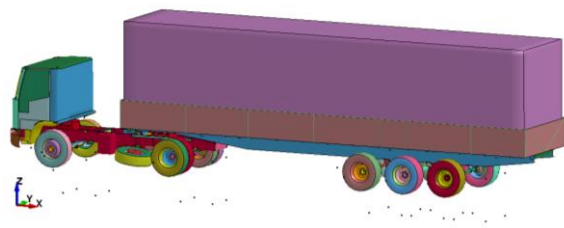
(a) Medium truck model (b) Heavy truck model

Figure 4-2 Two different FE vehicle models.

76

4.2.2. Model verification

The verification of the numerical simulation has been presented previously in the Section 2.2.2.4 and Section 3.2.3. Thus, they are not presented in this chapter.

Table 4-1 Column dimensions and properties

No	Column section	Dimensions (mm)			Reinforcements		P_{dyn}^{max} (kN)
		Width (W)	Depth (D)	Height (H)	Longitudinal	Transverse	
1	C800	800	800	6,400	16d25	d10a200	14,144
2	C1000	1,000	1,000	8,000	24d28	d12a200	22,100
3	C1200	1,200	1,200	9,600	24d30	d12a200	31,824
4	C1500	1,500	1,500	12,000	36d30	d14a200	49,725
5	C2000	2,000	2,000	16,000	44d36	d16a200	88,400

4.3. Impact force profile model and classification of column response

The impact force profile models from medium truck and heavy truck trailer impacting on structures which were proposed in Section 3.4 will be adopted in this section to design the RC columns. From the classification of column response under impact load (Section 3.6), in the following sections, the column displacement and the maximum value of internal forces, i.e. shear force and bending moment at critical sections when its response is governed by the flexural response are estimated. It should be noted that when the failure is governed by the shear response mode, these values are not required since the column damage is directly caused by the shear failure at the base, i.e. diagonal shear and punching shear failure, because the PIF is greater than the column dynamic shear capacity.

4.4. Internal forces and column responses of RCBC

4.4.1. Maximum shear force

4.4.1.1 Shear force at the base

Without loss of generality, taking Case 20 (C20 in Table 4-2) as an example here, from the numerical results, the typical time histories of the impact force and shear force at the column base are shown in Figure 4-3a. It can be seen that the maximum value of the shear force is smaller than the PIF from the collision, and shear force oscillates quickly as compared to the impact force. This is because of the influence of the inertia force (AASHTO, 2012; Do et al., 2018; Zhao et al., 2017). At the PIF, the loading acting on RCBC includes impact force, inertia force, and reaction force, as illustrated in Figure 4-3b. Therefore, at the PIF, the equilibrium equation of the horizontal force applied to the column can be expressed as

$$PIF = R_{base} + \int_0^{H_1} m_h a(h)dh \qquad (4\text{-}2)$$

77

where R_{base} is the maximum shear force at the base of the column; $\int_0^{H_1} m_h a(h)dh$ is the total inertia force distributed in a portion of the column, H_1 (see Figure 4-3b); m_h is the mass density per unit length of the column; $a(h)$ is the acceleration of column particles in the impact force direction at the location h; h is the distance measured from the column base. It should be noted that this equation is valid because during this stage of vehicle impact, i.e., usually engine impact, the top part of the column is not activated yet to resist the impact force as observed in numerical simulations. The impact force is balanced by the base shear and the inertia resistance from the part of the column that has been activated to resist the vehicle impact.

(a)   (b)
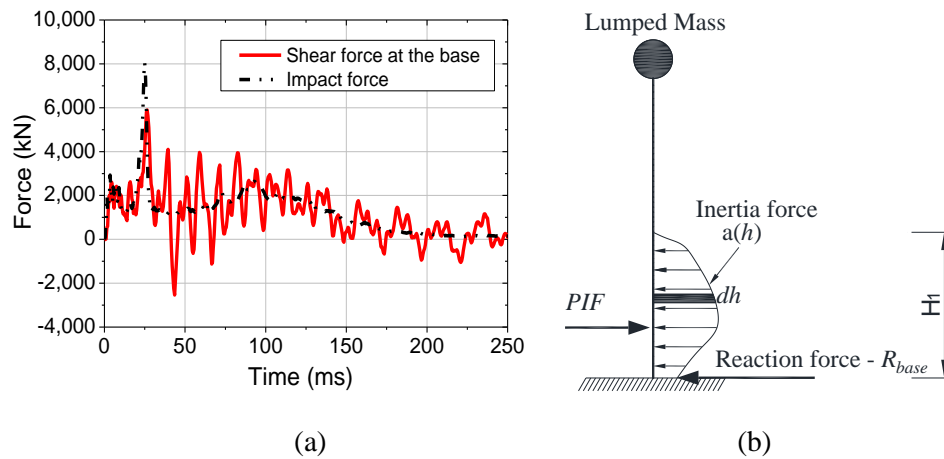
Figure 4-3 (a) Impact force and shear force time histories (C20); (b) Simplified illustration of the column free-body diagram at the PIF.

From the numerical results, the relation between the *PIF* and the total inertia force distributed on the column is presented in Figure 4-4a. It should be mentioned that the total inertia force in the figure is defined by subtracting the maximum shear force at the base from the *PIF* given in Table 4-2. As can be seen in the figure, under the similar PIF, the column with larger dimension has a smaller contribution of the inertia force because of the larger contribution of the column resistance represented by R_{base} in Eq. (4-2). From the numerical results (see Figure 4-4a), the best-fitted relation for estimating the total inertia force along the column at the PIF is as follows:

$$\int_0^{H_1} m_h a(h)dh = PIF \times \tan \alpha - 2,000 \geq 0 \tag{4-3}$$

$$\alpha = \begin{cases} 28.5^0 & (D < 1,100\,mm) \\ 45^0 - 0.015\,D & (1,100\,mm \leq D < 3,000\,mm) \end{cases} \tag{4-4}$$

where α is the slope coefficient which represents the effects of the column stiffness, as presented in Figure 4-4b.

From Eqs. (4-2) and (4-3), the maximum reaction force at the column base corresponding to the PIF can be written as follows:

$$R_{base} = PIF - \int_0^{H_1} m_h a(h) dh = PIF(1 - \tan \alpha) + 2,000 \qquad (4\text{-}5)$$

It was previously observed that the maximum shear force at the base of the column is almost unchanged when the PIF causes the shear failure at the impact area (Do et al., 2018, 2019b) because the shear force has reached the column dynamic shear capacity. Therefore, when the PIF is larger than $0.5 P_{dyn}^{max}$ which results in the diagonal shear failure from the contact point to the column – footing connection, the shear force at the column base can be predicted by the following equation:

$$R_{base} = 0.5 P_{dyn}^{max} (1 - \tan \alpha) + 2,000 \qquad (4\text{-}6)$$

(a)   (b)
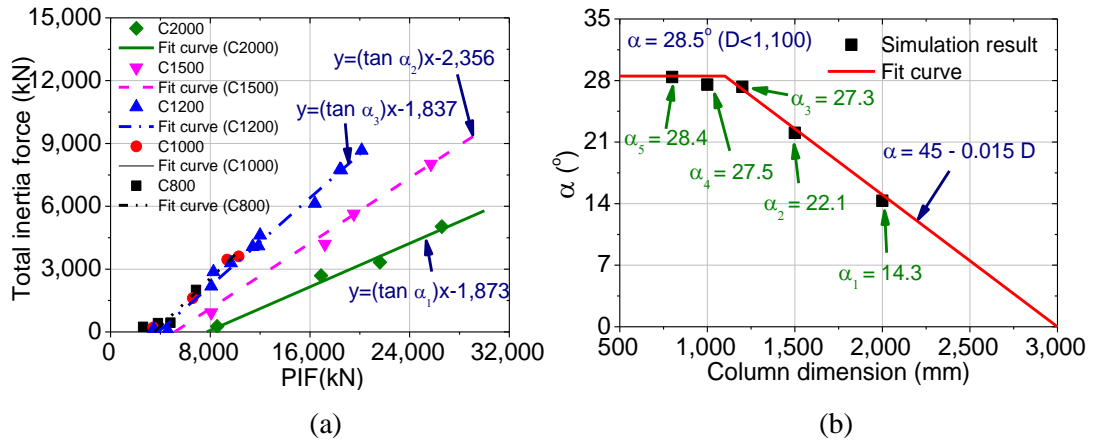
Figure 4-4 (a) Total inertia force – PIF relation; (b) Relation between the column dimension and α.

4.4.1.2 Shear force at the top

As presented in Figure 4-5a, after the shear force at the base of the column increases to the highest value within about 5-10 ms, the shear force at the top of the column also rises to its peak due to the stress wave propagation from the impact area to the column top. The shear force value at that section then oscillates around the zero level. The shear force at the top of the column in some cases is also considerably large and may cause damage as observed in previous studies (Do et al., 2018). Figure 4-5b shows the relation of the maximum shear force at the base and the top of the column. The figure illustrates that the maximum shear force at the column top, R_{top}, can be estimated by the following best-fitted equation:

$$R_{top} = \frac{1}{2} R_{base} = \frac{1}{2} \left[PIF(1 - \tan \alpha) + 2,000 \right] \qquad (4\text{-}7)$$

79

From Eqs. (4-5) and (4-7), and the *PIF* (see Eqs. (2-6) and (3-6)), the predicted shear force at the two ends of the columns are compared to the numerical results in Figure 4-6. The figure illustrates that the empirical equations can reliably predict the maximum shear force at the base and the top of the column as compared to the numerical simulation results.

Table 4-2 Initial conditions of the vehicle model and numerical results

Case	Column section	V (km/h)	m (ton)	m_e (ton)	PIF (kN)	Response	Shear force (kN) Base	Top	Bending moment (kNm) Base	Impact point
C1	C800	70	8	0.64	2,616	Flexural	2,077	789	1,442	1,140
C2		80	8	0.64	3,811	Flexural	3,394	1,271	2,510	1,980
C3		90	8	0.64	4,803	Flexural	4,362	1,942	3,020	2,470
C4		95	8	0.64	6,865	Flexural	4,862	2,709	3,350	3,030
C5	C1000	80	8	0.64	3,429	Flexural	3,224	1,353	2,460	1,869
C6		100	8	0.64	6,592	Flexural	4,982	2,892	3,307	3,529
C7		120	8	0.64	9,364	Flexural	5,913	3,241	3,900	3,825
C8		100	8	1.00	10,288	Flexural	7,082	3,489	4,772	4,799
C9	C1200	60	8	0.64	1,870	Flexural	1,880	795	2,112	631
C10		80	8	0.64	3,460	Flexural	3,325	1,396	2,885	1,410
C11		90	8	0.64	4,596	Flexural	4,528	2,526	3,087	2,507
C12		100	8	0.64	8,260	Flexural	5,398	2,772	4,145	3,118
C13		110	8	0.64	9,660	Flexural	6,371	3,150	4,613	3,462
C14		120	8	0.64	12,000	Flexural	7,386	3,796	5,582	4,359
C15		140	8	0.64	16,400	Shear	10,267	5,751	7,402	5,358
C16		100	8	1.00	11,400	Shear	7,332	3,734	5,391	4,089
C17		100	8	2.00	18,500	Shear	10,769	4,818	7,882	6,239
C18		140	8	1.00	20,150	Shear	11,483	6,506	8,531	6,379
C19		140	8	2.00	30,000	Shear	10,866	6,893	9,550	6,940
C20		100	11	0.64	8,079	Flexural	5,895	3,318	3,960	3,806
C21		100	12	1.00	11,868	Shear	7,770	3,489	5,672	4,376
C22		100	12	2.00	18,416	Shear	10,658	5,620	7,945	6,233
C23	C1500	100	8	0.64	8,079	Flexural	7,155	5,151	5,105	4,818
C24		100	8	2.00	19,522	Flexural	13,884	5,958	10,217	12,677
C25		120	8	2.00	25,708	Flexural	17,689	7,129	12,552	13,998
C26		120	8	1.00	17,159	Flexural	13,025	7,052	7,305	10,725
C27	C2000	100	8	0.64	8,544	Flexural	8,282	4,095	7,397	4,809
C28		100	8	2.00	21,611	Flexural	18,281	8,333	11,092	16,929
C29		120	8	2.00	26,589	Flexural	21,560	10,994	11,524	21,120
C30		120	8	1.00	16,890	Flexural	14,203	7,773	8,652	12,165

Note: *V* is the vehicle velocities; *m* is the total mass of the vehicle; and m_e is the engine mass.
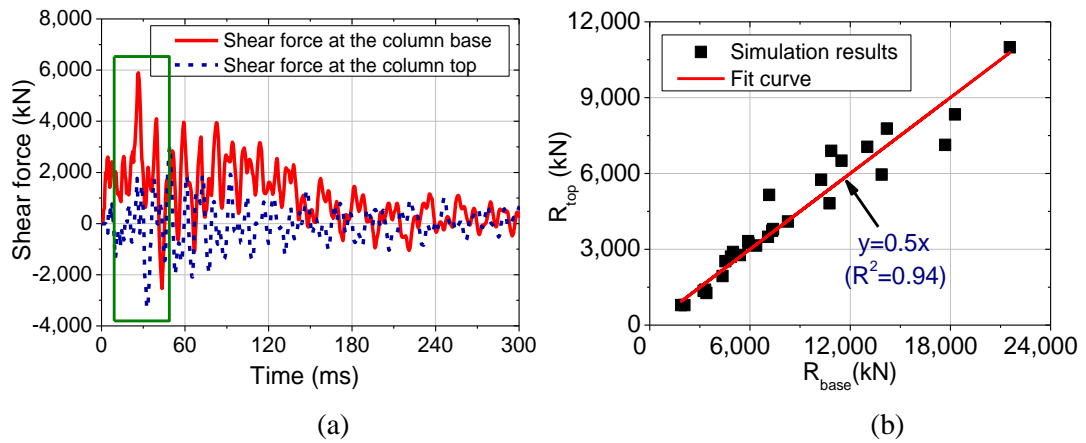
Figure 4-5 (a) Typical time histories of the shear force at the column ends (C20); (b) Relation between the maximum shear force at the base and the top.
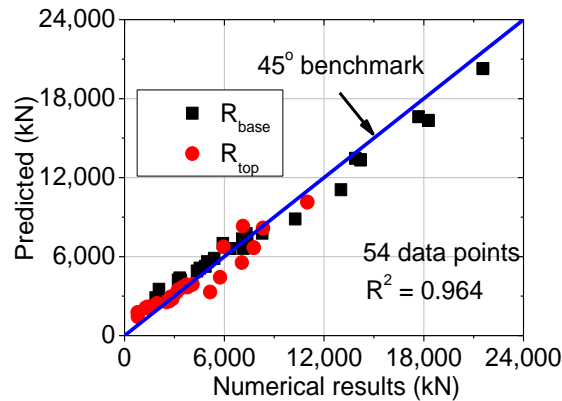
Figure 4-6 Comparison between the predicted results and numerical results.

4.4.2. Maximum bending moment

Many previous studies observed that at the peak value of impact force, just a portion of structures responds to the impact force (Fujikake et al., 2009; Pham & Hao, 2017; Zhao et al., 2017) and it causes the largest flexural bending moment at the local impact area. A similar observation was also seen in the RCBC under vehicle collisions when the impact force caused by the engine impact increased to the PIF, the bending moment at the impact area increased to the highest value (Do et al., 2019b) and the bending moment diagram is illustrated in Figure 4-7a. After about $1 - 2$ ms, the bending moment at the base of the column then increased to its peak as shown in the figure. After that, the bending moment distributed in the entire column and varied significantly with time due to the column vibration and the effect of the inertia force. The envelope of the column bending moment in an impact event is illustrated in Figure 4-7b. As illustrated in the figure, the negative bending moment at the column base is the highest value in the impacted side while the positive bending moment at the top portion of the column is almost similar to that at the impact point (see Figure 4-7b). It should be noted that when the flexural response governs the column response, the shape of the bending moment

envelope is consistent regardless of the different loading scenarios as observed in the previous study (Do et al., 2019b). Therefore, the maximum positive and negative bending moments at these two sections, i.e. column base and impact point are used for the design of the column.
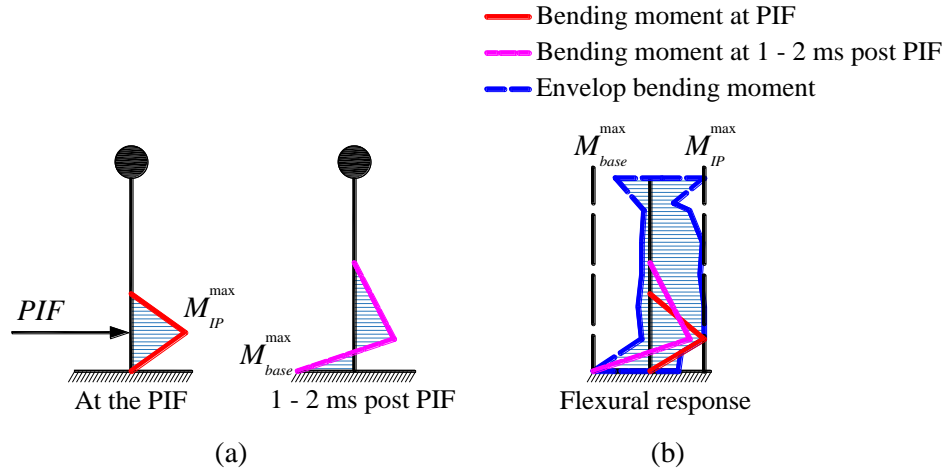
Figure 4-7 Simplified column bending moment: (a) at the PIF; (b) Envelop bending moment.

Since the bending moment diagram in the column at the instant of the PIF is a triangle (see Figure 4-7a), it is reasonable to assume the boundary conditions of the column as simply supported. Thus, the maximum positive bending moment at the impact point, M_{IP}^{max}, can be estimated by:

$$M_{IP}^{max} = k_I \; PIF \; \frac{L_e}{4} \; (kNm) \tag{4-8}$$

where k_I is the coefficient representing the effects of the inertia force on the bending moment; L_e is the effective length of the column at the PIF. In this study, the vehicle models impact on the RCBC at about 1.5 m above the footing, thus the effective length of the column at the PIF is assumed as 3 m. The relation between the maximum bending moment at the impact point $\left(M_{IP}^{max} \right)$ and the *PIF* from the numerical simulation is presented in Figure 4-8a. It should be noted that in the numerical simulation when the bending moment at the impact point reaches the bending moment capacity, *[M]*, the maximum bending moment then keeps constant, although the *PIF* continues increasing (see Figure 4-8a). In Figure 4-8, $[M_{C800}]$, $[M_{C1000}]$, $[M_{C1200}]$, $[M_{C1500}]$, and $[M_{C2000}]$ are the bending moment capacities of the column C800, C1000, C1200, C1500, and C2000, respectively. From the numerical results, the envelope curve of the bending moment is about $0.6375PIF$ when the flexural crack does not happen. From Eq. (4-8), the coefficient, k_I, is $\frac{0.6375}{L_e / 4} = \frac{0.6375}{3 / 4} = 0.85$. The maximum positive bending moment at the impact point is, therefore, expressed as

$$M_{IP}^{\max} = 0.85\, PIF\, \frac{L_e}{4}\ (kNm) \tag{4-9}$$
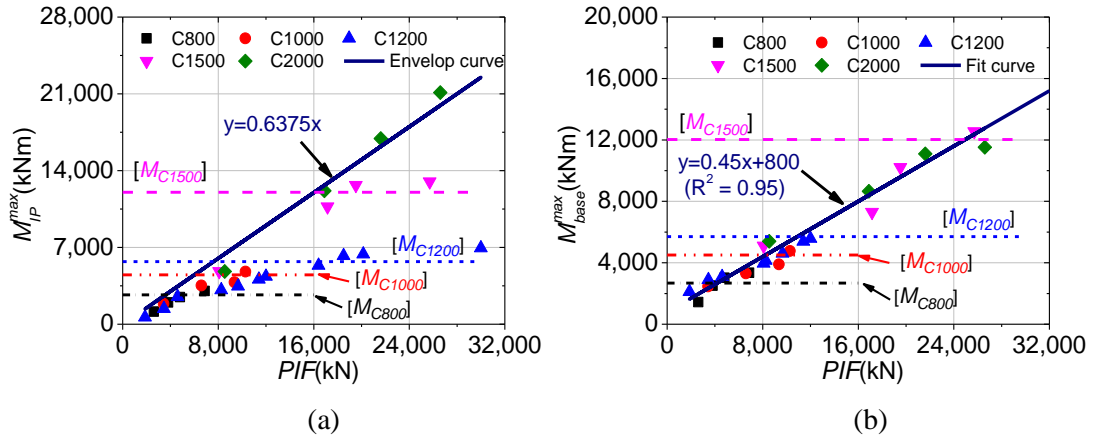
Figure 4-8 Maximum bending moment: (a) at the impact point; (b) at the column base.

To estimate the maximum bending moment at the column base, the impact force and inertia forces are required. As observed in the experimental and numerical studies on concrete structures subjected to impact loading, the inertia forces oscillate with high frequencies (Pham & Hao, 2017; Zhao et al., 2017) so that it is difficult to estimate the maximum bending moment at the column base from an analytical solution. Thus, the maximum bending moment at the base of the column is predicted based on the numerical results, as given in Table 4-2. Figure 4-8b shows the bending moment at the base of the column with respect to the *PIF*. From the numerical results, the maximum bending moment at the column base, $M_{base}^{\max}$, can be predicted by the following equation:

$$M_{base}^{\max} = 0.45\, PIF + 800\ (kNm) \tag{4-10}$$

4.4.3. SDOF model

In the design of structures subjected to dynamic loads, the SDOF is commonly used to predict the dynamic response of structures (Hao & Wu, 2003; Ngo et al., 2007; Pham & Hao, 2018; Sha & Hao, 2014). For instance, the SDOF was employed to predict the impact response of RC beams (Pham & Hao, 2018). In this analytical method, the elastic stiffness, plastic stiffness, crack section, and residual displacement of the beam can be taken into account. The analytical result shows a good agreement with the numerical simulation and experimental test in terms of the global response of the beam under impact loads. Furthermore, Sha and Hao (2014) used a SDOF system to predict the response of bridge piers under barge impacts. The bridge pier was assumed as a nonlinear SDOF system in which both elastic and plastic response of the bridge piers were considered. This analytical method can give a reasonable prediction of the maximum lateral displacement of the pier. To estimate the displacement response of the RCBC

under vehicle collisions, the SDOF approach is also adopted in this study, which is briefly discussed below.
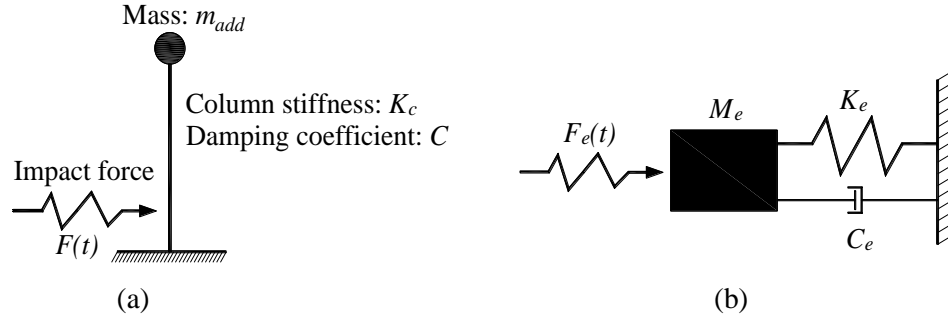
Figure 4-9 (a) Simplified model of the column under impact force; (b) Equivalent SDOF system.

Based on the proposed impact force profile and column properties, an equivalent SDOF model of the column under vehicle collision as illustrated in Figure 4-9 can be derived. The equation of motion of the SDOF system is written as follows:

$$M_e \ddot{x}(t) + C_e \dot{x}(t) + K_e x(t) = F_e(t) \tag{4-11}$$

where M_e, C_e, and K_e are the equivalent mass, damping coefficient, and column stiffness of the SDOF system, respectively; $F_e(t)$ is the equivalent load on the SDOF system; t is time and x is lateral displacement. The equivalent mass of the lumped-mass system, as given by Biggs (1964), can be expressed as

$$M_e = \int_0^H m_h \phi^2(h)dh + m_{add} \tag{4-12}$$

where m_h is the mass density per unit length of the column; $\phi(h)$ is the assumed deflection shape function with the displacement at the column top normalised to unit as shown in Figure 4-10; m_{add} is the added mass at the column top; h is the distance measured from the column base; and H is the column height.

Because the displacement at the column top is considered, the equivalent column stiffness is the actual stiffness of the column. By assuming a free top end as shown in Figure 4-9a, the equivalent stiffness is

$$K_e = \frac{3EI}{\left(H + H_{add}\right)^3} \tag{4-13}$$

where $E = 4700\sqrt{f_c'}$ is the Young's modulus and f_c' the concrete compressive strength; I is the moment of inertia of the column; H_{add} is the distance from the top of the column to the centroid point of the added weight.
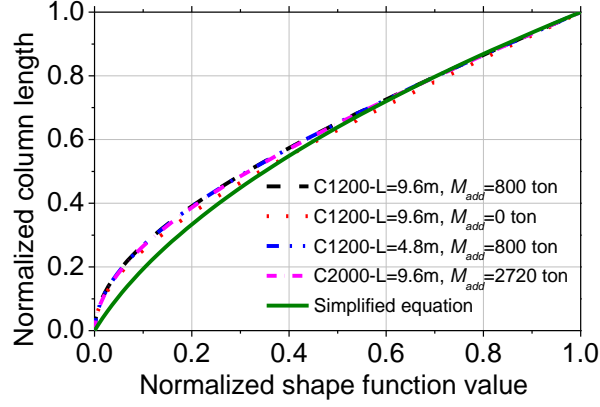
Figure 4-10 The dimensionless mode shape function of the first mode of the column.

In addition, the equivalent impact force on the SDOF system is estimated by:

$$F_e(t) = \sum_{j=1}^{n} F_j(t)\phi_j \tag{4-14}$$

where F_j is the impact force at a location j; ϕ_j is the value of the deflection shape function at the location j (Biggs, 1964).

The above equivalent mass and concentrated impact force highly depend on the deflection shape function of the column which is determined from the column properties, i.e. cross-section area, mass density, added weight, moment of inertia, Young's modulus, and column height (Biggs, 1964; Dutta et al., 2011; Jou, 2014). To achieve the equivalent mass and concentrated force in the lumped-mass system, the deflection shape function was usually assumed by a simple linear function as discussed in previous studies (Biggs, 1964; Sha & Hao, 2014). However, the linear function does not really reflect the actual shape of the structural response and thus does not provide good predictions (Sha & Hao, 2014). By varying the column height, cross-section, and the added weight at the column top, the dimensionless mode shapes of the column can be derived as presented in Figure 4-10. It should be noted that these deflection shape functions are extracted from the modal analysis (Bathe, 2006). From these curves, the best fitted normalised deflection shape function of the column is

$$\phi(h) = 0.6\left(\frac{h}{H}\right)^2 + 0.4\left(\frac{h}{H}\right) \tag{4-15}$$

To solve the equation of motion of the SDOF system, the central difference algorithm is adopted. The velocity and the acceleration of the SDOF system can be approximated by

$$\dot{x} = \frac{1}{2\Delta t}\left(x^{t+\Delta t} - x^{t-\Delta t}\right) \tag{4-16}$$

$$\ddot{x} = \frac{1}{\Delta t^2}\left(x^{t+\Delta t} - 2x^t + x^{t-\Delta t}\right) \tag{4-17}$$

The above equations can be solved with initial conditions of the column at the start time $t = 0$: $x^{t-\Delta t} = 0$, $\dot{x} = 0$, and $\ddot{x} = 0$. The first step of the solution starts to determine $x^{t+\Delta t}$ with the corresponding impact force obtained from the proposed impact force profile given in Section 3.4.

To verify the analytical method, the comparisons of the analytical result and simulation result are shown in Figure 4-11. In this case, the column which has a square section of 1,200 x 1,200 mm^2, is impacted by the medium truck model (8 ton) with the velocity of 80 km/h. The heights of the column and the cap beam are 9,600 mm and 1,500 mm, respectively. The added mass of 800 ton is placed on top of the cap beam with H_{add} equals to 2,100 mm. Since the displacement at the top of the cap beam is of interest and the impact location is 1.5 m above the footing, the value of the deflection shape function at the impact point is 0.065 (Eq. 4-15). The equivalent mass, damping ratio, and column stiffness of the SDOF system are 800 ton, 3.5 %, and 8,870 kN/m, respectively. The figure illustrates that the analytical model is able to estimate the maximum lateral displacement and the dynamic response of the column under vehicle collisions with a reliable prediction. It is worth mentioning that a slight difference in the lateral displacement of the column, as shown in Figure 4-11, is caused by the local deformation of the column at the contact area between the vehicle model and the column which cannot be predicted by the SDOF model. It should be noted that the column response predicted by using a linear assumption of shape function (Sha & Hao, 2014) is also presented in Figure 4-11. The result shows that using the linear assumption of shape function over-estimates the response of the column under vehicle collision.
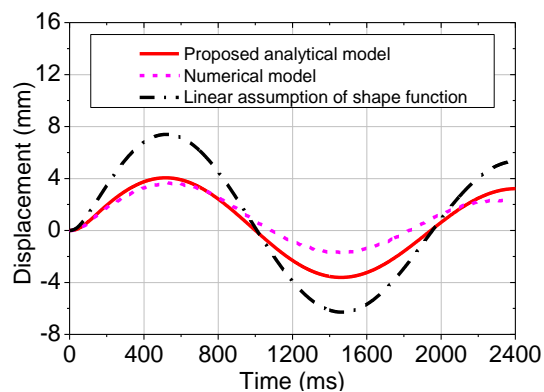
Figure 4-11 Displacement at the column top between the analytical prediction and numerical simulation.

4.5. Design example

4.5.1. Design procedure

Based on the column properties i.e. cross-section width, W, cross-section depth, D, compressive strength of concrete, f_c (MPa), tensile strength, f_t (MPa), and reinforcement area A_s (mm^2), yield stress f_y (MPa), and vehicle parameters, i.e. total vehicle mass, m (ton), vehicle velocity, V (m/s), and engine mass, m_e (ton), the dynamic shear capacity, P_{dyn}^{max} (kN), shear force R_{base} (kN) and R_{top} (kN), bending moment M_{IP} (kNm) and M_{base} (kNm), and the maximum column displacement, Δ_{max}, can be estimated by the above equations, as summarised in Figure 4-12. [V], [M], and [Δ] are the shear capacity, bending moment capacity, and the maximum allowable lateral displacement of the column, respectively. To provide more details in the design procedure, the following sections present two examples corresponding to two different responses of RCBC against vehicle collisions.
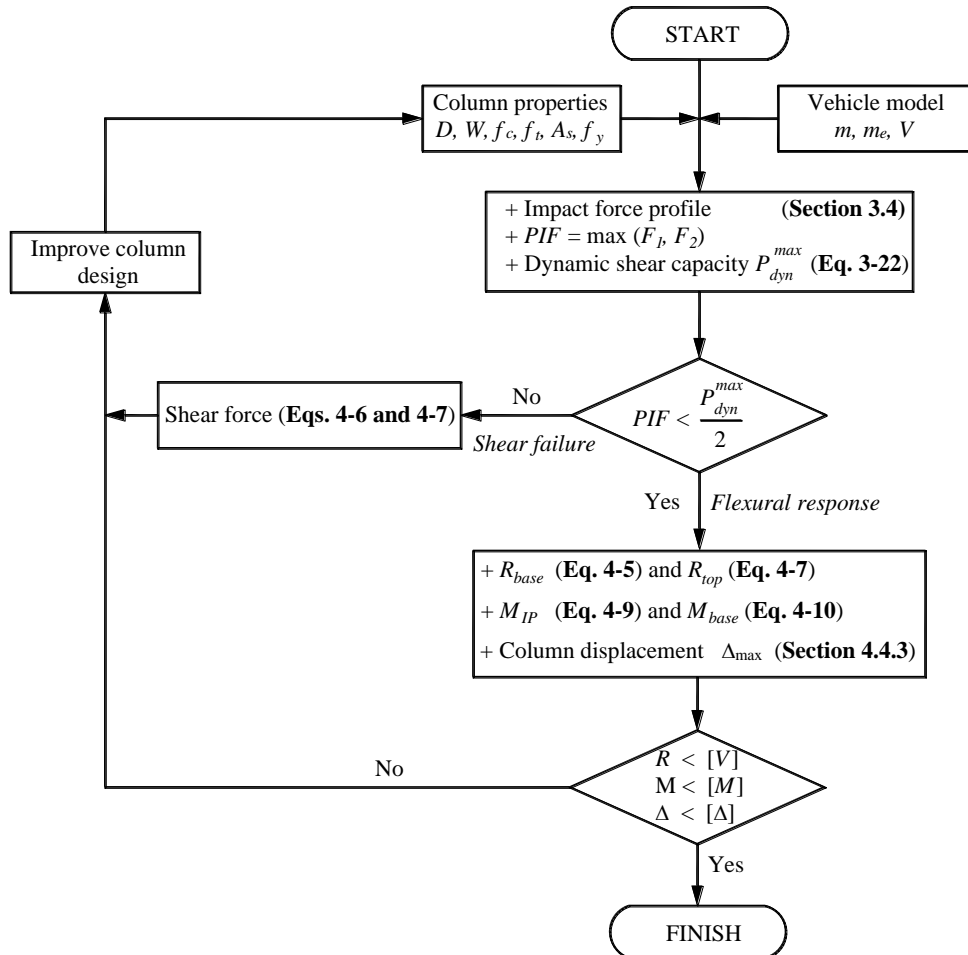
Figure 4-12 Design procedure of RCBCs under vehicle collisions.

Two RCBCs are designed to resist collisions from a medium truck and a heavy truck trailer associated with two different column responses, i.e. shear failure and flexural response. In the

first example, shear failure occurs in the impact area by the collision of the medium truck model. Three improvement methods of the column design are then proposed to resist the shear failure. In the second example, the column, which is impacted by the heavy truck trailer, has sufficient shear strength but is vulnerable to flexural failure. Longitudinal and lateral reinforcements are then designed based on the maximum shear force and bending moment estimated from the proposed equations. Numerical simulations are then conducted to verify the accuracy of the design analysis results.

4.5.2. Example 1: Define the column response

It is assumed that a passenger overpass bridge in a city which has a total length of 40 m is designed to cross over a busy street underneath. The continuous bridge is supported by three single RC columns which have a square section of 800 mm. Twenty-eight 30-mm-diameter straight longitudinal reinforcements and three-leg 12-mm-diameter stirrups at 100 mm spacing are used to reinforce the column. The compressive and tensile strength of the concrete is 30 MPa and 3 MPa, respectively, while the yield strength of reinforcements is 420 MPa. Only medium and small trucks are assumed to be allowed in the street.

<u>Solution</u>

In the worst case scenario, the medium truck model with a total mass of 12 ton is considered in the design stage. Although the maximum allowance velocity in the city is usually under 70 km/h, an accidental velocity of truck models in the design is considered as 100 km/h. Based on the total mass (12 ton), engine mass (0.64 ton), and velocity (100 km/h), the PIF (from engine impact) is:

$$F_1 = 969.3\sqrt{0.5 \times 0.64 \times 27.78^2} - 7,345.9 = 7,886\,(kN) \tag{4-18}$$

Meanwhile, the maximum dynamic shear capacity of the column is:

$$P_{dyn}^{\max} = \frac{6.5}{1,000} \times 800 \times 800 \times 3.0 = 12,480\,(kN) \tag{4-19}$$

In this conditions, the PIF from the engine impact is higher than $0.5\,P_{dyn}^{\max}$, thus the diagonal shear failure is expected to occur at the impact area. To verify the above statement, a numerical simulation of this case has been conducted. The numerical results show that the column exhibits diagonal shear failure at the impact area (see Figure 4-13). It is crucial to mention that this column would not fail if an ESF method is adopted for the design according to AASHTO (2012), i.e. the static shear capacity of the column is 2,816 kN (ACI, 2008), which is higher than the recommended impact force from AASHTO (2012) (2,668 kN). Thus, the diagonal

shear failure at the impact area should not happen if the ESF is utilised. This example confirms that simply using the ESF for the analysis may not result in a conservative/safe design.
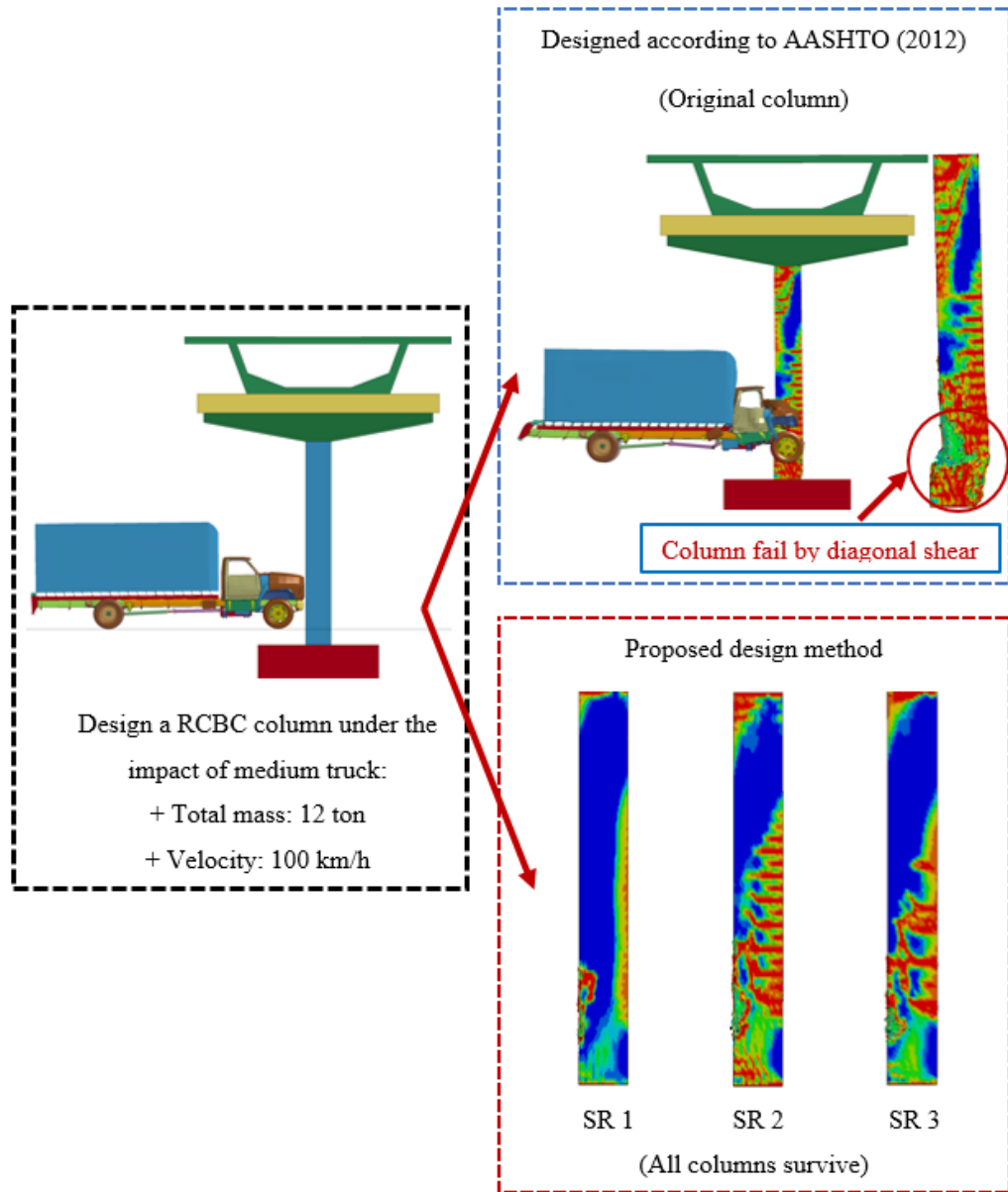
Figure 4-13 Crack patterns of the RCBCs under medium truck collision.

Since the column fails by diagonal shear under the collision of the medium truck, improvements of the column are required to enhance the dynamic shear capacity of the column. In this case, three different improvement methods are introduced including: (SR1): increase the cross section to 1,000 mm $\left(0.5P_{dyn}^{\max}=9,750\,(kN)\right)$;(SR2): keep the column cross-section at 800 mm but increase the tensile strength of concrete to 4.5 MPa (equivalent to concrete with 45 MPa compressive strength) $\left(0.5P_{dyn}^{\max}=9,360\,(kN)\right)$; (SR3): increase the size of column to 900 mm together with the tensile strength of concrete to 4.0 MPa

$\left(0.5P_{dyn}^{\max}=9,213(kN)\right)$. As shown in Figure 4-13, all the three designed columns survive the impacts from the truck collisions without diagonal shear cracks at the base. However, as shown in the figure, although the columns survive the diagonal shear failure, some intensive flexural cracks are observed (see Figure 4-13), indicating the column might experience flexural damage. Therefore designs of longitudinal and transverse reinforcements of these three columns are thus required to avoid flexural damage. From the above-proposed equations, the maximum shear force at the base and the top of the column are:

$$R_{base}=7,886\times\left(1-\tan 28.5^{o}\right)+2,000=5,604(kN) \tag{4-20}$$

$$R_{top}=\frac{1}{2}R_{base}=\frac{1}{2}\times 5,604=2,802(kN) \tag{4-21}$$

Furthermore, from Eqs. (4-9) and (4-10), the maximum bending moment at the base and the impact point are:

$$M_{IP}^{\max}=0.85\times\frac{3}{4}\times 7,886=5,027(kNm) \tag{4-22}$$

$$M_{base}^{\max}=0.45\times 7,886+800=4,349(kNm) \tag{4-23}$$
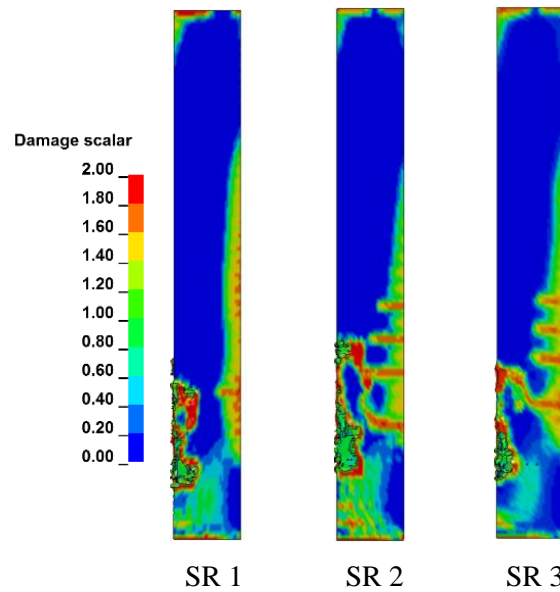
Figure 4-14 Plastic strain of the three designed columns.

From the above-calculated shear force and bending moment, designs of transverse and longitudinal reinforcements of these three columns are derived and given in Table 4-3. The numerical results of these three columns with the new reinforcements are re-simulated. The plastic strain of these columns after design modification is shown in Figure 4-14. The simulation results show that the flexural cracks in the columns are greatly reduced. This

example demonstrates that the proposed approach can give reliable predictions of the capacity of RC columns to resist vehicle impact and provide feasible solutions to improve the column design.

Table 4-3 Design of reinforcements.

| Column | Transverse reinforcements | | Longitudinal reinforcements |
	At the base	At the top	
SR1	four-leg 16-mm-diameter @100 mm	two-leg 14-mm-diameter @100 mm	28d36
SR2	three-leg 20-mm-diameter @100 mm	two-leg 14-mm-diameter @100 mm	32d40
SR3	four-leg 16-mm-diameter @100 mm	two-leg 14-mm-diameter @100 mm	28d36

4.5.3. Example 2: Column design under flexural response

In the second example, a RC column which has a cross-section of 1,300 x 1,300 mm^2 is designed to carry a deck and girder of a high-speed railway at an intersection with a highway. The total height of the column, cap-beam, and girder is assumed to be 9 m. The yield strength of steel, compressive strength and tensile strength of concrete are designed at 500 MPa, 50 MPa, and 5 MPa, respectively. The total mass of the train, deck, and girder is assumed to generate 20% of the column compressive strength.

Solution

In the highway, the column is assumed to be collided by a heavy truck model (30 ton) with the impact velocity is considered at 120 km/h. By using the proposed equations as provided in Section 3.4, the impact force profile of the collision event is predicted and shown in Figure 4-15a in which the engine mass is assumed to be 1.5 ton. Since the PIF from engine impact (20,635 kN) and cargo impact (7,000 kN) are smaller than a half of the dynamic shear capacity of the column $\left(0.5P_{dyn}^{\max} = 27,463(kN)\right)$, the column thus survives the direct vehicle impact. Therefore, only the flexural capacity is checked.

From Eqs. (4-5) and (4-7), the maximum shear force at the column base and column top are:

$$R_{base} = 20,635 \times \left(1 - \tan\left(45 - 0.015 \times 1,300\right)\right) + 2,000 = 12,793(kN) \tag{4-24}$$

$$R_{top} = \frac{1}{2}R_{base} = 6,396(kN) \tag{4-25}$$

Thus, four-leg 20-mm-diameter stirrups at 100 mm spacing with the yield strength of 500 MPa are used at the column base (1.5 m from the footing) while the diameter and spacing of the

stirrups at the remaining part of the column are 16 mm and 200 mm, respectively (see Figure 4-15b).
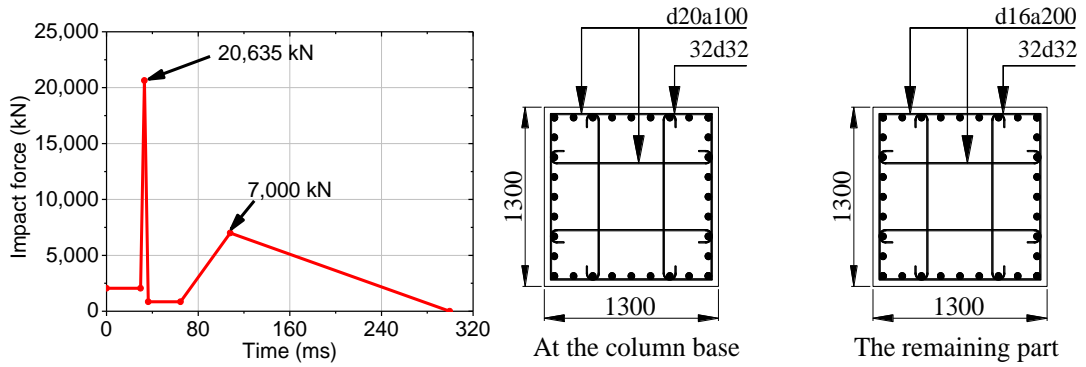
(a) Impact force time histories

(b) Column cross-section design
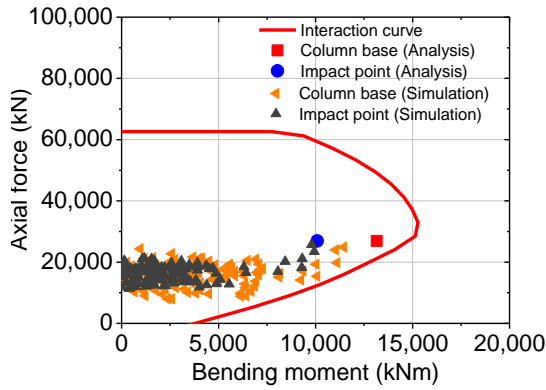
(c) Column interaction diagram
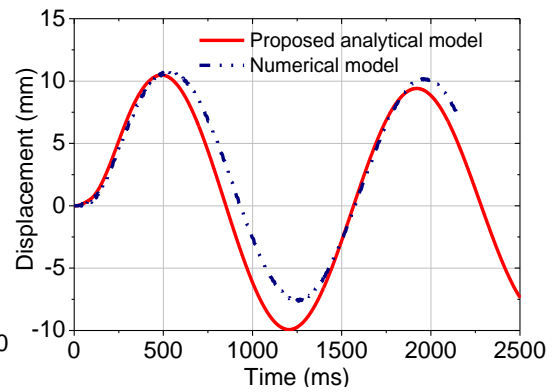
(d) Displacement time histories at the column top
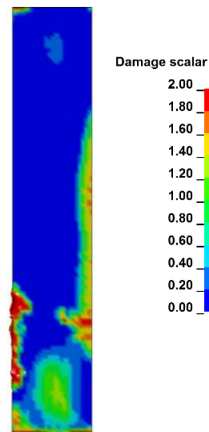
(e) Plastic strain of the column

Figure 4-15 Design of RCBC under the heavy truck trailer collision.

Based on Eqs. (4-9) and (4-10), the maximum bending moment at the base and the impact point are

$$M_{IP}^{\max} = 0.85 \times \frac{3}{4} \times 20,635 = 13,155 \, (kNm) \tag{4-26}$$

$$M_{base}^{max} = 0.45 \times 20,635 + 800 = 10,086 \, (kNm) \tag{4-27}$$

To meet the bending moment demand, the column is thus reinforced by thirty-two 32-mm-diameter longitudinal rebars with the maximum bending moment capacity of about 15,280 kN.m. The design of the column cross-section is shown in Figure 4-15b. It needs to be mentioned that at time when lateral impact force reaches the maximum, i.e. PIF, the axial compression force in the column is increased due to the stress wave propagation from the contact area to the top and the base of the column (Do et al., 2018), as presented in Section 2.4.2. Therefore, the maximum dynamic axial force, A_{dyn}, in the column at the moment of PIF is (Do et al., 2018):

$$A_{dyn} = \frac{0.2 \times 1300^2 \times 50}{1,000} + 8 \times 10^{-6} PIF + 0.32 PIF = 26,910 \, (kN) \tag{4-28}$$

The interaction diagram of the column, as followed by ACI (2008), together with the internal forces caused by the heavy truck trailer collision at different instants with time step 0.5 ms during the impact are presented in Figure 4-15c. It shows the column flexural capacity is sufficient to resist the vehicle impact. To examine the reliability of the above design, the numerical model of the designed column is then built and impacted by the heavy truck trailer. The bending moment and axial force from the numerical simulation are also compared to the analytical solutions (see Figure 4-15c). The lateral displacement time histories at the column top from SDOF model and numerical simulation is also presented in Figure 4-15d in which the maximum lateral displacement and the natural period of the column are well predicted by the analytical solution. Meanwhile, the plastic strain of the designed column is also checked by using numerical simulation where no shear failure or flexural failure occurs, as shown in Figure 4-15e. The results show that the analytical method can provide a useful tool and feasible application to design the column under vehicle collision with good predictions as compared to numerical simulations.

4.6. Conclusions

This study analytically and numerically examines the dynamic performance of RCBCs under vehicle collisions. The numerical results has been compared and verified against the experimental results and the observed damage modes in real vehicle accidents. Based on numerical results, empirical relations are proposed to estimate the maximum shear force and bending moment in RC columns collided by vehicles. The findings in this study are summarised as follows:

1. Empirical equations to determine the maximum shear force and bending moment at the critical section are proposed for use in design analysis. The accuracies of these proposed analytical predictions are verified against high fidelity numerical simulations.

2. The SDOF system of the column is also suggested to predict the dynamic response of the RCBC.

3. A complete procedure to design the RCBC against vehicle collision with different initial conditions is recommended.

Two design examples of RCBCs against the medium truck and heavy truck trailer impact are presented to demonstrate the proposed design analysis procedure. It is demonstrated that the proposed procedure avoids detailed FE modelling, but can yield accurate predictions of the column responses against truck collisions. The proposed procedure, therefore, can be used in design analysis for safe and economic designs of RC columns to resist vehicle impact.

4.7. References

AASHTO. (2012). *AASHTO LRFD bridge design specifications (customary U.S. units)*. 6th Ed., Washington, DC.

Abdelkarim, O. I., & ElGawady, M. A. (2016). Performance of hollow-core FRP–concrete–steel bridge columns subjected to vehicle collision. *Engineering Structures, 123*, 517-531.

Abdelkarim, O. I., & ElGawady, M. A. (2017). Performance of bridge piers under vehicle collision. *Engineering Structures, 140*, 337-352.

ACI. (2008). *Building code requirements for structural concrete (ACI 318-08) and commentary (ACI318R-08)*. Farmington Hills, MI: ACI 318.

Agrawal, A. K., Xu, X., & Chen, Z. (2011). *Bridge vehicle impact assessment* (C-07-10). University Transportation Research Center.

Bathe, K.-J. (2006). *Finite element procedures*: Klaus-Jurgen Bathe.

Biggs, J. M. (1964). *Introduction to structural dynamics* (Vol. 3): McGraw-Hill, New York.

Buth, C. E., Williams, W. F., Brackin, M. S., Lord, D., Geedipally, S. R., & Abu-Odeh, A. Y. (2010). *Analysis of large truck collisions with bridge piers: phase 1. Report of guidelines for designing bridge piers and abutments for vehicle collisions* (FHWA/TX-10/9-4973-1). College Station, TX.

CEN. (2002). *Actions on structures. Part 1-1: General actions-densities, self-weight, imposed loads for building*. Brussels, Belgium: BS EN 1991-1-1:2002.

CEN. (2006). *Actions on structures. Part 1-7: General actions-accidental actions*. Brussels, Belgium: BS EN 1991-1-1:2002.

Chen, L., El-Tawil, S., & Xiao, Y. (2016). Reduced models for simulating collisions between trucks and bridge piers. *Journal of Bridge Engineering, 21*(6), 04016020.

Chen, L., El-Tawil, S., & Xiao, Y. (2017). Response spectrum-based method for calculating the reaction force of piers subjected to truck collisions. *Engineering Structures, 150*, 852-863.

Chung, C. H., Lee, J., & Gil, J. H. (2014). Structural performance evaluation of a precast prefabricated bridge column under vehicle impact loading. *Structure and Infrastructure Engineering, 10*(6), 777-791.

Do, T. V., Pham, T. M., & Hao, H. (2018). Dynamic responses and failure modes of bridge columns under vehicle collision. *Engineering Structures, 156*, 243-259.

Do, T. V., Pham, T. M., & Hao, H. (2019a). Impact force profile and failure classification of reinforced concrete bridge columns against vehicle impact. *Engineering Structures, 183*, 443-458.

Do, T. V., Pham, T. M., & Hao, H. (2019b). Impact Response and Capacity of Precast Concrete Segmental versus Monolithic Bridge Columns. *Journal of Bridge Engineering, 24*(6), 04019050.

Dutta, R., Ganguli, R., & Mani, V. (2011). Swarm intelligence algorithms for integrated optimization of piezoelectric actuator and sensor placement and feedback gains. *Smart Materials and Structures, 20*(10), 105018.

El-Tawil, S., Severino, E., & Fonseca, P. (2005). Vehicle collision with bridge piers. *Journal of Bridge Engineering, 10*(3), 345-353.

Fan, W., Shen, D., Yang, T., & Shao, X. (2019). Experimental and numerical study on low-velocity lateral impact behaviors of RC, UHPFRC and UHPFRC-strengthened columns. *Engineering Structures, 191*, 509-525.

Fan, W., Xu, X., Zhang, Z., & Shao, X. (2018). Performance and sensitivity analysis of UHPFRC-strengthened bridge columns subjected to vehicle collisions. *Engineering Structures, 173*, 251-268.

Fujikake, K., Li, B., & Soeun, S. (2009). Impact response of reinforced concrete beam and its analytical evaluation. *Journal of Structural Engineering, 135*(8), 938-950.

Hallquist, J. O. (2007). *LS-DYNA keyword user's manual.* Livermore Software Technology Corporation. Vol. 970. (pp. 299-800).

Hao, H., & Wu, C. (2003, 12-14/11). *Effects of simultaneous ground shock and airblast force on structural response.* Paper presented at the 5th Asia-Pacific conference on shock and impact loads on structures, Hunan, China

Hao, Y., & Hao, H. (2014). Influence of the concrete DIF model on the numerical predictions of RC wall responses to blast loadings. *Engineering Structures, 73*, 24-38.

Jiříček, P., & Foglar, M. (2016). Numerical analysis of a bridge pier subjected to truck impact. *Structural Concrete, 17*(6), 936-946.

Jou, J. M. (2014). Theory and Simulation Analysis of the Mode Shape and Normal Shape Actuators and Sensors. *Open Journal of Acoustics, 4*(4), 184-203.

Malvar, L. J., & Crawford, J. E. (1998). *Dynamic increase factors for steel reinforcing bars [C].* Paper presented at the The Twenty-Eighth DoD Explosives Safety Seminar Held, Orlando, USA

Megally, S. H., Garg, M., Seible, F., & Dowell, R. K. (2001). *Seismic performance of precast segmental bridge superstructures* (SSRP-2001/24). University of California, San Diego.

Ngo, T., Mendis, P., Gupta, A., & Ramsay, J. (2007). Blast loading and blast effects on structures–an overview. *Electronic Journal of Structural Engineering, 7*, 76-91.

Pham, T. M., & Hao, H. (2017). Plastic hinges and inertia forces in RC beams under impact loads. *International Journal of Impact Engineering, 103*, 1-11.

Pham, T. M., & Hao, H. (2018). Influence of global stiffness and equivalent model on prediction of impact response of RC beams. *International Journal of Impact Engineering, 113*, 88-97.

Pham, T. M., Zhang, X., Elchalakani, M., Karrech, A., Hao, H., & Ryan, A. (2018). Dynamic response of rubberized concrete columns with and without FRP confinement subjected to lateral impact. *Construction and Building Materials, 186*, 207-218.

SA/SNZ. (2002). *Structural design actions Part 1: Permanent, imposed and other actions* Sydney, NSW 2001; Wellington 6020: AS/NZS 1170.1:2002.

Sha, Y., & Hao, H. (2014). A simplified approach for predicting bridge pier responses subjected to barge impact loading. *Advances in Structural Engineering, 17*(1), 11-23.

Sharma, H., Hurlebaus, S., & Gardoni, P. (2012). Performance-based response evaluation of reinforced concrete columns subject to vehicle impact. *International Journal of Impact Engineering, 43*, 52-62.

Zhang, X., Hao, H., & Li, C. (2016). Experimental investigation of the response of precast segmental columns subjected to impact loading. *International Journal of Impact Engineering, 95*, 105-124.

Zhao, D.-B., Yi, W.-J., & Kunnath, S. K. (2017). Shear Mechanisms in Reinforced Concrete Beams under Impact Loading. *Journal of Structural Engineering, 143*(9), 04017089.

Zhou, D., & Li, R. (2018). Damage assessment of bridge piers subjected to vehicle collision. *Advances in Structural Engineering, 21*(15), 2270-2281.

PART 2
DYNAMIC ANALYSIS, DESIGN, AND STRENGTHENING OF PRECAST CONCRETE SEGMENTAL COLUMNS

CHAPTER 5

NUMERICAL INVESTIGATION OF THE BEHAVIOUR OF PRECAST CONCRETE SEGMENTAL COLUMNS SUBJECTED TO VEHICLE COLLISION

ABSTRACT[4]

This study numerically investigates the response of precast concrete segmental columns with unbonded prestress tendons subjected to vehicle collision. Numerical models are developed using LS-DYNA and validated against experimental tests. The validated model is then used to perform intensive numerical simulations to analyse the effectiveness of prestressing level, number of segments, concrete strength, and vehicle velocity on the behaviour of precast segmental concrete columns. The numerical results have shown that the effect of the initial prestressing level and the number of segments are marginal on the impact force time history but significant on the residual displacement and the damage of the column. Better self-centring capacity as well as smaller lateral displacement can be achieved on segmental columns by reducing the number of column segments and increasing the prestress level. In addition, the height-to-depth ratio of a concrete segment should be smaller than two in order to minimise an undesirable local damage at the rear side opposite the impact point. Varying concrete strength from 20 MPa to 80 MPa shows an unnoticeable change of the impact force but its effects on mitigating the damage of the columns are considerable. Last but not least, increasing the impact velocity does not always increase the peak impact force of a segmental column. It is recommended that both the peak impact force and impulse should be taken into consideration in the analysis and design of segmental columns against vehicle impact.

5.1. Introduction

Precast concrete segmental columns (PCSCs) have been more intensively studied in recent years owing to their many advantages compared to conventional cast-in-place concrete structures (ElGawady et al., 2010; Ou, 2007). These include significantly reducing the construction duration, enhancing on-site efficiency, diminishing environmental impacts, improving work-zone safety, and better construction quality control in a prefabrication workshop. Apart from the mentioned benefits, precast segmental elements prepared in the

---

factory also offer a feasible solution to applications of new materials such as ultra-high performance concrete, fiber reinforced concrete which usually requires temperature control or careful mixing. Although PCSCs have been widely used over the world, studies on their performance and behaviour under impact loading such as vehicle collision are very rare (Chung et al., 2014; Zhang et al., 2016a, 2016b). With the rapid development of cities and highway networks around the world as well as the increase of traffic in urban areas, bridge columns and ground story columns of buildings are vulnerable to vehicle collision (Figure 5-1). The knowledge on the behaviour of PCSCs under vehicle impact are, therefore, necessary and crucial for their applications in construction.

(a) Chatfield Road Bridge   (b) Tancahua Street Bridge, Texas

Figure 5-1 Truck accident (Buth et al., 2010).

Recent knowledge on PCSCs under dynamic lateral loadings focuses mainly on their seismic capability. Many studies have reported the behaviour and failure modes of PCSCs under cyclic loading for their applications in high-seismicity regions (Bu et al., 2016; Chou et al., 2013; Dawood et al., 2014; Motaref et al., 2013; Ou, 2007; Sideris et al., 2014). Pros and cons of PCSCs in resisting seismic loading as compared to traditional monolithic columns have been therefore presented and possible design improvements were suggested. Comparing with many studies on PCSCs under seismic loading, studies on the impact-resistant capacity of PCSCs are very limited with only three studies can be found in the open literature (Chung et al., 2014; Hao et al., 2017; Zhang et al., 2016a, 2016b). Recently, the responses of PCSCs under vehicle collision are studied using numerical simulation by Chung et al. (2014). In that study, a numerical model of a PCSC which was 16.25 m in height and 2.3 m in diameter subjected to an 8-ton-vehicle impact was built. The dynamic performances of PCSCs were compared to a cast-in-place monolithic column. Resulting from the relatively smaller stiffness, the maximum displacement of the PCSC was higher than the conventional monolithic column. A relative lateral slip was also observed at the bottommost joint between the foundation and the first concrete segment which also contributed to the lateral displacement. The slip between the bottom segment and foundation raised a concern of using PCSCs in resisting impact forces.

However, in the latter numerical model, modelling of the prestress tendons was not mentioned in the study and thus the capability of prestress tendons in controlling the maximum and residual displacement of the column was probably ignored. The accuracy of the numerical model was not validated either. Since no severe damage or failure was observed due to the large size of the column modelled compared to the relatively small impact energy of the considered vehicle, the impact behaviour of the column with local concrete damage around the impacting point, as well as the large deformation and failure were not considered in the latter model.

On the other hand, Zhang et al. (2016b) used a pendulum impact testing system and performed impact tests of scaled PCSCs. The PCSCs post-tensioned with unbonded prestress tendon were experimentally investigated under progressively increasing impact velocities and the results were then compared with a reference monolithic column. It was observed that under the same initial impact conditions, the segmental joints opened, i.e., rocking of segments, to dissipate energy while the monolithic column showed concrete tensile cracks. Therefore, the PCSCs showed better impact-resistant and self-centring capacity than those of the counterpart. The effectiveness of the segment number was also discussed in the latter experimental study. The more segments in PCSCs, the more columns' flexibility was observed, resulted from joint openings. As a result, smaller peak impact force and more energy dissipation were observed. Zhang et al. (2016b) observed the similar problem reported in the previous numerical study that shear slips occurred between the impacted segment and its adjacent segments. To improve the shear resistance capability of PCSCs, unreinforced concrete tower shear keys were utilised in a subsequent study in segments of PCSCs to resist lateral impact forces by (Zhang et al., 2016a). By introducing tower concrete shear keys, under the same loading condition, the column with concrete shear keys significantly reduced the relative displacement between segments by about 70% as compared to the columns without shear keys. However, it was also observed that large concrete shear keys led to increasing stress concentration within the segment and resulted in more severe damage observed in the concrete segment subjected to impact. Hao et al. (2017) carried out experimental tests on a new design of dome shear keys between the concrete segments in the latest pendulum impact test. The testing results indicated that although the tower-shear-key column and the dome-shear-key column observed a similar concrete damage under similar small impact loading, the latter managed to survive and carried the top structures while the former was totally destroyed at the highest impact load. However, the dome-shear-key column showed a higher residual displacement at the column mid-height compared to the tower-shear-key column. Based on the impact performances of the segmental column with shear keys, it is found that the concrete shear keys significantly reduce the column lateral displacement, increase the column stability, and shear resistances of the segmental

columns but some limitations are still exist, i.e. stress concentration at the key corner (tower shear keys), easily slippage (dome shear keys). Therefore, further improvements on shear key design are needed and are under investigation by the authors.

From the above review, it is clear that a calibrated numerical model that properly considers the influences of prestress level in the tendons on the responses, failure modes, and local damage of columns needs be developed to realistically predict the performance of segmental columns subjected to vehicle impact. The model can also be used to study the influences of the varied number of segments, concrete strength, and impact velocities on the responses of the segmental columns.

In this study, a detailed 3D model is built with the commercial software LS-DYNA (Hallquist, 2007). The accuracy of the numerical model is then verified against the available experimental impact testing results by Zhang et al. (2016b). The performances of segmental precast concrete columns under vehicle collision are then investigated. The main objectives of this study are as follows: (1) present an effective modelling method of the responses of PCSCs under impact forces; (2) numerically investigate the responses of PCSCs under vehicle collision; (3) carry out a parametric investigation of the effectiveness of different parameters including prestress level, number of segments, concrete strength on the behaviour of PCSCs to resist vehicle impact with different velocities.

5.2. Numerical calibration

5.2.1. Available impact test

The experimental tests on PCSCs by Zhang et al. (2016b) as illustrated in Figure 5-2 are used to calibrate the developed numerical model. The test results of the PCSC with five segments are presented and compared with the numerical results. The designs of the segmental column and the impact tests are briefly described in this section. Figure 5-2 shows the schematic view of the specimen and the experimental pendulum impact test setup. The overall dimensions of the testing column were 800 mm in height and 100 mm x 100 mm in cross-section area. The column consisted of five precast concrete segments with 160 mm in height of each segment. A 15 mm diameter hole was left at the centre of each segment for the prestress tendon when casting the segments. A footing of 140 mm deep and 400 mm x 400 mm in cross – section area was built to connect the segmental columns to the laboratory strong floor. A constant weight of 288 kg consisting of 400 mm x 400 mm x 450 mm (L x W x H) concrete block and 5 pieces of 23 kg steel plates was firmly fixed to the top of the column. The compressive strength and flexural tensile strength of concrete material were 34 MPa and 5 MPa, respectively. Each segment was reinforced with four 6 mm diameter longitudinal bars (f_y = 500 MPa) which were discontinuous between the segments. Four 4 mm diameter ties (f_y = 300

MPa) were utilised as shear reinforcements. The bottommost segment is connected to the footing by two 6 mm diameter starter bars. Seven–wire strands with 9.3 mm in diameter and of grade 1860 MPa were used as a prestress tendon with the barrel anchored inside the footing and the wedge placed on the top of steel plates. After finishing the installation of the column, a 30 kN force which was equivalent to 23.7% of the yielding capacity of the tendon was applied.

The pendulum impact testing system consisted of a steel frame, a pendulum arm, and a steel impactor. Two pieces of solid steel impactor with a total mass of 300 kg were connected to strong steel frame through the 2.8 m long pendulum arm. The pendulum impactor was lifted to a designated angle and then released to impact the centre of column in each test. The impact velocity was progressively increased in the test by lifting the pendulum to a higher position until the collapse of the column specimen. The angles were 2.5 degrees, 7 degrees, and 15 degrees which corresponded to the impact velocity of 0.23 m/s (Impact 1), 0.64 m/s (Impact 2), and 1.37 m/s (Impact 3).
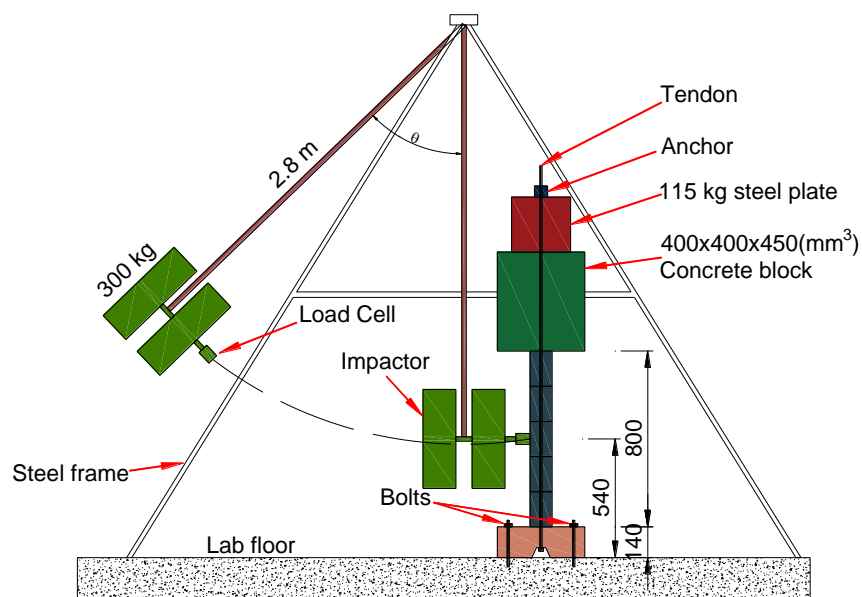
Figure 5-2 The pendulum impact test setup [Data from (Zhang et al., 2016b)].

5.2.2. Numerical simulation

5.2.2.1 Method of pre-stressing load

To apply the prestress load in a numerical model, many methods have been introduced in the literature. Li et al. (2017) modelled prestress on PCSCs subjected to blast load by applying a constant compressive load on concrete surface and a tensile force in the tendon. This pre-loaded force is applied by using LS-DYNA keyword card *LOAD_SEGMENT_SET with the pre-stressing load being unchanged during the whole response duration. Although this approach is easy and straightforward, it neglects the effect of tendon deformation and the

102

associated change in the prestress level in concrete structures during the dynamic response. Under intensive dynamic loading, the tendon is expected to experience large elongation because of large deformation of columns, which leads to an increase in the compressive force on structures. The latter method is not able to model the prestress variation during the dynamic response. Chen et al. (2015) modelled the response of prestressed concrete beam subjected to blast loading by using numerical simulation. The prestress on concrete beam was created by applying the initial hogging deformation at the mid-span of the beam. From the static analysis, the relationship between the prestress force and the initial hogging deflection of reinforced concrete (RC) beam is determined, which is applied to modify the beam initial geometry through the implicit analysis by using ANSYS. The response of the beam subjected to blast loading is then analysed using the explicit calculation in LS-DYNA. This method can solve the drawback of the former method reviewed above because the prestress variations are modelled with the beam deformation. However, the process of applying the initial hogging geometry to the beam model is tedious and time consuming. Moreover the initial deflection of RC beam is not straightforwardly calculated either if the prestress is not horizontal and uniform across the beam.

To overcome these problems, a temperature-induced shrinkage in pre-stressing strand offers a feasible solution (Jiang & Chorzepa, 2015; Nakalswamy, 2010). In this approach, the *DYNAMIC RELAXATION (DR) option is used to create the stress initialization process. The DR feature allows implementation of an explicit analysis before transferring the results to an implicit simulation (Hallquist, 2007). The ratio of current-to-peak distortional kinetic energy from applied prestress load will be checked every 250 cycles. The DR phase will terminate when the distortional kinetic energy has sufficiently reduced and the convergence factor is smaller than the defined tolerance value. The DR results then automatically proceed to the transient analysis phase. To optimise the converged results, the convergence tolerance can be defined by users (default value: 10^{-3}). The smaller value of the tolerance results in converged solution closer to the steady stage but it required longer computing time. In this study, the value of convergence tolerance is used at 10^{-5}. It should be noted that a damping coefficient must be designated in the DR to achieve converge of the DR results (Hallquist, 2007). For concrete structures, the damping coefficient normally ranges from 0.02 to 0.05 (Hesam et al., 2016; Hesameddin et al., 2015; Papageorgiou & Gantes, 2008). As a result, the value of 0.05 is used for the damping coefficient to converge the DR results.

The LS-DYNA material card *MAT_ELASTIC_PLASTIC_THERMAL (MAT_004) is used for defining the relation between material property of tendon and temperature. Following this material, *LOAD_THERMAL_LOAD_CURVE card is used for defining the time dependence of temperature through initial phase and explicit phase. LS-DYNA requires two

time-temperature curves for this option. The first curve is for dynamic relaxation phase (implicit analysis), where the temperature decreases suddenly from the reference temperature to the defined temperature and then levels off. The second time-temperature curve is kept constant for an explicit phase. An example of these two curves is shown in Figure 5-3.
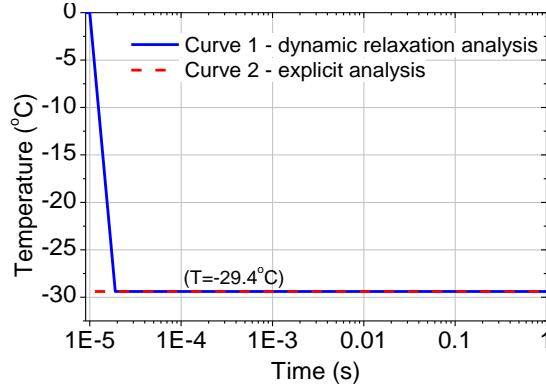

Figure 5-3 Temperature versus time curves.

To better understand this prestress method, a simple concrete block and a tendon located at the middle are employed as an example to illustrate the procedure. Figure 5-4a shows the un-bonded tendon is placed inside the concrete block with the top anchor being connected to the tendon for creating the pre-stressing load. The contact algorithm named Automatic_surface_to_surface (ASTS) is used to define a contact between the anchor and the concrete block. With this feature when the tendon is shortened by the dropping of temperature, the tensile force is created in the tendon and the compressive force is generated simultaneously in the concrete block. The total deformation of concrete and tendon is equal to the deformation of the tendon when the temperature drops without any restraint, which is illustrated by Figure 5-4b.

The deformations of the concrete block and tendon can be equated as follows:

$$\Delta L_C + \Delta L_{Te} = \Delta L_T \tag{5-1}$$

where ΔL_C is the shortening of the concrete element, ΔL_{Te} is the elongation of tendon element, and ΔL_T is the shortening of the tendon when the temperature drops without contact force.

The compatibility of strain between concrete and tendon is therefore written by Eq. (5-2a).

$$\varepsilon_c + \varepsilon_{Te} = \varepsilon_T \tag{5-2a}$$

Or
$$\frac{f}{A_c E_c} + \frac{f}{A_s E_s} = \Delta T \times \alpha \tag{5-2b}$$

104

where ε_c is the strain of the concrete, ε_{Te} is the strain of the tendon when the temperature drops with anchor plate and concrete block, ε_T is the strain of the tendon when the temperature drops without any restraints, f is the pre-stressing force, A_s and E_s are cross section area and elastic modulus of tendon, respectively, A_c and E_c stand for the corresponding measures of concrete, ΔT is the change of temperature, and α is the thermal expansion coefficient of tendons.
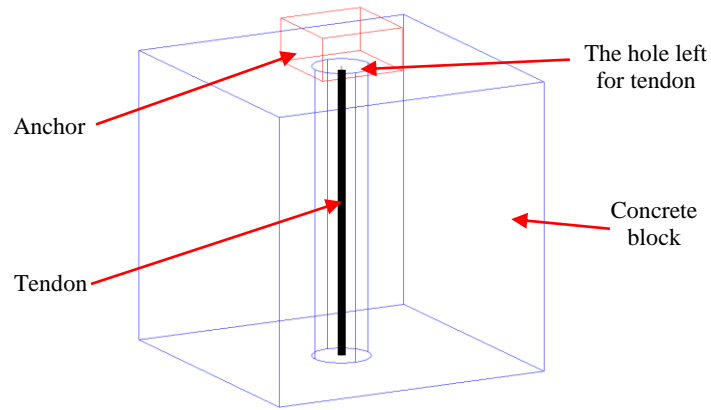
(a) Single concrete element for un-bonded prestress tendon
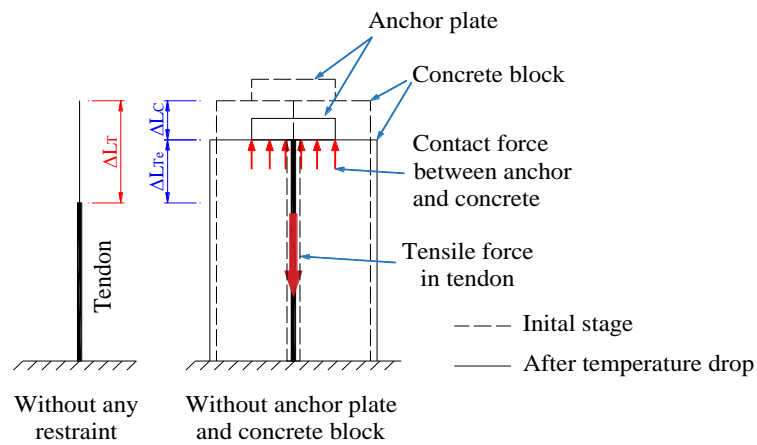
(b) Deformation of tendon when temperature drops

Figure 5-4 Illustration of the proposed method for application of un-bonded prestress in concrete structures.

From the expected pre-stressing force, the change of temperature, ΔT , can be obtained by the following equation:

$$\Delta T = \frac{f}{\alpha} \left(\frac{1}{A_c E_c} + \frac{1}{A_s E_s} \right) \tag{5-3}$$

105

5.2.2.2 Constitutive model of materials

There are various types of material models available for modelling concrete material subjected to blast and impact loads in LS-DYNA such as *Mat_Winfrith_Concrete (MAT_084-085), *Mat_CSCM_Concrete (MAT_159), *Mat_Concrete_Damage (MAT_072), and *Mat_Concrete_Damage_rel3 (MAT_072R3), etc. In this study, the MAT_072R3 material model is selected for the simulation of concrete material where strain-rate effect, plasticity, and shear failure damage are taken into consideration. The accuracy of this model in simulating the performance of concrete structures under extreme dynamic loading has been verified in many previous studies, e.g. (Li et al., 2017; Pham & Hao, 2017a, 2017b). The unconfined compressive strength of concrete is an important input parameter of this material model when the remaining parameters can be generated automatically from that value. It is worth mentioning that the generated material parameters can also be modified by users. In this study, the unconfined compressive strength of concrete material is 34 MPa.

For the steel reinforcements, an elastic-plastic material model named *Mat_Piecewise_Linear_Plasticity (MAT_24) is utilised, in which the failure based on the plastic strain, the stress – strain curve and the strain rate scaling effect on steel yield stress can be defined. In the present study, the steel yield strength, mass density, Young's modulus, strain rate curve and stress – strain curve are defined, which will be given below. *Mat_Elastic_Plastic_Thermal (MAT_004) is used to model the prestress tendon. The relationship between the material properties versus temperature needs to be defined. This material model requires a range of temperature input data larger than the expected change of temperature. It is defined by *Load_Thermal_Load_Curve card in LS-DYNA. Besides, the LS-DYNA material model named *Mat_Elastic (MAT_001) is employed to model the steel pendulum impactor. The input parameters of these materials are given in Table 5-1.

The LS-DYNA keyword *Mat_Add_Erosion is utilised to eliminate the damaged concrete elements which are no longer contributing to resisting the impact force. The erosion feature in LS-DYNA is important in studying the impact and blast response of RC structures, and has been commonly adopted in the previous studies (Chen et al., 2015; Jiang & Chorzepa, 2015; Li & Hao, 2013, 2014). In the explicit simulation, the concrete elements will be automatically removed when the tensile stress reaches the defined erosion tensile strength or the erosion principal strain. It should be mentioned that if the erosion principal strain defined by users is too high, large deformation of concrete elements may cause computation overflow. If this value is too low, the conservation of energy and mass will not be maintained, the analysis results are therefore no longer trustworthy (Li & Hao, 2013). The value of 0.9 is used for the erosion criterion of concrete material in the present study after trials to yield fairly good agreement with the experimental results. Similarly, an effective plastic strain of steel

106

reinforcements is defined to erode excessively deformed reinforcement elements. In this study, when the plastic strain of steel material reaches 0.18, the element is eliminated from the analysis.

Table 5-1 Material properties of numerical model.

Element	LS-DYNA model	Input parameter	Magnitude
Concrete	* Mat_072R3	Mass density	2400 kg/m³
		Unconfined strength	34 MPa
Tendon	* Mat_Elastic_Plastic_Thermal	Mass density	7800 kg/m³
		Young's Modulus	210 GPa
		Poisson's ratio	0.3
		Yield stress	1860 MPa
		Plastic hardening modulus	1200 MPa
		Thermal expansion coefficient	10^{-4}
Rebar	*Mat_Piecewise_Linear_Plasticity	Mass density	7800 kg/m³
		Young's Modulus	210 GPa
		Poisson's ratio	0.3
		Yield stress	500 MPa
Stirrup	*Mat_Piecewise_Linear_Plasticity	Mass density	7800 kg/m³
		Young's Modulus	210 GPa
		Poisson's ratio	0.3
		Yield stress	300 MPa
Impactor	*Mat_Elastic	Mass density	7800 kg/m³
		Young's Modulus	210 MPa
		Poisson's ratio	0.3

5.2.2.3 Strain rate effect

Strain rate effects of material models have been given in the previous section, please refer to Section 2.2.2.3.

5.2.2.4 Contact definition

The commercial software LS-DYNA has introduced some contact algorithms for users to simulate the contact among the parts of numerical model such as kinematic constraint method and the penalty method (Hallquist, 2007). Among these contact algorithms, the penalty method employed via the contact keyword namely AUTOMATIC_SURFACE_TO_SURFACE (ASTS) becomes popular and it has proven yielding reliable results (Dogan et al., 2012; Sha & Hao, 2013). However, this method is complicated in term of evaluating the contact stiffness which is based on bulk modulus, the area of the contact zone, the volume of the contact elements, the penalty scale factor and the scale factor (Hallquist, 2007). LS-DYNA normally

suggests the default value for penalty scale factor of 0.1 and the scale factor 1.0. Nevertheless, if the stiffness of the two parts in the contact is significantly different, the stiffness of the softer part is taken as the contact stiffness as the default choice. The default may not yield reliable results due to an excessively small stiffness. The scale factor can be, therefore, manually defined by users to modify the stiffness of two parts to make them compatible. The scale factor and friction coefficient of the contact algorithm used in this study are given in Table 5-2. Besides, perfect bond between reinforcing steel reinforcement, stirrups, and surrounding concrete is assumed in this study.

Table 5-2 Contact parameters.

Contact components	Keyword	Input parameter	Value
Concrete segments	ASTS	Static coefficient of friction	0.60
		Scale factor of slave penalty stiffness	0.10
		Scale factor of master penalty stiffness	0.10
Tendon and concrete segments	ASTS	Static coefficient of friction	0.00
		Scale factor of slave penalty stiffness	1.00
		Scale factor of master penalty stiffness	1.00

5.2.2.5 Finite element analysis model

A 3D non-linear finite element (FE) model of the scaled PCSC under pendulum impact test described in Section 5.2.1 is created in LS-DYNA, as illustrated in Figure 5-5. Both the concrete column and pendulum impactor are represented by hexahedral elements with one integration point. 3-nodes beam element with 2x2 Gauss quadrature integration is employed to model the longitudinal reinforcing steel bars and stirrups. A convergence test is also carried out to determine the optimal element size. The results indicate that the simulation converged when the mesh size of concrete element and reinforcement steel is 5 mm. Further decrease in the element size only has a slight variation of the numerical results but requires much longer computing time and may lead to computer memory overflow. The concrete segments, reinforcing steel bars and stirrups, therefore, have the mesh size of 5mm. The maximum mesh size for the impactor and top concrete block is 50 mm. In this study, the 3D FE model has 126,407 elements consisting of 124,247 solid elements and 2,160 beam elements. To prevent the initial penetration between pendulum impactor and concrete segments, the initial distance between these parts is assigned to be 2.5 mm.

According to the material properties of tendon element introduced in Section 5.2.2, the pre-stressing force of 30 kN was applied in the test, which is modelled here with a temperature drop of 29.4°C with respect to the reference temperature of 0°C. The temperature of the tendon then remains unchanged throughout the explicit simulation phase of the response of column subjected to impact forces (see Figure 5-3).
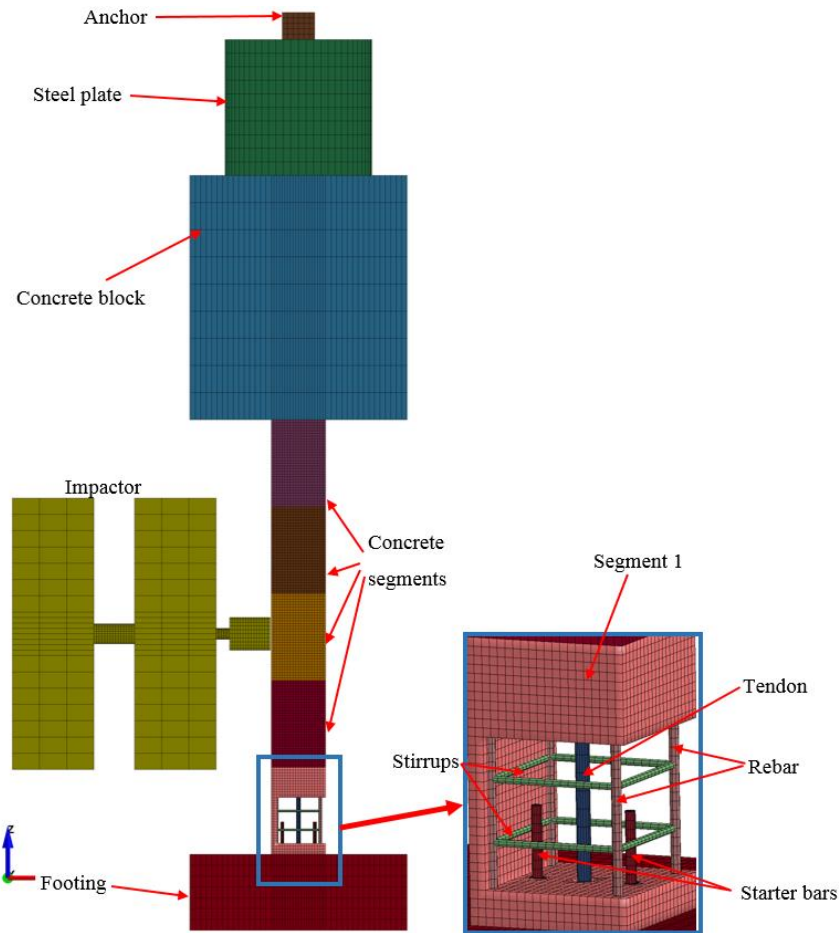
Figure 5-5 Numerical model of the PCSC with pendulum impactor.

In the experimental tests, the column foundation was anchored to laboratory floor through four bolts. No vertical and horizontal displacement or rotation at the base was recorded during the test (Zhang et al., 2016b). To represent the actual boundary condition, all of the nodes on the bottom face of the footing are constrained in all directions in the numerical model.

5.2.3. Model calibration and comparisons

To validate the accuracy of the FE model in predicting the column responses to pendulum impact, the time histories of resultant impact force in the contact area, displacement at the centre of the column and damage to the column by pendulum impact are compared in this section.

In the first impact test, the velocity of the pendulum impactor at the time in contact with column was 0.23 m/s (Impact 1). The comparison of impact force time histories between numerical simulation and experimental test is shown in Figure 5-6a. It can be seen from the figure that the numerical results agree reasonably well with the experimental test. The peak impact force and its duration in FE model are 8.29 kN and 28 ms compared to 7.30 kN and 40 ms in the experimental test, respectively. The corresponding impulse from the FE simulation

and experimental tests are 117 Ns and 141 Ns, respectively. The relatively large difference between the loading duration from the FE simulation and experimental test is because only two peaks are simulated while three peaks were recorded in the test. The third peak recorded in the test was caused by a repeated impact from the impactor, i.e., the pendulum rebounded and impacted on the column again. Although the third impact force is relatively small, it led to a larger column response as shown in Figure 5-7.

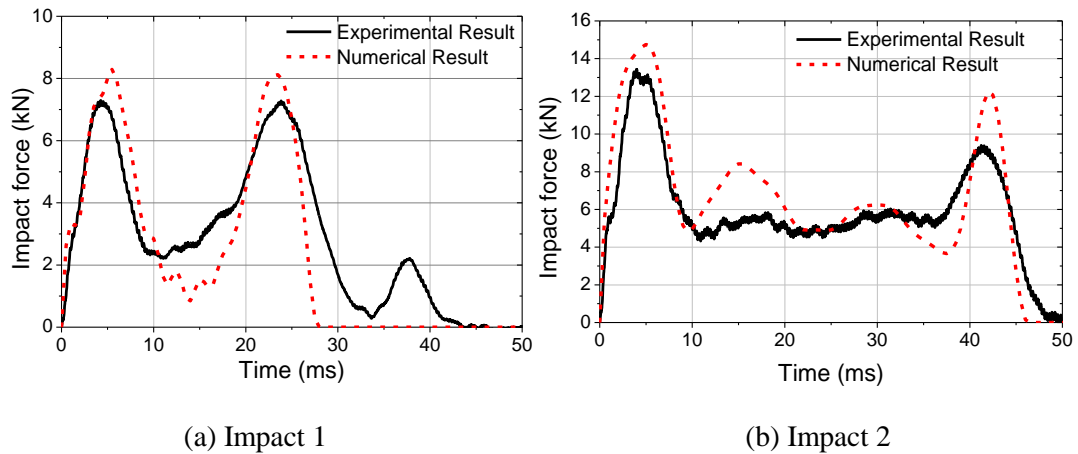(a) Impact 1   (b) Impact 2

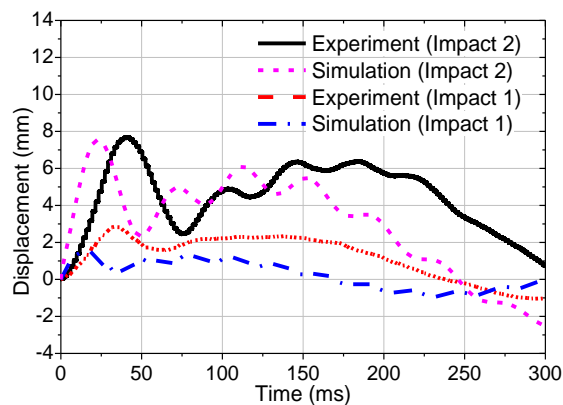Figure 5-6 Model verification – simulation and experiment: Impact force time histories.

Figure 5-7 Model verification – Displacement at the centre of the column.

To prevent this repeated impact, in the subsequent tests, a steel beam was used, which was quickly inserted into the steel frame when pendulum rebounded to stop it impacting the column specimen again. When the release angle was 7 degrees the impact velocity was 0.64 m/s (Impact 2), the impact force time history predicted by the FE model again compares well with the experimental result as shown in Figure 5-6b. The peak impact force, duration and impulse in the numerical model are 14.76 kN, 46 ms and 327.6 Ns while those in experimental test are 13.44 kN, 48 ms and 300 Ns, respectively. Figure 5-7 compares the numerical simulated and recorded displacement time histories at the centre of column. As shown although the difference in the maximum displacement from Impact 1 is observed because of the repeated impact as explained above, the global trend of two curves is in good agreement. Comparison of the

110

displacement time histories of Impact 2 shows better agreement because the repeated impact as discussed above was prevented in the test. The maximum displacement obtained from numerical simulation agrees well with the recorded maximum displacement. Because the impact forces in these two tests are relatively small, no concrete damage is observed in both the experimental test and numerical simulation.

When the impactor was released at 15 degrees in Impact 3, the impact velocity was 1.37 m/s, the FE analysis results and testing results are compared in Figure 5-8. It is very clear from Figure 5-8a that after the first peak impact force occurred owing to the interaction between the impactor and the column, another four peak impact forces were recorded in both numerical simulation and experimental test with the same period (about 20 ms). This observation can be attributed to the high-frequency concrete segment vibration. As shown in Figure 5-9, while the top of the column vibrates around its original position, the response of the five concrete segments consists of the segment-self vibration and the column vibration. The natural frequency of the concrete segment is considerably higher than that of the column with five segments. For example, the vibration period of a single segment was 40 ms while that of the column was more than 200 ms from the displacement response time history shown in Figure 5-9a. It should be noted that the vibration period of concrete segment will be reduced when the impact energy increases because of the change of boundary condition caused by relative slippage between segments. When the impact velocity was 1.37 m/s, the slippage between the concrete segments occurred and it affected the stiffness of the concrete segments. As a result, during Impact 3, the vibration period of the segment is reduced to around 20 ms (see Figure 5-9b). This vibration of the concrete segment in contact with the impactor resulted in the four peaks in the impact force time history at 20 ms, 42 ms, 63 ms, and 83 ms shown in Figure 5-8a. During the impact event the impact force will increase if the impactor and the impacted segment tend to move towards each other and it will decrease if the two parts tend to move together in the same direction. Further investigation in Figure 5-9b shows that the segment-self vibration has a period approximately of 20 ms which matches well with the period between the peaks in Figure 5-8a. It is noted that the instants of peak impact force shown in Figure 5-8a and the peak displacement shown in Figure 5-9b coincide with each other. The peak impact force and impact duration in FE model are 20.70 kN and 93 ms, which compared well to 20.91 kN and 93 ms in the experimental test (see Figure 5-8a). The impulse predicted from the numerical model is 537.4 Ns which is just 3.7% less than that of the experimental test (about 557.8 Ns).
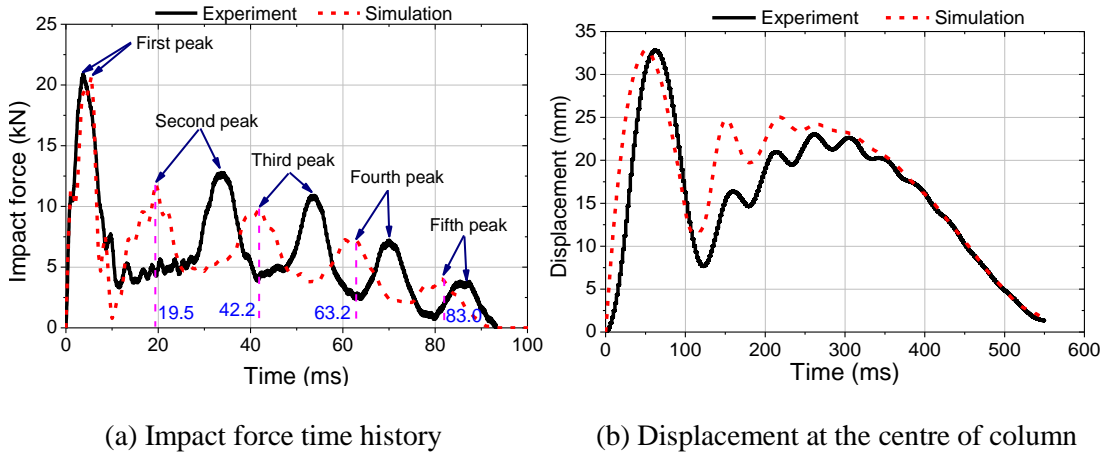
(a) Impact force time history

(b) Displacement at the centre of column

Figure 5-8 Model verification – simulation and experiment: Impact 3.
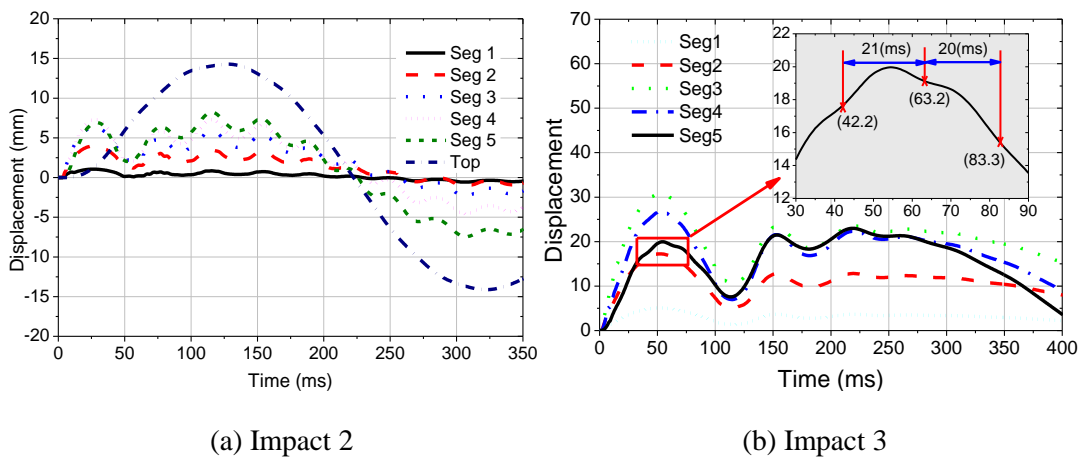

(a) Impact 2

(b) Impact 3

Figure 5-9 Displacement time histories by numerical simulation.

In terms of the displacement time history at the centre of column, the maximum values from the two models agree very well with 32.75 mm from the numerical simulation and 32.80 mm from the experimental test (see Figure 5-8b). Although, a faster displacement response can be found in the numerical model compared to experimental test (about 18 ms) due to a faster peak impact force, the global trends of the displacement response histories from numerical simulation and experimental test are in good agreement. Figure 5-10 shows the comparison of numerical and experimental column deformation and damage corresponding to the impact velocity of 1.37 m/s at different time instants. As shown the damage at the top left corner of Segment 3, the relative shear slip and joint opening between Segments 3 and 4, and the joint opening at the base are well simulated in the numerical model.

The above observations and comparisons indicate that the numerical model reliably predicts impact response of the PCSC. The current FE model also has the ability to capture the opening between segments, shear slip, local damage, plastic deformation and failure modes of the column.
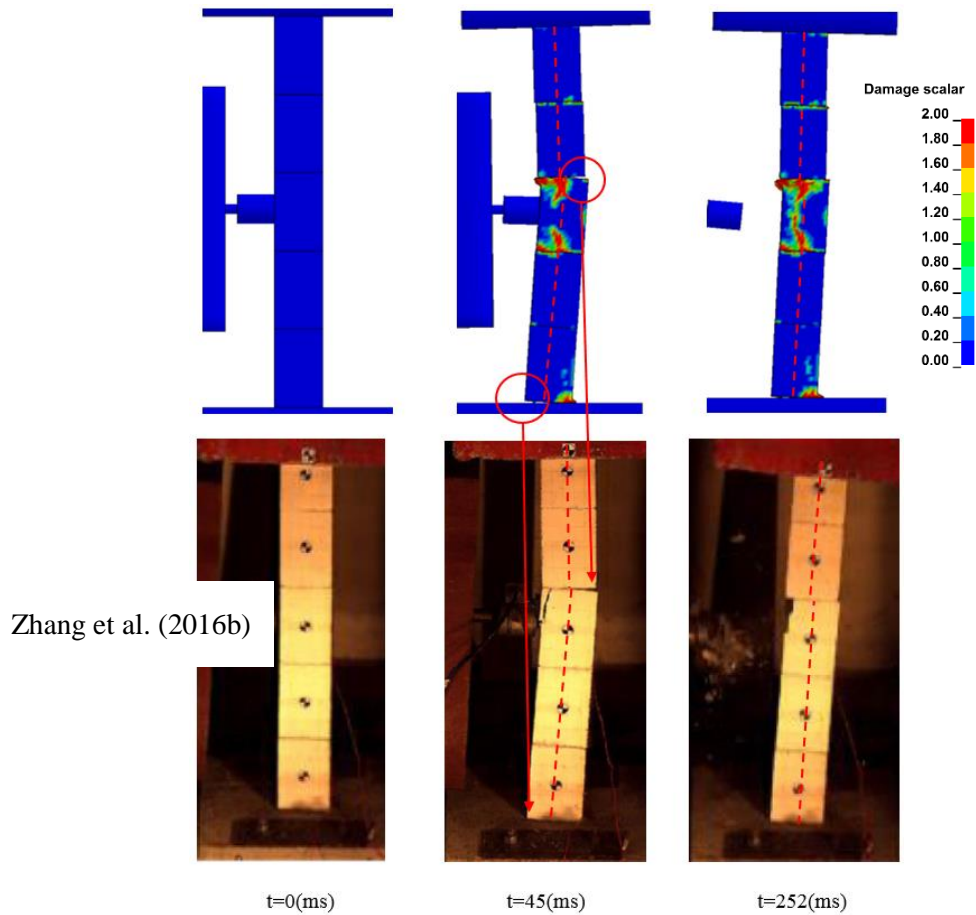
Figure 5-10 Progressive damage of the column under Impact 3.

5.3. Numerical results and parametric study

Using the same material models, strain rate relations of concrete and steel, prestressing method, and contact definitions, the above calibrated model is extended to create a full-scale model of a PCSC. The configuration of the column is presented in Figure 5-11. The dimensions of the column are 600 mm in depth, 600 mm in width, and 4800 mm in height. The top concrete block and steel plates in the test are replaced by a console beam placed on the top of the column. The size of the footing used in this model is 2600 mm x 2600 mm x 1000 mm. The design dead load is equal to 10% of the axial compressive capacity of the column ($0.1f'_cA_g$), where f'_c is the concrete compressive strength, and A_g is the gross cross-section area of the column. Four post-tensioned tendons (25 mm in diameter) are employed in the full-scale model and placed at the four corners of the column. The total area of four tendons is 1974 mm^2 with the initial prestress load equal to $0.36f_u$, where f_u is the tensile strength of the tendons. It is equal to $0.11f'_cA_g$. The hole left for the tendon is 35 mm in diameter. The compressive strength of concrete as well as the tensile strength of the tendon and reinforcing steel bars are the same as those previously presented. According to the convergence test, the smallest mesh size of the solid elements used in the model is 20 mm. The maximum mesh size for the top

concrete beam is 100 mm. In this study, the 3D segmental bridge column model has 301,978 elements consisting of 290,036 solid elements and 11,942 beam elements.
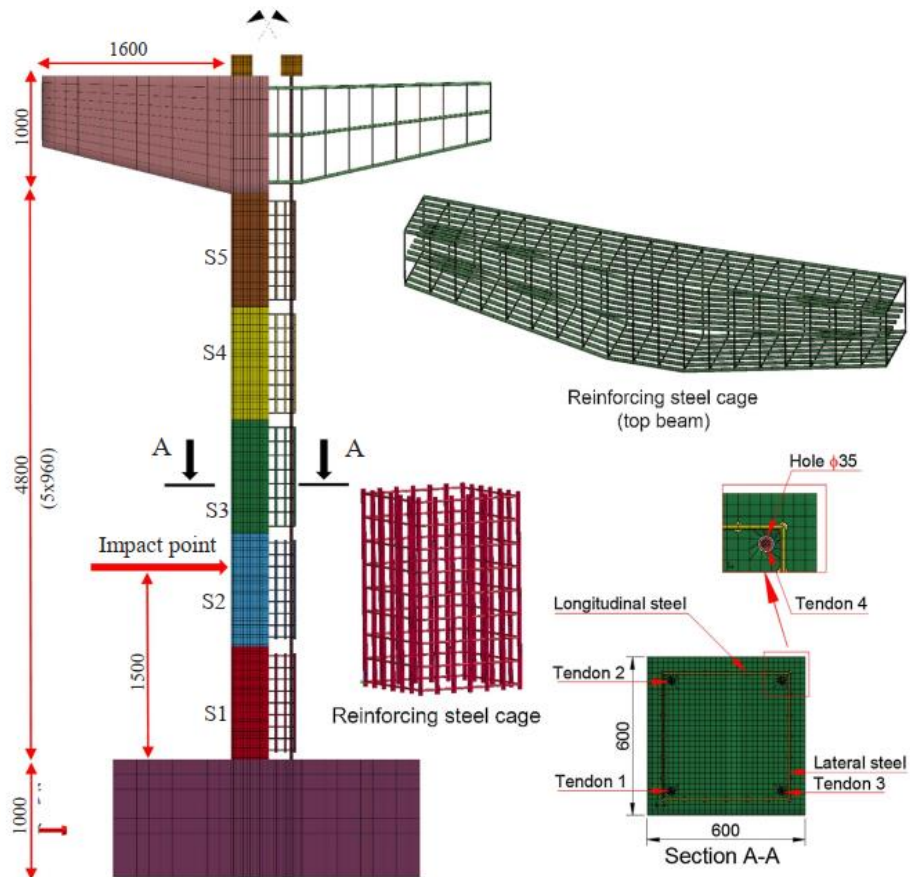

Figure 5-11 The configuration of the PCSC (reference case – C0).

The solid steel impactor is replaced by a 3D vehicle model with 216,400 elements and 220,499 nodes, representing the 1129 kg 1998 Chevrolet S10 pickup (Figure 5-12). This vehicle model was downloaded from National Highway Traffic Safety Administration (NHTSA). The accuracy of the vehicle model has been validated by FHWA/NHTS National Crash Analysis Centre at the George Washington University. According to the AASHTO (2012), the impact point locates at 1.5 m above the top of the footing in the simulation (Figure 5-11).
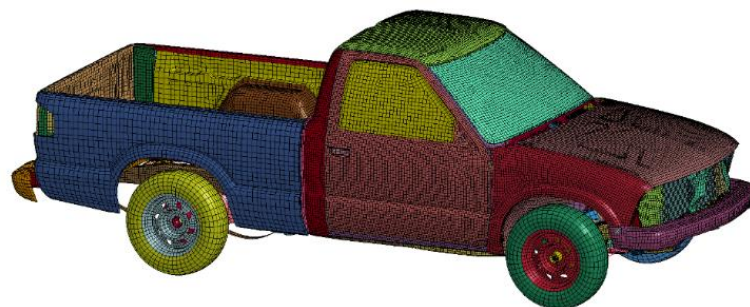

Figure 5-12 1998 Chevrolet S10 pickup FE model.

Under the impact of a Chevrolet S10 pickup at the velocity of 70 km/h, the calculated impact force time history on the PCSC is presented in Figure 5-13a. As shown, after gradually increasing to around 300 kN, the vehicle's engine collides with the column at $t = 30$ ms (see Figure 5-13b and Figure 5-13c) and it generates the peak impact force of 1861.5 kN ($t = 35.5$ ms). The impact force then significantly decreases to about 250 kN at $t = 40$ ms before reducing to zero at $t = 160$ ms. The impulse of the impact force is 22.96 kN.s.
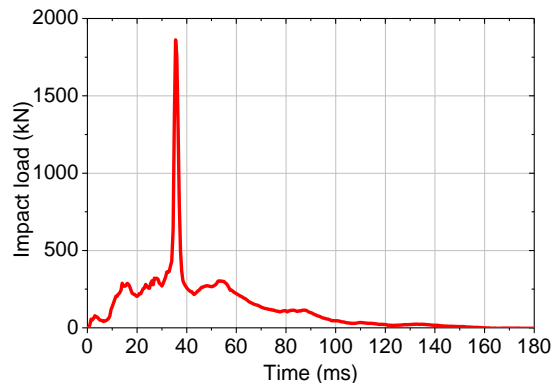
(a) Time history of the impact force
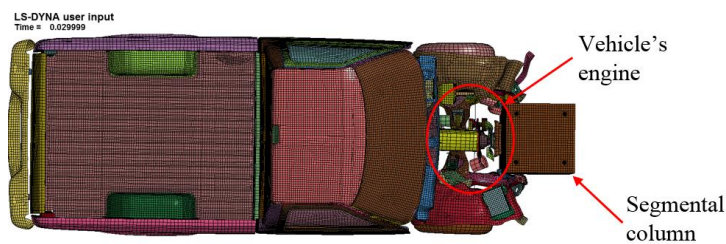
(b) Vehicle's engine starts to collide the column (t = 30 ms)
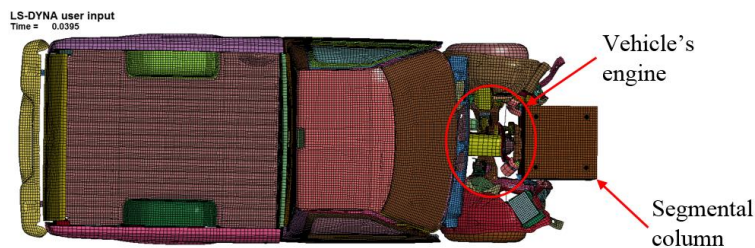
(c) After vehicle's engine hits the column ($t = 39.5$ ms)

Figure 5-13 Vehicle collision between the PCSC and Chevrolet S10 pickup.

The progressive deformation, displacement and damage to the PCSC and the vehicle are shown in Figure 5-14. After the impact force has reached the peak, the relative lateral shear slips between the impacted segment and its adjacent segments are observed. As shown in Figure 5-14b, at $t = 40$ ms the relative lateral displacement between Segment 2 (impacted segment – S2) and S1, between S2 and S3 are 17.7 mm and 6.4 mm, respectively. The slip between S1 and footing is 5mm. The relative displacements between the other segments are

also observed, as illustrated in Figure 5-14b. It could be explained that under high rate impulse load, the local response or shear deformation governs the behaviour of the PCSC while the friction force between the segments resulted from the initial pre-stressing load and the self-weight of the column is insufficient to resist the shear force. It leads to the lateral shear slips between the segments in the PCSC. Moreover, the relative displacement between the impacted segment and its adjacent segments is larger than the other segmental joints. The column then continues deforming to reach the maximum positive displacement at $t = 221$ ms and the maximum negative displacement at $t = 491$ ms. As can be seen in Figure 5-14c, when the base stops moving at the residual displacement of 9 mm, the other parts of column continues vibrating freely around the residual displacement of 25 mm. The 25 mm diameter tendon is placed inside the 35 mm posttensioning duct of the segments. There is, in general, a nominal gap of 5 mm between tendons and each side of the concrete segments. The total gap between tendon and concrete segment is 10 mm. Therefore after suddenly sliding 5 mm at 50 ms due to the impact force, the bottommost segment is in contact with the post-tensioned tendon. Both the concrete segment and tendon then slide with a continuous motion to the maximum value of 9 mm. For Segment 2, the contact force between concrete segments and the tendon is insufficient to resist the huge direct shear force from the vehicle collision. Hence, before ceasing the sliding of Segment 2 at 17.7 mm (35 ms), concrete damage is found in the duct of the segment. The relative displacement of Segment 2 with respect to the footing is about 27 mm. After the loading phase (160 ms), the contact force from the tendon is inadequate to pull the segments back to the original position and thus the relative lateral displacement between the concrete segments is nearly unchanged (see Figure 5-14b). The column, as well as the concrete segments then vibrates freely around their residual position. With the effect of the large inertial resistance force and located at a distance from the impact point, the column top responds slower than the other parts in the first stage of impact event (Figures 5-14b and c).
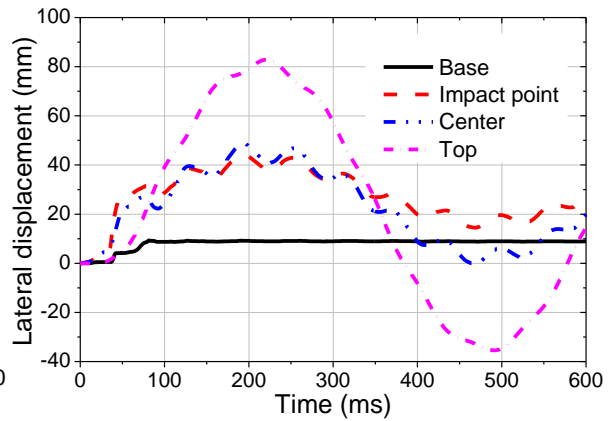
The pre-stressing force histories of the four tendons are shown in Figure 5-15. The prestress level in the tendons nearly remains stable (335.6 kN) before the vehicle's engine impacts to the column. After that, due to the huge impact force from the collision, the opening at the second joint and the large shear slips between the segments appear. The prestress forces slightly increase in the two tendons on the tension-side (Tendons 3 and 4) and and those in the compression side (Tendons 1 and 2) decrease. The prestress force then vibrates around its initial stress level with a minor prestressing loss (1%) being recorded. At the time the column top reaches the maximum lateral displacement, the prestress force reaches the highest value of 382.2 kN, about 14% higher than the initial stress level. It is worth mentioning that these changes in the tendon stresses cannot be monitored if the other methods reviewed above are used to model the pre-stressing of concrete structures.

(t=5ms) (t=50ms) (t=100ms)

(t=200ms) (t=400ms) (t=600ms)
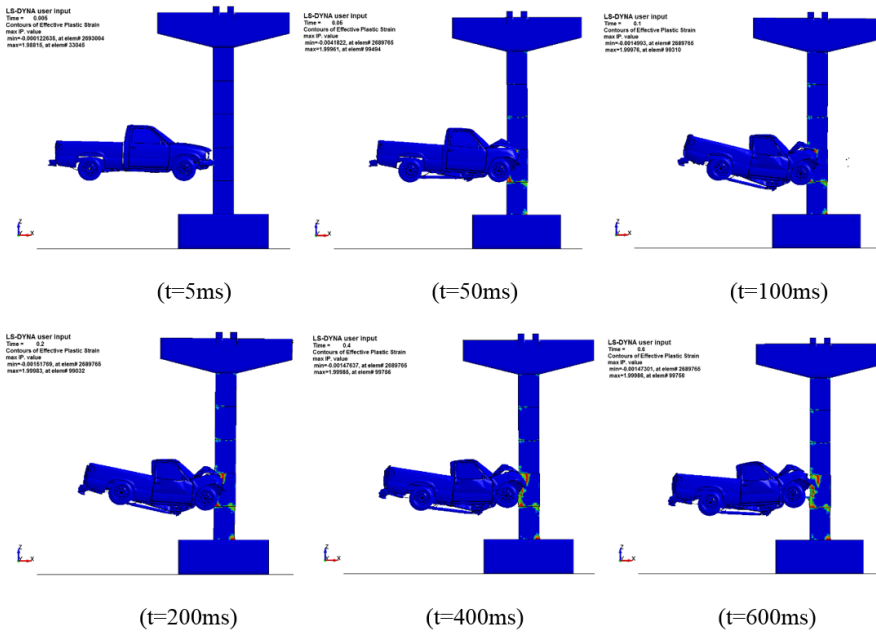
(a) Progressive collision between Chevrolet S10 pickup and the PCSC
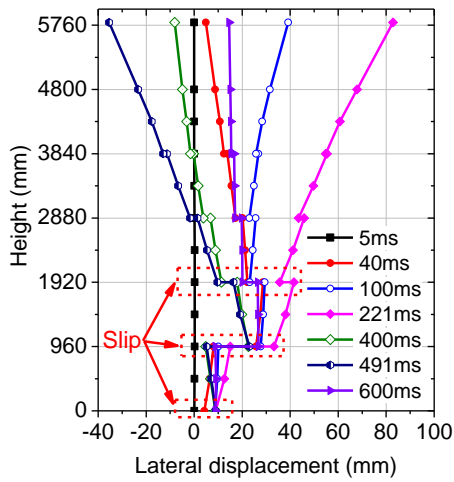
(b) Column displacement

(c) Time histories of displacement

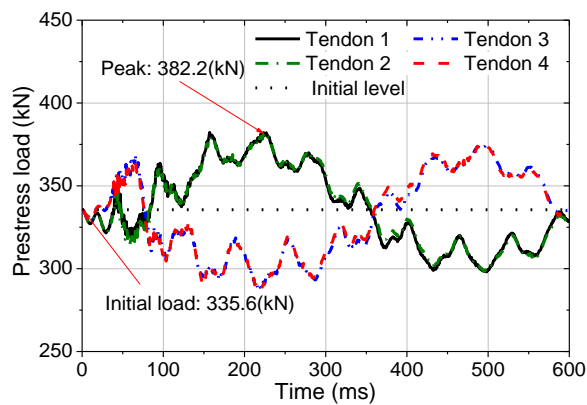Figure 5-14 Response of the PCSC under 70 km/h vehicle collision.

Figure 5-15 The prestress load time history in four tendons.

To further investigate the impact response of the PCSCs, a series of simulations are carried out to study the effect of the vehicle energy and column parameters on the column responses. These include the initial pretress level, number of segments, reinforcing steel ratio, and impact energy.

5.3.1. Effect of initial pre-stressing load

The behaviour of PCSCs under vehicle collision with different initial prestress levels including $0.089f'_cA_g$ (PL30), $0.11f'_cA_g$ (C0 and PL60_2), $0.15f'_cA_g$ (PL50), and $0.2f'_cA_g$ (PL60_1) is studied in this section. The description of these cases is given in Table 5-3. The initial compressive stress on concrete is varied from 9% to 18% of the column's capacity as indicated in Table 5-3.

Table 5-3 Input parameters of the PCSCs with different initial pre-stressing loads

Column	Tendon				Initial prestressing load		
	Diameter	Area	Total areas	$\%f_u$	Load	Total load	$\%f_cA_g$
	mm	mm^2	mm^2		kN	kN	
C0	25	490.9	1963.5	36.6	334.2	1336.7	10.9
PL30	25	490.9	1963.5	30.0	273.9	1095.6	9.0
PL50	25	490.9	1963.5	50.0	456.5	1826.1	14.9
PL60_1	25	490.9	1963.5	61.2	558.8	2235.1	18.3
PL60_2	20	314.2	1256.6	61.6	360.0	1440.0	11.7

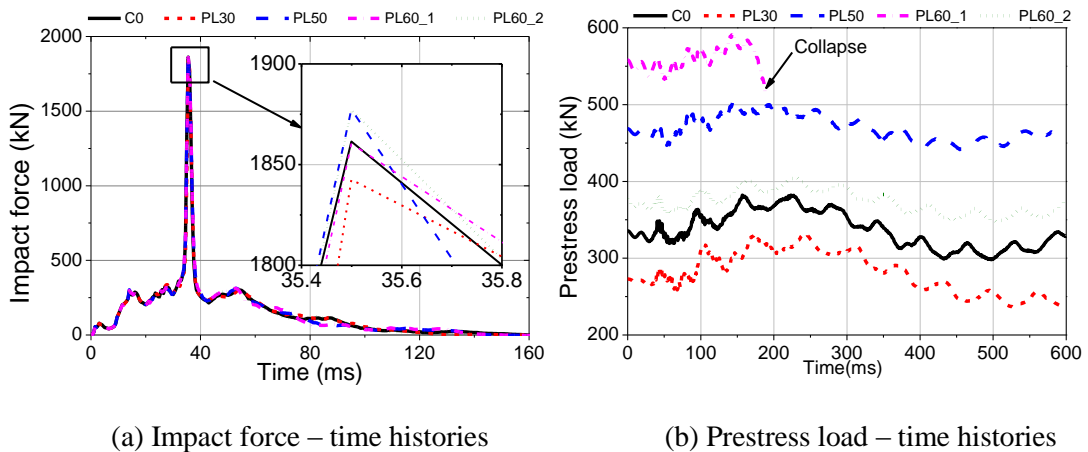(a) Impact force – time histories (b) Prestress load – time histories

Figure 5-16 The time histories of the impact force and prestress force corresponding to the different initial prestress levels.

As presented in Figure 5-16a, the impact force time histories of these columns show very small differences. The peak impact force of Column PL30 is 1842.6 kN, which is just about 1.5% and 1.8% smaller than that of Column PL60_1 (1860.4 kN) and Column PL60_2 (1877.5 kN), respectively. The impact duration of Column PL30 (167 ms) is slightly longer than that of Column PL60_1 (150 ms). Similar impulses are also recorded in the five columns

118

(approximately 23.0 kNs). This observation can be explained that under impact conditions, the impact force and impulse depend primarily on the initial impact energy and the concrete column – impactor interaction (Pham & Hao, 2017b) , which depends on the local stiffness at the beginning stage of the impact event (Fujikake et al., 2009). The change of the initial stress level enhances the strength and initial stiffness of PCSCs (Dawood et al., 2014), i.e., the global stiffness of the column, but has no effect on the local contact stiffness. As a result, the increase of prestress level does not have noticeable influences on the impact force of the PCSCs. The numerical results of these columns are presented in Table 5-4. Conversely, the initial prestress level is significantly important to the deformation of the PCSCs. Higher initial axial stress on the concrete column leads to enhancement of the friction force between the concrete segments and thus improves the shear strength of the column. As a result, the relative lateral displacement between the segments is reduced. As can be seen in Figure 5-17, the relative shear slip at the base is about 13 mm, and that between the impact point of Column PL30 and the footing is around 37 mm. The corresponding results of Column PL50 are only 6 mm and 20 mm, respectively. Besides, the column with higher initial prestress force leads to smaller lateral displacement than the counterparts (see Figure 5-17). However, when the initial axial load on concrete increases to $0.183 f_c' A_g$ (PL60_1), due to high compression stress from the initial axial load and the collision, severe concrete damage at the base of column is found at 180 ms and leads to the column collapse. These results demonstrate that a balance of the prestress force level needs be carefully determined. A larger prestress level is generally desirable provided it does not cause premature failure of the column when acted together with the impact load.

Interestingly, with different pretressing levels in the tendons but similar axial compression load on concrete, Columns C0 and PL60_2 show the same response to vehicle collision (Figure 5-17). The detailed comparisons are presented in Table 5-4. This is because the tendons are still in its elastic range at these different prestressing levels.
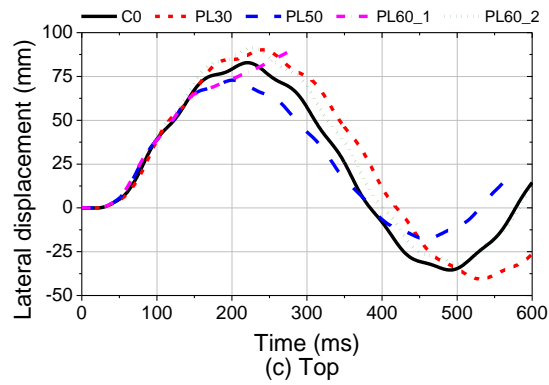

(a) Base   (b) Impact point
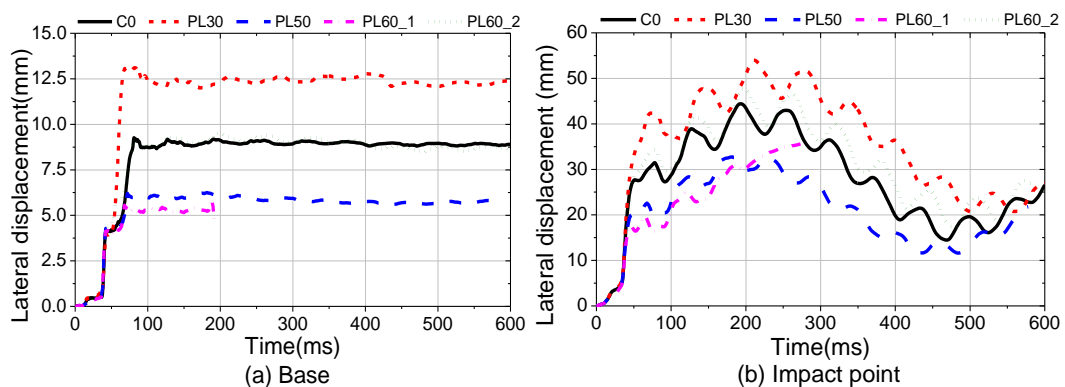
Figure 5-17 Displacement time histories of the column with varied initial prestress levels.

Figure 5-16b shows the prestressing force time histories in the tendons. With larger lateral displacement, the increase of prestressing force in the tendon of Column PL30 is, therefore, higher than the other columns. The peak prestressing force in the tendon of Column PL30 (332 kN) is about 22% higher than the initial prestress load (273.9 kN). That result reduces to 12% in Column C0, 8% in Column PL50, and 6% in Column PL60_2. Because of the damage and failure of Column PL60_1 at $t = 180$ ms, the prestress load in the tendon then plummets.

Table 5-4 Comparisons of the column responses with different initial prestress levels

Parameter			PL30	C0	PL50	PL60_1	PL60_2
Impact force	Peak	kN	1842.6	1861.5	1877.4	1860.4	1877.2
	Duration	ms	167.0	160.0	147.0	150.0	159.5
	Impulse	kNs	22.8	23.0	22.9	23.0	22.8
Shear slips	Joint 1	mm	9.6	8.9	6.3	--	8.9
	Joint 2	mm	23.8	17.0	11.4	--	18.0
	Joint 3	mm	13.2	6.6	4.6	--	6.1
Maximum displacement	Top (positive)	mm	90.2	82.8	72.9	--	91.5
	Top (negative)	mm	-40.5	-35.4	-17.7	--	-33.0
	Centre	mm	54.0	44.4	32.7	--	46.0
Peak prestress load		kN	332.0	382.2	504.9	--	405 .0

5.3.2. Effects of number of segments

In this section, numerical simulations are conducted to study the effect of number of segments on the responses of PCSCs under vehicle collision. Four segmental columns of the same height, but with different number of segments are employed in the analysis. They are designated as NOS2 (2 segments), NOS4 (4 segments), C0 (5 segments), and NOS8 (8 segments). The same 1998 Chevrolet s10 pickup with velocity of 70 km/h is considered in the analysis. As shown in Figure 5-18, although the column with more segments has smaller peak impact force and longer impact duration because it is more flexible, the differences in the impact force are marginal and the impulses are almost identical (see Table 5-5). This is because, as discussed in the previous section, the impact force highly depends on the contact

stiffness between the impactor and the concrete segment. Changing the number of segments mainly changes the global stiffness of the columns (Zhang et al., 2016b) but does not affect the contact stiffness. Moreover, as can be seen in Figure 5-19a, the column has not experienced large displacement response during the impact force phase. Therefore, the global stiffness of the column has only a minor effect on the impact force between vehicle and column. As a result, the effect of the number of segment on the impact force is insignificant.
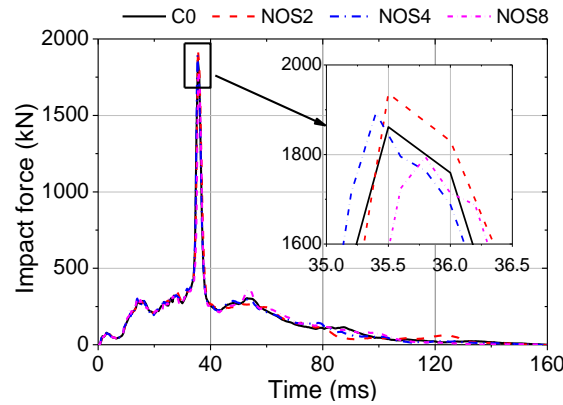

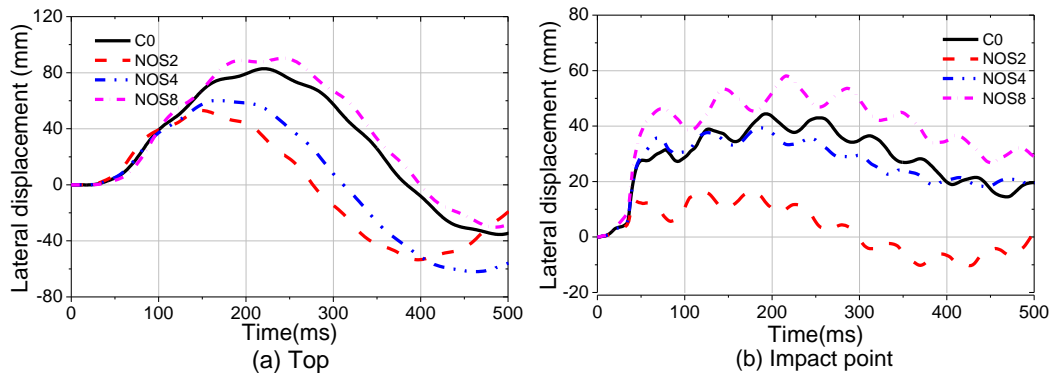Figure 5-18 Impact force time histories with varied number of segments.

Figure 5-19 Lateral displacement of PCSC with varied number of segments.

On the other hand, the lateral and residual displacements of the PCSC have a close relation with the number of concrete segments. Due to the relatively smaller stiffness, the PCSC with more segment joints experiences higher lateral displacement at the column top. Moreover, under lateral impact force, the column with more concrete segments shows more joint shear slips. Thus, the self-centring capacity of segmental column increases when the number of segments decreases (see Figure 5-19b and Table 5-5). The same observation was presented in the experimental tests (Zhang et al., 2016b). As shown in Figure 5-19, the maximum lateral displacement of Column NOS8 (90.3 mm) is nearly 1.7 times larger than that of Column NOS2 (53.0 mm). Besides, the residual displacement of Column NOS8 is about 40 mm while those of Columns C0, NOS4, and NOS2 are 27 mm, 26 mm, and 6.0 mm, respectively.
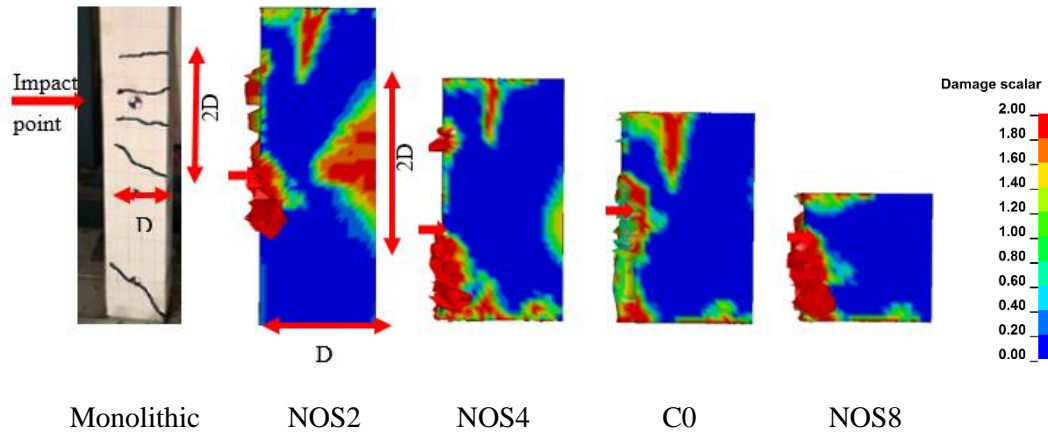
Figure 5-20 Plastic strain of the impacted segment with varied number of segments.

The damage of the impacted concrete segments of these four columns are presented and compared in Figure 5-20. The failure mode of the PCSCs is obviously affected by the number of segments. Severer damage of concrete material around the impact area is observed on the columns with more segments (Columns C0 and NOS8) while Column NOS2 exhibits more concrete cracks at the rear sides opposite the impact point. The length of concrete cracked area of Column NOS2 is approximately two times of the section depth as shown in Figure 5-20. This phenomenon is very similar to the monolithic column under impact test with concrete cracks observed at the rear concrete surface at the impact point (Zhang et al., 2016b). It could be explained that when the height of concrete segment is relatively large compared to the section depth, compressive stress wave propagates from the impact point and reaches the opposite side of the impacted segment before reaching the joints as illustrated in Figure 5-21. As a result, the mid-span of the segment deforms. The segment bends to cause flexural cracks on the large segment. To reduce the flexural cracks of the impacted segment, the compressive stress wave from impact event should reach the segment joints before reaching the opposite side of the concrete segment. Then slips and opening between the concrete segments might be induced to dissipate the energy and mitigate the flexural response of the segment. For this reason, the height-to-depth ratio of concrete segment, thus, should be smaller than two to inhibit an undesirable local damage at the rear concrete surface.

On the other hand, columns with more segments suffer severer local damage than those with less number of segments (see Figure 5-20). This can be attributed to the strong reflected stress wave from the segment joints. These different damage mechanisms need be carefully considered when designing the segmental columns to resist impact forces. Based on the numerical results, the crack patterns and damage of concrete under impact force are illustrated in Figure 5-21.
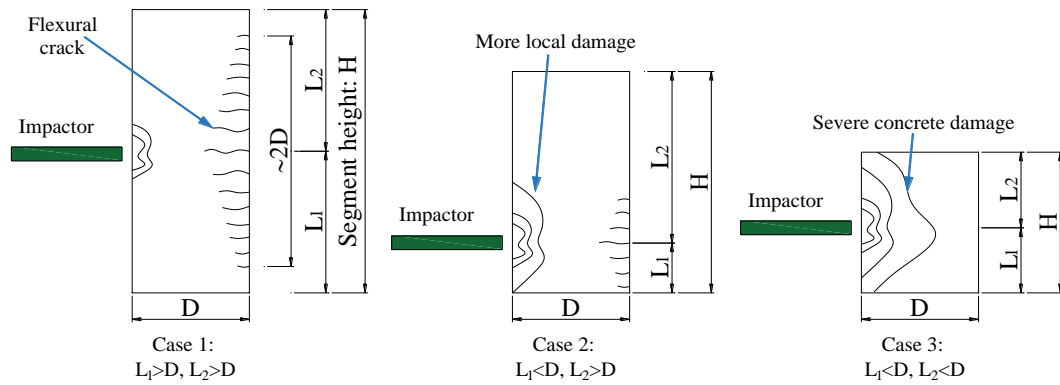
Figure 5-21 The crack patterns and damage of concrete with different segment height.

Table 5-5 Comparisons of the column responses with different number of segments

Parameter			NOS2	NOS4	C0	NOS8
Segment height		mm	2400	1200	960	600
Impact force	Peak	kN	1936	1893	1862	1794
	Duration	ms	150	155	160	169
	Impulse	kN.s	23.1	22.9	22.9	22.8
Maximum displacement (top)		mm	53.0	60.2	82.9	90.3
Residual displacement (impact point)		mm	6.3	26.0	27.0	40.0

5.3.3. Effect of concrete strength

To investigate the influences of concrete strength on the impact response of PCSCs, the compressive strength is varied from 20 MPa to 80 MPa, resulting in an increase by 2 times in the concrete modulus of elasticity. Four columns with four concrete strengths including CS20 (20 MPa), C0 (34 MPa), CS60 (60 MPa), and CS80 (80 MPa) are considered. All the other conditions including vehicle velocity remain unchanged as described above for Column C0. As shown in Figure 5-22a, the impact force increases with the concrete strength but the change is minor (about 8%) with the concrete strength varying from 34 MPa to 80 MPa. Except for Column CS20, the peak impact force is 1504 kN, around 25% smaller than that of the other columns. Column CS20 exhibits severe damage on the concrete surface after the vehicle's frontal collides with the column. The stiffness of the contact area is, therefore, reduced before the vehicle's engine hits the column, which results in the significant decrease of the peak impact force compared to the other considered columns. The damage to concrete surface of Columns C0, CS60, and CS80 is almost similar, therefore leading to the similar peak impact force and impact duration. The impulses of the impact force of these columns are almost identical (approximately 23 kNs) with the difference less than 3% (see Figure 5-22a). The same observation was reported in the impact behaviour of reinforced concrete beams with different concrete strengths by Pham and Hao (2017b). The increase of concrete strength

123

reduces the lateral displacement and residual displacement of PCSCs, but the change is marginal when the strength of concrete is higher than 60 MPa, shown in Figure 5-22b. As previously discussed, due to the high contact force between segments and tendons, concrete damage is observed inside the concrete hole. Thus, increasing the strength of concrete material tends to reduce the concrete damage leading to diminishing the residual displacement of the PCSCs.

The concrete strength has a noticeable effect on the failure mode of PCSC as shown in Figure 5-23. After reaching the maximum displacement at 260 ms, Column CS20 collapses because of severe concrete damage at the base while the PCSCs with concrete strength from 34 MPa to 80 MPa experience local concrete damage and minor damage at the base.

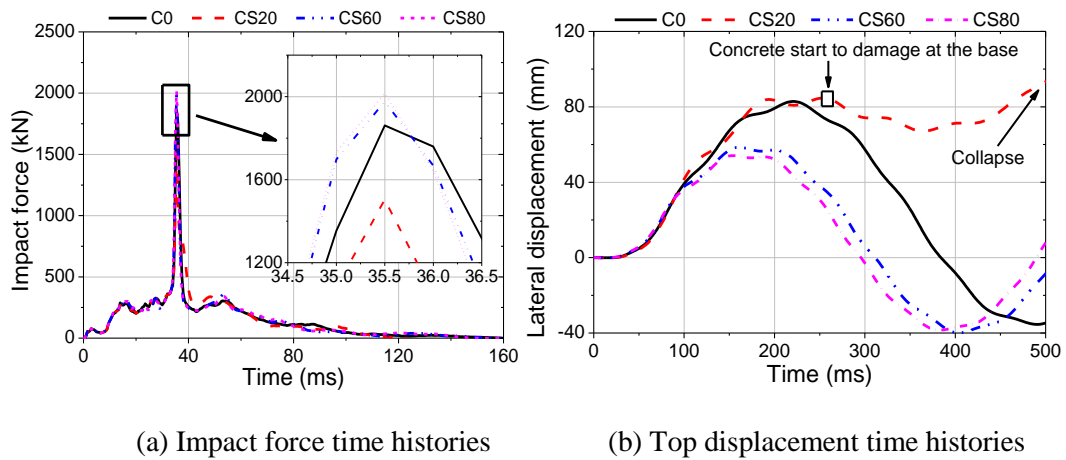(a) Impact force time histories   (b) Top displacement time histories

Figure 5-22 Impact responses of PCSCs with varied concrete strength.

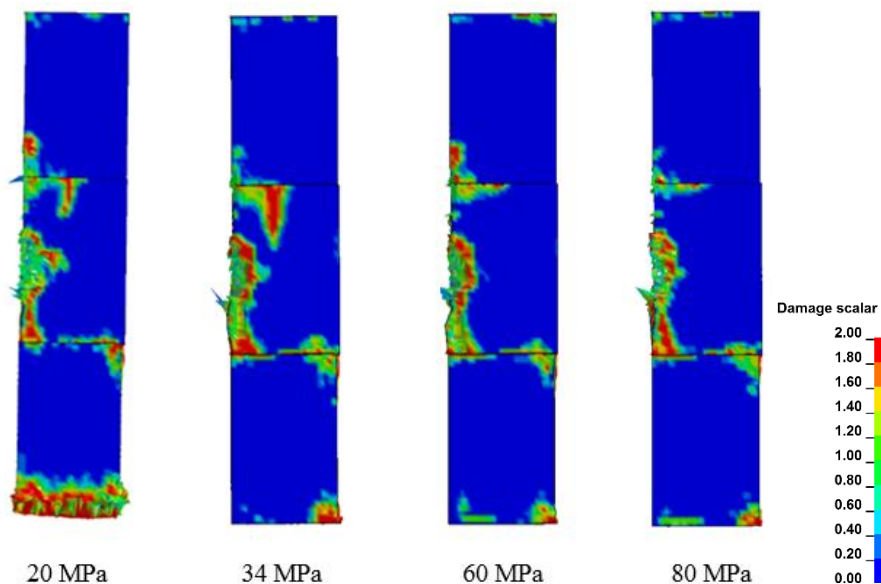

Figure 5-23 Plastic strain of the first three segments with different concrete strength ($t =$ 500ms).

5.3.4. Effect of impact energy

In this section, responses of column C0 subjected to impact from the same vehicle model at four different velocities, namely VL50 (50 km/h), VL60 (60 km/h), C0 (70 km/h), and VL80 (80 km/h), are compared to investigate the effect of impact energy on the column's performance. It can be seen from Figure 5-24 that the impulse increases with the impact velocity but the change of the peak impact force does not follow a clear trend. The peak impact force significantly increases from 314.5 kN (VL50) to 1861.5kN (C0) and the impulse rises by approximately 40% from 16.58 kNs (VL50) to 22.93 kNs (C0). Interestingly, although the impulse still grows to 25.94 kNs in Column VL80, the peak impact force suddenly drops to 1687.8 kN. This is caused by the local damage of concrete after the frontal of vehicle collides on the column with a relatively high velocity. Thus, the contact stiffness between vehicle's engine and concrete column reduces leading to the decrease of the peak impact force. The impact force curve, therefore, shows a longer duration. This observation again proves that the impact force profile is highly dependent on the concrete column – vehicle interaction. Damage to concrete surface during the collision of the column with vehicle bumper before the collision with the solid vehicle engine significantly affects the peak force and duration of impact events. Moreover, increasing the vehicle velocity or impact energy does not always increase the peak impact force on concrete structures. Thus, to design concrete structures under vehicle collision, both peak impact force and impulse should be taken into account.

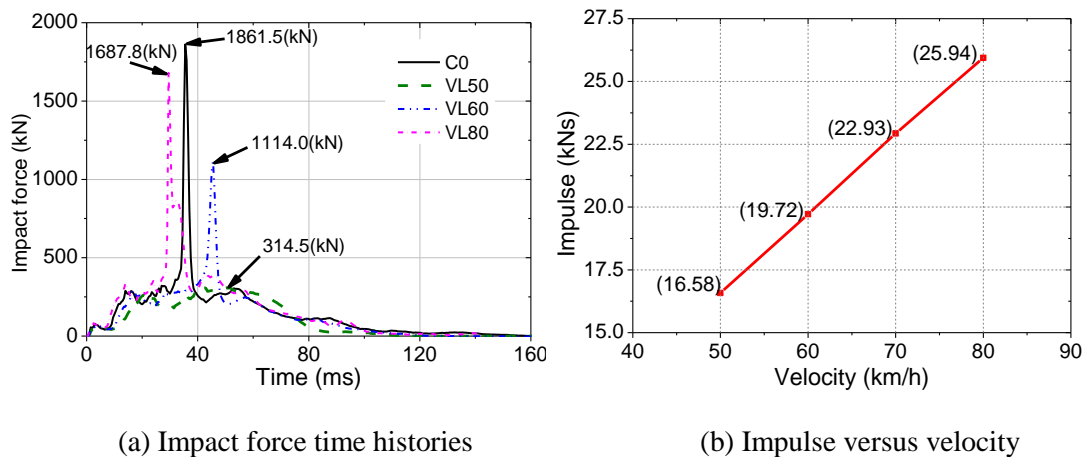(a) Impact force time histories   (b) Impulse versus velocity

Figure 5-24 Impact force time history of PCSC subjected to vehicle impact with four different velocities.

Figures 5-25 and 5-26a respectively present the plastic strain contours of impacted segment and lateral displacement at the top of column under different impact velocities. More local concrete damage and higher residual displacement are observed in the columns impacted by vehicle with higher impact energy. The column freely vibrates around its original position with very small concrete damage at the impact area when the velocity is 50 km/h (VL50) (see Figure

5-26) while Column VL80 exhibits severe local concrete damage and very high residual displacement (about 55 mm). The prestress load time histories of tendons under varied impact velocities are shown in Figure 5-26b. The column impacted with higher velocity shows larger increase in the prestress force. The increment in prestress force of column corresponding to the 50 km/h impact is 6.5% compared to the initial prestress force and they are about 10.5%, 14.0%, and 22.5% respectively for the impact velocities of 60 km/h, 70 km/h and 80 km/h.
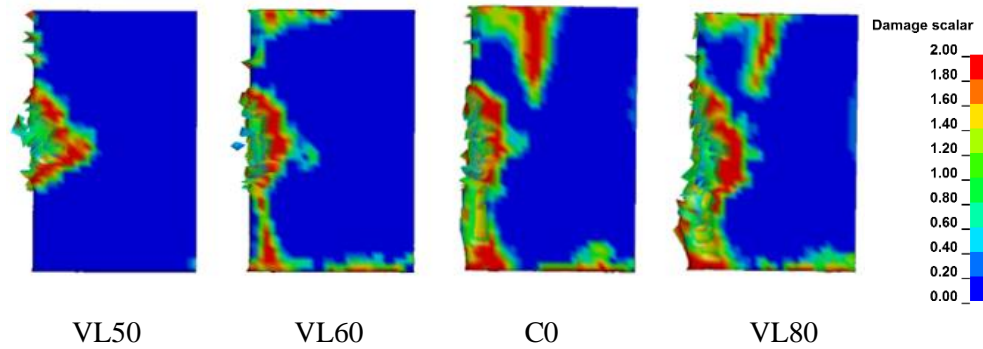

VL50   VL60   C0   VL80

Figure 5-25 Plastic strain of impacted segments with varied impact velocities.

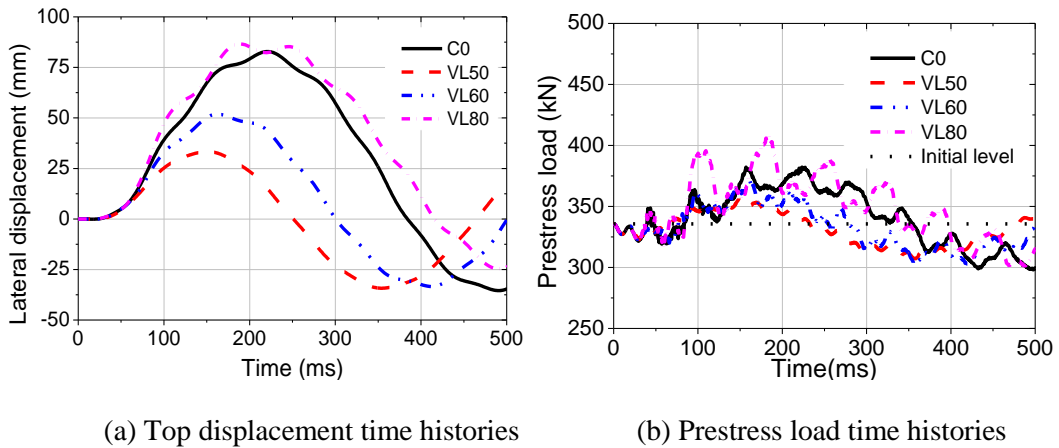(a) Top displacement time histories   (b) Prestress load time histories

Figure 5-26 Column response to vehicle impact with different impact energies.

5.4. Conclusions

In this study, the dynamic responses of PCSCs with un-bonded tendons subjected to vehicle collision have been numerically investigated. The accuracy of the numerical model was verified by the experimental testing results. The influences of different parameters on the performances of PCSCs are examined. The findings are summarised as follows:

1. The relative shear slips between the concrete segments and the lateral displacement of the whole column significantly decrease when the prestress force on segmental columns increases, but its effect on the impact force is negligible. On the other hand, combined with the impact force, large prestress could lead to crush damage of the base segment. Therefore the prestress level needs be determined through careful analysis.

126

2. The stress increase of a tendon during an impact event needs to be taken into consideration to maintain the safe working condition. An increase of the prestress force in the tendon by more than 20% was observed when the column is impacted by the vehicle with velocity of 80 km/h.

3. The columns with fewer concrete segments show better self – centring capability and smaller lateral displacement. However, the number of segments in a column has minimum influence on the impact force, but affects the damage mode to the concrete segment and the column. The height-to-depth ratio of a concrete segment should be smaller than 2 to mitigate the bending damage of the impacted segment.

4. The change of concrete strength shows unnoticeable effects on the residual displacement of the PCSCs but it considerably affects the failure modes of the segmental column. It may also affect the impact force if the concrete strength is so low such that excessive damage to concrete occurs upon collision of the vehicle bumper before the collision of vehicle engine with the column.

Due to the shear slippage between the plain concrete segments in the present study, the use of shear keys on segmental columns under vehicle collision is recommended to mitigate the residual displacement of the columns and increase the serviceability of the columns. The application of tower concrete shear keys with reinforcements or steel tube shear keys at the critical sections, i.e. the column base and the segment joint which closes to an impact point is suggested in order to minimise the compression damage of the concrete material. Moreover, the use of steel tubes or PVC tubes between tendons and concrete segments are recommended to avoid the damage of the concrete under high vehicle impact load.

5.5. References

AASHTO. (2012). *AASHTO LRFD bridge design specifications (customary U.S. units)*. 6th Ed., Washington, DC.

Bu, Z.-Y., Ou, Y.-C., Song, J.-W., & Lee, G. C. (2016). Hysteretic Modeling of Unbonded Posttensioned Precast Segmental Bridge Columns with Circular Section Based on Cyclic Loading Test. *Journal of Bridge Engineering, 21*(6), 04016016.

Buth, C. E., Williams, W. F., Brackin, M. S., Lord, D., Geedipally, S. R., & Abu-Odeh, A. Y. (2010). *Analysis of large truck collisions with bridge piers: phase 1. Report of guidelines for designing bridge piers and abutments for vehicle collisions* (FHWA/TX-10/9-4973-1). College Station, TX.

Chen, W., Hao, H., & Chen, S. (2015). Numerical analysis of prestressed reinforced concrete beam subjected to blast loading. *Materials & Design, 65*, 662-674.

Chou, C.-C., Chang, H.-J., & Hewes, J. T. (2013). Two-plastic-hinge and two dimensional finite element models for post-tensioned precast concrete segmental bridge columns. *Engineering Structures, 46*, 205-217.

Chung, C. H., Lee, J., & Gil, J. H. (2014). Structural performance evaluation of a precast prefabricated bridge column under vehicle impact loading. *Structure and Infrastructure Engineering, 10*(6), 777-791.

Dawood, H., Elgawady, M., & Hewes, J. (2014). Factors affecting the seismic behavior of segmental precast bridge columns. *Frontiers of Structural and Civil Engineering, 8*(4), 388-398.

Dogan, F., Hadavinia, H., Donchev, T., & Bhonge, P. (2012). Delamination of impacted composite structures by cohesive zone interface elements and tiebreak contact. *Open Engineering, 2*(4), 612-626.

ElGawady, M., Booker, A. J., & Dawood, H. M. (2010). Seismic behavior of posttensioned concrete-filled fiber tubes. *Journal of Composites for Construction, 14*(5), 616-628.

Fujikake, K., Li, B., & Soeun, S. (2009). Impact response of reinforced concrete beam and its analytical evaluation. *Journal of Structural Engineering, 135*(8), 938-950.

Hallquist, J. O. (2007). *LS-DYNA keyword user's manual.* Livermore Software Technology Corporation. Vol. 970. (pp. 299-800).

Hao, H., Zhang, X., Li, C., & Do, T. V. (2017). *Impact response and mitigation of precast concrete segmental columns.* Paper presented at the 12th International Conference on Shock and Impact Loads on Structures, Singapore

Hesam, P., Irfanoglu, A., & Hacker, T. (2016). Estimating Effective Viscous Damping and Restoring Force in Reinforced Concrete Buildings *Dynamics of Civil Structures, Volume 2* (pp. 265-273): Springer.

Hesameddin, P. K., Irfanoglu, A., & Hacker, T. (2015). *Effective Viscous Damping Ratio in Seismic Response of Reinforced Concrete Structures.* Paper presented at the 6th International Conference on Advances in Experimental Structural Engineering, Urbana-Champaign, United States

Jiang, H., & Chorzepa, M. G. (2015). An effective numerical simulation methodology to predict the impact response of pre-stressed concrete members. *Engineering Failure Analysis, 55*, 63-78.

Li, J., & Hao, H. (2013). Influence of brittle shear damage on accuracy of the two-step method in prediction of structural response to blast loads. *International Journal of Impact Engineering, 54*, 217-231.

Li, J., & Hao, H. (2014). Numerical study of concrete spall damage to blast loads. *International journal of impact engineering, 68*, 41-55.

Li, J., Hao, H., & Wu, C. (2017). Numerical study of precast segmental column under blast loads. *Engineering Structures, 134*, 125-137.

Motaref, S., Saiidi, M. S., & Sanders, D. (2013). Shake table studies of energy-dissipating segmental bridge columns. *Journal of Bridge Engineering, 19*(2), 186-199.

Nakalswamy, K. K. (2010). *Experimental and numerical analysis of structures with bolted joints subjected to impact load* (Doctoral dessertation). University of Nevada, Las Vegas Retrieved from https://core.ac.uk/download/pdf/62872865.pdf

Ou, Y.-C. (2007). *Precast segmental post-tensioned concrete bridge columns for seismic regions* (Doctoral dessertation). State University of New York at Buffalo Retrieved from https://ubir.buffalo.edu/xmlui/handle/10477/42969

Papageorgiou, A., & Gantes, C. (2008). Modal damping ratios for irregular in height concrete/steel structures. *I II III IV, 6*

Pham, T. M., & Hao, H. (2017a). Effect of the plastic hinge and boundary conditions on the impact behavior of reinforced concrete beams. *International Journal of Impact Engineering, 102*, 74-85.

Pham, T. M., & Hao, H. (2017b). Plastic hinges and inertia forces in RC beams under impact loads. *International Journal of Impact Engineering, 103*, 1-11.

Sha, Y., & Hao, H. (2013). Laboratory tests and numerical simulations of barge impact on circular reinforced concrete piers. *Engineering structures, 46*, 593-605.

Sideris, P., Aref, A. J., & Filiatrault, A. (2014). Large-scale seismic testing of a hybrid sliding-rocking posttensioned segmental bridge system. *Journal of Structural Engineering, 140*(6), 04014025.

Zhang, X., Hao, H., & Li, C. (2016a). The effect of concrete shear key on the performance of segmental columns subjected to impact loading. *Advances in Structural Engineering, 20*(3), 352-373.

Zhang, X., Hao, H., & Li, C. (2016b). Experimental investigation of the response of precast segmental columns subjected to impact loading. *International Journal of Impact Engineering, 95*, 105-124.

CHAPTER 6

IMPACT RESPONSE AND CAPACITY OF PRECAST CONCRETE SEGMENTAL VERSUS MONOLITHIC BRIDGE COLUMNS

ABSTRACT[5]

In this study, the performance of precast concrete segmental bridge columns (PCSC) against truck impacts is numerically investigated and compared to a corresponding monolithic reinforced concrete bridge column (RCBC). The numerical results have shown that although the impact force time histories of the two columns are quite similar under the same loading conditions, the PCSC shows a better performance in terms of the induced bending moment and shear force by high impact force due to shear slippage and joint rocking between concrete segments. Besides, the damage and failure of PCSC are localised at the two bottommost segments due to compression damage and/or combined flexural and shear failure of concrete segment while failure of the RCBC distributes widely with flexural cracks, shear cracks, and punching shear at multiple sections. Furthermore, the base segment which is found to be able to absorb about 80% of the total absorbed energy of the PCSC plays a crucial role in controlling the failure of the PCSC. An analytical method to estimate the bending moment required to open the segment joint and the ultimate bending moment is also developed with consideration of the dynamic increase factor and the increase in axial force associated with stress wave propagation in the column induced by impact load.

6.1. Introduction

The demands on Accelerated Bridge Construction (ABC) have been considerably increased during the last few decades due to its many benefits compared to the traditional cast-in-place construction. The ABC not only provides a feasible solution to increase site constructability and construction quality, improve work-zone safety for workers and traveling public, and minimise traffic disruption during the construction period, but also offers practical and economical methods to those of the traditional technology (Culmo, 2011). Among the ABC technology, a PCSC which is commonly used in the bridge construction can meet all the

---

objects of the ABC. Many projects using PCSC have already been implemented (ElGawady et al., 2010; Ou, 2007). A PCSC has to be designed to withstand hazardous loads during its service life such as seismic load, impact load, and blast load, etc. However, due to the lack of understanding of its dynamic behaviours under seismic and impact loads, PCSCs have been limited mainly in areas of low seismicity and low traffic flow. To overcome these difficulties, the performance and capacities of PCSCs under cyclic loading and seismic loading have been experimentally (Billington & Yoon, 2004; Hewes & Priestley, 2002; C. Li, H. Hao, X. Zhang, et al., 2017; Ou, 2007), numerically (Dawood et al., 2014; Hung et al., 2017; C. Li, H. Hao, & K. Bi, 2017) and analytically (Chou et al., 2013; Ou, 2007) investigated. It was found that PCSCs have many structural advantages, e.g. higher ductility, greater self-centring capacity, and less column damage compared to the reference RCBC.

However, studies of the behaviours of PCSCs under other extreme loading conditions such as truck impacts or blast loads are very limited with very few reports that can be found in the open literature (Chung et al., 2014; Do et al., 2018a, 2018b; Hao et al., 2017; J. Li et al., 2017; Zhang et al., 2016a, 2016b). An experimental study on PCSCs under pendulum impact by Zhang et al. (2016b) indicated that the PCSCs experienced a flexural response when an impactor hit the centre of the column. Compressive damage at the segment corner was observed on the impacted segment and the base segment due to the rocking and rotation of the concrete segment leading to the column failure. In the latest experiment study by Hao et al. (2017), a combined flexural and shear failure was observed on a PCSC which was impacted at a joint between the base segment and the second-base segment. The flexural compressive damage of concrete together with the diagonal shear failure of the base segment led to collapse of the PCSC. Besides, when the impactor smashed into the centre of the base segment, the column slipped away without flexural deformation and then collapsed owing to excessive damage of the concrete segment. These experimental studies showed that under different loading conditions, the PCSC showed various types of failure modes, i.e. flexural failure, combined shear and flexural damage, and shear failure. In order to control the impact response of PCSCs subjected to vehicle collisions, effects of critical parameters on their impact performance were numerically examined by Do et al. (2018b). By increasing the initial prestress level and reducing the number of segments, smaller lateral/residual displacement was resulted in the PCSCs. The height-to-depth ratio of the concrete segment was also suggested to be smaller than 2 in order to reduce flexural cracks and failure of the column.

6.2. Research significance

Though the previous studies provide an overall impact performance and response of the PCSC, the characteristics of axial force, bending moment, shear force, and failure modes induced by vehicle impact have not been well investigated. For safe and economic designs of PCSCs to

resist vehicle impact, it is important to understand these response characteristics. This study attempts to investigate the induced bending moment, shear force, and failure modes of PCSCs under truck impact. An analytical approach to estimate the bending moment capacities including the moment that results in the opening of the segment joint and the ultimate bending moment is also proposed.

6.3. Numerical validation

In this study, the impact responses of a monolithic RC column (RCBC) and a precast concrete segmental column (PCSC) are investigated and compared. The numerical simulations of these two column were introduced and presented in Section 2.2 and Section 5.2. Therefore, the previous simulation techniques, i.e. material models, strain rate effects, and contact mechanisms, will be used in this Chapter to develop the numerical simulations of the two columns under vehicle collisions.

## 6.4. Numerical models of bridge columns under truck impacts

6.4.1. Bridge and truck model

Based on the validated models, FE models of two bridge models with PCSC and RCBC respectively are developed in this section. The previous study by Consolazio and Davidson (2008) indicated that the dynamic behaviours of multi-span bridge structures could be accurately predicted by an analysis model which consists of one bridge column and two superstructure spans. This simulation approach was also used in previous studies (Abdelkarim & ElGawady, 2017; El-Tawil et al., 2005). As such, each bridge model consisting of one single column, two superstructure beams, footing, and two concrete abutments is considered in this study, as presented in Figure 6-1a. The overall dimensions and properties of superstructures are obtained from the study by Megally et al. (2001), and the span length is assumed to be 40 m. The superstructure's mass is transmitted to the column through a trapezoidal cap beam which a placed on top of the column. It should be noted that no rubber or bearing pad is used to connect the superstructures and the cap beam in this study because of its insignificant effect on the impact behaviours of a bridge column (El-Tawil et al., 2005). In these simulations, the superstructures are assumed to rest on top of the cap beam with the coefficient of friction between concrete and concrete surface 0.6 (ACI, 2008). The other end of the superstructure is designed to rest on a simplified solid block which represents the abutments (see Figure 6-1a). The total dead load consisting of the superstructures and the substructures is about 4,600 kN which equalled 10% of the axial capacity of each column. The detailed dimensions of the two bridge specimens are presented in Figure 6-1b and Table 6-1. The bridge column, cap beam, tendons, superstructures, concrete abutments, and footing of these models are modelled by using solid elements (constant stress solid elements) while steel reinforcements are simulated
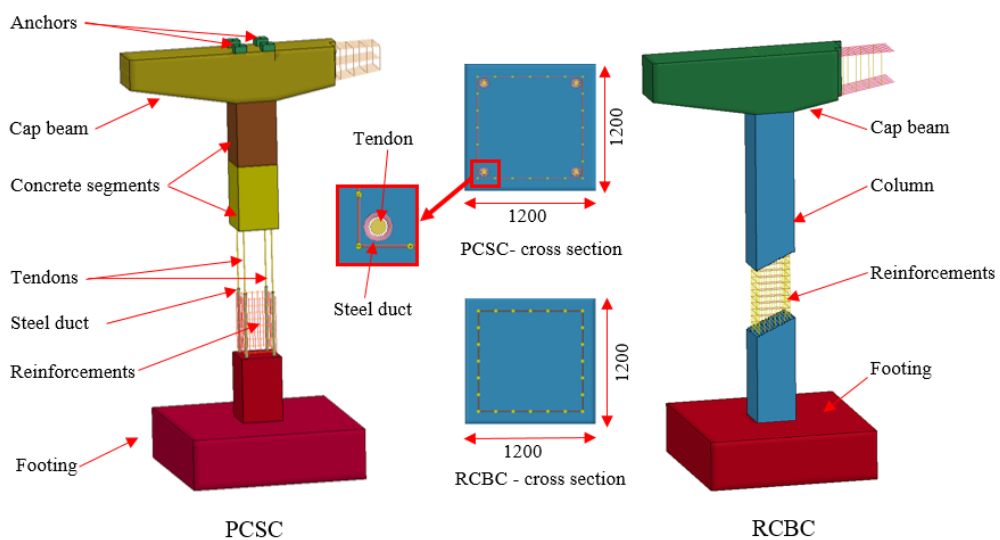
by beam elements (Hughes-Liu with cross section integration) (see Figure 6-1c). It should be noted that the longitudinal bars were discontinuous at segment joints and no ED bars is utilised in the PCSC.
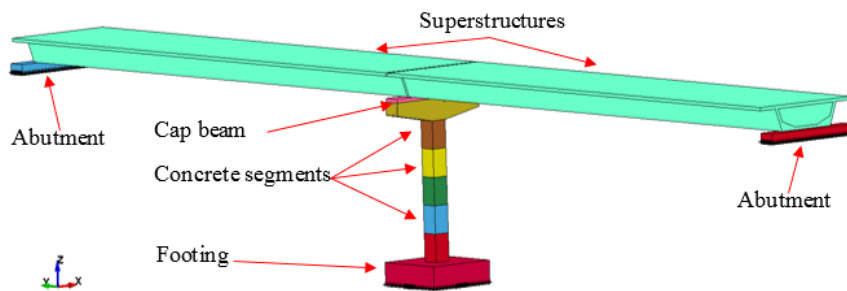
(a) 3D – view of the PCSC with superstructures
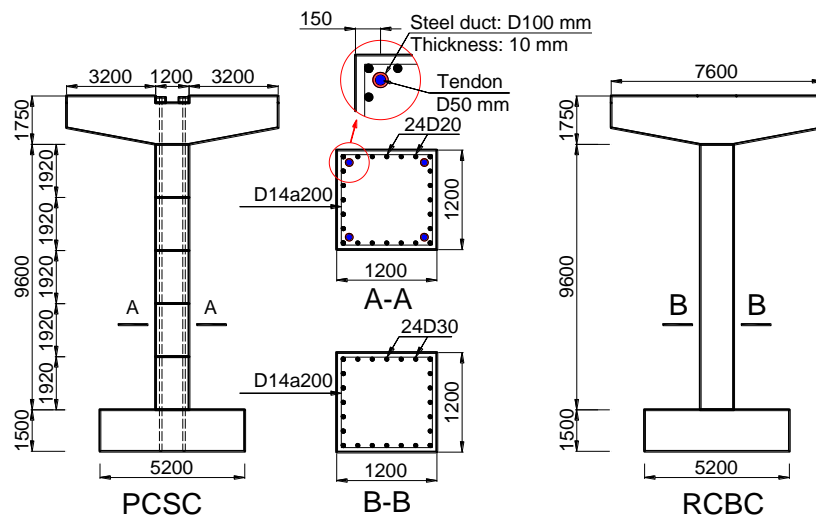
(b) Column design and dimensions

(c) Numerical model of the PCSC and RCBC

Figure 6-1 Design and simulation of the PCSC and RCBC.

A medium-duty truck, Ford truck (35,400 elements) model, is employed to simulate the collision on the bridge columns. This model was friendly shared by Sharma et al. (2012) and Abdelkarim and ElGawady (2016). The model has been used to examine the dynamic behaviour of structures subjected to vehicle collisions in previous studies (Abdelkarim & ElGawady, 2016; Agrawal et al., 2013; Chen et al., 2015; El-Tawil et al., 2005; Sharma et al., 2012). The accuracy of the model was verified by FHWA/NHTSA National Crash Analysis Centre at the George Washington University. The previous study by Do et al. (2018a) showed that the PIF noticeably depends on the kinetic energy of the truck's engine. Thus, to investigate the performances of the columns under different PIFs, the truck velocity and truck engine's mass are varied in this study. The engine's mass is varied from 0.64 ton to 2 ton and 3 ton by changing the mass density of the material model. By increasing the mass of the engine, the cargo mass is reduced from 3 ton to 0.64 ton to keep the total vehicle mass of 8 ton unchanged. The purpose of this analyses is to investigate the influence of the engine mass on the response of the columns which was usually neglected in previous studies and design guides. The total vehicle mass of 8 ton is kept the same in this study so that the influence of engine mass can be clearly observed. Moreover, the vehicle velocity is also varied from 60 km/h to 140 km/h in the simulations. In this study, the top of the footing is assumed to be placed under the ground level of 0.5 m.

Table 6-1 Detailed dimensions of the two bridge specimens

Parameters	PCSC	RCBC
Column height (mm)	9,600	9,600
Number of segment	5	--
Segment height (mm)	1,920	--
Section width (mm)	1,200	1,200
Section depth (mm)	1,200	1,200
Longitudinal steel	24D20 (discontinuous)	24D30 (continuous)
Lateral steel	D14a200	D14a200
Tendon diameter (mm)	50	--
Number of tendons	4	--

6.4.2. Modelling procedure

To apply an initial prestressing force in the tendon, a temperature-induced shrinkage option is employed, which was used in previous studies (Do et al., 2018b; Jiang & Chorzepa, 2015). In this method, the *DYNAMIC RELAXATION (DR) function is utilised to calculate the initial stress on concrete structures and tendons before transferring those results as an input data to an explicit analysis (Hallquist, 2007). An example to illustrate the procedure of this method was reported in the previous study by Do et al. (2018b). In this study, the prestress force in each tendon of the PCSC is 1,500 kN which equalled 40% of the yielding capacity of the tendons. As a result, the four tendons yield a total resultant force of 6,000 kN on the PCSC

which is equal to 13% of the axial compressive strength of the PCSC. In the explicit simulation, the gravity load of the structures is applied by gradually increasing the gravity acceleration in both the PCSC and the RCBC. It is worth mentioning that the abrupt application of the gravity acceleration (9.81 m/s^2) will lead to an undesirable dynamic responses of the structures, i.e. the vertical vibration of the superstructures (Consolazio et al., 2009). Therefore, the gravity acceleration should be applied for a relatively long duration, for example, this study used the duration of 150 ms before the vehicle model collides with the bridge column to mitigate the unexpected variation of the gravity load. In the following sections, the time is set to zero when the vehicle starts to collide on the bridge column. The simulation process of the study is presented in Figure 6-2.
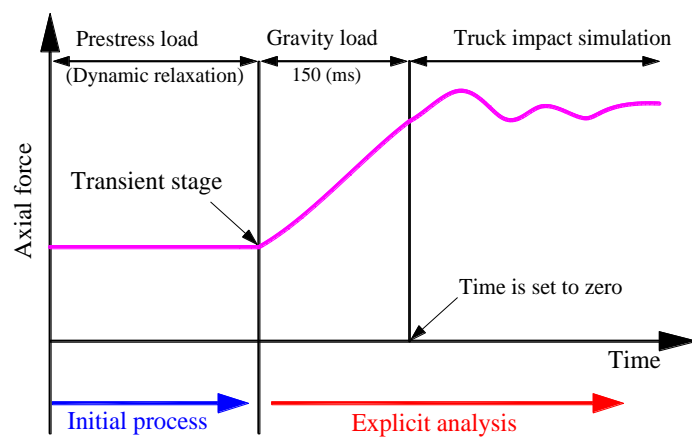
Figure 6-2 Modelling procedure.

6.5. Numerical results

To examine the performance and capacity of the PCSC against truck impacts, a series of numerical simulations are carried out and the numerical results are presented in Table 6-2. The numerical results of the PCSC are also compared to the corresponding results of the RCBC in terms of impact force time histories, bending moment, shear force, and failure modes.

6.5.1. Impact force time histories

For concrete bridge columns, the impact force time history under truck impact normally includes two different peaks caused by the truck's engine and cargo (Abdelkarim & ElGawady, 2016; Do et al., 2018a) in which the peak impact force could be associated with either the engine the cargo impact depending on the vehicle and column properties and interaction between vehicle and cargo. Cargo impact occurs after engine impact, therefore cargo impact could generate a larger impact force than engine impact only if the column survives the engine impact without experiencing significant damage. If engine impact causes significant damage to the column, which softens the column, the subsequent cargo impact is likely to generate a long duration impact but not necessarily large impact force. For example,

the numerical studies by (Chen et al., 2016, 2017) showed that the second peak impact force from the cargo collision was larger than the first peak impact force caused by the engine collision because the column was assumed to be rigid. Therefore, no concrete damage and column failure were modelled. When the cargo starts to collide on the column, the contact stiffness between the vehicle model and the column is similar to the initial contact stiffness of the column. With very high kinetic energy from the cargo due to the cargo's mass, the second peak is thus larger compared to the first peak. In the present study, damage of the concrete column and column deformation by the bumper and engine impact are simulated, leading to a significant reduction of the contact stiffness of the column. As a result, the second impact force from cargo collision, which depends on the interaction between vehicle and column, is smaller than the first impact force although the kinetic energy was larger. The results indicate the assumption of the rigid column does not reflect the actual interaction between the vehicle and column. Hence, the term PIF stands for the first peak of the impact force in this study. It should be noted that the peak impact force caused by the vehicle bumper is usually small compared to the engine and cargo impact, therefore is not explicitly discussed. It should also be noted that if stronger columns are considered and they survive the engine impact without suffering large damage, the peak impact force could correspond to the cargo impact. However, since the primary objective of the present study is to compare the performances of RCBC and PCSC subjected to vehicle impact, modelling stronger columns to get the larger impact force from cargo impact is not carried out. Instead, the impact force due to engine impact is discussed in detail because it is usually neglected in many previous studies and not covered in the current design guides.

The impact force time histories of the PCSC and the RCBC against truck impacts are presented in Figure 6-3. It is interesting to note that although these two columns have different lateral stiffness due to the dissimilar initial axial force and the discontinuous of concrete segments of the PCSC, the impact force time histories are almost identical for PIF, duration, and impulse when they are subjected to the same loading condition (see Table 6-2 and Figure 6-3). These results indicate the influence of the global stiffness of the bridge column on the PIF is insignificant. Similar observations were also reported in previous studies on concrete beams that the impact force was found to be dependent primarily on the local stiffness only (Pham & Hao, 2017a). The marginal effect of the global column stiffness on the PIF when concrete structures were subjected to vehicle or ship impacts has also been previously reported (Do et al., 2018b; Sha & Hao, 2013).

Meanwhile, an increase in the vehicle velocity corresponds to a substantial increase in the PIF on the PCSC as shown in Figures 6-3a-g. The PIF increases significantly from around 1,981 kN to 16,400 kN when the velocity rises from 60 km/h to 140 km/h. Interestingly, with the

same vehicle mass and vehicle velocity, the contribution of the engine's mass on the PIF is also noteworthy. Consider the velocity of 100 km/h and the total mass of 8 ton, increasing the engine's mass from 0.64 ton to 3 ton, the PIF increases proportionally from 7,891 kN to 24,476 kN, as shown in Figures 6-3d, h, and i. In general, in all the cases the PIFs of the two columns are almost identical. However, if the impact force is not intensive and fast enough to cause slippage or local damage, the impact force time history, affected by the interaction between the global/local stiffness of the column and the impact energy, is only slightly different. Otherwise, under intensive impact where only the local stiffness governs the impact force, the impact force time histories of the two columns are almost identical. The comparisons of the PIF and impulse of the two columns are also presented in Figure 6-4. The numerical results in this study also show a good agreement with the empirical equations which have been proposed by the authors (Do et al., 2018a) in the previous study.
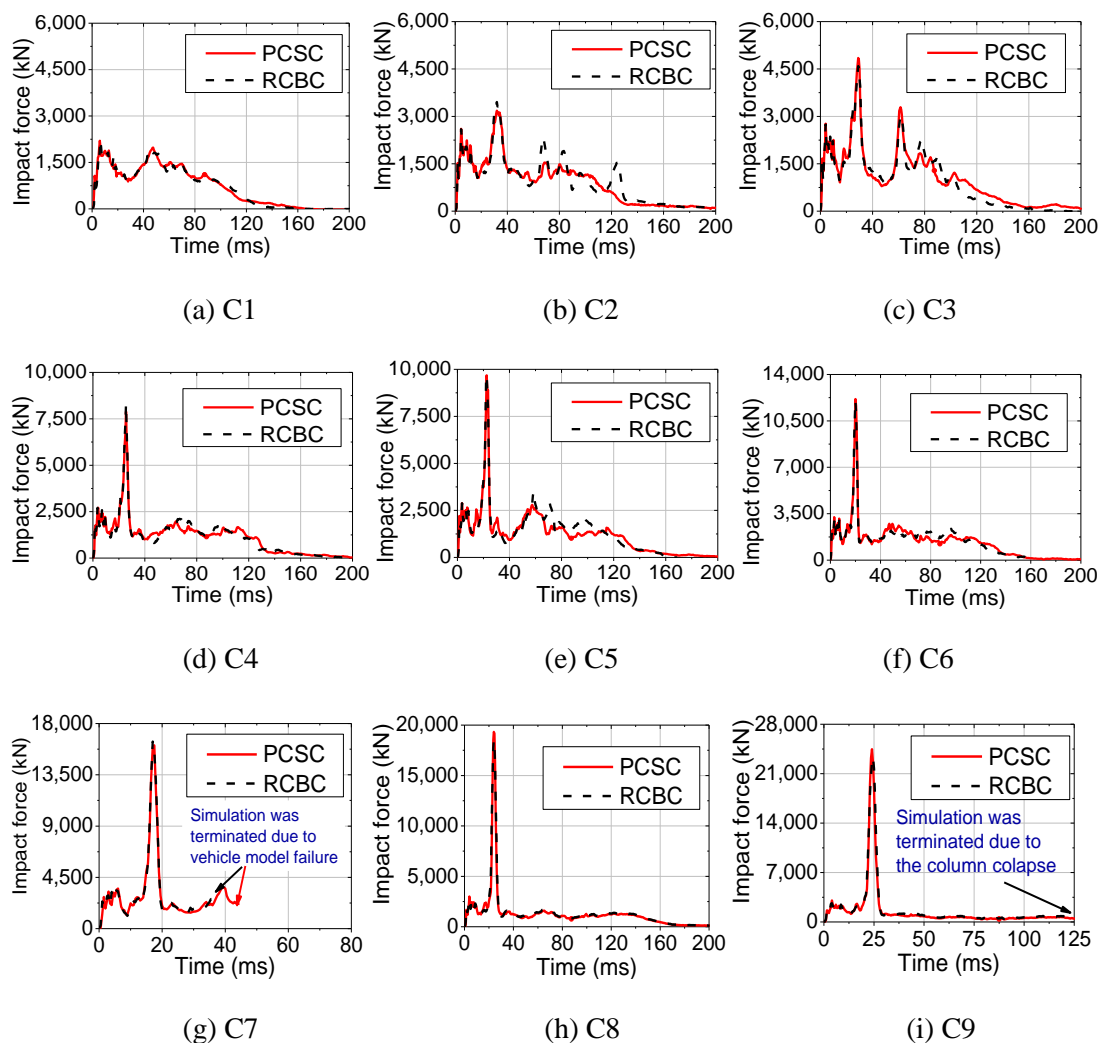
Figure 6-3 Impact force time histories with different initial conditions.
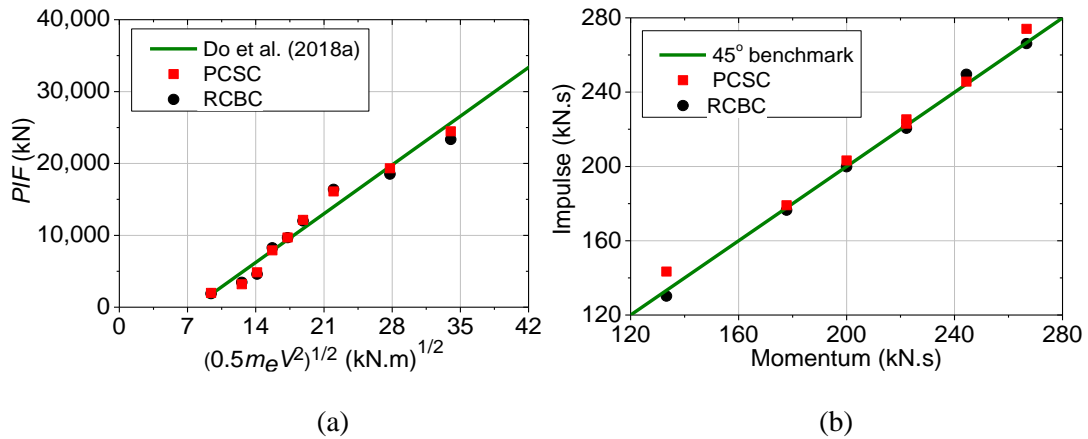
Figure 6-4 (a) The PIF - initial kinetic energy of the engine relation; (b) Vehicle momentum – impulse conversion.

Table 6-2 PCSC and RCBC under different initial loading conditions.

	Initial Condition					PCSC		RCBC	
Case	Total Truck's mass (T)	Engine's mass (T)	Velocity (km/h)	Momentum (T.m/s)	Kinetic energy (kN.m)	PIF (kN)	Impulse (kN.s)	PIF (kN)	Impulse (kN.s)
C1	8.0	0.64	60	133.3	1111.1	1,981	143.4	1,868	130.2
C2	8.0	0.64	80	177.8	1975.3	3,182	179.0	3,460	176.4
C3	8.0	0.64	90	200.0	2500.0	4,848	203.2	4,596	199.8
C4	8.0	0.64	100	222.2	3086.4	7,891	225.3	8,260	220.5
C5	8.0	0.64	110	244.4	3734.6	9,680	245.4	9,660	249.6
C6	8.0	0.64	120	266.7	4444.4	12,149	274.1	12,000	266.1
C7	8.0	0.64	140	311.1	6049.4	16,086	--[1]	16,400	--[1]
C8	8.0	2.00	100	222.2	3086.4	19,326	223.0	18,500	223.5
C9	8.0	3.00	100	222.2	3086.4	24,476	--[2]	23,333	--[2]

Note:--Simulation is terminated due to severe damage of the vehicle model[1] and/or the column[2]

6.5.2. Column shear force

Figure 6-5 shows the typical shear force time histories of the PCSC and the RCBC under truck impact (C6). When the impact force reaches a peak at 12,149 kN, the shear force at the column base of the two columns also increases to the highest value of about 7,500 kN (see Figure 6-5a). It should be highlighted that the shear force at the column base is substantially smaller than the PIF because of the contribution of the inertia force to resist the impact as discussed in (Do et al., 2018a), implying directly applying PIF in equivalent static analysis without considering the distribution of the inertia force would significantly overestimate the shear force in the column. The stress wave propagates from the impact area to the column top causing the maximum value of the shear force at about 3,800 kN (see Figure 6-5b). The time lag between the PIF and the maximum shear force at the column top is about 10 ms. When the

138

impact force drops to about 2,500 kN after 30 ms, with the contribution of the inertia force, the shear force time histories at the column base fluctuates around the impact force values while those at the column top oscillates around the zero level. It is clear from the figure that the shear force time histories of the PCSC at the column base fluctuates with large amplitude and high frequency while those of the RCBC is almost equal to the impact force. This is because the PCSC experiences the high-frequency vibration of the concrete segment during impact loading (Do et al., 2018b), which causes the variation of the inertia force distributed along the segment. Since the PCSC is discontinuous at the segment joints, the stiffness of the column is smaller than the RCBC. The high-frequency vibration of the shear force with larger amplitude compared to the corresponding RCBC is therefore mainly associated with the vibrations of the individual segment instead of the segmental column.

(a) At the column base   (b) At the column top
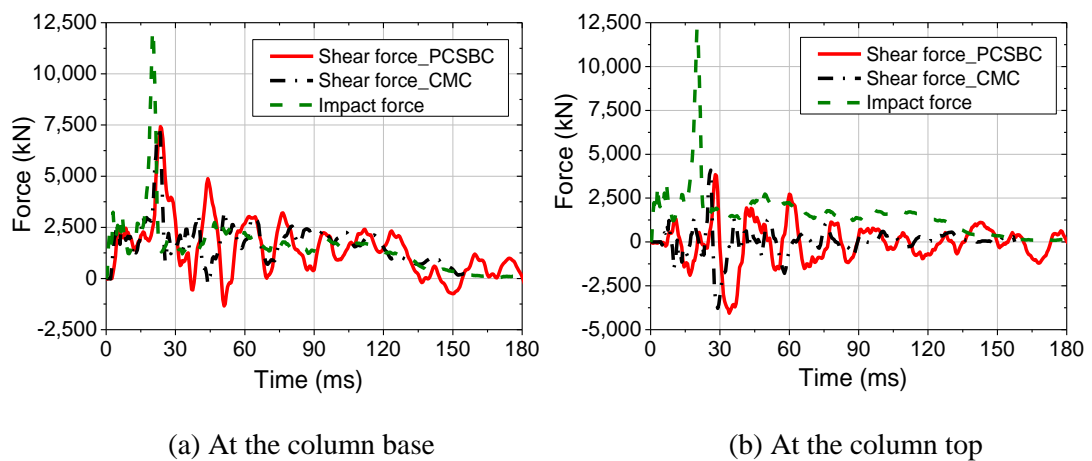
Figure 6-5 Shear force time histories of the two columns under truck impact (C6).

The maximum value of the shear force at the column ends of the PCSC and RCBC are compared in Figure 6-6. It is clear that minor differences at the two ends can be found between the PCSC and the RCBC when the PIF is smaller than 12,149 kN (C1-C6). The reason is that no shear damage or slippage at the impact area (between segment 1 and segment 2) is observed during the force phase in these columns (see Figure 6-7a) which leads to the similar impact energy from the collision transferred to the PCSC and the RCBC, and similar responses of the two columns. As a result, the induced shear forces in the two columns has a trivial difference (see Figure 6-6). Besides, no shear crack or shear failure is observed in these columns when the shear force at the base is less than 7,500 kN (PIF = 12,149 kN). However, considerable differences in the maximum shear force at the column ends are observed when these columns are subjected to more intensive impact loading (C7 – C9), as presented in Figure 6-6. When the PIF increased from 12,149 kN (C7) to 24,476 kN (C9), the shear force at the column base of the PCSC is nearly steady at 7,700 kN while that of the RCBC continues increasing to about 10,500 kN before levelling off (see Figure 6-6a). This is because the shear force (7,700 kN)

reaches the anti-slip capacity of the PCSC causing the slippage between the base segment and the footing (Figure 6-7a). Moreover, an excessive local failure occurs at the base segment, evident by diagonal shear failure in the PCSC. Meanwhile, a diagonal shear failure and punching shear failure are observed in the RCBC when the shear force reaches the column's shear capacity at about 10,500 kN. Furthermore, due to the slippages, segment vibrations, and the large deformation of the base segment which dissipates a large amount of the impact energy, the shear force at the column top of the PCSC is thus smaller than that of the RCBC. Envelopes of the shear force diagram of the PCSC and the RCBC in the last three loading conditions are also compared and presented in Figure 6-6c. These results showed that both columns react similarly to truck impact when no slippage between the segments occurs in the PCSC. However, under high impact force, the slippage between the segments reduces the shear force at the column ends of the PCSC resulting in less shear damage of the column as will be presented in the subsequent section.
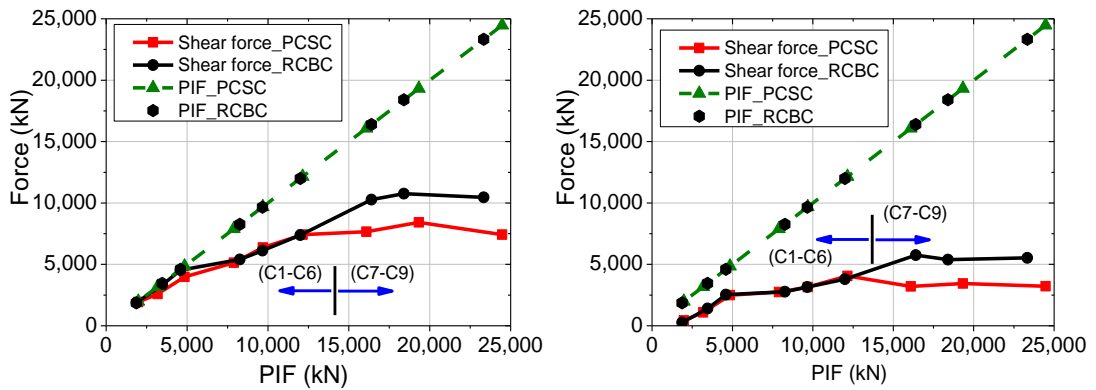
(a) Maximum shear force at the column base   (b) Maximum shear force at the column top
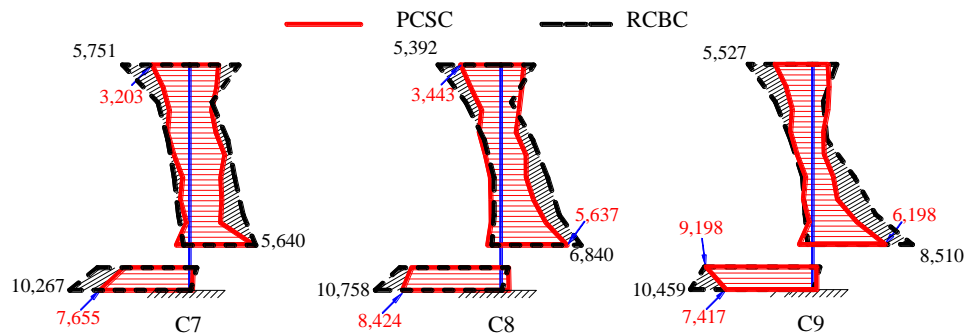
(c) Envelopes of the shear force

Figure 6-6 Comparisons of the shear force between the PCSC and RCBC.

| (a) Joint sliding | (b) Joint opening |
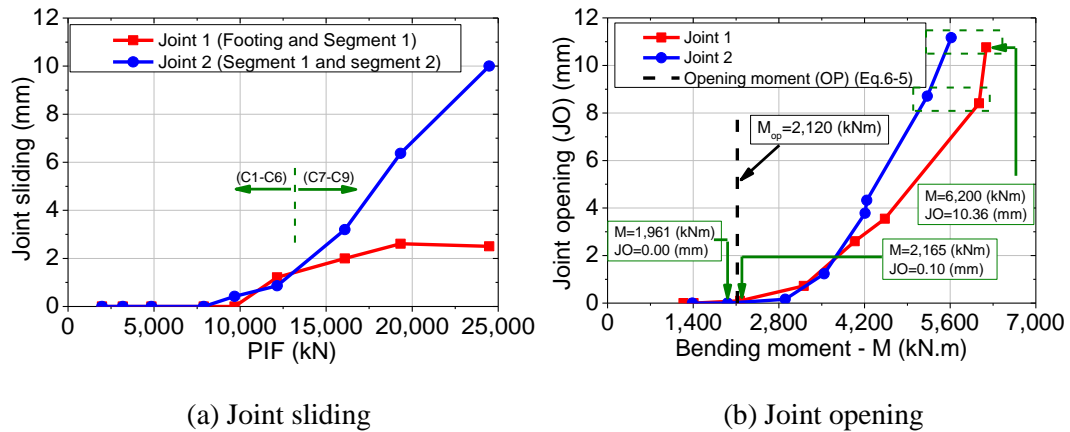
Figure 6-7 Joint sliding and joint opening of the PCSC under truck impacts.

6.5.3. Column bending moment

Due to the variation of the inertia force which distributed along the column, the bending moment shape of the PCSC and the RCBC varies considerably, as presented and compared in Figure 6-8a (C6). When the impact force increases to the highest value of 12,149 kN at $t = 20.5$ ms, the bending moment at the second joint (between segment 1 and segment 2) reaches the maximum positive value at 4,171 kNm. After about 0.5 ms, the bending moment of the PCSC at the base also increases to the maximum negative value at 4,533 kNm. The compression stress also spread to the column top leading to the vibration of the whole column. When the bending moment at the column top appears ($t \approx 25.5$ ms), the bending moment at the intermediate section reaches its maximum negative value. It is worth mentioning that the negative bending moment, occurs on the top part of the column, is caused by the inertia force which distributed along the column after the PIF and the inertia resistance of the superstructures (Do et al., 2018a). Moreover, the intermediate section, which happens when the column top starts vibrating and locates between the column top and the impact point, varies considerably under different loading conditions as defined and explained in the previous study (Do et al., 2018a). Then, the negative bending moment at the column top together with the positive bending moment at the intermediate section increases to its highest value at about $t = 32.5$ ms because of the effect of the cap beam and the superstructures. Figure 6-8a also compares the bending moment diagrams of the bridge column by using the equivalent static force (ESF) (AASHTO, 2012) with the bending moment envelope from the dynamic simulation. It is clear that the ESF results in the highest bending moment at the base while the actual truck impact causes the large bending moment at multiple sections of the column, i.e. the column base, the segment joint close to the impact point, the intermediate section, and the column top. The ESF does not yield a negative moment along the column while the numerical simulation shows the magnitude of the negative moment at the intermediate section was even

greater than the negative moment at the base. It is, therefore, essential to note that the use of the ESF model might lead to an underestimation of the impact responses of the structures.
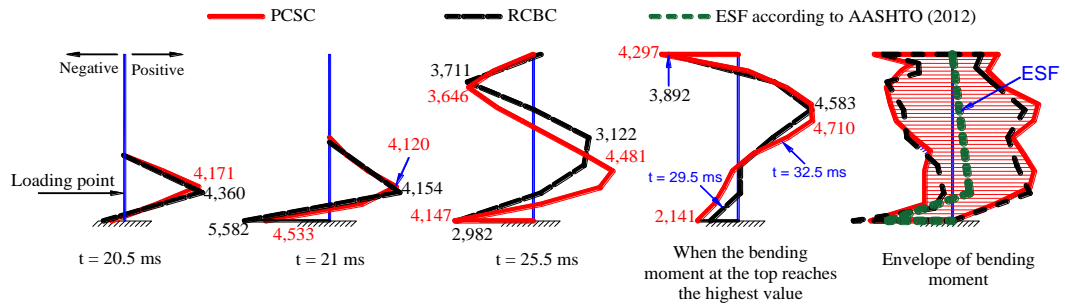
(a) Bending moment along the columns after the impact force reaches the peak (C6)
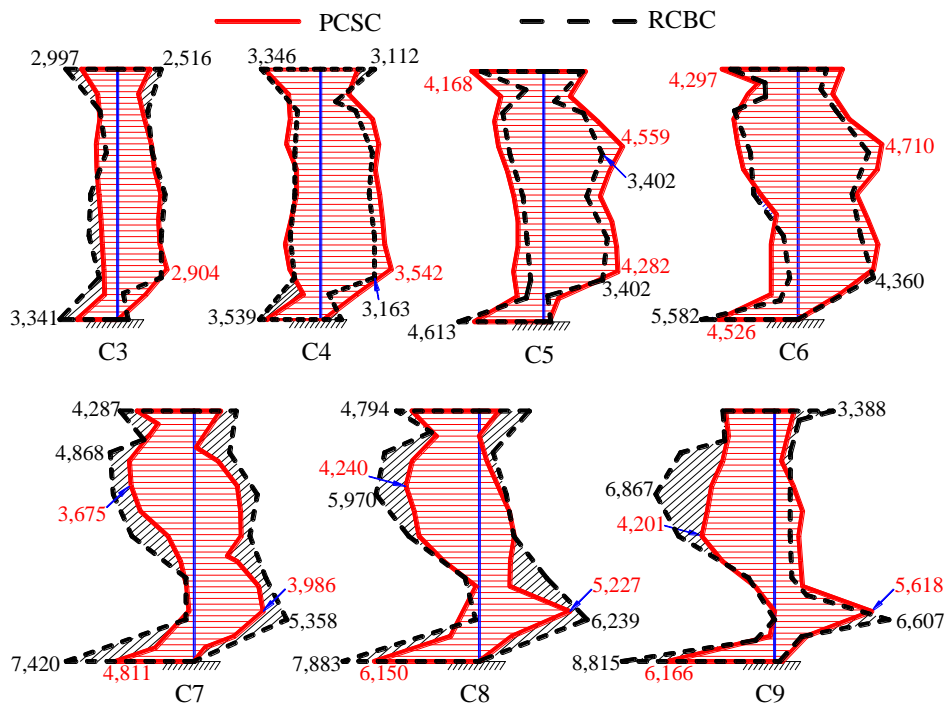
(b) Envelopes of the bending moment

Figure 6-8 Column bending moment diagrams under truck impacts.

The comparisons of the bending moment diagrams between the PCSC and RCBC against different truck impact conditions are also presented in Figure 6-8b. Similar to the shear force, when the PIF is smaller than 12,149 kN (C1 - C6), only minor difference can be found between the two columns because of no significant shear slippages between the concrete segments happens so that the PCSC under these loading conditions behaves like a RCBC. However, very large differences can be observed between the two columns under higher impact energy (C7 - C9) when the slippage between the segment 1 and segment 2 occurs, as shown in Figure 6-8b. It is because a large amount of the impact energy is absorbed due to shear slippages and rocking of the segments in PCSC. Thus, the bending moment diagrams of the PCSC at the

four critical sections are considerably smaller than those of the RCBC. Additionally, in the RCBC, the bending moment at the intermediate section proportionally increases with the PIF while its location moves downward, which causes an uncertain parameter in the design stage. For the PCSC, even the PIF kept increasing, the bending moment at the intermediate section is nearly steady and its location is close to the segment joint due to the rocking of the segment. These bending moment diagrams again demonstrate that the PCSC outperforms the RCBC when the bridge column is subjected to high impact energy due to joint sliding and joint opening, which absorb a significant amount of impact energy.

6.5.4. Failure modes

The comparison of the PCSC and the RCBC under truck impact in terms of cracks and failure modes is presented in Figure 6-9. Although the impact force time histories are almost identical, these columns respond differently with distinguished types of column damage and failures. As shown in Figure 6-9a, the failure mode of the RCBC varies significantly from the flexural crack at the impact area to the local punching shear failure with the column damage spreading from the column base to its top. When the impact force was small (C1-C6), a minor concrete damage at the impact area and a flexural crack at the impact point and the column top are observed. Increasing the PIF to about 16,400 kN (C7), flexural cracks appears at the column mid-height due to the positive bending moment at the intermediate section while a large diagonal shear crack occurs in the negative side of the column top. Additionally, when the truck impacts on the column with the velocity of 100 km/h and the engine's mass of 2 ton (C8), yielding the PIF of 18,400 kN, a diagonal shear failure is observed at the column base. That large PIF also yields other shear cracks at the two-third of the column. Further increasing the velocity to 140 km/h with the engine's mass of 2 ton (PIF = 30,000 kN), the column exhibits a severe punching shear damage at the impacted area leading to the collapse of the RCBC (Do et al., 2018a). These simulated cracks and failure modes provide an explanation for the different failures of the bridge column under vehicle impacts in reality documented by Buth et al. (2010), which were underestimated by the equivalent static analysis.

For the PCSC under vehicle impact, when slippage occurs at the segment joint due to the PIF, the relative displacement between the segments remains stable in the whole impact process because the contact forces from the tendon and the segments are inadequate to pull the segments back to their original position. This observation was reported in the previous study (Do et al., 2018b). Therefore, the slippage at the segment joints under the PIF, which is presented in Figure 6-7a, is also the residual slippage between the segments. Moreover, when the impact force reaches the peak, the opening also happens at the first two segments of the PCSC as presented in Figure 6-9b. For Cases 1-6, after the impact force phase, the opening between the segments closes due to the effects of the initial prestress tendon. For Cases 8-9,

the combined flexural-shear failure occurs at the first segment which causes the collapse of the column. Hence, in this study, no residual opening is obtained.
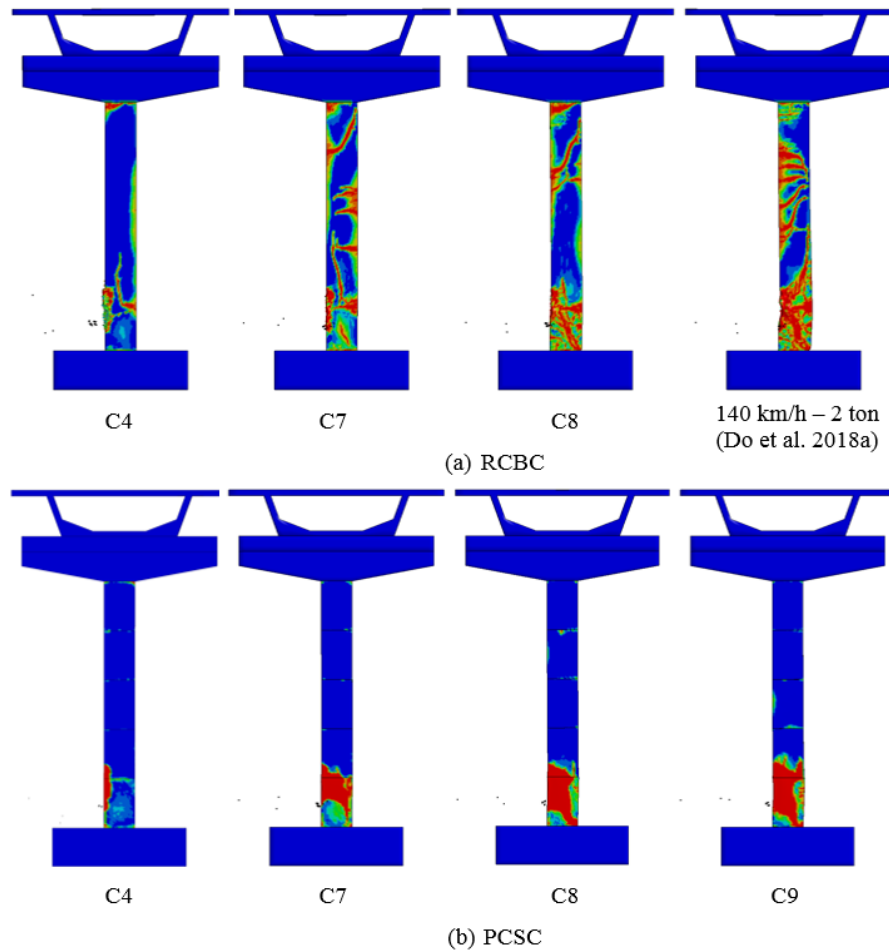

(a) RCBC

(b) PCSC

Figure 6-9 Failure modes of the bridge columns under truck impacts.

Owing to the advantages of the segment-to-segment sliding and rocking, the behaviours of the PCSC thus differ from the RCBC. As presented in Figure 6-9b, when the impact force was small (C1-C6), only local concrete damage at the impacted area is observed whereas no flexural crack develops along the column. Although the PIF increases considerably from 16,086 kN (C7) to about 24,476 kN (C9), the failures of the concrete segment are similar. When the truck engine collides on the column, a large slip and opening between the first and the second segment are generated. Due to the column rocking, the concrete compressive damage is, therefore, produced in the compression area of the two segments. Meanwhile, the large shear force from the impact area also transfers to the footing through the base segment leading to a predominant diagonal crack of the base segment. That diagonal shear crack together with the flexural bending damage at the base joint causes the severe damage of the base segment leading to the collapse of the column. Importantly, no sliding, cracks, and damage of concrete are observed in the other sections of the PCSC. The failure mode of the PCSC in this study was consistent with that in the experimental pendulum impact tests (Hao

et al., 2017), which confirmed again the reliability of these numerical results. It should be highlighted that regardless the integrity of the upper part of the columns above the mid-height is continuous or discontinuous, it does not affect the response of the column at the PIF. As presented in Figure 6-8a, when the impact force reaches the PIF, only a part of the column vicinity to the impact point reacts to the impact while other parts of the column remains in the stationary condition. This observation was also obtained in previous studies (Pham & Hao, 2017a, 2017b; Zhao et al., 2017; Zhao et al., 2018). If the PIF is intensive enough to cause failure in the PCSC and RCBC, the shear cracks immediately occur at the impact area with no involvement of the other parts of the column. In Cases 7-9, the flexural-shear failure of the PCSC and the diagonal shear or punching shear of the RCBC happen immediately when the impact force time histories reaches the peak. Thus, the top part of the two columns does not involve in resisting the PIF. After that period, the stress wave propagates from the impact point to the column top which causes another flexural-shear cracks in the RCBC while the PCSC observes the joint opening at the other segmental joints. These results proves the merits of the PCSC in controlling the damage and failure of the bridge column under truck impacts compared to the RCBC where the PCSC fails at the base segment due to the combined shear and bending damage while damage occurs at multiple sections of the RCBC. In general, very localised damage is observed in the PCSC while distributed damage occurs in the RCBC.

6.6. Discussion and analysis investigation

6.6.1. Energy absorption

The energy absorption of the PCSC and the RCBC under truck impacts is presented and compared in Figure 6-10a. The absorbed energy of the column is defined by adding up the internal energy of all the column elements. The internal energy of each element is computed from the six directions of element stress and strain (Hallquist, 2007). In each direction, the energy is defined by multiplying the stress, incremental strain, and the element volume (Hallquist, 2007). Figure 6-10a indicates that the two columns show a similar amount of the energy dissipation when no shear slippages or minor joint opening occurs in the PCSC (C1-4). When the segmental joint starts to open at the first two joints which absorbs an amount of the impacted energy in the C5-6, the absorbed energy by the PCSC is thus slightly higher than that of the RCBC. When the shear slippages between the segments due to the PIF occurs in the PCSC (C8-9), the absorbed energy by the PCSC (1041 kN.m-C9) is about 2.5 times higher than that of the RCBC (405.8 kN.m-C9). This observation indicates that owing to the opening and sliding at the joints between the concrete segments, the PCSC outperforms the RCBC in terms of the energy absorption under truck collision.
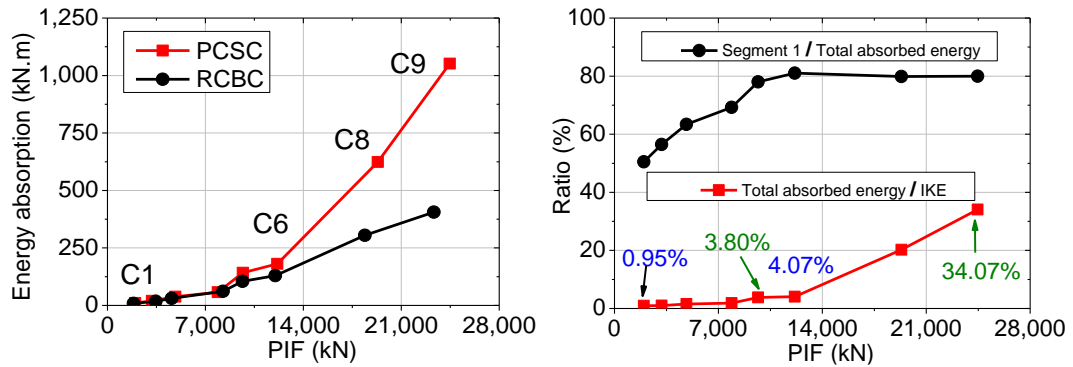
(a) Comparison between the PCSC and RCBC   (b) PCSC (IKE = initial kinetic energy)

Figure 6-10 Energy absorption of the PCSCs and RCBCs under truck impacts

The ratio of the absorbed energy by the PCSC to the initial kinetic energy (IKE) of the vehicle model is also presented in Figure 6-10b. The figure shows that when quadrupling the IKE of the truck model from 1111 kN.m (C1, PIF = 1,981 kN) to 4444 kN.m (C6, PIF = 12,148 kN), the absorbed energy of the PCSC shows a moderate increase from 0.95% to about 4.07%. It is because in these cases the response of the column is almost in the elastic range with no cracks or shear slippages as previously mentioned while the truck model which is less stiff experiences a large deformation and absorbs most impact energy. The PIF shows a significant influence on the energy absorption, for example, C9 and C5 have the similar IKE but the PIF of C9 is greater than that of C5, the energy absorption of the PCSC in C9 is about 34.07% (1051.6 kN.m) of the total kinetic energy (3086.4 kN.m) while the corresponding energy absorption in C5 is 3.80% (57.18 kN.m). This is because of the column damage, i.e., large diagonal shear cracks, flexural damage, and concrete damage of the column in C9 absorbs the impact energy. It proves again that the PIF corresponding to the engine impact plays a crucial role in the performances of the structures against truck impact.

The ratio between the energy absorption by segment 1 and the total energy absorption is also presented in Figure 6-10b. It is clear that the ratio proportionally increases with the PIF from 50% (C1) to 79% (C6) when the PIF increases from 1,981 kN to 12,148 kN, respectively. That ratio remains nearly unchanged (80%) after the diagonal shear crack appears on the segment 1 (C7-C9), though the PIF and the total absorbed energy still increase. It is shown that the impacted segment (base segment) is the key segment of the PCSC when the column is collided by a truck. The base segment does not only absorb a large amount of the impact energy but also governs the capacity of the column because the failure of the base segment leads to the collapse of the whole bridge structures.

146

6.6.2. Bending moment capacity

6.6.2.1 Opening bending moment

Under lateral impact forces, the behaviour of the segmental joint can be characterised by three main stages, i.e. initial stage, opening stage, and ultimate stage. The section equilibrium analysis at the interface between the base segment and the footing is presented in Figure 6-11. At the initial stage (Figure 6-11b), the column is under compression by the pre-stressing force and the gravity load. When the lateral force increases, the compressive stress develops on one side while stress on another side decreases. During this stage, the column is still under compression and all the segment joints remained in contact (see Figure 6-11b). From the prestressing force of one tendon, P_o, the number of tendons, n, and the total gravity load, W, the initial strain, ε_o, on a concrete section can be estimated as follows:

$$\varepsilon_o = \frac{nP_o + W}{S_1 \, S_2 \, E_o} = \frac{T}{S_1 \, S_2 \, E_o} \tag{6-1}$$

where S_1, S_2 are the section depth and the section width, respectively; E_o is the Young's modulus of concrete; and T is the total vertical force on the PCSC at the initial stage.
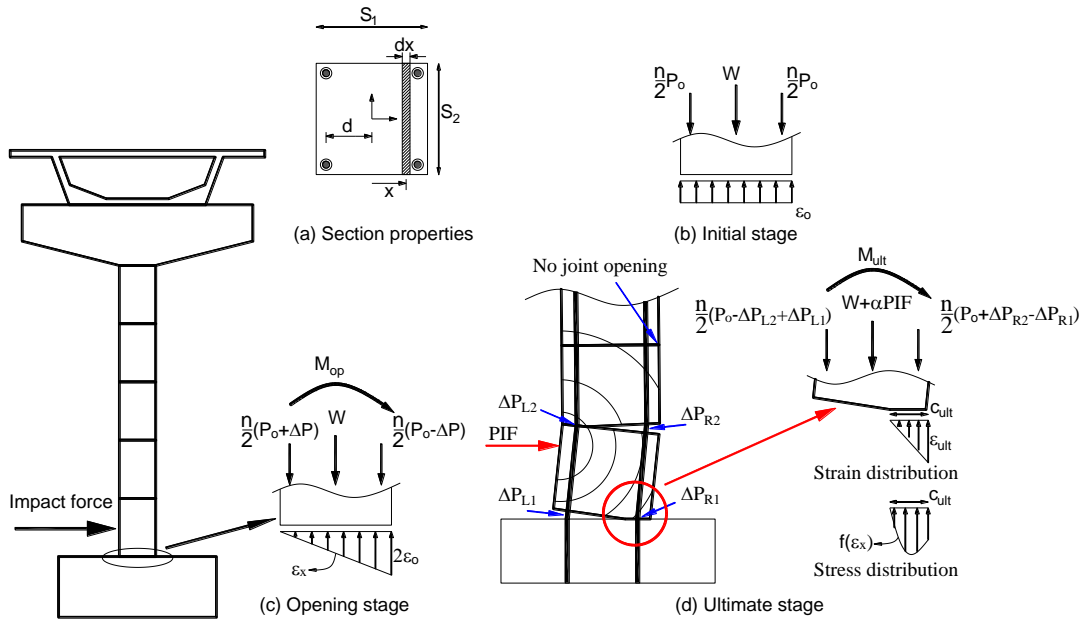
Figure 6-11 Segmental joint's behaviour under impact force.

The opening moment at the base joint (see Figure 6-11c) can be estimated by the following equation:

$$M_{op} = \int_{-S_1/2}^{S_1/2} S_2 \, x \, f(\varepsilon_x) dx + \frac{n}{2}(P_o + \Delta P)d - \frac{n}{2}(P_o - \Delta P)d \tag{6-2}$$

where d is the distance from the tendon to the origin (Figure 6-11a); ΔP is the deformation of the prestressed tendon; x is the distance from the infinitesimal, dx, to the origin; $f(\varepsilon_x)$ is the stress of concrete corresponding to the strain, ε_x. In this analytical method, the stress-strain curve of concrete proposed by Thorenfeldt et al. (1987), is employed.

Normally, the initial stress in PCSC caused by the prestressing force and the self-weight was suggested from 0.2 to 0.3 f_c' (Ou, 2007), where f_c' is the compressive strength of the concrete. In this study, the initial stress on the column is approximately 0.2 f_c'. Hence, in the opening stage (Figure 6-11c), the maximum stress on segment joint must be less than $2 \times (0.2 - 0.3) f_c' =$ 0.4-0.6 f_c'. According to Thorenfeldt et al. (1987), the change of the concrete modulus is minor when the stress is smaller than $0.6 f_c'$. Thus, it is assumed that the modulus of elasticity of concrete is unchanged up to this stage. As a result, the stress of concrete can be derived as

$$f(\varepsilon_x) = E_o \varepsilon_x = E_o \varepsilon_o \frac{S_1 + 2x}{S_1} \tag{6-3}$$

Thus, the opening bending moment at the segment joint can be expressed by:

$$M_{op} = \frac{TS_1}{6} + n\Delta P_1 d \tag{6-4}$$

In general, the opening moment is dependent on the section geometry, vertical force, and the stress increase in tendons. However, unlike the column under static or cyclic load where the elongation in the tendons was normally observed due to the deformation of the column during the loading process (Hewes & Priestley, 2002; Ou, 2007; Sideris et al., 2014), under truck impacts, no additional deformation of the pre-stressed tendons is recorded during the loading phase. This is because when the impact reached its peak, just a part of the column is activated and responded to the impact force with no movement at the column top (Figure 6-8a). Thus, the influence of the column deformation on the tendon during this period is neglected. Moreover, no contact between the concrete segments and the tendons during the peak impact force is observed since the joint sliding generally occurs after the joints opening, as shown in Figure 6-7. Therefore, the vibration of the pre-stressed tendon due to the interaction between the segments and the tendons does not happen. As a result, the change of the prestress tendon force before the joint opens is minimum. The opening moment thus can be approximated by the following equation:

$$M_{op} = \frac{TS_1}{6} \tag{6-5}$$

148

In this study, the total vertical load from the prestress tendons and the gravity load is 10,600 kN. From Eq. (6-5), the opening moment is thus 2,120 kNm. This result is compared to that from the numerical simulation. Very good agreement is achieved, as shown in the Figure 6-7b.

6.6.2.2 Ultimate bending moment

It is worth mentioning that the entire column fails if the base segment is severely damaged due to the combined flexural bending and the diagonal shear cracks at the PIF. This is usually associated with damages in the second segment due to the flexural compression while the other segments are still intact. These failures of the concrete segments (Segments 1 and 2) occur immediately when the impact force reaches the peak (C7-C9). The column response at the ultimate stage is presented in Figure 6-11d. The equilibrium of the axial force acting on the section is, therefore, equated as:

$$\int_{\frac{S_1}{2}-c_{ult}}^{\frac{S_1}{2}} S_2 \, DIF \, f(\varepsilon_x) \, dx = W + \alpha \, PIF + \frac{n}{2}(P_0 - \Delta P_{L2} + \Delta P_{L1}) + \frac{n}{2}(P_0 + \Delta P_{R2} - \Delta P_{R1}) \tag{6-6}$$

where c_{ult} is the compressive depth at the ultimate stage; DIF is the dynamic increase factor; $\alpha \times PIF$ is the increase of the axial force due to the stress propagation caused by the PIF ($\alpha = 0.2289$) as shown in Figure 6-12; $\Delta P_{L1}, \Delta P_{L2}$ are the elongation and the shrinkage of the tendons on the left side (impacted side), respectively; and $\Delta P_{R1}, \Delta P_{R2}$ are the shrinkage and the elongation of the tendons on the right side, respectively.

As presented in Figure 6-7b, the joint opening at these two sections at the ultimate stage are almost similar (C8, C9), it thus leads to the magnitude of the elongation and shrinkage of the tendons at the impact side equal to the corresponding elongation and shrinkage of the tendons at the other side ($\Delta P_{L1} = \Delta P_{R2}, \Delta P_{L2} = \Delta P_{R1}$). Further investigation, by examining the prestress load in the tendons at the ultimate stage, shows only minor difference in the tendon force at the two sides of the columns (less than 3%). This is the difference between the impact response and quasi-static response of the PCSC. In the static analysis, when the load is applied at the column top, the whole tendon is elongated in one side while the tendon of the other side shrinks (Bu et al., 2016; Ou, 2007). Based on the above observation, Eq. (6-6) can be re-written as:

$$\int_{\frac{S_1}{2}-c_{ult}}^{\frac{S_1}{2}} S_2 \, DIF \, f(\varepsilon_x) \, dx = T + \alpha \, PIF + n(\Delta P_{L1} - \Delta P_{L2}) \tag{6-7}$$

The ultimate bending moment can be expressed as:

$$M_{ult} = \int_{\frac{S_1}{2}-c_{ult}}^{\frac{S_1}{2}} S_2 \, DIF \, x \, f(\varepsilon_x) dx \tag{6-8}$$

Besides, the tendon elongation and shrinkage can be achieved from the rotation at the segment, θ_p, which was defined by Hewes and Priestley (2002):

$$\theta_p = \left(\frac{\varepsilon_{cu}}{c_{ult}} - \frac{2\varepsilon_0}{S_1} \right) L_p \tag{6-9}$$

where c_{ult} is the depth of section under compression; θ_p is the plastic rotation angle; and $L_p = 1920(mm)$ is the plastic hinge length which is recommended equalizing to segment height for the PCSC under truck impact.
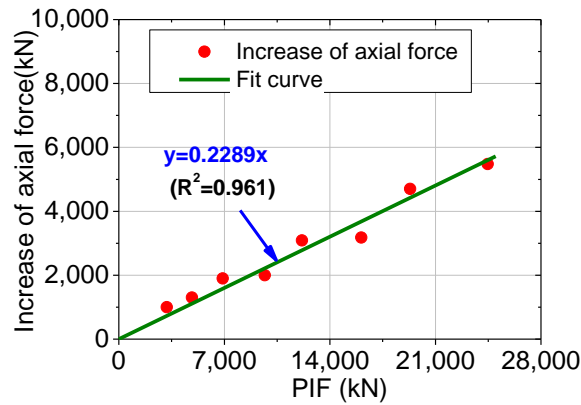
Figure 6-12 Axial force versus PIF.

In this study, the DIF of the concrete material at the ultimate strength is 1.325 corresponding to the strain rate of 65 s^{-1} (Hao & Hao, 2014). However, that DIF in each concrete element in the compressive area varies. Therefore, in the analytical approach, the average DIF of 1.16 is used for concrete material in the compressive area. As a result, the ultimate bending moment and the joint opening are about 6,863 kNm and 9.14 mm. The corresponding results from the numerical simulation are about 6,200 kNm and 10.36 mm, respectively (see Figure 6-7b).

6.7. Conclusions

In this study, the performance and capacity of the precast concrete segmental bridge columns (PCSCs) subjected to truck impacts have been investigated and compared to the monolithic RC bridge columns (RCBCs). The findings of the present study can be summarised as follows:

1. Under different truck impact conditions, similar impact force time histories for PCSCs and RCBCs are observed because the vehicle-column interaction is mainly governed by the column local stiffness instead of the global stiffness.

2. The influences of the PIF on the induced bending moment and shear force diagrams of the PCSC and RCBC have been presented. The bending moment of the PCSC is significantly smaller than that of the RCBC under high impact force due to the shear slippage and opening of segmental joints in PCSC.

3. The failure of the PCSCs mainly occurs at the two bottommost segments with the combined compression, shear, and flexural failure. The results also prove the advantages of the PCSC in localising the damage of bridge structures under truck impact compared to the RCBC.

4. Under truck impact, the base segment is a crucial element of the PCSC which can absorb up to 80% of the total energy by the whole column. The failure of this segment may lead to the total collapse of the bridge structure. Thus, the capability of the base segment needs to be considered carefully in the design stages.

5. The analytical method to estimate the opening bending moment and the ultimate bending moment of the segmental joint has been proposed. In this method, the dynamic increase factor (DIF) and the increase of the axial force due to the PIF have been taken into consideration.

In general, PCSCs exhibit better impact resistant performance than RCBCs. The damage of the PCSCs is localised at the two bottommost segments so that it is recommended to strengthen these two segments instead of the whole column in case of RCBCs.

6.8. References

AASHTO. (2012). *AASHTO LRFD bridge design specifications (customary U.S. units)*. 6th Ed., Washington, DC.

Abdelkarim, O. I., & ElGawady, M. A. (2016). Performance of hollow-core FRP–concrete–steel bridge columns subjected to vehicle collision. *Engineering Structures, 123*, 517-531.

Abdelkarim, O. I., & ElGawady, M. A. (2017). Performance of bridge piers under vehicle collision. *Engineering Structures, 140*, 337-352.

ACI. (2008). *Building code requirements for structural concrete (ACI 318-08) and commentary (ACI318R-08)*. Farmington Hills, MI: ACI 318.

Agrawal, A. K., Liu, G. Y., & Alampalli, S. (2013). Effects of truck impacts on bridge piers. *Advanced Materials Research, 639*, 13-25.

Billington, S. L., & Yoon, J. (2004). Cyclic response of unbonded posttensioned precast columns with ductile fiber-reinforced concrete. *Journal of Bridge Engineering, 9*(4), 353-363.

Bu, Z.-Y., Ou, Y.-C., Song, J.-W., & Lee, G. C. (2016). Hysteretic Modeling of Unbonded Posttensioned Precast Segmental Bridge Columns with Circular Section Based on Cyclic Loading Test. *Journal of Bridge Engineering, 21*(6), 04016016.

Buth, C. E., Williams, W. F., Brackin, M. S., Lord, D., Geedipally, S. R., & Abu-Odeh, A. Y. (2010). *Analysis of large truck collisions with bridge piers: phase 1. Report of guidelines for designing bridge piers and abutments for vehicle collisions* (FHWA/TX-10/9-4973-1). College Station, TX.

Chen, L., El-Tawil, S., & Xiao, Y. (2016). Reduced models for simulating collisions between trucks and bridge piers. *Journal of Bridge Engineering, 21*(6), 04016020.

Chen, L., El-Tawil, S., & Xiao, Y. (2017). Response spectrum-based method for calculating the reaction force of piers subjected to truck collisions. *Engineering Structures, 150*, 852-863.

Chen, L., Xiao, Y., Xiao, G., Liu, C., & Agrawal, A. K. (2015). Test and numerical simulation of truck collision with anti-ram bollards. *International Journal of Impact Engineering, 75*, 30-39.

Chou, C.-C., Chang, H.-J., & Hewes, J. T. (2013). Two-plastic-hinge and two dimensional finite element models for post-tensioned precast concrete segmental bridge columns. *Engineering Structures, 46*, 205-217.

Chung, C. H., Lee, J., & Gil, J. H. (2014). Structural performance evaluation of a precast prefabricated bridge column under vehicle impact loading. *Structure and Infrastructure Engineering, 10*(6), 777-791.

Consolazio, G., & Davidson, M. (2008). Simplified dynamic analysis of barge collision for bridge design. *Transportation Research Record: Journal of the Transportation Research Board,*(2050), 13-25.

Consolazio, G. R., Getter, D. J., & Davidson, M. T. (2009). *A Static Analysis Method for Barge Impact Design of Bridges with Consideration of Dynamic Amplification*: University of Florida, Department of Civil and Coastal Engineering.

Culmo, M. P. (2011). *Accelerated bridge construction-experience in design, fabrication and erection of prefabricated bridge elements and systems*. Washington, DC.

Dawood, H., Elgawady, M., & Hewes, J. (2014). Factors affecting the seismic behavior of segmental precast bridge columns. *Frontiers of Structural and Civil Engineering, 8*(4), 388-398.

Do, T. V., Pham, T. M., & Hao, H. (2018a). Dynamic responses and failure modes of bridge columns under vehicle collision. *Engineering Structures, 156*, 243-259.

Do, T. V., Pham, T. M., & Hao, H. (2018b). Numerical investigation of the behavior of precast concrete segmental columns subjected to vehicle collision. *Engineering Structures, 156*, 375-393.

El-Tawil, S., Severino, E., & Fonseca, P. (2005). Vehicle collision with bridge piers. *Journal of Bridge Engineering, 10*(3), 345-353.

ElGawady, M., Booker, A. J., & Dawood, H. M. (2010). Seismic behavior of posttensioned concrete-filled fiber tubes. *Journal of Composites for Construction, 14*(5), 616-628.

Hallquist, J. O. (2007). *LS-DYNA keyword user's manual.* Livermore Software Technology Corporation. Vol. 970. (pp. 299-800).

Hao, H., Zhang, X., Li, C., & Do, T. V. (2017). *Impact response and mitigation of precast concrete segmental columns.* Paper presented at the 12th International Conference on Shock and Impact Loads on Structures, Singapore

Hao, Y., & Hao, H. (2014). Influence of the concrete DIF model on the numerical predictions of RC wall responses to blast loadings. *Engineering Structures, 73*, 24-38.

Hewes, J. T., & Priestley, M. N. (2002). *Seismic design and performance of precast concrete segmental bridge columns* (SSRP-2001/25). University of California.

Hung, H.-H., Sung, Y.-C., Lin, K.-C., Jiang, C.-R., & Chang, K.-C. (2017). Experimental study and numerical simulation of precast segmental bridge columns with semi-rigid connections. *Engineering Structures, 136*, 12-25.

Jiang, H., & Chorzepa, M. G. (2015). An effective numerical simulation methodology to predict the impact response of pre-stressed concrete members. *Engineering Failure Analysis, 55*, 63-78.

Li, C., Hao, H., & Bi, K. (2017). Numerical study on the seismic performance of precast segmental concrete columns under cyclic loading. *Engineering Structures, 148*, 373-386.

Li, C., Hao, H., Zhang, X., & Bi, K. (2017). Experimental study of precast segmental columns with unbonded tendons under cyclic loading. *Advances in Structural Engineering, 21*(3), 319-334.

Li, J., Hao, H., & Wu, C. (2017). Numerical study of precast segmental column under blast loads. *Engineering Structures, 134*, 125-137.

Megally, S. H., Garg, M., Seible, F., & Dowell, R. K. (2001). *Seismic performance of precast segmental bridge superstructures* (SSRP-2001/24). University of California, San Diego.

Ou, Y.-C. (2007). *Precast segmental post-tensioned concrete bridge columns for seismic regions* (Doctoral dessertation). State University of New York at Buffalo Retrieved from https://ubir.buffalo.edu/xmlui/handle/10477/42969

Pham, T. M., & Hao, H. (2017a). Effect of the plastic hinge and boundary conditions on the impact behavior of reinforced concrete beams. *International Journal of Impact Engineering, 102*, 74-85.

Pham, T. M., & Hao, H. (2017b). Plastic hinges and inertia forces in RC beams under impact loads. *International Journal of Impact Engineering, 103*, 1-11.

Sha, Y., & Hao, H. (2013). Laboratory tests and numerical simulations of barge impact on circular reinforced concrete piers. *Engineering structures, 46*, 593-605.

Sharma, H., Hurlebaus, S., & Gardoni, P. (2012). Performance-based response evaluation of reinforced concrete columns subject to vehicle impact. *International Journal of Impact Engineering, 43*, 52-62.

Sideris, P., Aref, A. J., & Filiatrault, A. (2014). Quasi-static cyclic testing of a large-scale hybrid sliding-rocking segmental column with slip-dominant joints. *Journal of Bridge Engineering, 19*(10), 04014036.

Thorenfeldt, E., Tomaszewicz, A., & Jensen, J. (1987). *Mechanical properties of high-strength concrete and application in design.* Paper presented at the Proceedings of the symposium utilization of high strength concrete, Tapir Trondheim Norway

Zhang, X., Hao, H., & Li, C. (2016a). The effect of concrete shear key on the performance of segmental columns subjected to impact loading. *Advances in Structural Engineering, 20*(3), 352-373.

Zhang, X., Hao, H., & Li, C. (2016b). Experimental investigation of the response of precast segmental columns subjected to impact loading. *International Journal of Impact Engineering, 95*, 105-124.

Zhao, D.-B., Yi, W.-J., & Kunnath, S. K. (2017). Shear Mechanisms in Reinforced Concrete Beams under Impact Loading. *Journal of Structural Engineering, 143*(9), 04017089.

Zhao, D.-B., Yi, W.-J., & Kunnath, S. K. (2018). Numerical simulation and shear resistance of reinforced concrete beams under impact. *Engineering Structures, 166*, 387-401.

CHAPTER 7

EFFECTS OF STEEL CONFINEMENT AND SHEAR KEYS ON THE IMPACT RESPONSES OF PRECAST CONCRETE SEGMENTAL COLUMNS

ABSTRACT[6]

The impact responses of three precast concrete segmental columns (PCSCs), i.e. a conventional PCSC, a PCSC with the two bottommost segments confined by steel tubes, and a PCSC with all the segments confined by steel tubes (PCSC-FST), are numerically investigated and compared in this study. The behaviours of the columns subjected to various impact loads at two different impact locations, i.e. at the top and at the centre of the first segment, are considered. It is found that the use of steel confinement does not only enhance the impact resistant capacity of the PCSC but also significantly change the impact behaviours of the PCSC. While the local failure of concrete at the impacted segment governs the response of the conventional PCSC, the failure of Column PCSC-FST is associated with the fracture of the prestress tendon. The confinement with steel tubes of the two bottommost segments shifts the failure mode of the PCSC from local to global failure. Steel shear keys (SSKs) are also integrated into the PCSC-FST to increase the column shear capacity. The numerical results show that the SSKs significantly reduce the lateral displacement and shear force in the tendon when the column response is dominated by shear slippages between segments.

7.1. Introduction

Precast concrete segmental columns (PCSCs) have exhibited well-known advantages over conventional cast-in-situ concrete columns and attracted more research interests in the recent years since prefabrication constructions significantly reduce construction time, minimise site disruption and environmental impacts, and provide better constructability and construction quality control (Culmo, 2011; Ou, 2007; Sideris, 2012). Many accelerated bridge construction projects using PCSCs have been built around the world (Ou, 2007). Although PCSCs have been constructed in many projects, there are very limited studies of PCSCs under impact loads (Hao et al., 2017; Zhang et al., 2018) and vehicle collisions (Do et al., 2018b, 2019) in the

---

open literature. Most previous studies of dynamic responses of PCSCs focussed on seismic and cyclic responses (Chou & Hsu, 2008; Hewes & Priestley, 2002; Li, Hao, Zhang, et al., 2017; Ou, 2007). Since some PCSCs during their service life might be subjected to impact loads from various sources such as ship/vehicle collisions or falling rocks, understanding of the impact response of PCSCs is therefore needed for safe and economic designs of PCSCs.

Previous studies have revealed that flexural response usually dominates the response mode of PCSCs under seismic loads while they may experience different response and failure modes under lateral impact loads. These failure modes include the flexural, shear, and combined flexural-shear failure when the column is impacted by a solid impactor at the column mid-height, the base segment, and the second segment joint, respectively (Hao et al., 2017; Zhang et al., 2018). Also, by conducting the vehicle collision simulations on PCSCs, Do et al. (2019) showed that the PCSCs experienced flexural-shear failure in the first segment and the flexural damage in the second segment when the vehicle collided in the vicinity of the top of the base segment. Under vehicle collision, failure of concrete was observed concentrating mainly at the impacted region, i.e., the bottom and the second from the bottom segment. Thus, the two bottommost segments of the PCSC are suggested to be strengthened for resisting vehicle impact loads (Do et al., 2019). These two segments are also the most vulnerable segments of the PCSC when it is subjected to seismic loads with flexural cracks and concrete damage at the segment edge (Ou et al., 2009; Shim et al., 2008). Therefore, strengthening methods, i.e. steel tubes (Li, Hao, & Bi, 2017) and concrete dual-shell steel tubes (Guerrini et al., 2014; Lee et al., 2018) have been employed to enhance the seismic performance of the PCSCs. However, so far no study on PCSCs confined by steel tubes under impact loads can be found in the open literature. Besides, in the previous experimental and numerical studies, the failure of PCSCs was always governed by the failure of concrete segments while failure of tendons has not been observed even when a concrete column was strengthened by FRP wraps (Hao et al., 2017). The previous study by Do et al. (2018b) showed that when the failure occurred in the PCSC due to vehicle collisions, the maximum axial force in tendons was just about 70% of its tensile capacity. The results also indicated the imbalance between the strength of concrete segments and the prestress tendon. Since the brutal damage of concrete segment may lead to the collapse of PCSCs, the impact resistant capacity of concrete segments in the PCSCs needs be improved. Furthermore, under impact loads, PCSCs commonly exhibit an excessive lateral slippage between the segments in the vicinity of the impact point when the local shear response governs the column behaviours (Do et al., 2018b; Zhang et al., 2018). Therefore, concrete shear keys, i.e. trapezoidal prism shear keys and domed shear keys were utilised in the PCSCs to minimise the lateral slippages of the concrete segments (Hao et al., 2017; Zhang et al., 2018). The results showed that the trapezoidal prism shear keys significantly diminished the relative

155

displacement between the concrete segments, but stress concentrations around the shear keys may result in severe damages to concrete segment under impact loads, while the domed shear keys reduced the stress concentration and thus mitigated the concrete damage at the key edges but it was less effective in mitigating the relative displacement between segments. Therefore, more effective shear key designs to improve the impact performance of structures are still required.

As a continuation of the previous studies, this study aims to propose a strengthening method in PCSCs, i.e. concrete-filled steel tubes, to increase their impact-resistant capacity. It is noted that the effects of steel confinement on improving the dynamic capacity of a monolithic column under impact loads have been well investigated and discussed in many previous studies (Aghdamy et al., 2017; Han et al., 2014; Hu et al., 2018; Wang et al., 2013). Thus, in this study, numerical models of PCSCs consisting of concrete filled steel tubes are developed and carefully verified against experimental results from the previous studies (Wang et al., 2013; Zhang et al., 2016). Then, the impact responses of three PCSCs including a conventional PCSC, a PCSC with the two bottommost segments made of concrete-filled steel tube, and a PCSC with all segments made of concrete filled steel tubes (PCSC-FST) are considered. Two different impact locations, i.e. at the top and the centre of the base segment, are considered to examine the response of the columns. Besides, steel shear keys (SSKs) are also utilised at the first two segment joints of the PCSC-FST to reduce the lateral slippage between concrete segments and thus minimise the shear force and prevent the shear damage of the prestress tendon.

7.2. Finite element model

7.2.1. Numerical model development

7.2.1.1 Material models and strain rate effects

For concrete, reinforcements, and posttensioned tendons, the material models and strain rate effects have been introduced in Sections 2.2.2 and 5.2.2.

In addition, the material model, namely *Mat_Plastic_Kinematic (Mat_003), is used to model steel tubes and steel ducts. Five parameters of steel including the yield strength, elastic modulus, Poisson's ratio, tangent modulus, and ultimate plastic strain are required in this material model, as given in Table 7-1. To consider the strain rate effects of steel tubes under impact loads, Cowper and Symonds (1957) model is adopted. The dynamic yield strength f_{yd}, at the strain rate $\dot{\varepsilon}_d$ is expressed below:

156

$$f_{yd} = f_{ys} \left[1 + \left(\frac{\dot{\varepsilon}_d}{c} \right)^{\frac{1}{p}} \right]$$

(7-1)

where f_{ys} is the static yield strength of the steel tubes; p and c are the constant parameters for determining the strain rate effect, taken as 5 and 40.4, respectively (Yan & Yali, 2012).

Furthermore, to generate the initial prestress load in the steel tendon and the column, a temperature-induced shrinkage method, which was introduced in the previous studies (Do et al., 2018b; Jiang et al., 2012; Nakalswamy, 2010) is employed in this study. The LS-DYNA material model named *Mat_Elastic_Plastic_Thermal (Mat_004) is utilised to simulate the steel tendons. Moreover, longitudinal and transverse reinforcements are modelled by an elastic-plastic material model, namely *Mat_Piecewise_Linear_Plasticity (MAT_24). The DIF of the tensile strength of reinforcement steel proposed by Malvar and Crawford (1998) is used. The solid steel impactor and anchors are simulated by an elastic material model, namely *Mat_Elastic (Mat_001). The input parameters of the material models are given in Table 7-1.

7.2.1.2 Erosion criterion

In this study, the LS-DYNA keyword named *Mat_Add_Erosion is employed to remove the damaged elements of concrete and tendon during the simulation. This erosion function is crucial in studying the impact and blast behaviours of structures since it avoids computation over-flow caused by large deformation of damaged elements. The reliability of this erosion feature has been proven in many previous studies (Do et al., 2018a, 2018b; Li & Hao, 2014). The maximum principal strain at failure is used in the simulation as a criterion to eliminate failed elements. In the present study, the value of 0.7 is used as the erosion criterion for concrete elements because it gives good predictions of concrete damage as compared to experimental tests (Do et al., 2019). For steel tendon, the maximum principal strain at failure (0.05) is used based on its mechanical properties (Naaman, 1982). It is noted that for steel tube material, damaged elements will be deleted when the maximum principal strain reaches the ultimate plastic strain of 0.12 (Abdelkarim & ElGawady, 2016), as defined in the material model, presented in Section 7.2.1.1 and Table 7-1.

7.2.1.3 Numerical model and contact definitions

In the simulation, steel tubes, steel tendons, shear keys, impactor, and all concrete elements, i.e. concrete segments, added mass, and footing are modelled by constant stress solid elements while steel reinforcements are simulated by using 3-nodes beam elements. The contact between the impactor and column, between segments, between steel tube and infilled concrete, and between concrete segment and prestress tendon are simulated by the LS-DYNA keyword *Contact_Automatic_Surface_to_Surface while the perfect bonded contact is assumed for the

steel reinforcements and their surrounding concrete. The static and dynamic friction coefficient of the concrete-to-concrete contact and the steel and the concrete in this study are taken as 0.6 and 0.5 (Abdelkarim & ElGawady, 2016; ACI, 2008; Aghdamy et al., 2015; Do et al., 2018b, 2019), respectively. The column is fixed at all degrees of freedom at the bottom face of the footing in the simulation as in the experimental tests (Zhang et al., 2016).

Table 7-1 Material properties in the LS-DYNA model

Column components	FE material model	Material properties	Value	Unit
Concrete segments	*Mat_072R3	Compressive strength	34	MPa
Steel tubes	*Mat_003	Yield strength	298	MPa
		Elastic modulus	200	GPa
		Poission's ratio	0.3	
		Tangent modulus	1,102	MPa
		Ultimate plastic strain	0.12	
Tendon	*Mat_004	Tensile strength	1,860	MPa
		Elastic modulus	210	GPa
		Poission's ratio	0.3	
		Thermal expansion coefficient	10^{-4}	
Longitudinal reinforcements	*Mat_024	Yield strength	500	MPa
		Elastic modulus	210	GPa
		Poission's ratio	0.3	
Transverse reinforcements	*Mat_024	Yield strength	300	MPa
		Elastic modulus	210	GPa
		Poission's ratio	0.3	
Anchors, steel impactor	*Mat_001	Elastic modulus	210	GPa
		Poission's ratio	0.3	

7.2.2. Model verifications

It is noted that currently no available impact tests on PCSC-FSTs can be found in the open literature. Hence, in this study, a pendulum impact test on the PCSC (Zhang et al., 2016) and a lateral impact test on Concrete Filled Steel Tubular (CFST) columns (Wang et al., 2013) are used to calibrate the proposed numerical model.

7.2.2.1 PCSC under pendulum impact loads

The verification of the numerical model of PCSC under pendulum impact loads has been presented previously, please refer to Section 5.2.3.

7.2.2.2 CFST columns under transverse impact loads

The experimental tests of CFST columns under impact loads conducted by Wang et al. (2013) is adopted in this section to verify the accuracy of the numerical model in simulating the responses of concrete columns with steel tube confinement subjected to impulsive loading. In the experiment, two different CSFT groups, i.e. DBF and DZF, which had a length of 1,200 mm and an outer diameter of 114 mm, were tested under a drop weight of 229.8 kg at various impact velocities ranging from 3.9 m/s to 11.7 m/s (see Figure 7-1a). In the DBF group, the thickness of the steel tube and steel tensile strength were 1.7 mm and 232 MPa, respectively, while those in the DZF group were 3.5 mm and 298 MPa, respectively. In the present study, the impact responses of these columns under three different impact velocities, i.e. 5.4 m/s (DBF12), 7.6 m/s (DBF11), and 11.7 m/s (DZF26) are simulated. These tests are chosen since they represent columns with different steel tube thicknesses and tensile strengths under a wide range of impact velocities.
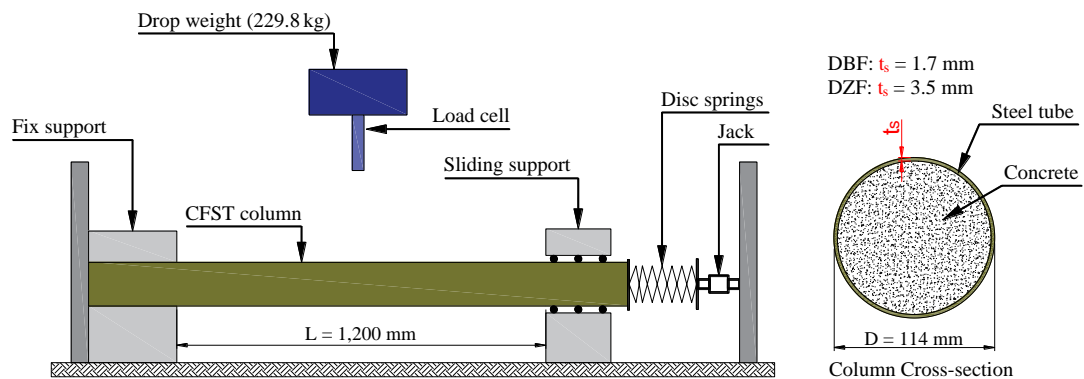
(a) Experimental set up [Data from Wang et al. (2013)]
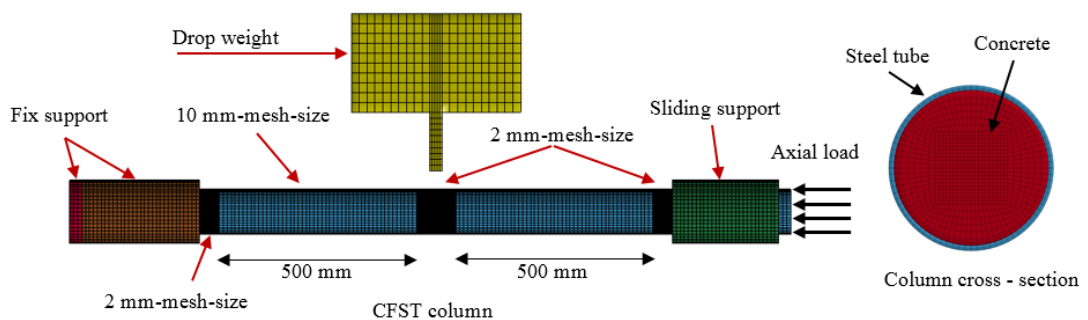
(b) Numerical simulation

Figure 7-1 Experimental test and numerical model of the CFST under impact loads.

The numerical model of these tests is shown in Figure 7-1b. In the test, axial load was applied to the column specimen through disc springs as shown in Figure 7-1a. This axial force is simulated by applying pressure on the top surface of the column in the numerical model as

shown in Figure 7-1b. One side of the column is fixed while the other side can move in the axial direction with sliding support as shown in Figure 7-1. Based on the convergence test, the column includes 80 meshes along the perimeter while the minimum mesh size at the column ends and mid-height in the longitudinal direction is 2 mm, see Figure 7-1b. It is noted that the mesh size at these locations is 2 mm, which is smaller than the mesh size of 10 mm at the other part of the column, for simulating the fracture of the steel tube as observed in the experiment. The material model, strain rate effects, erosion criterion, and contact definitions are the same as those described in Section 7.2.
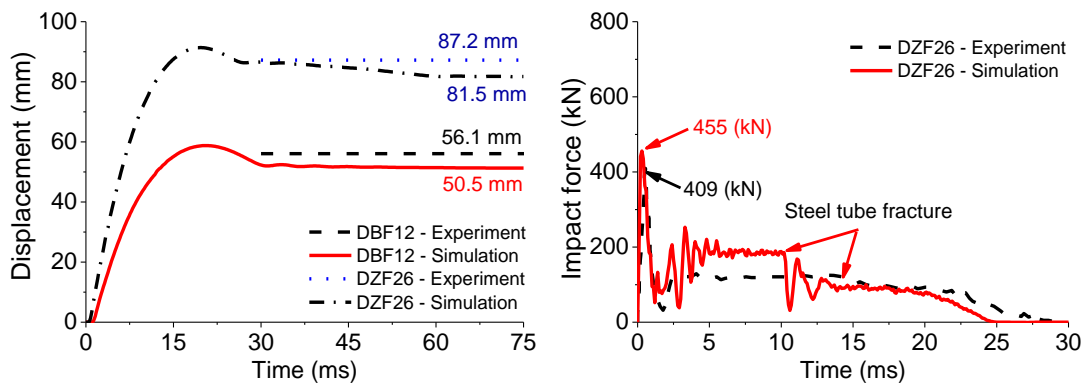
(a) Lateral displacement

(b) Impact load time histories

Experimental test

Numerical simulation
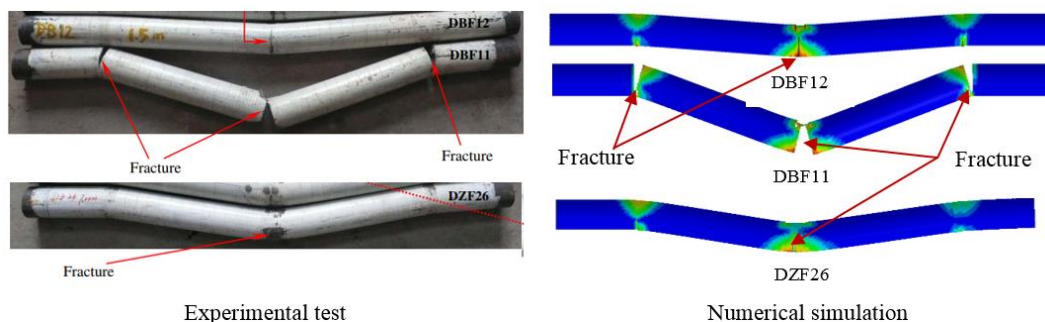
(c) Column failure mode: DBF12 (V=5.4 m/s), DBF11 (V=7.6 m/s), and DZF26 (V=11.6 m/s)

Figure 7-2 Numerical verification of the CFST under impact loads.

The comparisons between the numerical results and the experimental results in terms of displacement, impact force time histories, and failure mode are shown in Figure 7-2. The residual displacement of Columns DBF12 and DZF26 in the numerical simulation are 50.5 mm and 81.5 mm, respectively while those in the experimental tests are 56.1 mm and 87.2 mm, respectively (see Figure 7-2a). Also, the impact force time histories in the experiment are reasonably simulated by the numerical model in which the PIF in the experiment and simulation are 409 kN and 455 kN, respectively (see Figure 7-2b). The impact duration, the plateau value of the impact force and the fracture point from the experimental test are also

160

predicted by the numerical simulation, as presented in Figure 7-2b. Moreover, both the global deformation of the columns and the fracture of the steel tube at the column mid-height and at the column end are well simulated by the numerical model (see Figure 7-2c). These results show that the numerical model has the ability to predict the impact responses of CFST columns with different thicknesses and tensile strengths of the steel tube under various impact velocities.

The above calibrations and comparisons confirm that the present material models, strain rate effects, contact definitions, and numerical techniques are able to predict well the dynamic responses of the PCSC and CFST columns under impact loads.

7.3. Simulations of PCSC-FST

7.3.1. Column configurations

Based on the proposed modelling techniques, the numerical models and impact responses of three PCSC columns including a conventional PCSC without confinements (PCSC1), a PCSC with steel tubes confining the two bottommost segments (PCSC2), and a PCSC with steel tubes confining all concrete segments (PCSC3), are then built and investigated, as presented in Figure 7-3a. Each PCSC consists of five segments of 200-mm diameter circular cross-section. The column slenderness and the compressive strength of concrete are 8 and 34 MPa, respectively, the same as those used in the experimental tests (Zhang et al., 2016; Zhang et al., 2018). A solid block with the mass of 10.5 ton representing the superstructures is placed on the top of the column. A concrete footing of dimensions of 800 mm x 800 mm x 250 mm (Depth x Width x Height) is also included in the model to support the column. A steel tendon which has a cross-section area of 150 mm^2 and the tensile strength of 1,860 MPa is placed at the centre of each column to generate a prestress load on the PCSCs. The tendon is initially tensioned with the prestress level of 50% of its capacity, producing a compression load of 135 kN on the columns. Thus, the total vertical load from the tendon and the added mass is about 240 kN which equals 22.5% of the axial compressive strength of Column PCSC1. Moreover, a steel duct with an outer diameter of 30 mm and a thickness of 2 mm is placed at the centre of each concrete segment to reduce stress concentration on concrete segment caused by the contact force between column segments and the tendon when shear slippages occur (see Figure 7-3). Furthermore, each concrete segment of Column PCSC1 is reinforced by 8-mm-diameter stirrups at 50 mm spacing and eight 10-mm-diameter longitudinal deformed bars evenly placed in the segment along the circumference with the concrete cover of 15 mm. The yield strength of these reinforcements is 300 MPa and 500 MPa, respectively. Meanwhile, the thickness and the yield strength of the steel tube which replaces the reinforcements in the first and the second segment of Column PCSC2 and all segments in Column PCSC3 are 2 mm and 298 MPa,

respectively. It should be noted that no reinforcements are used in these segments covered by the steel tubes. Also, the total volume of the longitudinal and transverse reinforcements in the concrete segment of Column PCSC1 is similar to the volume of the tube in each segment of Columns PCSC2 and PCSC3. The column is simply placed on the footing with the only anchor from the posttension tendon as shown in the figure. The design of these columns is presented in Figure 7-3a. In the simulation, the column is modelled with 80 meshes along the circumferential direction of the cross-section while the vertical mesh size is 5 mm, as shown in Figure 7-3b. The bottom face of the footing is fully fixed in the simulation.

(a) Column configurations

(b) Numerical simulation
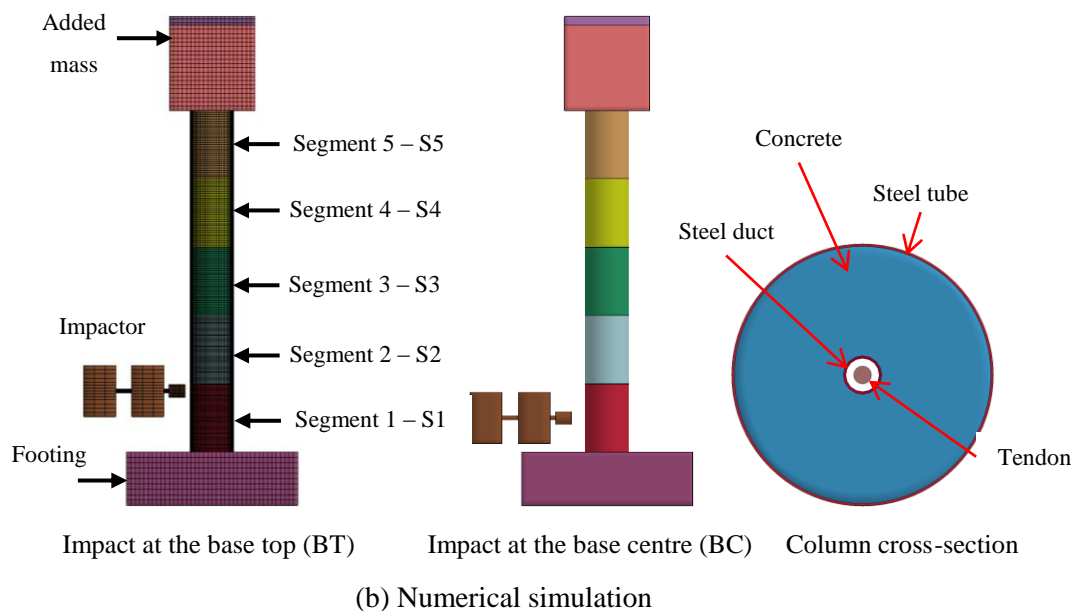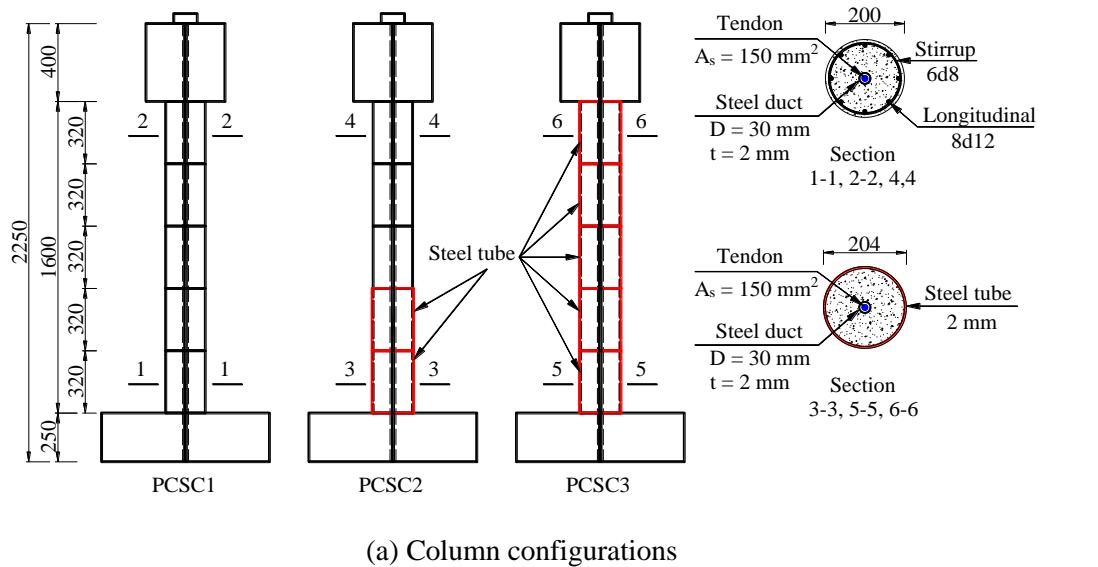
Figure 7-3 Design of the three PCSCs and impact loading locations.

7.3.2. Loading conditions

The steel solid impactor (300 kg) will be used in this study to impact the columns. For Columns PCSC1 and PCSC2, six velocities, i.e. 1.5 m/s (IP1.5), 2.0 m/s (IP2), 2.5 m/s (IP2.5), 3.0 m/s (IP3), 4.0 m/s (IP4) and 5.0 m/s (IP5) are used to impact the column to failure, while Column PCSC3 is subjected to three more impacts of velocities of 6.0 m/s (IP6), 8.0 m/s (IP8), and 10.0 m/s (IP10) to failure. These impact velocities are selected since they generate distinguished failure modes on these columns from minor damage of concrete to the failure of the tendon or collapse of the entire column. In addition, in the design of structures under vehicle collisions, a bridge column is usually assumed to be impacted at about 1.5 m above the ground level (AASHTO, 2012). Thus, the contact point between a vehicle model and a bridge column in a real accident might be at the vicinity of the centre or the top of the base segment depending on column dimensions and vehicle models. Hence, in this study, two different impact locations, i.e. the top of the base segment (the base top - BT) which is close to the joint between Segments S1 and S2, and the centre of the base segment (the base centre - BC), are considered, as shown in Figure 7-3b. The initial conditions of impact loading are also given in Table 7-2.

7.3.3. Impact force time histories
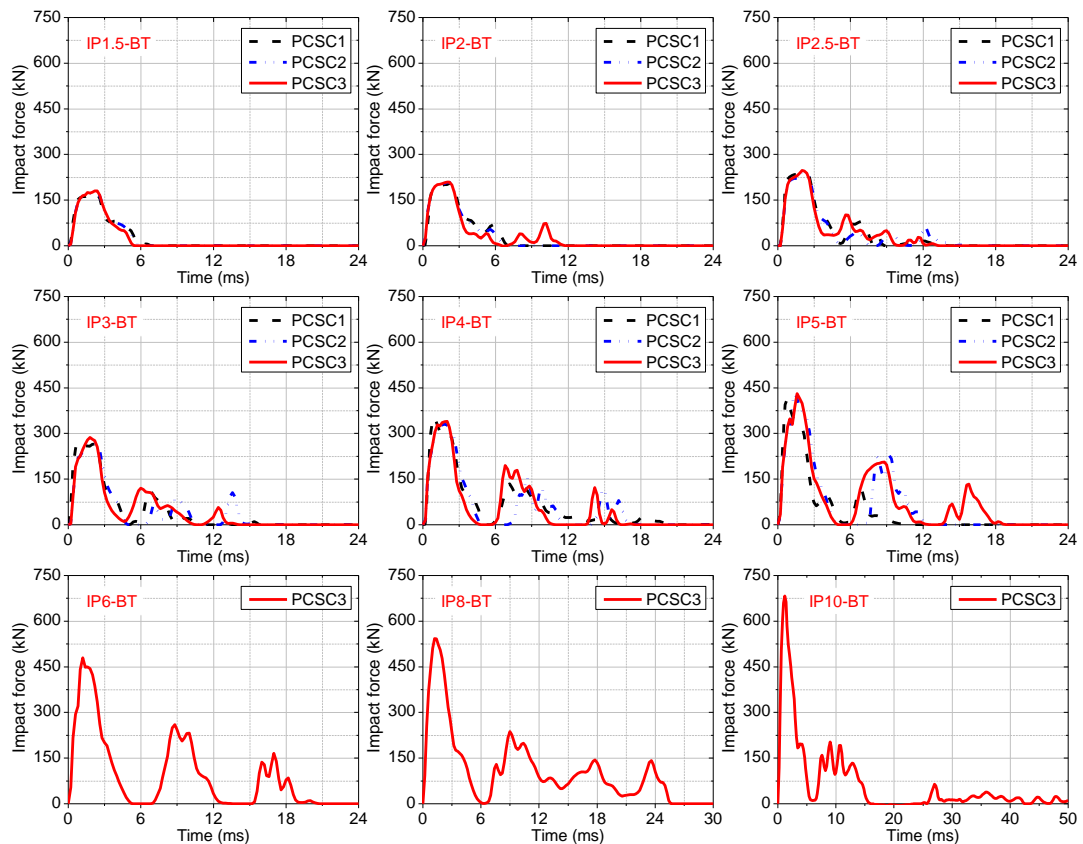
(a) Impacted at the base top (BT)

163
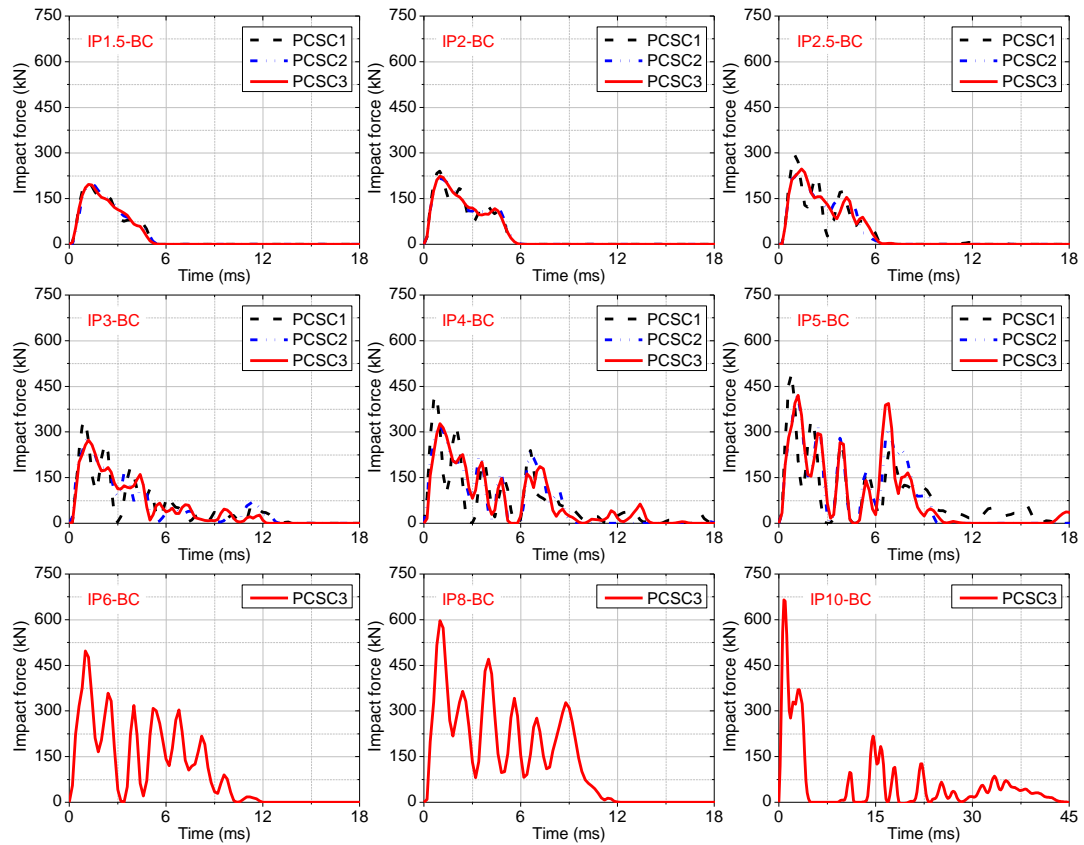
(a) Impacted at the base centre (BC)

Figure 7-4 Impact force time histories.

Figure 7-4 presents the impact force time histories of the three columns under various impact velocities when the impactor hits the PCSCs at the top and the centre of Segment 1, respectively. It can be seen in all the graphs that the first interaction between the column and impactor always generates the PIF at about 2-3 ms, followed by several PIFs with a smaller magnitude associated with a high-frequency vibration of the concrete segment during the impact force phase (Do et al., 2018b). Except for the first three impact conditions, only one PIF is produced due to the lower impact energy due to the low velocity of the impact load. It is worth mentioning that when the column is impacted at the base centre, more number of PIFs with a shorter time gap between these peaks (about 1.5 ms) are produced in the column as compared to the impact at the base top (about 6 ms). For example, under impacts IP6 and IP8, with the impact location at the top of the base segment, four peaks are formed in about 24 ms of the impact force phase (see Figure 7-4a), while there are seven PIFs in about 10.5 ms when the impact location is at the base centre (see Figure 7-4b). These differences can be explained by the change of the natural period of the segment-self vibration when varying the impact location. When the impactor hits the column at the top of Segment 1, the bottom segment reacts as a propped cantilever with the applied load at the top. Meanwhile, the segment responds to the impact force more like a simply supported beam in case the column is impacted

164

at the segment centre. Therefore, the stiffness of the impacted segment in the latter is much higher than that of the former. The higher stiffness leads to shorter vibration period of the segment which results in the occurrence of more PIFs. It is worth mentioning that the difference between the number of PIFs when changing the impact location has also been recorded in the previous experimental test (Zhang et al., 2018) but it has not been clearly discussed and explained. The numerical results show that with the similar initial impact energy, the variation of the impact location may change the impact force time histories in the PCSC owing to the dissimilar of the segment stiffness. For Column PCSC3 under IP10 in both impact locations, the fracture of the tendon occurs after the first PIF which significantly reduces the column stiffness leading to the reduction of the magnitude of the latter PIF, as shown in Figure 7-4. Thus, the impact force time histories under this impact velocity is dissimilar to the other velocities. Moreover, a slight difference can be found in the impact force time histories of the three columns due to the difference in the contact stiffness, see Figure 7-4. The PIF and impulse of these columns also increase with the impact velocity, as given in Figure 7-4 and Table 7-2.

7.4. Impact responses and failure modes

7.4.1. Impact at the top of the base segment

7.4.1.1 Column responses and failure modes

Figures 7-5, 7-6, and 7-7 show the progressive deformation and damage of the three columns under different impact velocities when the impactor strikes the columns at the base top. Since the first four impact velocities cause insignificant deformation and damage to concrete, the progressive deformation of the columns under these impact conditions are not presented herein but the column plastic strain and the axial force in the tendon will be discussed in the subsequent section. Generally, although the three columns are designed with the same amount of materials, these columns perform differently under impact loads and experience different column failure modes. The partial strengthening at the local impacted segments, i.e., the two bottom segments, shifts the failure of the PCSC from the local diagonal shear failure in Column PCSC1 to the compressive damage of the concrete segment owing to segment rocking response in the upper part in Column PCSC2. Meanwhile, the response of Column PCSC3 is significantly affected by the joint openings resulting in the fracture of tendon. Columns PCSC 1 and PCSC2 fail under the impact velocity of 4m/s and 5 m/s, respectively; while Column PCSC 3 can withstand higher impact velocities up to 10 m/s.

For Column PCSC1, when the impact velocity is 4 m/s, a diagonal shear crack appears in Segment 1 at $t = 4$ ms due to the column – impactor interaction. Then, at $t = 14$ ms, the previous shear crack in Segment 1 is further enlarged due to the later impact force leading to the collapse

of the column by a diagonal shear failure at $t = 22$ ms. Besides, a vertical crack in the upper segments is also observed in Column PCSC1, as presented in Figure 7-5a, because of the application of the large axial force in the compressive side of the column when the joint opens. It was previously reported that under impact loads, the axial force in the PCSC increases significantly due to the stress wave propagation from the impact location to the column end (Do et al., 2018a, 2019). In addition, the joint openings also increase the axial force in the tendon, producing more compression force on the column. The significant increase of the axial force in the compression side of the segment thus causes vertical cracks in the concrete segments (see Figure 7-5a). It is noted that the vertical crack in the concrete segment was also observed in the previous experimental tests (Zhang et al., 2018). With the impact velocity of 5 m/s, a local diagonal shear failure directly appears in Segment 1 (at $t = 6$ ms) after the first PIF acting on the column, leading to the failure of the column at $t = 10$ m/s (see Figure 7-5b). It is worth mentioning that the diagonal shear failure of Column PCSC1 in these simulations is similar to the failure of the PCSC observed in the previous impact tests (Zhang et al., 2018) and under vehicle collisions (Do et al., 2019; Hao et al., 2018) (see Figure 7-5b), which again shows the reliability of the current simulation in predicting the response of the PCSC under impact loads. The results also demonstrate that the base segment is the most critical segment of the PCSC under impact loads where the diagonal shear failure of the segment governs the column failure mode.

(a) IP4 (V = 4 m/s) (b) IP5 (V = 5 m/s)
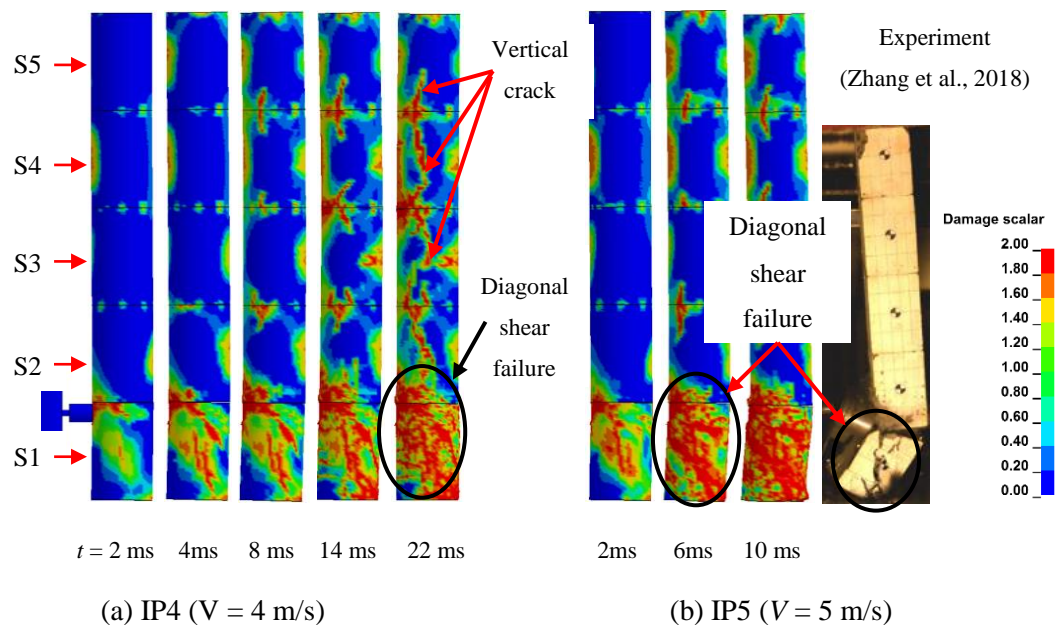
Figure 7-5 Impact response of conventional PCSC – Column PCSC1 (BT).

On the other hand, the impact response of Column PCSC2 is completely different from Column PCSC1 in which compressive damage of concrete at the segment edge leads to the failure of the column. Under impact IP4, when the PIF occurs on the column at $t = 2$ ms, minor

concrete damage at the edges of the impacted segment is observed due to the opening of the second joint while the other segments have no damage (see Figure 7-6a). Afterward, the joints in the upper part of the column start to open on the right side whilst the added mass on the top slightly moves to the left side. The movement of the heavy added mass on the column top together with the axial load in the tendon results in a large eccentric load applied on the left side of the segment joints. Thus, at $t = 10$ ms, compressive damage at the edge of Segments 3 and 4 occurs on the left side of the column, as shown in Figure 7-6a, but the column still survives under this impact condition. Moreover, the increase of impact velocity to 5 m/s (IP5), which enlarges the joint opening and increases the eccentric load on the top, results in a huge stress concentration and thus severe damage of concrete at the edge of Segments 3 and 4 at $t = 8$ ms (see Figure 7-6b). The column then fails because of the failure of Segment 4 at $t = 14$ ms. It should be noted that the diagonal shear failure in the impacted segment does not occur in Column PCSC2. This observation indicates that the dynamic shear capacity of concrete segments has been considerably increased by using the steel tube to confine the concrete segment as compared to the traditional transverse reinforcements.

(a) IP4 (V = 4 m/s)   (b) IP5 (*V* = 5 m/s)
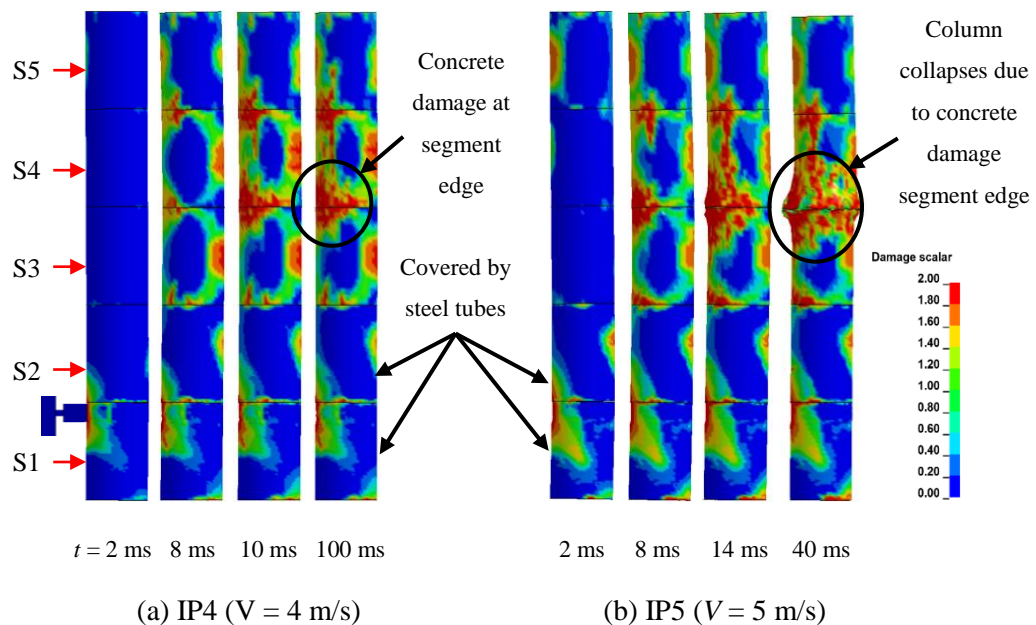
Figure 7-6 Impact response of PCSC with partial strengthening – Column PCSC2 (BT).

The deformation and impact response of Column PCSC3 are shown in Figure 7-7. Under impact IP5 (*V* = 5 m/s), the column exhibits concrete damage at the edge of Segment 1 and some flexural cracks at the mid-height of Segments 2, 3, and 4 due to the flexural response of the column, but no severe failure of concrete occurs in Column PCSC3 during this impact event (see Figure 7-7a – IP5). The stress distribution in the steel tubes of Column PCSC3 under the impacts IP5 is also presented in Figure 7-7b – IP5. As can be seen that the stress in the steel tubes generally consists of three main phases, i.e. at the PIF (Stage 1), when all the joints

open (Stage 2), and free-vibration (Stage 3). When the impact force reaches the PIF (at $t = 2$ ms), the stress is mainly concentrated in the two compression edges of Segment 1 due to the joint openings at the two bottommost joints while that in the other segments is less significant (see Figure 7-7b – Stage 1). Stress in the steel tubes of the upper segments then appears in the left side of the column at $t = 12$ ms when all the joints open caused by the global deformation of the column (see Figure 7-7b – Stage 2). It is noted that during this period if steel confinement is not provided in the upper part of the column, the compressive damage at the segment edge, e.g. Column PCSC2, will occur due to the stress concentration on the compression side. In Stage 3, stress in the steel tubes still concentrates at the edge of all the segments but becomes less significant. However, the residual stress remains in the top edge of Segment 1 because of the plastic deformation of the concrete around the impact point and segment edge (see Figure 7-7b – Stage 3). When the impactor collides to the column with the impact velocity of 6 m/s (IP6), a diagonal shear crack occurs in Segment 1 at $t = 12$ ms while just minor compressive damage at the edge of Segments 3 and 4 is observed (see Figure 7-7a – IP6). In this case, the stress in the steel tubes is also distributed along the shear crack because of the expansion of the concrete segment, as presented in Figure 7-7b – IP6 – Stage 2. Although the diagonal shear crack appears in Segment 1, the column still stands after this impact owing to the effect from the steel confinement. This is the primary advantage of the PCSC-FST as compared to the conventional PCSC where a diagonal shear failure of the base segment causes the collapse of the conventional PCSC. It is worth mentioning that the stress in the steel tubes is sometimes higher than its static yield strength of 298 MPa, e.g. 350 MPa (IP5) and 370 MPa (IP6, IP10) as presented in Figure 7-7b, but no damage occurs owing to the strain rate effects. The results indicate that both the local strengthening at the impacted segment and the confinement in the upper segments can significantly enhance the impact load resistant capacity of the PCSC. While the use of steel tube at the base segment only protects the column from the brutal shear damage of concrete segment (Stage 1), it shifts the damage to the upper segments with a marginal increment of the impact resistant capacity of the segmental column. Confining all the concrete segments of the PCSC can significantly increase the impact load resistant capacity of the column because the compressive damage of the concrete at the segment edge due to the global deformation (Stage 2) can be well mitigated. Thus, strengthening all concrete segments of the PCSC is suggested instead of strengthening only the bottom or impacted segment. The deformation and response of Column PCSC3 at the impact velocity of 10 m/s is presented in Figure 7-7a – IP10. The first PIF from the impactor causes a severe diagonal shear crack in Segment 1, local concrete damage at the impact area and openings at the first and second joints at $t = 2$ ms. The opening at these joints then continues increasing due to the large impact energy from the impactor while the other segment joints in the upper part of the column also start to open. With the large joint opening and increase in the number of opened joints, the axial force

in the tendon reaches its maximum principal strain at $t = 12$ ms causing the fracture of the posttension tendon (see Figure 7-7a – IP10).
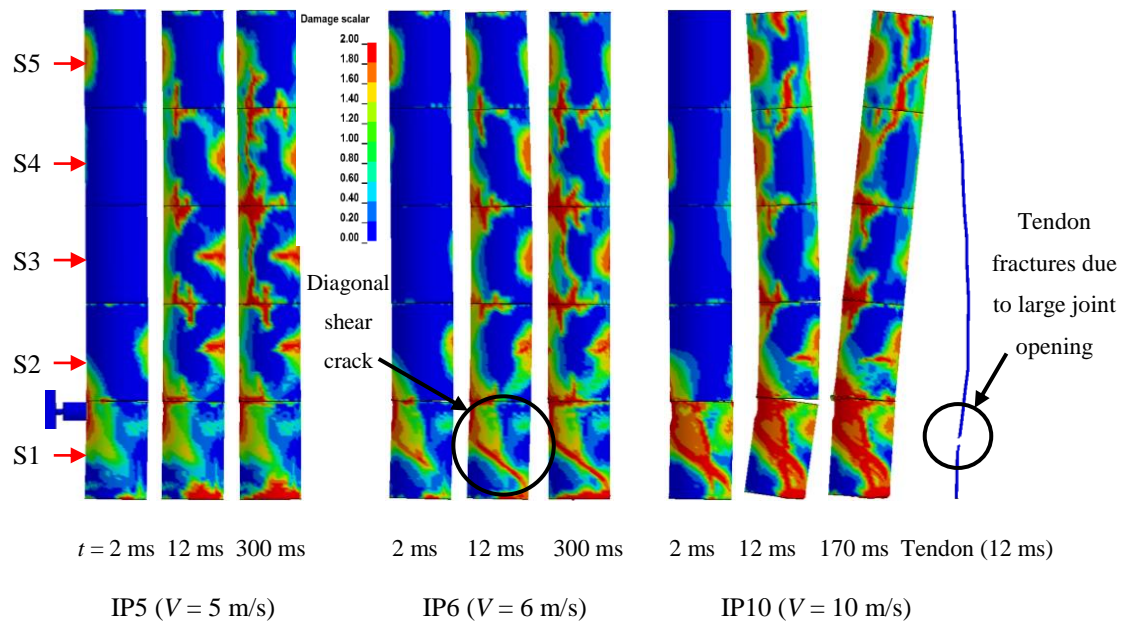
(a) Concrete and tendon
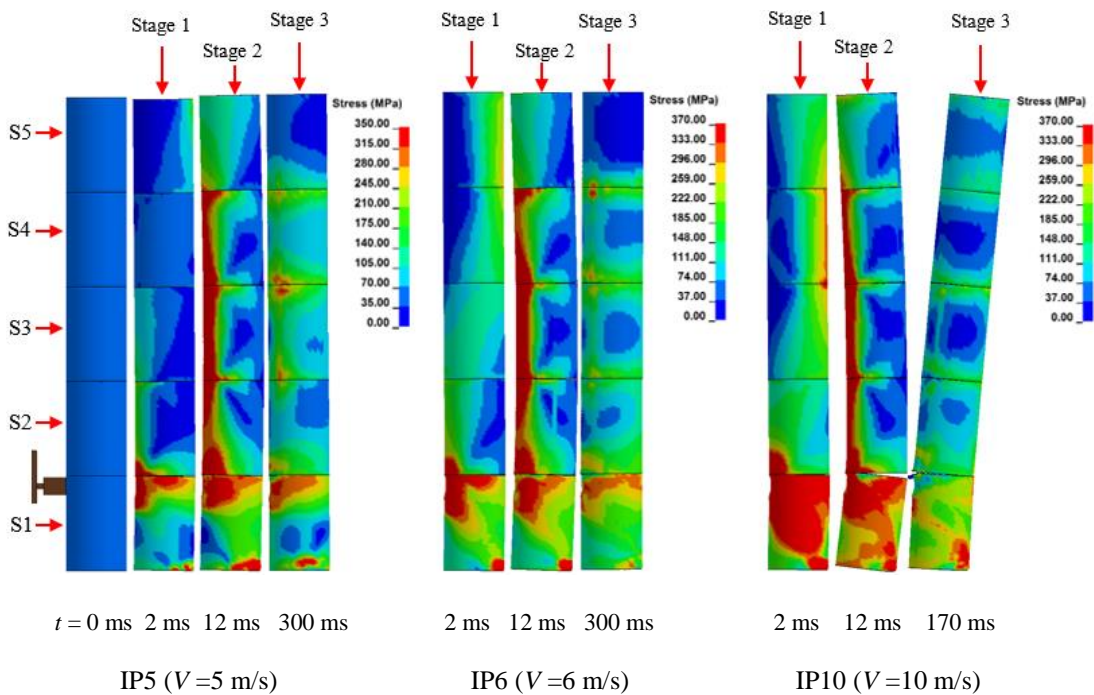
(b) Steel tube

Figure 7-7 Impact response of PCSC-FST – Column PCSC3 (BT).

Table 7-2 Impact conditions and numerical results

Impact location	No.	Velocity V (m/s)	PCSC1					PCSC2					PCSC3				
			PIF (kN)	Impulse (Ns)	Maximum force in Tendon			PIF (kN)	Impulse (Ns)	Maximum force in Tendon			PIF (kN)	Impulse (Ns)	Maximum force in Tendon		
					Axial (kN)	Shear (kN)				Axial (kN)	Shear (kN)				Axial (kN)	Shear (kN)	
Segment joint	IP1.5	1.5	173.1	581.8	146.3	1.8		175.4	574.1	144.8	2.7		180.4	544.2	144.9	1.0
	IP2	2.0	205.9	731.3	153.9	1.8		209.7	703.7	150.9	1.3		209.3	732.0	149.2	1.7
	IP2.5	2.5	238.0	888.4	163.2	2.2		244.9	878.7	156.1	2.0		247.2	896.1	153.7	2.3
	IP3	3.0	276.4	1051.9	174.6	2.8		273.2	1039.9	163.2	1.8		286.9	1069.3	158.4	2.6
	IP4	4.0	351.9	1504.3	195.4	2.6		330.5	1385.8	183.0	2.4		339.6	1376.2	175.5	2.8
	IP5	5.0	415.3	1110.4	197.5	5.6		431.3	1597.9	205.9	4.3		431.1	1860.3	190.2	4.1
	IP6	6.0											499.8	2312.7	225.3	6.9
	IP8	8.0											581.3	3204.4	259.2	16.8
	IP10	10.0											682.8	3313.9	277.4*	29.1*
Base centre	IP1.5	1.5	203.3	549.9	137.6	1.2		197.4	556.0	136.2	1.0		197.0	547.9	139.1	0.6
	IP2	2.0	241.2	676.7	139.1	2.6		216.8	703.7	138.3	1.9		224.1	683.5	140.7	1.3
	IP2.5	2.5	293.0	745.8	141.7	1.8		249.1	756.8	140.9	2.7		247.1	770.6	143.2	2.7
	IP3	3.0	337.3	957.5	146.4	2.1		277.7	972.5	144.5	2.0		273.4	954.9	144.3	2.7
	IP4	4.0	420.8	1250.6	155.1	6.0		321.1	1227.6	155.8	4.6		327.3	1247.4	155.7	4.9
	IP5	5.0	491.9	1598.3	160.3	30.5		418.0	1576.3	171.8	58.7		420.7	1563.7	168.4	63.8
	IP6	6.0											496.7	1846.7	179.1	92.1
	IP8	8.0											597.1	2505.4	191.4	114.5
	IP10	10.0											664.8	2811.2	143.2*	125.4*

(a) PCSC1   (b) PCSC2

(c) PCSC3

Figure 7-8 Damage to columns and its failure mode (BT).

It is noted that in PCSCs, a tendon plays two important roles: (1) the axial force induced from the tendon provides the shear resistance due to friction between the segments against lateral loads and (2) the tendon resists the tensile stress in the PCSC when the column is under flexural bending. If the tendon fractures, the column loses its flexural capacity and significantly reduces its shear resistance since the friction-based shear resistance is now only based on the self-weight of the upper segments and superstructures. As a result, the segmental column is considered failed when tendon fracture occurs. It is worth mentioning that the failure of the prestress tendon has not been observed in any previous studies of PCSCs under impact loads or vehicle collisions. Without steel tube confining concrete segment, failure of the concrete

171

material absorbs significant amount of energy and causes the column collapse. When the concrete segment is confined by steel tube, damage to concrete material is less severe. Impact force induces larger joint openings between concrete segments and large flexural response of the column. These increase the stress in posttensioned tendons and result in the rupture of tendons. The results also indicate that the dynamic capacity of the PCSC has been significantly increased when it is confined by steel tubes in all concrete segments. While the failure of the concrete segment in Column PCSC1 occurs at $V = 4$ m/s, Column PCSC3 survives until the impact velocity of 10 m/s that causes tendon fracture, instead of the significant damages to the concrete segment. It is noted again that the total volume of reinforcements in Column PCSC1 is equal to the total volume of steel tube in Column PCSC3.

The concrete damage and failure mode of the three columns under various impact loading conditions when impacted at the segment joint are compared in Figure 7-8. As can be seen that even though the conventional PCS column usually fails by local damage at the two bottommost segments (see Figure 7-8a), partially strengthening the two segments only marginally improves the impact resistant capacity of the column because it shifts the failure upwards with the compressive damage at the edge of the concrete segment (see Figure 7-8b). In addition, strengthening all the concrete segments of the column results in excellent performance. Although a diagonal shear crack appears at the base segment from impact IP6 ($V = 6$ m/s), the column still firmly stands until impact IP10 ($V = 10$ m/s) where the fracture of the tendon is observed (see Figure 7-8c). The use of steel tube at the base segment increases the dynamic shear capacity of the segment as the diagonal shear failure occurs in Column PCSC1 under the impact IP4 while a shear crack of Column PCSC3 appears at the impact IP6.

7.4.1.2 Tendon force time histories

The axial force time histories of the tendon of the three columns are presented in Figure 7-9. The results show that the axial force in the tendon generally increases to its peak by the occurrence of the openings at the two bottommost joints (at $t = 5$-6 ms) at the PIF before reducing and oscillating around its initial prestress level in the free vibration phase of the column, e.g. the first four impact velocities (see Figures 7-9a, b and c). When failure of concrete occurs in the columns, the axial force in the tendon then significantly drops from the peak value. For instance, under impact IP5, when the diagonal shear failure occurs in Column PCSC1 due to the first PIF, the axial force in the tendon plunges from its peak at 200 kN to 80 kN just in about 6 ms (see Figure 7-9a). For Column PCSC2, after returning to the initial prestress level, the axial force in the tendon then considerably decreases at 14 ms due to the compressive damage of concrete at the joint between Segments 3 and 4 (see in Figure 7-9b). Different from the other two columns, after the first peak, the axial force in the tendon of Column PCSC3 exhibits another peak with the similar magnitude in the last four impact

velocities, i.e. IPs 5-10, because of the openings of all segment joints (see Figure 7-9c). After the first peak at about 5–6 ms, the segment joints in the upper part of Columns PCSC3 open due to the global deformation of the column caused by the first PIF. In the meantime, the latter PIF from the impactor again causes the opening at the two bottommost joints. These openings of the segment joints thus result in the second peak in the axial force of the tendon. After these two peaks, the axial force time histories in the tendon then drops and fluctuates around its initial prestress level except in the last impact IP10 where the tendon fractures at the second peak due to the large opening of all segment joints. It is noted that the tendon ruptures at the second peak when the strain in the tendon reaches the maximum principal strain at failure (0.05), as defined in Section 7.2.1.2.

(a) PCSC1

(b) PCSC2

(c) PCSC3

(d) Maximum axial load level versus PIF
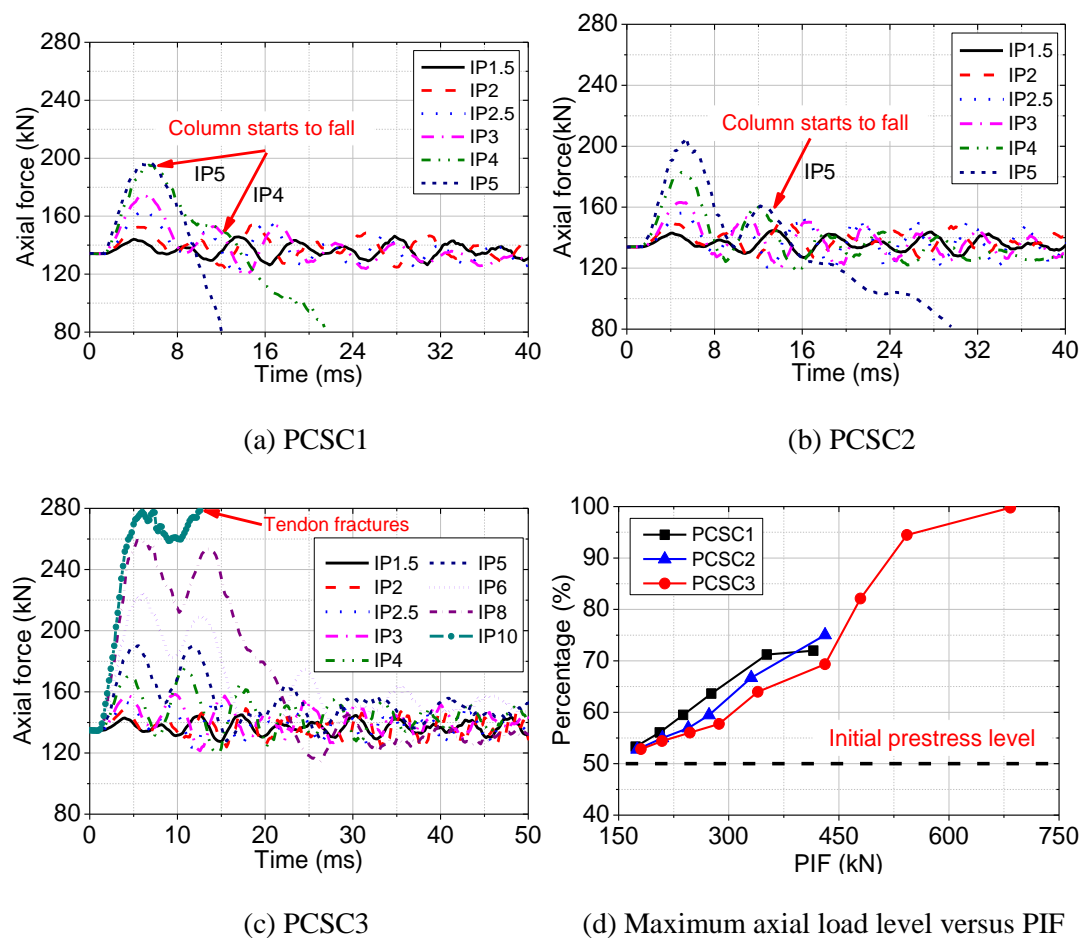
Figure 7-9 Axial force in the tendon (BT).

Furthermore, the maximum axial force level in the tendon of the three columns under various impact velocities is presented and compared in Figure 7-9d. The results indicate that the axial force in the tendon, which is associated with the joint openings, is significantly affected by the change of the impact velocity when the column is impacted at the top of the base segment. The increase of the impact velocity, which generates a higher PIF on the columns thus causes a higher maximum value of the axial force in the tendon. This is because the higher PIF causes

larger opening at the segment joints and thus a larger elongation in the tendon resulting in the higher maximum stress. It needs to be mentioned that the maximum values of the axial force in the tendon under IP4 and IP5 are almost the same because under these impact conditions, the column exhibits the diagonal shear failure of the impacted segment which absorbs a large amount of impact energy instead of the joint openings (see Figure 7-9d). The openings of the column at the two bottommost joints is thus almost identical, leading to the same maximum axial force in the tendon. Moreover, Figure 7-9d shows that the use of the steel tubes to confine the PCSC does not only reduce the maximum axial force in the tendon of the strengthened columns as compared to the conventional PCSC but also maximise the contribution of the tendon in controlling the impact response of the PCSC. Under the same impact velocity, the maximum axial force in the tendon of Column PCSC3 is slightly smaller than the others owing to the effect of the steel confinements (see Figure 7-9d). The use of steel tubes in Column PCSC3 increases the vertical stiffness of the segments and thus diminishes the vertical deformation in the compressive side of the concrete segment when the segment joints open. The smaller vertical deformation at the compression side of the column which reduces the width of the joint opening thus minimises the vertical elongation in the tendon. In the final stage, the maximum axial force in the tendon of Columns PCSC1 and PCSC2 is about 75% of its capacity (IP5) while that of Column PCSC3 is 100% at impact IP10 (see Figure 7-9d).

7.4.2. Impact at the centre of the base segment

7.4.2.1 Column responses and failure modes

Figures 7-10, 7-11, and 7-12 present the progressive damage and responses of the three PCSCs when they are impacted at the centre of Segment 1. Different from the above cases of columns being impacted at a different location in which the joint opening commonly results in the collapse of the columns, when the impact location is at the base-segment centre, the columns exhibit an excessive lateral movement at the base with a minor joint opening. The response of the column is thus associated with local damage at the impacted segment, i.e. PCSC1 and PCSC3 while the global deformation again dominates the response of Column PCSC2 owing to the influence of the steel tubes at the two bottommost segments. Under the impact velocity of 5 m/s (IP5), Column PCSC1 exhibits a flexural crack in Segment 1 at the PIF ($t = 3$ ms) while a large relative displacement between the footing and Segment 1 occurs since the friction force at the segment joint is insufficient to resist the shear force. The movement of Segment 1 is then interrupted by the contact between the steel duct and the tendon. The contact force between the tendon and Segment 1 together with the lateral impact force from the impactor thus cause an inclined shear crack in Segment 1 from the impact point toward the base segment joint at $t = 7$ ms (see Figure 7-10). Meanwhile, the opening at the second joint also results in a vertical crack in Segment 1. These cracks then enlarge and cause severe damage in Segment

174

1 at t =15 ms before resulting in the collapse of the entire column, as presented in Figure 7-10. It is worth mentioning that this failure mode of Column PCSC1 associated to the impact at the base segment was also observed in the previous experimental study (Zhang et al., 2018) (see Figure 7-10), indicating the reliability of the simulation results in this study.
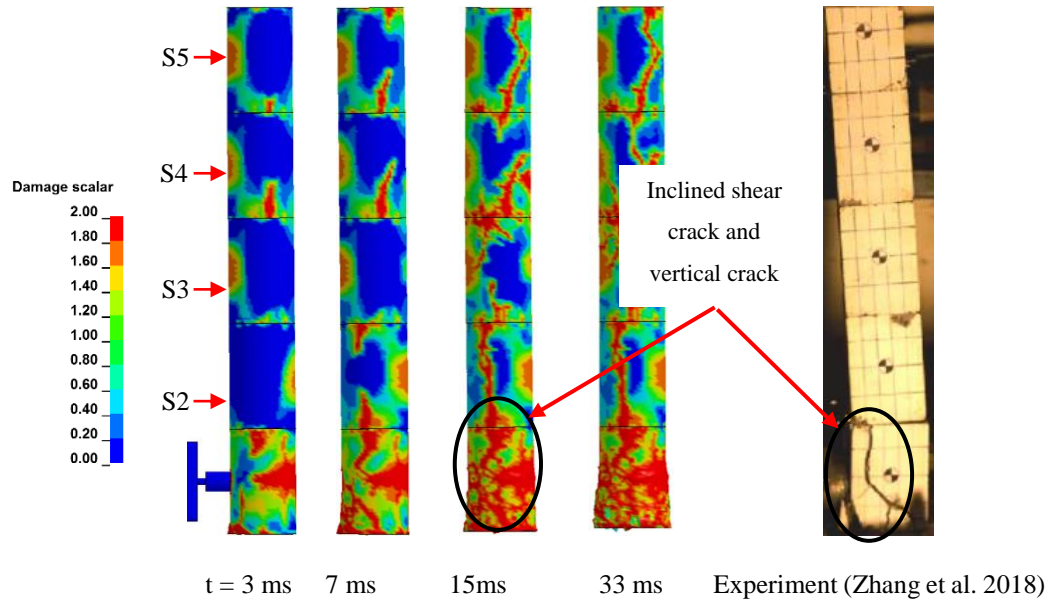
Figure 7-10 Response of the conventional PCSC - Column PCSC1 under impact IP5 – V = 5 m/s (BC).
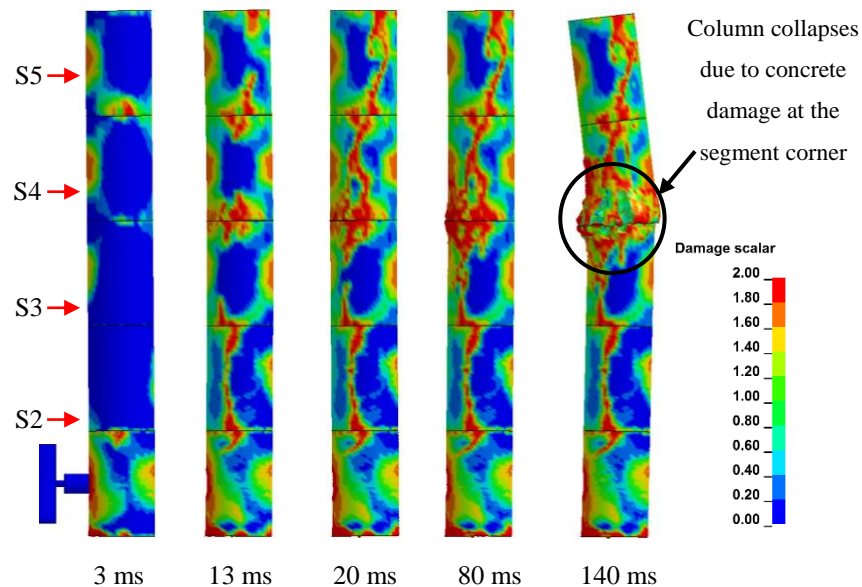
Figure 7-11 Response of the PCSC with partial strengthening – PCSC2 under impact IP5 – V = 5 m/s (BC).

On the other hand, the response of Column PCSC2 when impacted at the base centre is comparable with the previous impact condition where damage to the column is found at the segment joint between Segments 3 and 4 (see Figure 7-11). When the impact velocity is 5 m/s,

the column exhibits a vertical crack in Segments 1, 2, and 3 and shear cracks in segments 4 and 5 at t = 20 ms due to the joint openings and the increase of the axial force in the compression side of the column, as explained in the previous section as shown in Figure 7-11. Due to the vibration of the top mass, the high-frequency self-vibration of the concrete segments, and the joint openings, severe concrete damage happens at the edge of Segments 3 and 4 at t = 80 ms. The column then fails because of the excessive damage of Segment 4 at t = 140 ms.
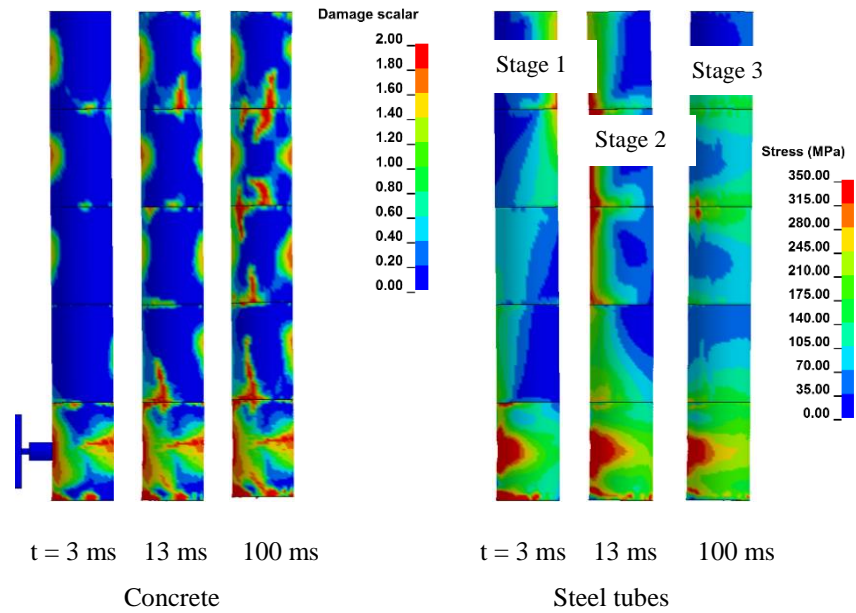
(a) IP5 (*V*= 5 m/s)
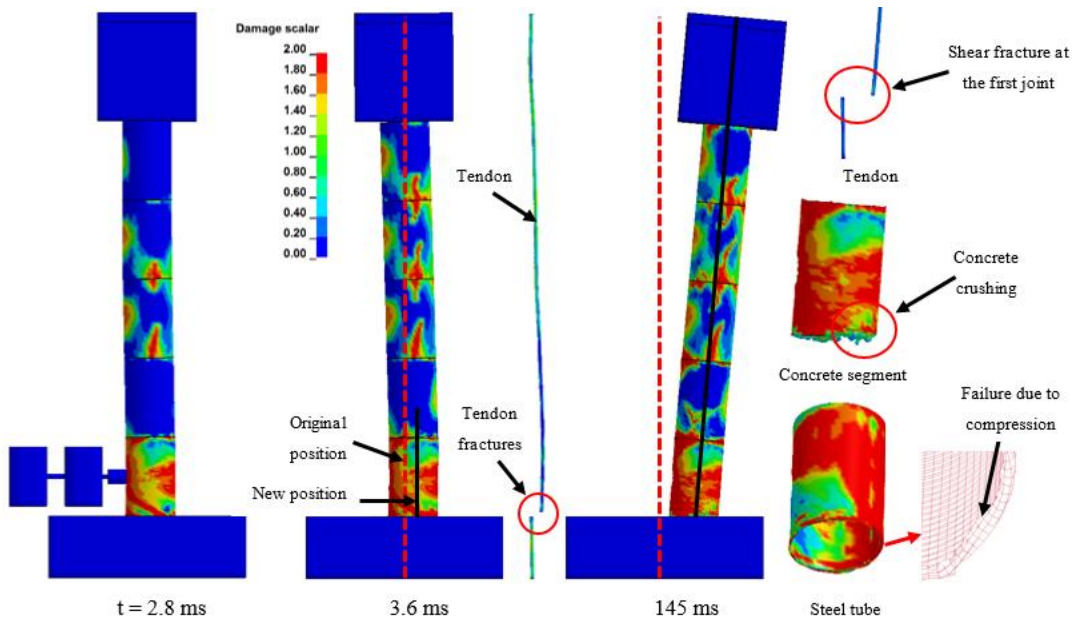
(a) IP10 (*V*= 10 m/s)

Figure 7-12 Impact responses of the PCSC-FST – Column PCSC3 (BC).

The impact response of Column PCSC3 under the impacts IP5 and IP10 is different from the other two columns, as illustrated in Figure 7-12. As can be seen that although a flexural crack and an inclined shear crack in Segment 1 occurs at about $t = 3$ ms under impacts IP5, Column PCSC3 securely stands after the whole impact process with no visible damage at the segment edge in the top part of the column as compared to Column PCSC2, see Figure 7-12a. It demonstrates that the steel tubes at Segments 3, 4, and 5 considerably mitigate the concrete damage in the compressive side of the column when the joints open, thus prevents collapse of the column. The stress distribution in the steel tubes of Column PCSC3 under this impact load is also presented in Figure 7-12a.

Similar to the column impacted at top of the bottom segment presented in the previous section, when impacted at the base centre, the stress in the steel tubes also includes three main stages. In Stage 1, the stress in the steel tube is mostly concentrated at the impact area at the PIF ($t = 3$ ms) while that at the edges of Segment 1 is marginal due to the small opening at the two bottommost joints. The joint opening then appears in the upper part of the column after the impact force phase, leading to the occurrence of the stress in the edge of the steel tubes in Stage 2 (see Figure 7-12), but it is less significant because of smaller joint opening. In the free vibration stage (Stage 3), the residual stress is also observed in the base steel tube due to damage of concrete at the impact area and the inclined shear crack of concrete in Segment 1. The results indicate that when the impactor strikes the column at the base centre, the base steel tube plays a significant role in mitigating the inclined shear cracks in Segment 1, thus prevents the collapse of the whole column. However, the contribution of the steel tubes in the upper segments of the column in resisting the impact loads is less prominent as compared to the above case when the column is impacted at the base top because of the less global response of the column and smaller opening of the segment joints. Under impact IP6 and IP8, the impact responses of the column, which are not shown here for brevity, are similar to that under impact IP5 with more plastic deformations at the impacted segment, but no severe damage occurs. Under impact IP10 ($V = 10$ m/s), the flexural crack and the inclined shear crack occur in Segment 1 at $t = 2.8$ ms and the entire column is shifted to the right side by the large PIF and a lack of anchorage of the bottom segment to the foundation (see Figure 7-12b). The excessive movement of the column causes a huge contact force between the tendon and the impact segment and thus results in a large shear force in the tendon. Hence, at $t = 3.6$ ms, the shear fracture occurs in the tendon at the joint between Segment 1 and the footing and more damage is induced in Segment 1 (see Figure 7-12b). The entire column then continues sliding due to the impact force while the supported mass on top of the column starts to move to the right side which causes a large eccentric load on the column top. The slippage of the column together with the eccentric load cause severe damage at the bottom face of Segment 1 at $t = 145$ ms, as

presented in Figure 7-12b. With the damage of concrete, the compression force leads to buckling and thus failure in the steel tube at the base segment. The column thus fails due to the failure of the posttensioned tendon, concrete, and steel tube, as shown in Figure 7-12b.

(a) PCSC1   (a) PCSC2

(c) PCSC3
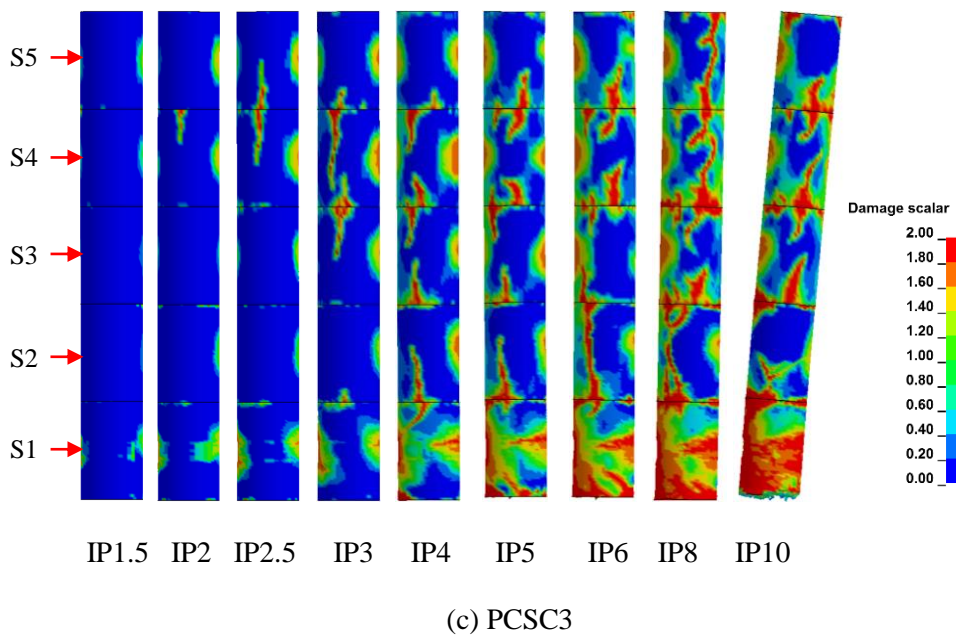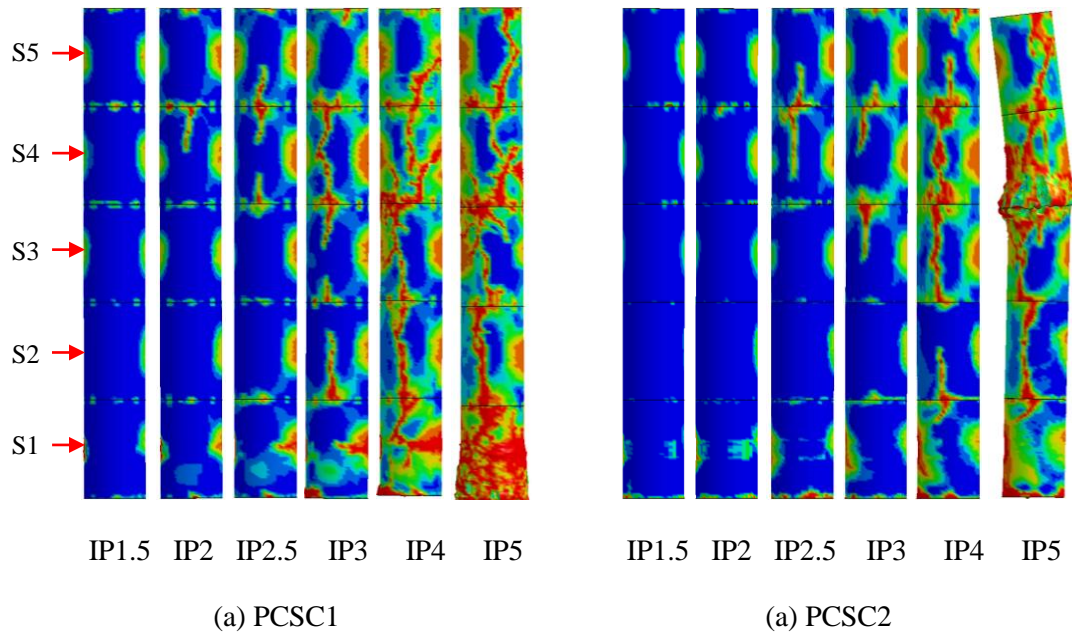
Figure 7-13 Damage to columns and its failure modes (BC).

Damage to the columns and failure mode of the three PCSCs under various impact velocities are compared in Figure 7-13. The figure indicates that the impact response of the PCSC is significantly changed by the use of steel tubes in the concrete segments. The local failure of Column PCSC1 at the impacted segment is altered to the global failure mode in Column PCSC2 where the damage at the segment edge between Segments 3 and 4 causes the collapse of the column. Meanwhile, the failure mode of Column PCSC3 is a combination of a severe

178

damage to concrete, steel tube, and the shear fracture of the tendon. The results also demonstrate that the concrete filled steel tubes provides a higher dynamic bending capacity for the concrete segment when the flexural crack occurs in Column PCSC1 under impact IP3 while similar flexural cracks only occur in Column PCSC3 under impact IP5. Furthermore, the PCSC incorporating with steel confinement in all the segments shows a better impact performance than the others when it is able to resist the impact velocity of 10 m/s while the other columns fail when being impacted by the velocity of 5 m/s (see Figure 7-13).

7.4.2.2 Tendon force time histories

The shear force and axial force time histories in the tendon at the section between Segment 1 and the footing of Column PCSC3 are presented in Figure 7-14. As can be seen that the impact response of the tendon in this impact condition is significantly different from that in the previous condition with the occurrence of the residual shear force and axial force due to the shear yielding of the tendon. Figure 7-14a shows that the maximum and residual shear force in the tendon increase with the impact velocity when large slippages at the segment joint occur, e.g. impacts IP5, IP6, and IP8. This is because, from the impact IP5, the PIF causes an excessive lateral slippage at the joint between Segment 1 and the footing, resulting in a huge contact force between the tendon and Segment 1. At this moment, the shear force in the tendon, therefore, reaches its maximum value (see Figure 7-14a). Likely, the contact force from the tendon is insufficient to pull the column back to its original position while the enormous movement of Segment 1 results in a shear yielding in the tendon (see Figure 7-14c). Hence, under the impacts IP5-8, after the impact force phase, the residual shear force is observed in the tendon while the axial force oscillates at a higher level than the initial prestress level (see Figures 7-14a and b). Furthermore, Figure 7-14 also shows that higher impact velocities, which result in more shear deformation in the tendon, cause larger residual axial force and shear force in the tendon. On the other hand, when the shear slippage at the joint is smaller than the gap between the tendon and the concrete segment, no contact between the tendon and concrete segments occurs during the impact force phase, e.g. the first five impact conditions (IP1.5 – IP4). Thus, the shear force in the tendon (under 3 kN) mostly occurs in the free vibration phase of the column (see Figure 7-14a) while the axial force in the tendon oscillates around its initial level after reaching the peak level at $t = 13$ ms when all the joints open (see Figure 7-14b). For the impact IP10, both the shear force and axial force in the tendon of Column PCSC3 suddenly drop to zero at $t = 3.6$ ms due to the shear fracture of the tendon. The results mainly show that when the base segment is impacted, the shear yielding and the residual shear force might occur in the tendon at low impact velocities before the column collapse. Thus, in the design of a PCSC under impact loads, the base segment should be properly anchored to the footing or shear keys should be provided to avoid shear yielding of the tendon.
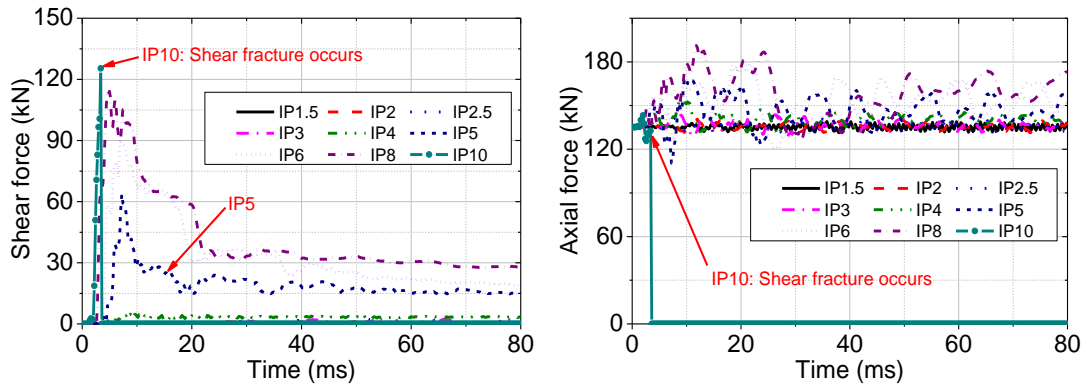
(a) Shear force time histories

(b) Axial force time histories
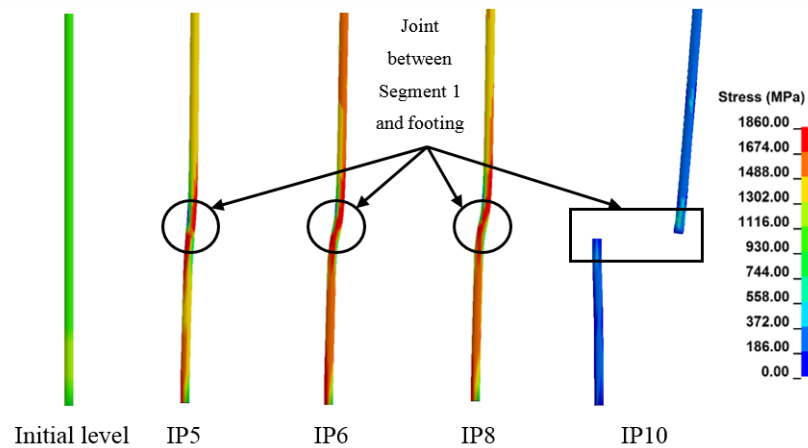
(c) Deformation and stress in the tendon

Figure 7-14 Shear force, axial force, and stress in the tendon of Column PCSC3 (BC).

Furthermore, the maximum shear force and axial force in the tendon of the three columns are also compared in Figure 7-15. The figure shows that the steel confinement has an insignificant effect on the shear force and axial force in the tendon when the impact velocity is relatively small, i.e., before IP5. This is because the shear capacity at the segment joint of these columns is provided by the friction force between the segments and therefore is the same, hence the shear slippage at the segment joint under the same impact condition is also the same. Moreover, only minor shear slippage and joint openings occur in the columns under impact IP1.5 to IP4 due to the moderate impact velocities. Therefore, similar maximum shear force and axial force in the tendon are observed for these columns. For Column PCSC1 under impact IP5, the inclined shear failure in Segment 1 occurs when the tendon and the concrete segment come in contact. Hence, smaller shear force and axial force in the tendon are observed. For Column PCSC3 under impact IP10, the shear fracture occurs when the shear force reaches 125.4 kN. Thus, the maximum axial force in the tendon in this impact velocity is only slightly higher than its initial prestress level before dropping to zero due to the shear fracture of the

tendon as shown in Figures 7-14b and c. The maximum shear force and axial force in the tendon of the columns are also given in Table 7-2.
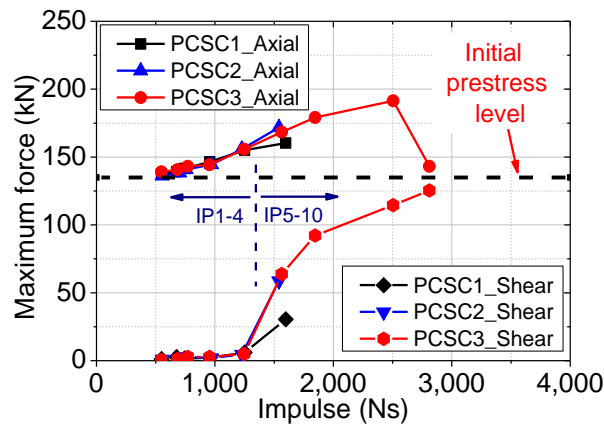
Figure 7-15 Comparisons of the maximum shear force and axial force in the tendon.

7.5. Effects of using steel shear keys

(a) SSK design   (b) Numerical simulation
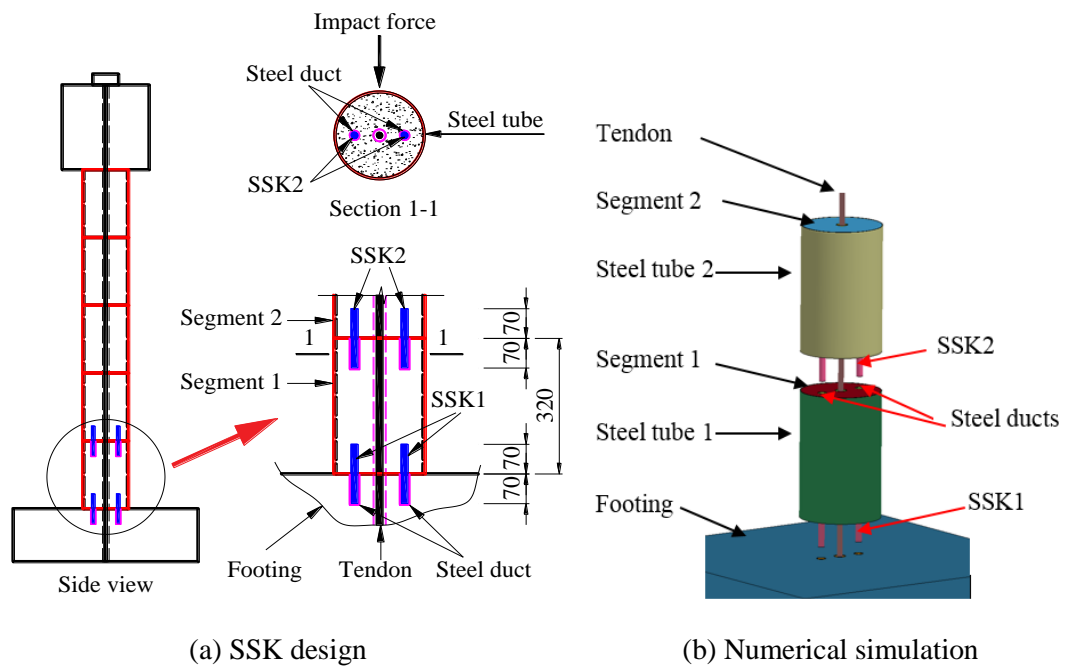
Figure 7-16 Column PCSC3 with SSK at the two bottommost joints.

The above results show that steel tube effectively mitigates the damage of concrete segments, and shifts the damage mode to excessive global flexural responses and large slippage between segments, which may lead to rupture of prestress tendons. To mitigate the large slippage between segments for protection of prestress tendons under impact load, adding shear keys between segments is suggested. To investigate the influence of shear keys, Column PCSC3 is integrated with steel shear keys (SSKs) at the two bottommost joints, namely Column SSK (see Figure 7-16). Each SSK connection includes a SSK and its joint hole, wherein the SSK is embedded in one segment to work as a tenon tongue while the joint hole is a steel duct which

181

is cast in another segment to serve as a mortise hole (see Figure 7-16a). This use of the SSKs in PCSCs to resist cyclic loads has been investigated in the previous study (Hung et al., 2017). The design of the SSK, which has a diameter of 16 mm and a length of 140 mm in this study, relies on the pure shear capacity of the steel section to sustain the impact force from impact events. The nominal gap between the SSK and the mortise hole is 2 mm which allows the concrete segment to rotate and slip before interrupting by the steel duct. The numerical model of Column SSK is presented in Figure 7-16b.
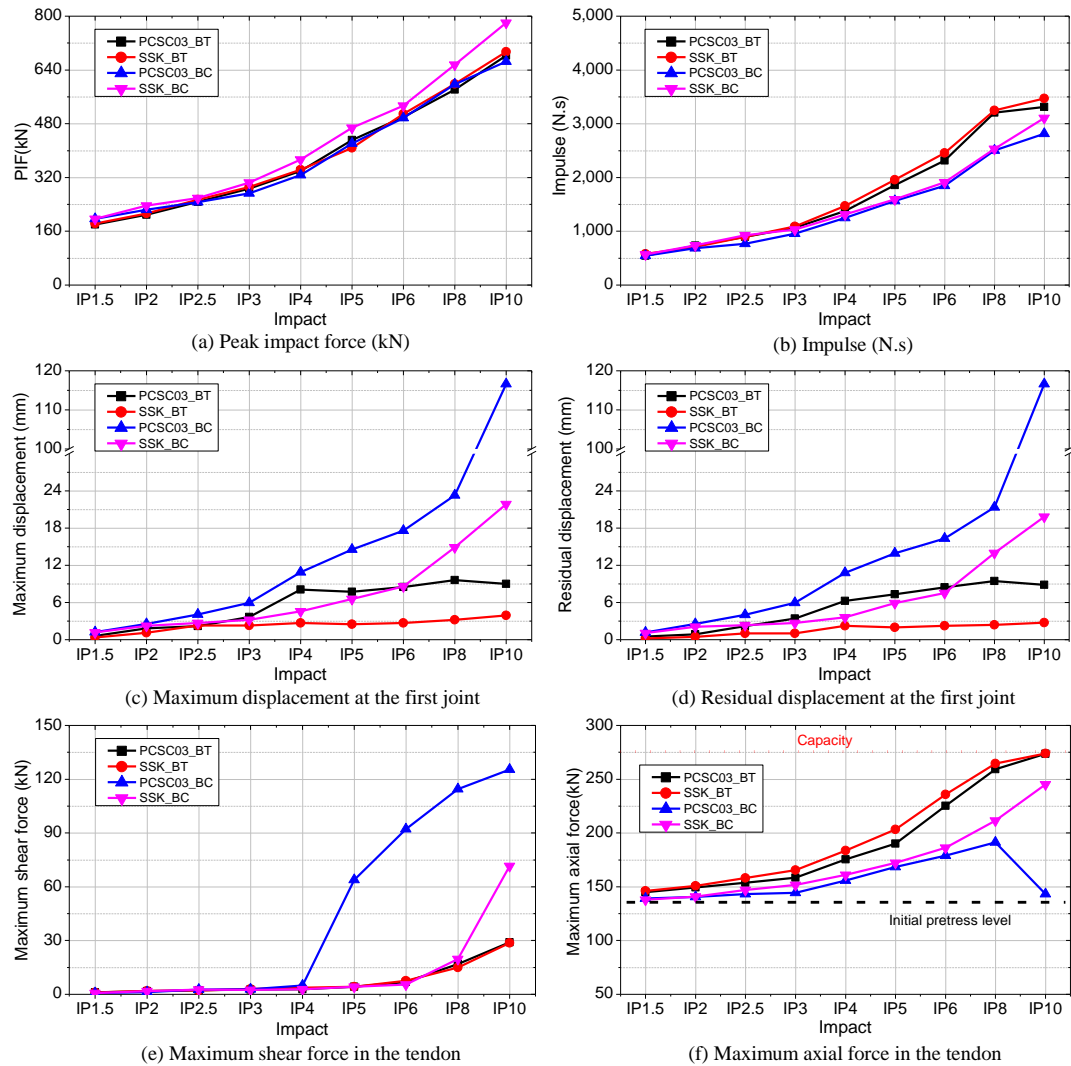
Figure 7-17 Comparisons of the column responses with and without shear keys.

The comparison of the impact responses between Columns PCSC3 and SSK under various impact velocities at two different locations are presented in Figure 7-17. It is noted that Columns SSK_BT and SSK_BC represent Column SSK impacted at different locations, i.e. at the base segment top and base segment centre, respectively. The results show that although the PIF and impulse in the two columns are comparable because of the similar contact stiffness, the column responses are significantly affected by the use of the SSKs (see Figure 7-17c, d

and e). Owing to the small gap between the SSK and its mortise hole, the lateral slippage between the concrete segments is obstructed when the SSK and the steel are in touch. This significantly reduces the maximum and residual slippage of the column (see Figure 7-17c and d), thus prevents the shear force and yielding in the tendon (see Figure 7-17e). The shear yielding in the tendon only occurs when the SSK is bent and its deformation is larger than the gap between the tendon and steel duct (see Figure 7-17e - IP10). It can be seen in Figure 7-17c and d that the reduction in the maximum and residual displacement at the base segment joint of Column SSK is about 5 mm and 10 mm when the columns are impacted at the base top and the base centre, respectively. It is highlighted that the gap between the tendon and steel duct in Column PCSC3 is 7 mm in each side while the gap between the SSK and its joint hole is 2 mm in Column SSK. Since no shear yielding of the tendon and the SSKs is observed in the two columns when the columns are impacted at the base top, the maximum displacement of Columns PCSC3 and SSK (impacts IP4-IP10) is thus around 7 mm and 2 mm, respectively (see Figure 7-17c). On the other hand, when being impacted at the base centre, the columns are totally pushed to slide away by the impact force. The maximum lateral displacement of the columns is thus much larger than their total free gap because of the occurrence of the inclined cracks of concrete and the shear deformation of the tendon and the SSKs. In these cases, the difference of the maximum and residual displacement between these columns is also the difference of the total free gap (10 mm), except for impact IP10 where the tendon fractures in Column PCSC3. Since the impacted segment could not return to its original position after the impact force, the residual displacement of these columns under two impact locations is thus nearly the same with its maximum value, as given in Figure 7-17d. Furthermore, the smaller lateral displacement of Column SSK at the segment joint thus greatly reduces the maximum shear force in the tendon as compared to Column PCSC3 when these columns are subjected to impact at the base centre (see Figure 7-17e). As can be observed in the figure that the shear force in the tendon of Column PCSC3_BC significantly increases from the impact IP5 while that in Column SSK_BC just appears in the impact IP9 when the SSKs are already bent. The shear yielding of the tendon is thus eliminated in Column SSK_BC from IP1.5 to IP8. However, the influence of the SSKs in reducing the shear force in the tendon when the column is impacted at the top of the base segment is insignificant because the columns are dominated by the joint openings in this condition (see Figure 7-17e). Similarly, the axial force in the tendon caused by the opening of the joints is also less affected by the use of the SSKs in the PCSC when the similar maximum axial force in the tendon is simulated in the two columns, as shown in Figure 7-17f. Therefore, the posttensioned tendon of Column SSK_BT fractures at the same impact velocity with Column PCSC3_BT. Generally, the contributions of the SSK are substantial in reducing the lateral shear slippages between the segments, thus preventing

the shear plastic deformation of the tendon, but its contribution is less prominent when the joint opening dominates the column response.

7.6. Conclusions

This study numerically investigates the effects of the steel confinement on the behaviour of precast segmental columns under impact loads. The impact responses of three PCSCs including a conventional PCSC, a PCSC confined by steel tubes at the two bottommost segments, and a PCSC with all the segments made of concrete-filled steel tubes are thus considered and simulated. The contributions of steel shear keys in resisting the impact force are also examined. The conclusions of the study are as follows:

1. The impact response of a PCSC has significantly changed by using the steel tubes to cover the concrete segments. While the local failure mode of the concrete segment, i.e. diagonal shear failure and inclined shear crack, dominates the response of the conventional PCSC, the failure of a PCSC with segments confined by steel tubes is associated with failure of the tendon and/or concrete crushing at the impacted segment.

2. The use of steel confinement in all concrete segments does not only prevent the brutal damage of concrete at the impacted segment and reduce the axial force in the tendon but also enhance the impact capacity of the column. The PCSC-FST survives until the impact velocity of 10 m/s compared to 4 m/s of the conventional PCSC.

3. The use of the steel tubes at the two bottommost segments shifts the failure of the PCSC from local to the global response, i.e. the failure of the concrete at the segment edge.

4. The change of the impact location significantly affects the responses of the PCSCs. The shear slippage at the base segment joint governs the column response when the column is impacted at the centre of the base segment while the opening at the segment joint causes the failure of the column when it is impacted at the top of the base segment.

5. The incorporation of the steel shear keys at the two bottommost joints in the PCSC-FST considerably reduces the lateral displacement of the column and shear force in the tendon, thus prevents the shear yielding, especially when the joint sliding dominates the column response. However, it is not effective in reducing the axial force in the tendon.

The above findings showed that confining the concrete segments greatly enhanced the impact resistant capacity of the segmental columns, but under large impact loads the tensile stress in the tendon caused by the joint openings could be large and lead to tendon fracture, therefore the initial prestress load in the tendon of the PCSC is suggested to be smaller than 70% of its ultimate tensile strength to prevent the premature failure of the tendon under moderate to large impact loads. It is also recommended that all concrete segments should be confined instead of only the local impact area when a PCSC is under impact loads. The cover of all segments does

not only protect the column from the local failure at the impacted segment but also mitigate the damage at the segment edge in the upper segments caused by the global response of the column. Also, the impact point is suggested to be designed in the vicinity of the top of the bottom segment (close to the segment joint) to prevent shear yielding of the tendon and reduce the residual displacement of the column caused by the impact loads.

7.7. References

AASHTO. (2012). *AASHTO LRFD bridge design specifications (customary U.S. units)*. 6th Ed., Washington, DC.

Abdelkarim, O. I., & ElGawady, M. A. (2016). Performance of hollow-core FRP–concrete–steel bridge columns subjected to vehicle collision. *Engineering Structures, 123*, 517-531.

ACI. (2008). *Building code requirements for structural concrete (ACI 318-08) and commentary (ACI318R-08)*. Farmington Hills, MI: ACI 318.

Aghdamy, S., Thambiratnam, D., Dhanasekar, M., & Saiedi, S. (2017). Effects of load-related parameters on the response of concrete-filled double-skin steel tube columns subjected to lateral impact. *Journal of Constructional Steel Research, 138*, 642-662.

Aghdamy, S., Thambiratnam, D. P., Dhanasekar, M., & Saiedi, S. (2015). Computer analysis of impact behavior of concrete filled steel tube columns. *Advances in Engineering Software, 89*, 52-63.

Chou, C. C., & Hsu, C. P. (2008). Hysteretic model development and seismic response of unbonded post-tensioned precast CFT segmental bridge columns. *Earthquake Engineering & Structural Dynamics, 37*(6), 919-934.

Cowper, G. R., & Symonds, P. S. (1957). *Strain-hardening and strain-rate effects in the impact loading of cantilever beams*.

Culmo, M. P. (2011). *Accelerated bridge construction-experience in design, fabrication and erection of prefabricated bridge elements and systems*. Washington, DC.

Do, T. V., Pham, T. M., & Hao, H. (2018a). Dynamic responses and failure modes of bridge columns under vehicle collision. *Engineering Structures, 156*, 243-259.

Do, T. V., Pham, T. M., & Hao, H. (2018b). Numerical investigation of the behavior of precast concrete segmental columns subjected to vehicle collision. *Engineering Structures, 156*, 375-393.

Do, T. V., Pham, T. M., & Hao, H. (2019). Impact Response and Capacity of Precast Concrete Segmental versus Monolithic Bridge Columns. *Journal of Bridge Engineering, 24*(6), 04019050.

Guerrini, G., Restrepo, J. I., Massari, M., & Vervelidis, A. (2014). Seismic behavior of posttensioned self-centering precast concrete dual-shell steel columns. *Journal of Structural Engineering, 141*(4), 04014115.

Han, L.-H., Hou, C.-C., Zhao, X.-L., & Rasmussen, K. J. R. (2014). Behaviour of high-strength concrete filled steel tubes under transverse impact loading. *Journal of Constructional Steel Research, 92*, 25-39.

Hao, H., Do, T. V., & Pham, T. M. (2018, 25-26/10). *Structural Performance Evaluation of Prefabricated Concrete Segmental Columns and Conventional Monolithic Columns against Vehicle Impact.* Paper presented at the 7th International Conference on the Protection of Structures against Hazards, Hanoi, Vietnam

Hao, H., Zhang, X., Li, C., & Do, T. V. (2017). *Impact response and mitigation of precast concrete segmental columns.* Paper presented at the 12th International Conference on Shock and Impact Loads on Structures, Singapore

Hewes, J. T., & Priestley, M. N. (2002). *Seismic design and performance of precast concrete segmental bridge columns* (SSRP-2001/25). University of California.

Hu, C.-M., Han, L.-H., & Hou, C.-C. (2018). Concrete-encased CFST members with circular sections under laterally low velocity impact: Analytical behaviour. *Journal of Constructional Steel Research, 146*, 135-154.

Hung, H.-H., Sung, Y.-C., Lin, K.-C., Jiang, C.-R., & Chang, K.-C. (2017). Experimental study and numerical simulation of precast segmental bridge columns with semi-rigid connections. *Engineering Structures, 136*, 12-25.

Jiang, H., Wang, X., & He, S. (2012). Numerical simulation of impact tests on reinforced concrete beams. *Materials & Design, 39*, 111-120.

Lee, Y. W., Seo, J., Kim, S., Kang, Y. J., & Won, D. (2018). Cyclic Lateral Performance Evaluation of Precast Double-Skinned Composite Tubular Columns. *International Journal of Steel Structures, 18*(1), 97-113.

Li, C., Hao, H., & Bi, K. (2017). Numerical study on the seismic performance of precast segmental concrete columns under cyclic loading. *Engineering Structures, 148*, 373-386.

Li, C., Hao, H., Zhang, X., & Bi, K. (2017). Experimental study of precast segmental columns with unbonded tendons under cyclic loading. *Advances in Structural Engineering, 21*(3), 319-334.

Li, J., & Hao, H. (2014). Numerical study of concrete spall damage to blast loads. *International journal of impact engineering, 68*, 41-55.

Malvar, L. J., & Crawford, J. E. (1998). *Dynamic increase factors for steel reinforcing bars [C].* Paper presented at the The Twenty-Eighth DoD Explosives Safety Seminar Held, Orlando, USA

Naaman, A. E. (1982). *Prestressed concrete analysis and design: Fundamentals*: McGraw-Hill New York.

Nakalswamy, K. K. (2010). *Experimental and numerical analysis of structures with bolted joints subjected to impact load* (Doctoral dessertation). University of Nevada, Las Vegas Retrieved from https://core.ac.uk/download/pdf/62872865.pdf

Ou, Y.-C. (2007). *Precast segmental post-tensioned concrete bridge columns for seismic regions* (Doctoral dessertation). State University of New York at Buffalo Retrieved from https://ubir.buffalo.edu/xmlui/handle/10477/42969

Ou, Y.-C., Wang, P.-H., Tsai, M.-S., Chang, K.-C., & Lee, G. C. (2009). Large-scale experimental study of precast segmental unbonded posttensioned concrete bridge columns for seismic regions. *Journal of structural engineering, 136*(3), 255-264.

Shim, C. S., Chung, C.-H., & Kim, H. H. (2008). Experimental evaluation of seismic performance of precast segmental bridge piers with a circular solid section. *Engineering Structures, 30*(12), 3782-3792.

Sideris, P. (2012). *Seismic analysis and design of precast concrete segmental bridges* (Doctoral dessertation). State University of New York at Buffalo Retrieved from https://search.proquest.com/docview/1114474220?pq-origsite=gscholar

Wang, R., Han, L.-H., & Hou, C.-C. (2013). Behavior of concrete filled steel tubular (CFST) members under lateral impact: Experiment and FEA model. *Journal of Constructional Steel Research, 80*, 188-201.

Yan, X., & Yali, S. (2012). Impact behaviors of CFT and CFRP confined CFT stub columns. *Journal of Composites for Construction, 16*(6), 662-670.

Zhang, X., Hao, H., & Li, C. (2016). Experimental investigation of the response of precast segmental columns subjected to impact loading. *International Journal of Impact Engineering, 95*, 105-124.

Zhang, X., Hao, H., Li, C., & Do, T. V. (2018). Experimental study on the behavior of precast segmental column with domed shear key and unbonded Post-Tensioning tendon under impact loading. *Engineering Structures, 173*, 589-605.

CHAPTER 8
CONCLUSIONS

8.1. Findings

In this study, the dynamic responses of monolithic RC columns and precast concrete segmental columns (PCSCs) against vehicle collisions and impact loads have been numerically and analytically investigated. The effect of column parameters and initial impact conditions on the impact force time histories and dynamic performances of the columns has been systematically examined. Based on the numerical results and analytical derivations, the dynamic shear capacity of a RC column, as well as the dynamic bending moment capacity of a PCSC, were determined. Furthermore, PCSCs with steel confinements were studied in this research to address the issues arising from the local failure of concrete segments under impact loads. The major contributions of this study are summarised as follows:

Part 1 Monolithic reinforced concrete columns under impact loads

Dynamic analysis of reinforced concrete (RC) columns under vehicle collisions

- A collision from a vehicle usually produces two peak impact forces (PIFs) on RC columns caused by the engine impact and cargo impact. The impact from the engine generates the highest PIF on the column while the cargo impact causes a smaller magnitude of PIF but with longer duration and hence a larger impulse. The PIF from the engine impact governs the maximum bending moment and shear force induced by the vehicle collision, and thus the column failure but it is currently ignored in design codes and provisions. The results imply that in the design of structures under vehicle collisions both the engine mass and vehicle mass have to be considered instead of only total mass of a vehicle.

- Assuming a rigid column or using an elastic material model for bridge pier in numerical simulations, which neglects concrete damage at the contact area between vehicle model and column structure, likely causes an overestimation of the impact force, especially from the cargo impact.

- The common assumption of the linear distribution of the inertia force along the column under vehicle collision is un-conservative in some scenarios since it ignores the stress wave propagation and high-modes column responses to impact load. The use of the SDOF in predicting the behaviour of the structures under impact loads might not yield reliable predictions either.

- In the dynamic analyses and design of RC columns to resist impact loads, four critical sections, i.e. impact location, column base, column top, and an intermediate section, need

to be carefully considered and designed. Under different impact conditions, the location of the maximum internal bending moment at intermediate section varies from the column top to the impact location and from the positive side to the negative side of the column.

- The numerical simulations in this study can produce almost all the failure modes of RC columns observed in real collision events. The explanation of each failure mode was therefore able to be given in this study.

Design of RC columns under vehicle collisions

- An analytical model is proposed to predict the vehicle impact loading profile on square RC columns corresponding to four continuous stages, i.e. bumper impact, engine impact, truck rail impact, and cargo impact. In this model, the influences of the initial impact conditions of a vehicle, column parameters, and column failures have been considered. Predictions from the proposed analytical model match well with the numerical simulations

- Based on the shear mechanism of RC columns under impact loads, the maximum shear capacity of the column, $P_{dyn}^{\max}$, is determined by taking into consideration the strain rate effects and inertia resistance.

- From the impact force profile model and dynamic shear capacity of a RC column, the dynamic response of the RC columns is categorised into two groups, i.e. flexural response ($PIF < 0.5P_{dyn}^{\max}$) and shear response ($PIF \geq 0.5P_{dyn}^{\max}$). In the former group, damage to the column is related to flexural cracks at the three critical sections including the column base, impact location, and the intermediate section while in the latter group, diagonal shear failure or punching shear failure occurs at the impact area. Thus, in the design of a RC column under vehicle collisions, the dynamic resistance capacity of the column needs to be able to resist both the global damage caused by the flexural response and the local shear failure.

- Empirical equations to determine the maximum shear force and bending moment at the critical sections are proposed for use in design analysis. The accuracies of these proposed analytical predictions are verified against high fidelity numerical simulations.

- Based on the impact force profile, maximum induced bending moment and shear force, failure classification, and the dynamic capacity of the column, a complete procedure to design the RCBC against vehicle collision is proposed. The procedure can be used to design a wide range of column dimensions under various initial impact loading conditions. Meanwhile, two design examples which represent two different failure modes of RC columns under impact loads are also presented to illustrate the proposed design procedure for users. The results indicate that the proposed procedure can reliably predict

the column responses under impact loads but avoids detailed finite element models. The procedure, therefore, can be used in the design analysis of RC columns under vehicle collisions.

Part 2 Precast concrete segmental columns under impact loads

Dynamic analysis of precast concrete segmental columns

- A detailed finite element model of a precast segmental concrete column (PCSC) under impact loads has been built in this study with an effective modelling technique to simulate the prestressing force for unbonded tendons in structures. The contact between concrete segments is also carefully considered. The simulation results agree well with the experimental results, hence are used to explain some phenomena, i.e. the occurrence of multiple PIFs, as observed in the experimental tests.

- Under impact loads, the response of the PCSC contains two types of vibration, i.e. segment self-vibration and column vibration. The vibration of segments at the local contact area usually produces several PIFs which might affect the response and failure of the entire column. The variation of the impact location along the segment height also considerably influences the occurrences of multiple peaks of impact load.

- The increase in the initial prestressing force enhances the shear resistance at segment joints, reduces the relative slippage between the concrete segments, and diminishes the lateral displacement of the column. However, the initial prestressing force does not show a considerable influence on the impact force.

- Owing to the rotation and slippage of the segments under impact loads, the induced bending moment and shear force of a PCSC are much smaller than those of a monolithic RC column when these columns are subjected to the same impact conditions. Therefore, more energy dissipation but less damage to concrete is observed in the PCSC as compared to the monolithic one.

- Under vehicle collisions, the failure of the PCSC is associated with the compressive damage and combined flexural-shear damage at local impacted segments while damage to concrete of the monolithic RC column occurs at various sections along the column height. The result shows the advantages of the PCSC in localising the damage of column structures under vehicle collisions and impact loads.

Design of precast concrete segmental columns under impact loads

- The initial prestressing load in post-tensioned tendons is suggested to be smaller than 70% of their tensile strength to prevent the premature failure of the tendon under low–to-moderate impact conditions.

190

- The height-to-depth ratio of a segment should be lower than two to avoid the flexural cracks at the rear surface of the segment. Meanwhile, this ratio should not be too small to prevent severe damage of concrete segment at the local contact area. In this study, the ratio of the segment height to column depth ranges from 1.4 to 1.8 is suggested.

- Under vehicle collisions, the base segment of the PCSC is extremely important. It can absorb up to 80% of the total absorbed energy of the entire columns.

- To design a PCSC against vehicle collision, the impact location is recommended to be close to the top of the base segment to prevent shear yielding and failure of the tendon and reduce the residual displacement of the column caused by the impact loads.

- An equation to predict the bending moment that leads to the opening of segments joints is proposed in which the initial compressive loads and column dimensions provide the main contributions.

- The ultimate bending moment capacity of the PCSC at the joint is determined where the dynamic increase factor and stress wave propagation caused by impact loads are taken into account.

Strengthening of precast concrete segmental columns under impact loads

- Partially strengthening a PCSC, i.e., strengthening only the impacted segments by using steel tubes increases the dynamic capacity of the segments, and thus the dynamic capacity of the entire column. Its effect, however, is insignificant since the failure of the column shifts to upper segments due to the global response.

- Confining all concrete segments by steel tubes is more effective in protecting the PCSC under impact when both local shear failure of the impacted concrete segments and compressive damage at upper segments caused by global response are diminished. In this condition, the rupture of the posttensioned tendons occurs in the PCSC at the ultimate impact load.

- The use of steel shear keys at segment joints significantly mitigates the relative slippage between the segments in the PCSC, which thus prevents the shear deformation and shear fracture of the tendon, especially when the column response is governed by joint slippages. However, its effect is marginal when the joint opening dominates the column response.

8.2. Recommendations for future studies

From the findings and conclusions in this study, the following recommendations are given for possible future studies:

1. This study carries out numerical and analytical analysis on the dynamic response of monolithic and segmental reinforced concrete (RC) columns under vehicle collisions. Experimental collision tests on these columns are needed to further validate the observation in the present study.

2. It is well known that unbonded steel tendons in segmental columns might suffer from corrosion during its service life. In this case, using non-corrosive posttensioned tendon, e.g. FRP tendon, in segmental columns could be an effective way to protect tendons, and thus the column. The dynamic analysis of segmental columns with non-corrosive tendons could be an interesting topic. Moreover, the general aging of construction materials which significantly affects the performance of segmental concrete structures needs also to be carefully considered in future works.

3. During working conditions, the fatigue of posttensioned tendons and their connections might occur caused by oscillating service loads from vehicle loads on bridges. The failure of one or several posttensioned tendons may significantly change the static and dynamic responses of precast segmental columns. Therefore, this topic also requires further studies.

4. Most of the current studies focus on the seismic and impact responses of segmental columns while studies on blast resistance capacity of the column have received limited attention, which could be investigated.

APPENDIX I: ATTRIBUTION OF AUTHORSHIP

Paper 1: "**Dynamic responses and failure modes of bridge columns under vehicle collision**". Engineering Structures, Vol 156, pages 243-259.

Authors and full affiliations: Van Tin Do, Curtin University

Dr. Thong Pham, Curtin University

Professor Hong Hao, Curtin University

	Conception and design	Acquisition of data & method	Data conditioning & manipulation	Analysis & statistical method	Interpretation & discussion	Final approval
Van Tin Do	X	X	X	X	X	
I acknowledge that these represent my contribution to the above research output. Singed: ▓▓▓▓▓▓▓						
Dr. Thong Pham	X			X	X	X
I acknowledge that these represent my contribution to the above research output. Singed: ▓▓▓▓▓▓▓						
Prof. Hong Hao	X				X	X
I acknowledge that these represent my contribution to the above research output. Singed: ▓▓▓▓▓▓▓						

Paper 2: "**Impact force profile and failure classification of reinforced concrete bridge columns against vehicle impact**". Engineering Structures, Vol 183, pages 443-458.

Authors and full affiliations: Van Tin Do, Curtin University

Dr. Thong Pham, Curtin University

Professor Hong Hao, Curtin University

	Conception and design	Acquisition of data & method	Data conditioning & manipulation	Analysis & statistical method	Interpretation & discussion	Final approval
Van Tin Do	X	X	X	X	X	
I acknowledge that these represent my contribution to the above research output. Singed: ▓▓▓▓▓▓▓						
Dr. Thong Pham	X			X	X	X
I acknowledge that these represent my contribution to the above research output. Singed: ▓▓▓▓▓▓▓						
Prof. Hong Hao	X				X	X
I acknowledge that these represent my contribution to the above research output. Singed: ▓▓▓▓▓▓▓						

Paper 3: **"Proposed Design Procedure for Reinforced Concrete Bridge Columns against Vehicle Collisions"**.

Authors and full affiliations: Van Tin Do, Curtin University

Dr. Thong Pham, Curtin University

Professor Hong Hao, Curtin University

	Conception and design	Acquisition of data & method	Data conditioning & manipulation	Analysis & statistical method	Interpretation & discussion	Final approval
Van Tin Do	✗	✗	✗	✗	✗	
I acknowledge that these represent my contribution to the above research output. Singed:						
Dr. Thong Pham	✗			✗	✗	✗
I acknowledge that these represent my contribution to the above research output. Singed:						
Prof. Hong Hao	✗				✗	✗
I acknowledge that these represent my contribution to the above research output. Singed:						

Paper 4: **"Numerical investigation of the behavior of precast concrete segmental columns subjected to vehicle collision"**. Engineering Structures, Vol 156, pages 375-393.

Authors and full affiliations: Van Tin Do, Curtin University

Dr. Thong Pham, Curtin University

Professor Hong Hao, Curtin University

	Conception and design	Acquisition of data & method	Data conditioning & manipulation	Analysis & statistical method	Interpretation & discussion	Final approval
Van Tin Do	✗	✗	✗	✗	✗	
I acknowledge that these represent my contribution to the above research output. Singed:						
Dr. Thong Pham	✗			✗	✗	✗
I acknowledge that these represent my contribution to the above research output. Singed:						
Prof. Hong Hao	✗				✗	✗
I acknowledge that these represent my contribution to the above research output. Singed:						

Paper 5: "**Impact response and capacity of precast concrete segmental versus monolithic bridge columns**". Journal of Bridge Engineering, Vol 24, pages 04019050.

Authors and full affiliations: Van Tin Do, Curtin University

Dr. Thong Pham, Curtin University

Professor Hong Hao, Curtin University

	Conception and design	Acquisition of data & method	Data conditioning & manipulation	Analysis & statistical method	Interpretation & discussion	Final approval
Van Tin Do	✕	✕	✕	✕	✕	
I acknowledge that these represent my contribution to the above research output. Singed: ▆▆▆▆▆▆▆						
Dr. Thong Pham	✕			✕	✕	✕
I acknowledge that these represent my contribution to the above research output. Singed: ▆▆▆▆▆▆						
Prof. Hong Hao	✕				✕	✕
I acknowledge that these represent my contribution to the above research output. Singed: ▆▆▆▆▆▆						

Paper 6: "**Effects of steel confinement and shear keys on the impact responses of precast concrete segmental columns**". Journal of Constructional Steel Research, Vol 158, pages 331-349.

Authors and full affiliations: Van Tin Do, Curtin University

Dr. Thong Pham, Curtin University

Professor Hong Hao, Curtin University

	Conception and design	Acquisition of data & method	Data conditioning & manipulation	Analysis & statistical method	Interpretation & discussion	Final approval
Van Tin Do	✕	✕	✕	✕	✕	
I acknowledge that these represent my contribution to the above research output. Singed: ▆▆▆▆▆▆						
Dr. Thong Pham	✕			✕	✕	✕
I acknowledge that these represent my contribution to the above research output. Singed: ▆▆▆▆▆▆						
Prof. Hong Hao	✕				✕	✕
I acknowledge that these represent my contribution to the above research output. Singed: ▆▆▆▆▆▆						

APPENDIX II: COPYRIGHT CLEARANCE

The proof of the rights and permissions, granted by Elsevier and American Society of Civil Engineers (ASCE) for the publications that embedded in this thesis, to reproduce the contribution in thesis are attached below.

Do, T. V., Pham, T. M., & Hao, H. (2018). Dynamic responses and failure modes of bridge columns under vehicle collision. *Engineering Structures, 156*, 243-259. https://doi.org/10.1016/j.engstruct.2017.11.053

Do, T. V., Pham, T. M., & Hao, H. (2019). Impact force profile and failure classification of reinforced concrete bridge columns against vehicle impact. *Engineering Structures, 183*, 443-458. https://doi.org/10.1016/j.engstruct.2019.01.040

Do, T. V., Pham, T. M., & Hao, H. (2019). Proposed Design Procedure for Reinforced Concrete Bridge Columns against Vehicle Collisions. Structures, 22(2019), 213-229. https://doi.org/10.1016/j.istruc.2019.08.011

Do, T. V., Pham, T. M., & Hao, H. (2018). Numerical investigation of the behavior of precast concrete segmental columns subjected to vehicle collision. *Engineering Structures, 156*, 375-393. https://doi.org/10.1016/j.engstruct.2017.11.033

Do, T. V., Pham, T. M., & Hao, H. (2019). Effects of steel confinement and shear keys on the impact responses of precast concrete segmental columns. *Journal of Constructional Steel Research, 158*, 331-349. https://doi.org/10.1016/j.jcsr.2019.04.008

Do, T. V., Pham, T. M., & Hao, H. (2019). Impact Response and Capacity of Precast Concrete Segmental versus Monolithic Bridge Columns. *Journal of Bridge Engineering, 24*(6), 04019050. https://doi.org/10.1061/(ASCE)BE.1943-5592.0001415

Figure 5-10 and Figure 2-6 – Experimental results (the figures are reused from the previous work by Zhang el al., (2016))

Figure 7.2c – Experimental test (The figure is reused from the previous work by Wang el al., (2013))

BIBLIOGRAPHY DISCLAIMER

Every reasonable effort has been made to acknowledge the owners of copyright material. I would be pleased to hear from any copyright owner who has been omitted or incorrectly acknowledged.